PHD

An ab-initio theoretical description of vibrational, and electronic states, in pristine and doped organic semiconductors.

(Alternative Format Thesis)

Fontanesi, Claudio

Award date:
2017

Awarding institution:
University of Bath

An ab-initio theoretical description of vibrational, and electronic states, in pristine and doped organic semiconductors.

Claudio Fontanesi

A thesis submitted for the degree of Doctor of Philosophy

University of Bath

Department of Physics

June 2017

Abstract

This PhD thesis deals with research activity in organic electronics, an extremely exciting field of fundamental science, which is complemented by relevant applications in every-day life: optoelectronics, solar energy conversion (photovoltaics), sensing and information technology, just to mention a few. In this area, charge transfer/energy transfer processes, as well as light matter interaction, play a major role. Within this topic, this work focus on the theoretical study of the electronic structure and related charge transfer/spectroscopic properties of various molecular systems: Coronene crystals, F4TCNQ/perylene co-crystals, polythiophenes, PCPDT/PCPDT-BT homo- and co-polymer based on thiophene, chemisorbed ferrocene on Si(111) substrate. Particular attention was devoted to the calculation of infrared (IR) and electronic spectra associated with the so-called "polaron signature" in doped organic semiconductors.

To assess the reliability and physical meaning of electronic quantities involved in the calculations (like the HOMO/LUMO gap, theoretical spectroscopic intensity and vibrational modes, pursuing the comparison between neutral and charged systems) a number of different levels of the theory have been systematically varied from HF (Hartree-Fock) to "pure" DFT (Density Functional Theory), as well as hybrid B3LYP (Becke 3-Parameter (Exchange), Lee, Yang and Parr [1,2]) and long range corrected Coulomb-Attenuating Method (CAM-B3LYP) functionals. In the attempt to untangle the physics underlying the polaron formation in charged molecular systems (as evidenced by the occurrence of giant intensity bands found in IR spectra), the mapping of the vibrational mode between neutral and charged systems has been calculated. A major achievement in this work is that the vibrational (giant) mode associated with the "polaron" emerges as a new mode (peculiar of the charged state) not related to any mode existing in the neutral system.

Acknowledgements

Dr. Enrico Da Como is very much acknowledged for sharing with me his cutting-edge and exciting science, and the opportunity he gave to me to study with him. Then, I must acknowledge Dr. Davide Vanossi and Prof. Francesco Battaglia for their infinite patience and clearness in introducing and explaining me details about classical (and quantum) mechanics, this during infinite and (for me) fruitful discussions.

Contents

1) Introduction

1.1 State-of-the-art

Proper manipulation of electricity and of relevant electric circuitry it is one of the most striking achievements of human kind, and yet it is an area of growing and, apparently, limit-less development. The most different activities and technologies rely on it, just to mention a few: worldwide communications (spanning from radio broadcasting to the whole of the phone system), power electric tools based on electric motors, energy production and storage (photovoltaics, batteries), building applications (the dawning domotics), remote controls (remotely driven actuators), autonomous driving, military/civil navigation (radio beacons, GPS, …), display devices (TV, monitor), computing machines (from out-of-use Texas Instruments pocket computers to nowadays super-computers and portable computing units). Within this field silicon, and other inorganic materials, based semiconductors played and still play a major role. Nonetheless, a more and more important role is gained by organic based electronic devices (together with the design and applications of hybrid, organic/inorganic, molecular architectures) [3–6]. Indeed, carbon-based (organic) materials offer a unique opportunity to exploit and combine, at the molecular level, the charge conducting ability of alternating π-conjugated bonds carbon chains and the "electric-insulator" character of single C-C bond chains, a concept implemented in the field of organic conductive polymers. The number of conceivable variations is further expanded by the possibility to integrate in the same system photoactive moieties, so to suitably combine "electric or photo-modulated" functions: for instance, electroluminescent polymers take advantage to combine easy materials processing, coupled with the possibility to fine tune the final photo-physical properties (via suitable selection of the polymer electronic characteristics). Sure enough, organic based electronics is a sector of strong development. Organic molecular crystals, with particular reference to pi-conjugated based compounds, are an extremely active field in fundamental scientific research [7,8]. In recent times, after a rather long incubation time of roughly 30 years, technological applications stemming from the "organic electronics" (OLED, Organic Light-Emitting Diodes [9–13]) branch of science are on the market: for instance OLED based screens and light sources, liquid crystal and touch screen devices. Within this field, organic pi-conjugated molecules, PAH (Polycyclic Aromatic Hydrocarbons: tetracene, pentacene, coronene, perylene, fullerenes just to mention a few examples), and a rigid backbone (minimization of the intramolecular degrees of freedom), are maybe the most promising compounds.

Fields of great interest for still-developing/future applications are organic based transistors and the area of photovoltaic systems for solar energy harvesting [14]. In addition, the search for suitable high temperature organic superconductors is active, this is due to the laboratory easiness/flexibility, as well as a virtually infinite number of possible structural variations, allowed by organic synthesis. This, coupled to a through suitable modification of substituent groups, thus allowing to modify, ad-hoc (at least in principle), the electronic (photo oriented characteristics, *in primis* the ubiquitous HOMO and LUMO[1] energy gap), chemical (for instance, solubility) and mechanical properties. What is more, besides applicative aspects, organic electronics has a substantial, and exciting, role in fundamental scientific research, where a number of phenomena related to charge localization and transport constitute an intriguing and challenging field of study for both physicists and chemists, see for instance the Nobel Prize in Chemistry 2000 which was awarded to Alan J. Heeger, Alan G. MacDiarmid and Hideki Shirakawa with the motivation "for the discovery and development of conductive polymers".

Organic electronics, “per se”, is a fascinating scientific subject as it is also witnessed, at an academic level, by the flourishing of a number of publications, journals[15,16] and books [3–5] devoted to such an area of science. Concerning the subject of charge transport in organic materials, the decisive move for inducing an appreciable electrical conductivity, in basically insulating organic architecture, was obtained by exposing polyacetylene to oxidazing (or reducing) reagents [17]. Usually, this redox reaction is addressed as a "doping process" in tight analogy with the doping process of inorganic semiconductors, even if the analogy is somehow misleading: from the quantitative point of view the doping process in inorganic systems (silicon as the prominent example here) involves a ratio of atoms of dopant over millions of atoms of semiconductor. Thus, the physics and chemistry of the doping is quite peculiar, because in the inorganic systems the dopants are embedded in the crystal structure, whilst the “doping concept” of organic compounds is implemented via a “net charge transfer process” involving a donor and an acceptor species, which will bring a positive and negative net charge. Concentrations are thus higher than in inorganics. This involves the presence of net charges, as well as charge-separated states, (localized and/or moving within the organic system) which play the more important role. The presence of net charges (donor/acceptor charge separation in an overall neutral system, within the “embedded cluster approach” [18]) is accompanied by a complex interplay between electronic and structural properties. Such a complex system requires to invoking the occurrence of non-linear processes: via the use of the “coupling” concept. This led to the use and exploitation of the quasi-particle concept, yielding a number of entities elevated to the rank

[1] HOMO stands for Highest, in energy, Occupied Molecular Orbital; LUMO stands for Lowest, in energy, Unoccupied Molecular Orbital.

of quasi-particle, just for instance solitons and polarons, to account for charge transport and dynamics in molecular systems [19].

In this thesis we focus on the study of organic-based molecular semiconducting solid systems. In particular, “charge transfer molecular complexes” (CT complex) are considered, which are also addressed as electron-donor-acceptor complexes: these are molecular architectures built from the reaction of two or more molecules in which a non-negligible fraction of electronic charge is transferred between a “donor” and an “acceptor” molecules, constituting the final CT complex. In some cases this concept is also implemented in a single molecule: a complex-molecule whose constituents feature at least two substituents are characterized by a great difference in ionization potential and electron affinity. Our aim is to rationalize the molecular transitions probed by photons of suitable energy with condensed matter, with particular attention to the theoretical description of CT states in molecular systems, where the presence of localized net-charges affect electronic and vibrational properties (with particular reference to polaron quasi-particles behaviour and characterization) [20–24].

1.2 Challenging questions:

1.2a the fundamental problem concerning the relationship between structural parameters and the HOMO/LUMO energy gap (optical vs electronic gap), moreover its role in determining the efficiency of organic materials in photovoltaic systems. A subject related also to the experimental tools employed to determine such energy gap: UV/Vis spectra, electrochemical reduction/oxidation potentials [25]. In the publication ref. [26,27] we tried to clarify on these aspects, with particular consideration on the relation between theoretical calculated quantities with experimental physical observables.

1.2b despite the success of DFT calculations obtained in the description of both physical and chemical systems and processes, some aspects are still challenging areas within the Density Functional paradigm, with particular reference to i) improving the activation reaction barriers description ii) van der Waals interactions; compare results discussed in ref [27] and in the "*Further theoretical insight on Coronene β and γ crystals physical properties"* section in chapter 4.2.1 of the present thesis iii) delocalization and static electron correlation errors iv) electron transfer, interaction energy and size-consistency in charged systems [28–30]. In the publication ref. [31,32] some of these points are considered, focusing on charge transfer systems and also on the influence of dispersion energies on the structure of molecular crystals. A paper relating on the charge-transfer dynamics between silicon and ferrocene, in a hybrid silicon/spacer/ferrocene interface, has been submitted too.

1.2c eventually a major challenging area concerns the calculation of charge transport/mobility, as well as the related excitation energies, in both polymeric (disordered) and organic molecular crystals (featuring long range order). Indeed, these two molecular organic based systems come into play in a natural way, because while small (in general highly symmetric) organic molecules can be forced in an ordered crystalline state, polymeric systems are extremely difficult to be obtained in crystalline form (quite often originating rubber/lacquer-like films.) The latter systems can be easily manipulated to obtain solid-blends with proper donor/acceptor concentrations [14,21,33–37].

1.3 Experimental evidence

The experimental evidence suggesting the existence of peculiar electronic states (charge transfer donor/acceptor systems featuring polaronic states), due to charge transfer within a doped[2] organic system, refer to both electric and spectroscopic experimental techniques. Electrical conductivity is probed by measurements made both in d.c. (direct current) and a.c. (alternating current – impedance spectroscopy) regimes [38]. Spectroscopic measurements are made both under reflectance [39–41] and transmission spectroscopy [22,37], which allow for the detectin of the typical "Polaron signature" both in infra-red and UV-Vis spectroscopies [21,22].

From the historical point of view, the very first article reporting a rather puzzling unforeseen appearance of very large intensity, low-lying in energy, peaks in infra-red spectra of doped polyacetylene is found in a fundamental paper of Fincher, Ozaki, Heeger, MacDiarmid [42] (compare Figure 1). Note that, the concept of the occurrence of giant amplitude infrared intensity modes was addressed explicitly for the first time in a seminal writing by Ehrenfreund, Vardeny and Brafman [43].

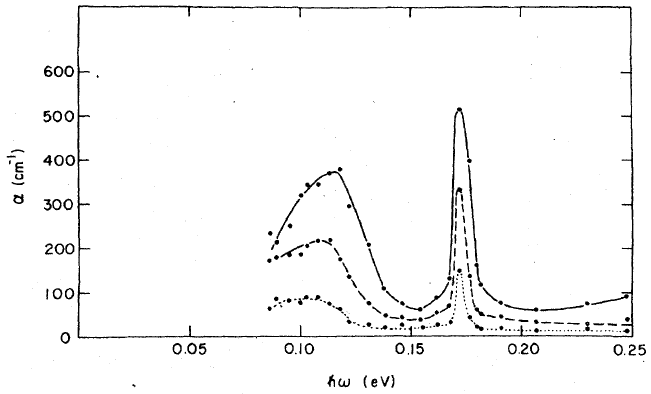

Figure 1. **a)** Infra-red absorption as a function of energy: two prominent peaks (900 cm^{-1} = 0.11 eV and 1370 cm^{-1} = 0.17 eV) show up upon doping of polyacetylene (AsF_5 is used as the dopant): 0.1-mole%, 0.06-mole%, 0.03-mole% AsF_5 in upper, intermediate and lower curves, respectively. Reproduced with permission (page 125) [42].

To introduce one of the materials of interest in this thesis Figure 2 shows the VIS/NIR spectrum of doped PCPDT-BT (F6-TCNNQ, is used as the dopant). Three prominent peaks are found at about 1000, 3300 and 8500 cm^{-1}. They can be assigned as polaron excitations. However, there is a general agreement in considering electronic P2 (3300 cm^{-1}, 3030 nm), P1 (8500 cm^{-1}, 1176 nm) and vibrational (1000 cm^{-1}, 10000 nm) transitions as experimental polaron signatures [44]. The P2 and 1000 cm^{-1} peaks are rather close in energy, being characterized by a non-negligible overlap, suggesting some coupling between the two relevant physical excitation processes, see for instance Horovitz

[2] In general the organic pristine systems (polymers or organic crystals) are non-conducting.

and Vardeny [45]. At further higher energy, > 10000 cm^{-1}, the spectrum shows some resonances, here not shown, due to excitons.

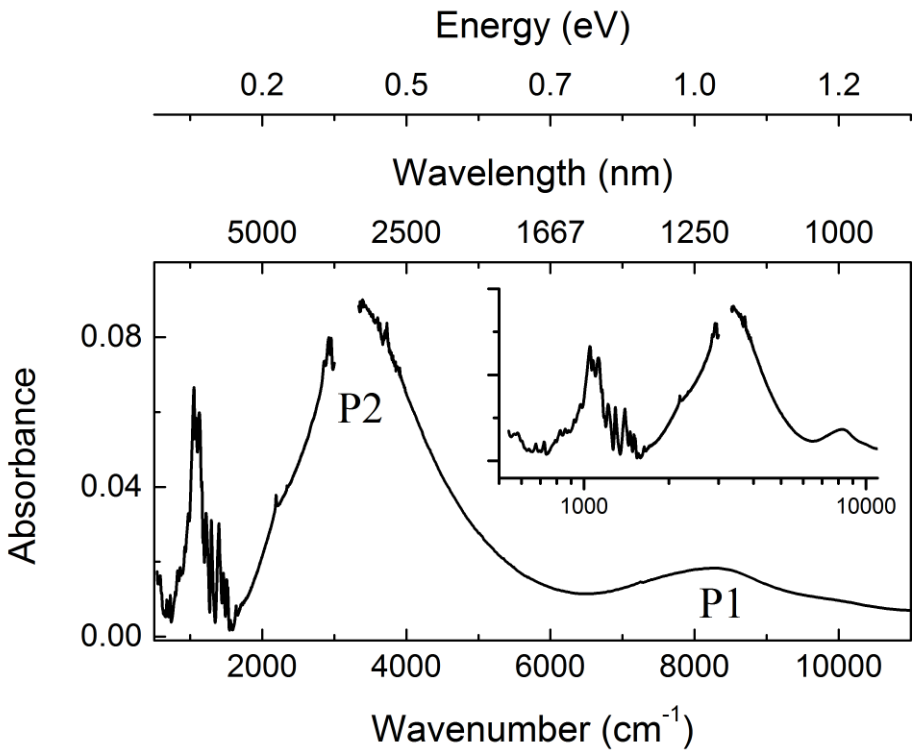

Figure 2. IR NIR combined spectra of PCPDT-BT/F6-TCNNQ [44]. Polaron peaks, P2 and P1, are visible at 3300 and 8500 cm^{-1}, respectively. A giant IR peak, compare figure 1, is evident at 1000 cm^{-1}. Inset: same spectrum with logarithmic wavenumber scale.

Indeed, polaron related[3] scientific activity dates back to almost 40 years ago, thus a more than relevant question is: why keep studying this subject? What is still there to be understood or any possible application? Answers span an infinite range of possible aspects. From a purely academic point of view it must be emphasized that a clear-cut definitive explanation of the physics underlying the presence of giant absorption response, ”polaron signature”, in IR spectra is yet to come, this despite the number of papers present in the literature [46,19,35,47,8,45,48] devoted to this subject. As well as a definitive theory allowing for a quantitative/semi-quantitative calculation of conductivity in organic “conductive” systems (even the *experimental* method to measure the mobility in organic molecular systems, see for instance Podzorov measurements concerning rubrene [49], is a matter of discussion [4]). What is more, important technological applications, of the polaron large IR absorption, are con-

[3] Or rather in a more ample view: “conductivity in doped semiconductors”.
[4] The source/drain/gate transistor configuration to “measure” the mobility implies the application of more than 200 V in d.c. between the source and the gate, this high potential value stems, undoubtedly, from the application of the conductivity band concept to a highly-localized-electron system represented by an aromatic molecule, and eventually using the same “device” for measuring a quantity, the mobility of electrons, in a system where the electrons are tightly localized.

ceivable: from optical amplification cavity systems in non-linear optics, to IR imaging in night vision light amplification devices. Eventually, note that hole states, in organic conducting polymers, can be produced in a variety of ways: photo-induced [50], chemical doping [31], and electrochemically [26]. In particular, electrochemical doping is achieved applying small d.c. potential values in the 0.5 to 1.0 Volt range. Then, a polymer could be maintained in “doped” state by application of a small d.c. potential, and the “giant” IR absorption could be exploited to capture and store low wavenumber energy, “heat”, to be exploited in heating (or pre-heating) systems for energy conversion and/or production.

2) Theoretical scenario and tools

Within the field of doped π-conjugated-polymers (PCPs) the polaron concept plays a leading role. The introduction of the polaron as quasi-particle is due to Solomon I. Pekar in 1946, subsequently developed in collaboration with D. Landau [51]. Then, the endeavour for finding a rationale underlying the peculiar observations found in both electronic and vibrational spectra of doped PCPs tightly mirrored the developments in the experimental field. Leading to the wide diffusion of the concept of "polaron" [19,51,52,24]. The common line-of-reasoning is the attempt to account for the interaction between a "net-free-charge" moving within the PCP structure and the lattice distortion induced by its presence. Indeed, the term polaron stems from the idea of lattice *polar*ization induced by the electr*on* (electron-phonon interaction). Theoretical tools devoted to study the effect of dopant charges in PCPs span a wide range of complex theories.

The more natural way to treat such a problem is to consider the equation of motion of a single-charged-particle in one dimension, where the interaction of the particle with the elastic properties of the lattice are somehow accounted for by a suitable potential energy function. In fact, a solid consists of a regular distribution of ions, each one oscillating about its equilibrium position; thus the charge particle moves in a changing, with time, potential field. Fröhlich proposed an interaction Hamiltonian built to study this charge-transport process [53,54].

Thus, a rather exhaustive form for the Hamiltonian describing a coupled electron-phonon system, using second quantization formalism, can be written as [55,56]:

$$\hat{H} = \sum_{n\boldsymbol{k}} \varepsilon_{n\boldsymbol{k}} \hat{c}^{\dagger}_{n\boldsymbol{k}} \hat{c}_{n\boldsymbol{k}} + \sum_{\boldsymbol{q}\nu} \hbar\omega_{\boldsymbol{q}\nu} \left(\hat{a}^{\dagger}_{\boldsymbol{q}\nu} \hat{a}_{\boldsymbol{q}\nu} + \frac{1}{2} \right) + \frac{1}{N_P^{0.5}} \sum_{\substack{\boldsymbol{k},\boldsymbol{q} \\ mn\nu}} g_{mn\nu}(\boldsymbol{k},\boldsymbol{q}) \hat{c}^{\dagger}_{m\boldsymbol{k}+\boldsymbol{q}} \hat{c}_{n\boldsymbol{k}} \left(\hat{a}_{\boldsymbol{q}\nu} + \hat{a}^{\dagger}_{-\boldsymbol{q}\nu} \right)$$
$$+ \left[N_P^{-1} \sum_{\substack{\boldsymbol{k},\boldsymbol{q},\boldsymbol{q}' \\ mn\nu\nu'}} g^{DW}_{mn\nu\nu'}(\boldsymbol{k},\boldsymbol{q},\boldsymbol{q}') \hat{c}^{\dagger}_{m\boldsymbol{k}+\boldsymbol{q}+\boldsymbol{q}'} \hat{c}_{n\boldsymbol{k}} \left(\hat{a}_{\boldsymbol{q}\nu} + \hat{a}^{\dagger}_{-\boldsymbol{q}\nu} \right) \left(\hat{a}_{\boldsymbol{q}'\nu'} + \hat{a}^{\dagger}_{-\boldsymbol{q}'\nu'} \right) \right], \quad (1)$$

Right hand term in equation 1: first line describes (from right to left) the electron kinetic energy term, phonon vibrational energy, the third term accounts for the electron/phonons coupling (to first order); second line accounts for second order electron-phonon coupling in the atomic displacements. $\varepsilon_{n\boldsymbol{k}}$ is the is the single-particle eigenvalue for a particle in band n and momentum k, $\omega_{\boldsymbol{q}\nu}$ phonon frequency branch ν momentum q, $\hat{c}^{\dagger}_{n\boldsymbol{k}}$ and $\hat{c}_{n\boldsymbol{k}}$ ($\hat{a}^{\dagger}_{\boldsymbol{q}\nu}$ and $\hat{a}_{\boldsymbol{q}\nu}$) are the fermionic (bosonic) creation and destruction operators, N_P is the number of unit cells (within the Born von Karman supercell), the $g_{mn\nu}(\boldsymbol{k},\boldsymbol{q})$ and $g^{DW}_{mn\nu\nu'}(\boldsymbol{k},\boldsymbol{q},\boldsymbol{q}')$ terms are the electron/phonon coupling constants (in energy units) where "DW" stands for Debye-Waller and relates to the Debye-Waller electron self-energy [55,56].

Thus, in a hierarchical approach climbing a ladder of increasing complication, it is worth mentioning two different elementary approaches, which, despite the quite simple level, allow grasping, as a first approximation, some peculiar features of the physics underlying the polaron entity, like its size and electron-"lattice distortion" energy interaction, the second right hand term in equation 1 [57–59].

a) three different contributions are considered to affect the electron (hole) energy: 1) potential energy: $V(x) = \epsilon_0(\nabla \cdot U)$, assumed constant within the accessible electron space and zero otherwise, where ϵ_0 is the electron/lattice distortion interaction energy and $U(x)$ is the ion displacement from the equilibrium position; 2) elastic energy: due to lattice distortion, in the form $\frac{1}{2}B(\nabla \cdot U)^2$, where B is the bulk modulus defined as $B = -V(\partial P/\partial V)_T$, where V is the volume, P the pressure and T the temperature. Eventually leading, for a distortion of linear size L, to: $E_D = \int_0^L {}^1\!/_2\, B(\nabla \cdot U)^2 dV = {}^1\!/_2\, B(\nabla \cdot U)^2 L^d$, d is the dimensionaly $d = 1$ one-dimensional, $d = 2$ two-dimensional, $d = 3$ three-dimensional; 3) electron kinetic energy: which is the kinetic energy in the particle in a one-dimensional box in an infinite square well potential, of size L, i.e. volume L^d. Thus, the kinetic energy, unfortunately in general identified with T (not to be confused here with the temperature) $T = (d\hbar^2\pi^2)/(2mL^d)$. Thus, the relevant total electron energy is:

$$E(L) = \frac{d\hbar^2\pi^2}{2mL^d} + \frac{1}{2}B(\nabla \cdot U)^2 L^d + \epsilon_0(\nabla \cdot U)\,. \tag{2}$$

Minimizing with respect to the potential energy, $V(x) = \epsilon_0(\nabla \cdot U)$ for a fixed value of L, a minimum is found for: $V_0 = -\epsilon_0/BL^d$

Leading to:

$$E(L) = \frac{d\hbar^2\pi^2}{2mL^2} + \frac{\epsilon_0^2}{2BL^d} - \frac{\epsilon_0^2}{BL^d} = \frac{d\hbar^2\pi^2}{2mL^2} - \frac{\epsilon_0^2}{2BL^d}, \tag{3}$$

notably, $E(L)$ as a function of L shows a minimum when $d = 1$. Figure 3 shows the graph, assuming $\frac{d\hbar^2\pi^2}{2m} = \frac{\epsilon_0^2}{2B} = 1$, of the simplified function $E(L) = \frac{1}{L^2} - \frac{1}{L^d}$

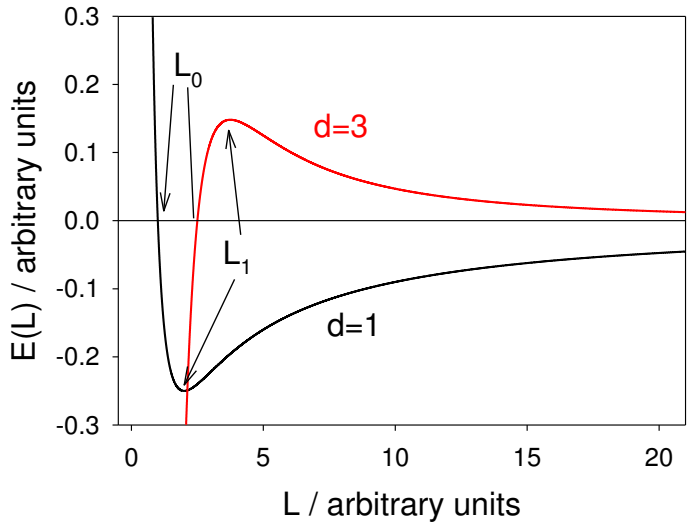

Figure 3. Qualitative representation of the $E(L)$ pattern as a function of L. Black line, one-dimensional case $d = 1$. Red line 3D case.

there is a well-defined minimum of $E(L)$, which will correspond to a stable polaron of size L_1. Even with its quite basic assumptions, the application of this modelistic approach allows for a crude estimation of the polaron size and energy stabilization.

b) a more refined approach is obtained considering one electron in a 1D continuous system [57,59]. The potential energy term, $V = \lambda(dU/dx)$, is assumed to represent the electron/lattice-distortion interaction (the crystal lattice is considered as a continuous medium, characterized by a bulk modulus B), where: $U(x)$ is the ion displacement from the equilibrium position and λ is the electron-phonon coupling constant. Then, in one dimension $E_{Deformation} = {}^1/_2\, B(dU/dx)^2$ is the energy associated to the lattice distortion.

The Schrödinger 1D equation relevant to this simplified model is written in the form [57]:

$$-\frac{\hbar^2}{2m}\left(\frac{\mathrm{d}^2\psi}{\mathrm{d}x^2}\right) - V_0 cosh^{-2}\left(\frac{x}{a_0}\right)\psi = E_{electron}\psi\,, \tag{4}$$

where $V_0 = \lambda u_0/a_0$. Solution of equation 4 lattice deformation is represented by the trial potential function $U(x) = u_0 \tanh(x/a_0)$, where u_0 and a_0 are parameters, in particular a_0 is the reciprocal of the polaron size.

Equation 4 can be solved by introducing an auxiliary variable: $r = u_0 \tanh(x/a)$. Eventually, the electron energy takes the discrete values [59]:

$$E_{electron} = -\frac{\hbar^2}{8ma_0^2}\left[-(1+2n) + \sqrt{1+\left(\frac{8ma_0^2V_0}{\hbar^2}\right)}\right]^2\,, \tag{5}$$

with $n = 0, 1, 2, \ldots$

The total distortion energy is:

$$E_{LatticeDistortion} = \frac{1}{3}Bu_0^2/a_0\,. \tag{6}$$

Minimization of the total energy of the coupled electron-phonon system:

$$E_{Total} = E_{electron} + E_{LatticeDistortion}, \tag{7}$$

allows for a crude estimation of the polaron size: $(a_0)^{-1} = \hbar^2 B/m\lambda^2$.

Introduction of the auxiliary variables η and ξ, with $u_0 = 3\lambda\eta/2B$ and $a_0 = (\hbar^2 B/12m\lambda^2)\xi$, in equation (5) and assuming $n = 0$ (ground state) leads to the following simple relation for ϵ, which is proportional to the total energy, [5]

$$\epsilon = -2\frac{\left(\sqrt{(1+\eta\xi)}-1\right)^2}{\xi^2} + \frac{\eta^2}{\xi}, \tag{8}$$

ϵ shows a minimum when represented as a function of η and ξ, compare figure 4.

[5] $\epsilon = E_{Total}(\hbar^2 B^2/9m\lambda^4)$.

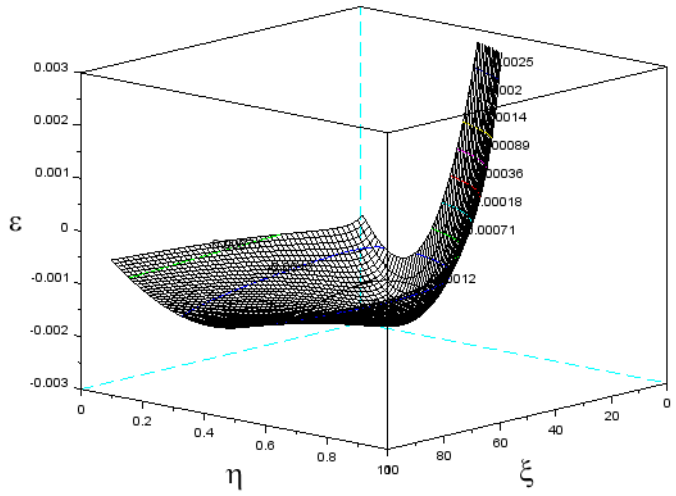

Figure 4. 3D graph of equation (8).

The latter modelistic approach relies on the original Landau theoretical work on the introduction of the polaron concept [51].

c) Infra-Red Active Vibrations (IRAV) models

Spanning the period from the Heeger/Shirakawa/MacDiarmid discovery of the metallic-like behaviour of doped polymers, a number of different models, aiming to account for the electron/phonon interaction (i.e. coupling energy), have been proposed. Notably, in all of these different approaches the attention is mainly focused on the shift of vibrational energies upon doping of the system (rather than on intensity), where the calculation of both electronic and vibrational energies of the doped system are obtained using, as an essential starting reference state, the data of the parent original neutral state. Compare for instance the elegant theoretical models developed by Bredas/Beljonne [35,47], Kato/Yamabe [60,61], Zoos/Girlando/Painelli [62], Zerbi [46].

Within the *local electron-phonon coupling* approach the free charge carrier (electron or hole) is assumed to be mainly localized on a single lattice site. This causes geometrical deformations in both molecular, as well as lattice, parameters. The energy associated with such a geometrical rearrangement is addressed as the polaron binding energy, E_{pol}. The intramolecular contribution to E_{pol} is represented by a series expansion of site energy, ϵ_m, in powers of the molecular vibrational normal-modes, classical harmonic approximation [47]: $\epsilon_m = \epsilon_m^0 + \sum_j V_m(j)Q_m(j) + \ldots$ In practical calculations ϵ_m is the proper frontier molecular orbital energy (i.e. HOMO and LUMO energies for hole and electron transport, respectively), $Q_m(j)$ is the m-th normal-mode coordinate of the molecule (the j index refers to the relevant phonon branch in periodic systems or the proper point-group symmetry label when symmetrical molecular systems are concerned). This is with reference to the

adiabatic potential surface of the charged molecular system calculated within the single-particle (i.e. one-electron) framework (Koopmans' theorem). The electron-vibration coupling constant can be computed by using equation (9) [47]:

$$V_m(j) = \left(\frac{\partial \epsilon_m}{\partial Q_m(j)}\right)_{Q=0} \tag{9}$$

Assuming no variation between the normal vibrational modes of the neutral and charged states, the relevant relaxation energy variation, occurring upon a vertical transition is: $\lambda_{rel}^{(1)} = \lambda_{rel}^{(2)}$ compare figure 5 for the graphical representation of the relevant quantities. It is assumed that the normal vibrational modes of both the ground and charged states have the same wavefunction (implying that the neutral and charged species potential energy curves, black and red curves respectively in Figure 5, are identical; they are just shifted of a constant quantity on the abscissa and ordinate axes with respect to origin).

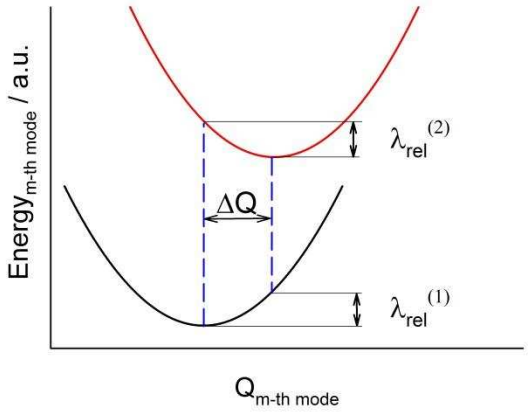

Figure 5. Model potential energy surfaces (PES) for neutral state (black solid line) and charged molecule state (red solid line), vertical transitions (dashed lines) are shown, with reference to the Q_m normal vibrational mode. Relevant displacement ΔQ and relaxation energies $\lambda_{rel}^{(1)}$ and $\lambda_{rel}^{(2)}$ are illustrated.

Then, considering a vertical geometry relaxation (i.e. the initial and final states feature the same value of Q_m) the corresponding relaxation energies are equal, implying

$$\lambda_{rel} = \sum_j \lambda_j = \sum_j \frac{V_j^2}{2M_j\omega_j^2} \tag{10}$$

where: M_j and ω_j are the reduced mass and the wavenumber relevant to vibrational mode Q_j, respectively. The m index, equation (9), which is the label identifying the "site" (i.e. the molecule in a molecular crystal) can be neglected. In fact, due to crystal translational symmetry, each m site/molecule features the same vibrational wavefunction. Moreover, assuming that the intra-

molecular contribution to the polaron binding energy is equal to the geometric relaxation energy upon charging the molecular system allows to obtaining

$$E_{pol} = \lambda_{rel} = \sum_j \lambda_j = \sum_j \frac{M_j \omega_j^2 \Delta Q_j^2}{2}, \tag{11}$$

where: E_{pol} is the polaron binding energy (moreover, upon definition of $\lambda_{reorg} = \lambda_{rel}^{(1)} + \lambda_{rel}^{(2)}$ as the intramolecular reorganization energy due to a intermolecular charge transfer process [35,63,64], the polaron binding energy can be written as $E_{pol} = \lambda_{reorg}/2$, assuming $\lambda_{rel}^{(1)} = \lambda_{rel}^{(2)}$ vide-supra [47].

An alternative modelistic approach has been proposed by Kato and Yamabe, within a "one-electron approximation framework". Here, the vibronic coupling constant of the m-th vibrational mode, $g_{electronic\ state}(\omega_m)$, is defined as a sum of all he orbital vibronic coupling constants, $g_i(\omega_m)$, spanning the contributions from all of the occupied molecular orbitals [60,61]:

$$g_{electronic\ state}(\omega_m) = \sum_i^{occupied} g_i(\omega_m)\,. \tag{12}$$

Then, within the one-electron approximation[6] (and considering that the derivative of the ground state energy - as function of the spatial displacement - is zero at the equilibrium geometry) the vibronic coupling constant is obtained as: $g_{cation}(\omega_m) = g_{HOMO}(\omega_m)$ for the hole ($g_{anion}(\omega_m) = g_{LUMO}(\omega_m)$ for the electron). Moreover, the dimensionless vibronic coupling constant relevant to the m-th vibrational mode can be written, in the case of a cation species, as:

$$g_{HOMO}(\omega_m) = \frac{1}{\hbar\omega_m}\left\langle HOMO\left|\frac{\partial h_m}{\partial q_m}\right|HOMO\right\rangle. \tag{13}$$

Where: $q_m = Q_m\sqrt{(\omega_m/\hbar)}$ is the dimensionless normal coordinate relevant to m-th mode expressed as a function of the normal coordinate Q_m, h_m is the vibronic coupling matrix element. The latter, i.e. h_m, is calculated from the slope of the HOMO energy (in the case of a cation), of the charged system, at the value of geometry equilibrium of the neutral parent system (i.e. at $Q_m = 0$) [60,61].

[6] All of the doubly occupied molecular orbitals are assumed to maintain their dependence as a function of the normal-mode coordinate variation, when passing from the neutral closed-shell to the charged open-shell state.

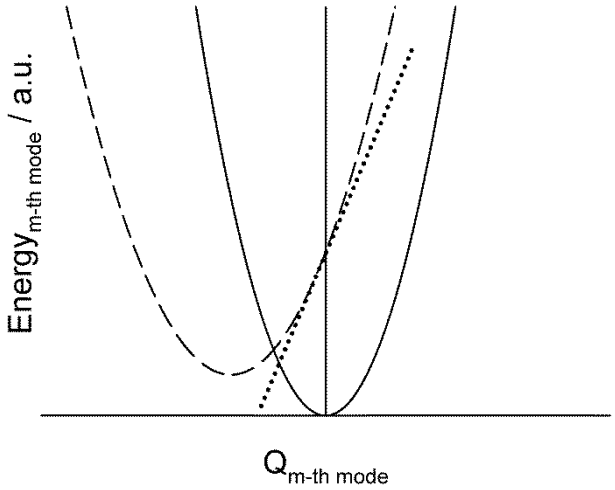

Figure 6. Graphical representation of the strategy underlying the calculation of the vibronic coupling constant following Kato and Yamabe. The potential energy (PE) curve is reported as a function of the m-th normal coordinate mode of the neutral system. Solid line: neutral system PE. Dashed line: ionized (cation or anion, or photoexcited state) system PE. The dotted line is the slope of the ionized system PE curve, determined at the Qm-th value relevant to the equilibrium of the neutral system [60,61]

Within the *nonlocal electron-phonon coupling* approach the main role, in the calculation of charge transport properties, is played by the variation of the transfer integral, t_{mn} (i.e. the transfer interal between the m-th and n-th interacting systems) [47]. Notably, t_{mn} is a function of internuclear distances due to ion vibration, resulting in the variation/modulation of both intramolecular and intermolecular distances. Eventually, the nonlocal electron-phonon coupling is described by how the transfer integral varies as a function of the intermolecular distances (R_{mn}) at the equilibrium geometry, i.e [47]: $(\partial t_{mn}/\partial R_{mn})_0$. Although the role played by the variation of t_{mn} as a function of R_{mn} has been proved to be of primary importance, a clear-cut theory allowing for both a reasonably reliable evaluation of $(\partial t_{mn}/\partial R_{mn})_0$ and feasible computational time is yet to come.

A possible solution to this problem has been proposed recently, "*Elementary Semiclassical Model*" [65,66]. In this modelistic approach, the system is considered as a one dimensional ordered collection of planar units (the latter meant to represent conjugated molecules), featuring one single molecular orbital per molecule (HOMO in case of hole transport, LUMO in case of electron transport). Each molecule j (mass m) has a relevant $|j\rangle$ molecular orbital, it has a transversal displacement by a length u_j (with respect to its equilibrium position), around which j oscillates with frequency ω. The transfer integral τ, between orbitals $|j\rangle$ and $|j+1\rangle$, is modulated linearly with respect to α, α being the electron–phonon coupling constant, $a\alpha(u_{j+1}-u_j)$. The relevant semiclassical Hamiltonian for this system:

$$H = \sum_j \left(-\tau + \alpha\left(u_{j+1} - u_j\right)\right)\left(|j\rangle\langle j+1| + |j+1\rangle\langle j|\right) + \sum_j \frac{1}{2} m\dot{u_j^2} + \sum_j \frac{1}{2} m\omega^2 u_j^2. \qquad (14)$$

Solution of the semiclassical Hamiltonian, following the Troisi model, is able to provide absolute values of mobility which are in good agreement with the experiment (in particular for the case of rubrene). This seems due to the fact that the model underlying Eq. (14) catch all the essential elements that determine the charge mobility. Moreover, the mobility (μ) computed as a function of temperature (the diffusion constant is calculated as[7] $D = lim_{t\to\infty}\langle R^2(t)\rangle/2t$, and the Einstein relation $\mu = eD/k_BT$ is used for the mobility), decreases as $\mu \propto T^{-\alpha}$, in tight agreement with the rubrene experimental data.

Within this field it is also worth mentioning the work, later on developed in a more sophisticated theory, by Baruch Horovitz (Amplitude Mode), where it is accounted for the resonant/anti-resonant Fano type resonance due to the partial overlapping (i.e. interaction) between the vibrational/phonon excitations and the typical electronic polaron signature found in electronic spectra [45].

Eventually, it should be noted that all of the mentioned theoretical approaches are based on the existence of a large separation in the band gap energy. Because the assumptions adopted in this section to calculate electron-phonon (or vibronic) interactions rely on an effective single determinant description of electronic properties [62]. When the band gap gets smaller, correlation effects grow in importance/weight. Thus, multi-determinant, for instance MultiConfiguration Self Consistent Field (MCSCF), based methods or other many-body techniques able to account for strong electron correlation effects, Moller-Plesset (MP) or Green effective coulomb screened (GW), must be used [67–69].

[7] Here t is the time and T the temperature.

3) Fundamentals of Density Functional Theory

In the present work, the focus is on the calculation of vibrational and electronic excitations, in the attempt to rationalize the experimental behaviour of π conjugated molecules. The calculation of excitation energies and intensities has been carried out with a number of different level of the theory (HF, DFT, hybrid HF/DFT), without applying periodic boundary conditions (i.e. considering a oligomer of suitable size as representative of the properties of the polymer). Calculation of the vibrational spectra has been carried out by using the Coupled Perturbed Hartree Fock (CPHF) approach [70,71]. Both Time Dependent (TD-DFT) and Configuration Interaction (Single excitation only, CI(S)) methods were used for the calculation of electronic excitation intensities. In general, the starting point for the theoretical calculation of electronic properties of any system is the search for a solution to the ubiquitous one-electron Schrödinger equation [69,71–73]:

$$\left(-\frac{\hbar^2}{2m}\nabla^2 + V(\boldsymbol{r})\right)\Psi(\boldsymbol{r}) = \varepsilon\Psi(\boldsymbol{r})\,, \tag{15}$$

in quantum mechanics the crucial point is to devise a suitable and effective theory for the representation of $V(\boldsymbol{r})$: this is the question. Indeed, the $V(\boldsymbol{r})$ term must account also for all the interactions between a single electron and the potential field associated with the presence of all the other electrons (electron correlation). The well-known, and yet to be solved exactly, many-body problem [74,75].

In the Hartree-Fock (HF) treatment the ground-state many-electron (N electrons) wavefunction is assumed in the form:

$$\Psi_{HF}(\boldsymbol{r}_1\sigma_1 \ldots \boldsymbol{r}_N\sigma_N) = \frac{1}{\sqrt{N!}}\begin{vmatrix} \phi_1(\boldsymbol{r}_1\sigma_1) & \ldots & \phi_1(\boldsymbol{r}_N\sigma_N) \\ \vdots & \ddots & \vdots \\ \phi_N(\boldsymbol{r}_1\sigma_1) & \ldots & \phi_N(\boldsymbol{r}_N\sigma_N) \end{vmatrix} \tag{16}$$

of a single Slater determinant. The prominent characteristics of the wavefunction written as a Slater determinant is the ability to encompass the Pauli principle in its mathematical features, i.e. the determinant is zero if two rows or columns are identical which corresponds to a couple of electrons having the same quantum numbers. The sign of Ψ_{HF} changes (i.e. Ψ_{HF} is antisymmetric) with respect to interchange of any two electron coordinates [71,73]: N is the number of electrons, $\boldsymbol{r}_i$ and σ_i denote the spatial and spin coordinates of the i-th electron, the ϕ_i are single-particle orbitals (spin-orbital). The latter are calculated by implementing an iterative self-consistent procedure (variational principle), requiring that the variation of the energy with respect to variation in any of the single-electron ϕ_i states is zero:

$$\frac{\partial\langle\Psi_{HF}|H|\Psi_{HF}\rangle}{\partial\phi_i} = 0\,, \tag{17}$$

the H term in equation (17) is the Hamiltonian operator.

Invoking the variational method allows to writing a set of single-particle coupled equations, Hartree- Fock SCF (Self Consistent Field) method:

$$\begin{aligned} -\tfrac{\hbar^2}{2m}\nabla^2\phi_i(\boldsymbol{r},\sigma) + V_{ion}(\boldsymbol{r})\phi_i(\boldsymbol{r},\sigma) + V_H(\boldsymbol{r})\phi_i(\boldsymbol{r},\sigma) + \\ \textstyle\sum_{\sigma'}\left(\int V_X(\boldsymbol{r},\boldsymbol{r}',\sigma,\sigma')\,\phi_i(\boldsymbol{r}',\sigma')d\boldsymbol{r}'\right) = \varepsilon_i\phi_i(\boldsymbol{r},\sigma)\,. \end{aligned} \tag{18}$$

$V_{ion}(\boldsymbol{r})$ accounts for the attractive electron-ion Coulomb potential and:

$$V_H(\boldsymbol{r}) = \int d\boldsymbol{r}'\frac{e^2}{|\boldsymbol{r}-\boldsymbol{r}'|}\sum_{\sigma'}\sum_{j}^{occ}\left|\phi_j(\boldsymbol{r}',\sigma')\right|^2 \tag{19}$$

$$V_X(\boldsymbol{r},\boldsymbol{r}',\sigma,\sigma') = -\textstyle\sum_j^{occ}\frac{e^2}{|\boldsymbol{r}-\boldsymbol{r}'|}\phi_j^*(\boldsymbol{r}',\sigma')\phi_j(\boldsymbol{r},\sigma)\,. \tag{20}$$

The V_H and V_X potentials correspond to the Coulomb ($\boldsymbol{J}$) and Exchange ($\boldsymbol{K}$) operators in the effective one-electron energy Fock operator $\boldsymbol{F}_i$:

$$\boldsymbol{F}_i = \boldsymbol{h}_i + \sum_j^N\left(\boldsymbol{J}_j - \boldsymbol{K}_j\right). \tag{21}$$

$\boldsymbol{h}_i$ is a one-electron operator which represents the motion of the i-th electron in the field of the fix ions of the lattice (compare appendix 1).

The HF-SCF ansatz is based on the search of a set of orbitals ϕ_i (Molecular Orbitals, MOs) which makes the energy a minimum. This mathematical constrained optimization (the ϕ_i are constrained to remain orthonormal throughout the iterative procedure) is carried out by using the method of the Lagrange multipliers. Eventually leading to the final set of Hartree–Fock equations which can be written as:

$$\boldsymbol{F}_i\phi_i = \sum_j^N\lambda_{i,j}\phi_j\,. \tag{22}$$

The diagonalization of the Lagrange multipliers matrix, performed by application of a unitary transformation, leads to $\lambda_{i,j} = 0$ and $\lambda_{i,i} = \varepsilon_i$. Finally the pseudo-eigenvalue equation is obtained:

$$\boldsymbol{F}_i\phi_i^{trasf} = \varepsilon_i\phi_i^{trasf}\,. \tag{23}$$

Quite often, in the case of solid state physics systems which feature translation symmetry, the single-particle orbitals are represented by a plane wave times a spin function :

$$\phi_i^{HF} = \phi_{\boldsymbol{k}\lambda} = \frac{1}{\sqrt{\Omega}} e_i^{i\boldsymbol{k}\cdot\boldsymbol{r}} \chi_\lambda \,, \tag{24}$$

where Ω is the sample volume, $\boldsymbol{k}$ and λ are quantum numbers and χ_λ is the spin function $\binom{1}{0}$ for $\sigma = \uparrow$ (spin up) and $\binom{0}{1}$ for $\sigma = \downarrow$ (spin down). In general, solutions to the HF equation can be pursued with reference to two different systems *i)* "infinite-periodic" systems featuring translational symmetry (periodic boundary conditions, PBC: i.e. crystals – which is the "natural" choice when dealing with solid state physics) *ii)* "finite" molecular systems (single molecules up to polymers). These two different class of systems call for the use of different "basis sets" to pursue for the solution. As a rule of thumb, calculations concerning PBC systems use plane waves basis set, "opposite to them" molecular (finite) systems use localized functions (atomic orbitals: leading to LCAO - localized linear combination of atomic orbitals - methods) [69,71].

A completely different approach to the solution of the Schrödinger equation is pursued within the Density Functional Theory paradigm. Hohenberg and Kohn (1964) proved that there is a one-to-one correspondence between the electron density of a system, $\rho(\boldsymbol{r})$, and its energy [76]. Thus the attention is shifted to the proper calculation of $\rho(\boldsymbol{r})$ rather than $\Psi(\boldsymbol{r})$. What is more, the DFT approach allows for the **exact** treatment, ***in principle***, of electron-electron interaction (correlation), for the ground-state properties, via transforming the many-electrons problem to a self-consistent-field one-particle problem. Possibly the most important relation within DF theory is the energy functional [69,77]:

$$E_v[\rho] = \int v(\boldsymbol{r})\, \rho(\boldsymbol{r}) d\boldsymbol{r} + \mathrm{F}[\rho] \,, \tag{25}$$

where $v(\boldsymbol{r})$ is the external potential (normally taken as the potential due to the ions). $\mathrm{F}[\rho]$ is a functional of the electron density, whose form is unknown: this is the problem. Moreover, $\mathrm{F}[\rho]$ accounts for both the electron kinetic energy and for the electro-electron interaction. Kohn and Sham reformulated equation 25 (interacting system), on the basis of the features of a non-interacting system (potential $v'(\boldsymbol{r})$ and electron density $\rho'(\boldsymbol{r})$): considered as a limiting case for which the $\mathrm{F}[\rho]$ functional could be determined straightforwardly. Indeed, if exchange and correlation effects are neglected the interaction energy is reduced to the classical Hartree term [77,69]:

$$E_H = \frac{1}{2} e^2 \int \frac{\rho(\boldsymbol{r})\rho(\boldsymbol{r}')}{|\boldsymbol{r} - \boldsymbol{r}'|} d\boldsymbol{r} d\boldsymbol{r}' \,, \tag{26}$$

for the non-interacting system the kinetic energy is considered:

$$T_s[\rho] = -\frac{\hbar^2}{2m}\sum_i^{occ}\int \varphi_i^*(\boldsymbol{r})\nabla^2\varphi_i(\boldsymbol{r})d(\boldsymbol{r})\,. \tag{27}$$

In particular, equation 25 is now expressed as:

$$E_v[\rho] = \int v(\boldsymbol{r})\,\rho(\boldsymbol{r})d\boldsymbol{r} + T_s[\rho] + \frac{1}{2}e^2\int\frac{\rho(\boldsymbol{r})\rho(\boldsymbol{r}')}{|\boldsymbol{r}-\boldsymbol{r}'|}d\boldsymbol{r}d\boldsymbol{r}' + E_{XC}[\rho] \tag{28}$$

now all of the unknowns are contained in the last three terms on the right hand side of equation 28. Where the $E_{XC}[\rho]$ is the so-called exchange-correlation energy functional, which accounts for the electron-electron interaction energy as well as part of the kinetic energy of the interacting electrons (because $T_s[\rho]$ is the kinetic energy of the non-interacting electrons, by definition). For the non-interacting system and N electrons $\rho'(\boldsymbol{r})$ can be determined by solving:

$$\left(-\frac{\hbar^2}{2m}\nabla^2 + v'(\boldsymbol{r})\right)\varphi_i{}'(\boldsymbol{r}) = \varepsilon_i{}'\varphi_i{}'(\boldsymbol{r})\ , \tag{29}$$

using $\rho'(\boldsymbol{r})$ as a guess and going through application of the variational theorem is it possible to derive a set of Euler-Lagrange equations:

$$\left(\frac{p^2}{2m} + v(\boldsymbol{r}) + v_H(\boldsymbol{r}) + v_{XC}(\boldsymbol{r})\right)\varphi_i(\boldsymbol{r}) = \varepsilon_i\varphi_i(\boldsymbol{r})\,, \tag{30}$$

where the main problem remains the knowledge of the potential term:

$$v_{XC}(\boldsymbol{r}) = \frac{\delta E_{XC}}{\delta\rho(\boldsymbol{r})} \tag{31}$$

again E_{XC} is the unknown term and a number of approximations have been adopted to make an estimation, in general it is considered:

$$E_{XC} = \int \rho(\boldsymbol{r})\varepsilon_{XC}(\boldsymbol{r})d\boldsymbol{r} \tag{32}$$

invoking $\varepsilon_{XC}(\boldsymbol{r})$ being a function of the local density in the LDA or a function of both $\rho(\boldsymbol{r})$ and $\nabla\rho(\boldsymbol{r})$ in the generalized gradient approximation (GGA). In the very end the Kohn-Sham equations take the form of the Hartree-Fock equations, this allowed for an “easy” extension of DFT-based calculations in computational codes exploited by chemists (where correlation effects are accounted for by using CI, MPn, MCSCF methods, compare for instance the GAMESS, Firefly or ORCA suite of programs).

4) Results

4.1 Conducting Polymers: Polythiophenes

Organic electronics is a mature, yet still in substantial expansion, branch of "material science", with a number of practical applications. Which take advantage of the simple synthesis and handling typical of organic compounds, together with the virtual infinite possibility of fine tuning their electric and electronic characteristics. Within this field polythiophene are one of the most studied and promising class of polymers [14,37,78–81]. This section shows theoretical results aimed to rationalize spectroscopic results (concerning vibrational and electronic spectroscopies, as well as HOMO/LUMO gap revealed by using electrochemical measurements), an actual hot topic [82–84].

4.1.1 *Nat. Commun.* 6 (2015) 7460 [31]

Preamble

The focus of this paper is on the use of IR spectra as a tool to get further insight into the characterization of Charge Transfer (CT) organic doped semiconductor systems. This, having to deal with i) the detection and characterization of the polaron formation ii) its interplay with the order/disorder problem (this in comparison with the information associated to the "polaron signature", quite often probed and assessed on the basis of VIS/NIR spectroscopy results). To this aim, experimental IR spectra are collected for the PCPDT-BT/F4TCNQ and PCPDT/F4TCNQ donor/acceptor systems (PCPDT-BT co-polymer, PCPDT homo-polymer). In a broader view, the general scope of this paper deals with the study of the relationship between molecular structure[8] and spectroscopic evidence, also taking into account donor/acceptor interactions as a function of various reciprocal orientations (different "reciprocal orientation" is targeting the order/disorder problem in organic semiconductors). Thus, a thoroughly analysis is made comparing IR experimental spectra with calculated ones. On the theoretical side a number of issues has to be considered, to mention a few: i) the theoretical method to be used: plane waves *vs.* localized orbitals ii) the level of the theory: suitable basis-set selection, how to account for electron correlation iii) reasonable geometrical guess(es) for the donor/acceptor reciprocal orientation and position (in particular for the co-polymer, which features two different moieties, PCPDT and BT, within the single repeating unit), this because the sys-

[8] Here we made the choice to approximate the polymer (in principle an infinite collection of repeating units) as a sizeable single molecule (oligomer) featuring a fixed number of repeating units. Also dealing with the omnipresent problem to find a compromise between "how-much" of the *alkyl later chains* has to be considered to play a role in determining the overall spectroscopic properties, in relation to the humungous increase in conformational degree of freedom associated with long *alkyl later chains* substituents.

tem is not in a crystalline state (X-ray data are in general a useful initial geometrical guess) iv) last but not the least, the need to "force" the theoretical electronic structure of the Donor/Acceptor cluster into two distinct electronic configurations D/A (with negligible charge transfer) and D^{+}/A^{-} (CT system featuring a net/complete one electron transfer from the donor to the acceptor). All of these issues must also keep into account the compromise between level of the theory and calculation resources. Eventually, vibrational spectra (giant IR) were rationalized by exploiting both restricted and unrestricted DFT based calculations (CAM-B3LYP), giving due evidence of the formation of a charge transfer donor/acceptor interaction. Indeed, the physics underlying the presence of the low frequency huge IR absorption (giant IR [43]) is still an active area of research in this lab.

The candidate contribution concerned the theoretical part, concerning both scientific as well as "technical" issues: i) critical comparison of different *level of the theory* to be adopted, emerging from a compromise between "theoretical-method"/accuracy/resources ii) proper selection of suitable theoretical indices able to give proper insight on the experimental results, this beyond the simple calculation of the vibrational spectrum (mainly: Mulliken net charges, bond lengths, stabilization energy, critical <S^2> eigenvalue assessment) iii) discussion of the physics underlying the theoretical results (with particular reference to the recognition of the "polaron" signature).

Statement of Authorship

<table>
<tr><td colspan="5">This declaration concerns the article entitled:

How intermolecular geometrical disorder affects the molecular doping of donor–acceptor copolymers</td></tr>
<tr><td colspan="5">Publication status (tick one)</td></tr>
<tr><td>draft manuscript</td><td>Submitted</td><td>In review</td><td>Accepted</td><td>Published X</td></tr>
<tr><td colspan="5">Publication details (reference): Nat. Commun. 6 (2015) 7460</td></tr>
<tr><td colspan="2">Candidate's contribution to the paper (detailed, and also given as a percentage).</td><td colspan="3">The candidate contributed to theoretical interpretation and actual calculations (vide supra).

Formulation of ideas: 50 %

Design of methodology: 90 %

Experimental work: 0%

Presentation of data in journal format: 20%</td></tr>
<tr><td colspan="2">Statement from Candidate</td><td colspan="3">This paper reports on original research I conducted during the period of my Higher Degree by Research candidature.</td></tr>
<tr><td colspan="2">Signed  </td><td colspan="3">Date 15 May 2017</td></tr>
</table>

Title:	How intermolecular geometrical disorder affects the molecular doping of donor–acceptor copolymers
Author:	Daniele Di Nuzzo, Claudio Fontanesi, Rebecca Jones, Sybille Allard, Ines Dumsch et al.
Publication:	Nature Communications
Publisher:	Nature Publishing Group
Date:	Mar 10, 2015

Author Use

Authors of NPG articles do not require permission to use content from their article in most cases as stated in the author's guidelines.

Authors wishing to use their article for commercial purposes must request permission in the normal way.

For further questions, please contact NPG's permissions department: permissions@nature.com

Publication title:
How intermolecular geometrical disorder affects the molecular doping of donor–acceptor copolymers

the thesis page numbers that it spans:
31 to 59

nature COMMUNICATIONS

ARTICLE

Received 14 Aug 2014 | Accepted 30 Jan 2015 | Published 10 Mar 2015

DOI: 10.1038/ncomms7460

How intermolecular geometrical disorder affects the molecular doping of donor–acceptor copolymers

Daniele Di Nuzzo[1], Claudio Fontanesi[1,2], Rebecca Jones[1], Sybille Allard[3], Ines Dumsch[3], Ullrich Scherf[3], Elizabeth von Hauff[4], Stefan Schumacher[5,6] & Enrico Da Como[1]

Molecular doping of conjugated polymers represents an important strategy for improving organic electronic devices. However, the widely reported low efficiency of doping remains a crucial limitation to obtain high performance. Here we investigate how charge transfer between dopant and donor–acceptor copolymers is affected by the spatial arrangement of the dopant molecule with respect to the copolymer repeat unit. We p-dope a donor–acceptor copolymer and probe its charge-sensitive molecular vibrations in films by infrared spectroscopy. We find that, compared with a related homopolymer, a four times higher dopant/polymer molar ratio is needed to observe signatures of charges. By DFT methods, we simulate the vibrational spectra, moving the dopant along the copolymer backbone and finding that efficient charge transfer occurs only when the dopant is close to the donor moiety. Our results show that the donor–acceptor structure poses an obstacle to efficient doping, with the acceptor moiety being inactive for p-type doping.

[1] Department of Physics, University of Bath, Bath BA2 7AY, UK. [2] Dipartimento di Scienze Chimiche e Geologiche, Universita' di Modena e Reggio Emilia, Modena 41125, Italy. [3] Macromolecular Chemistry Group and Institute for Polymer Technology, Bergische Universität Wuppertal, Wuppertal 42119, Germany. [4] Department of Physics and Astronomy, Physics of Energy, VU University Amsterdam, Amsterdam 1081 HV, The Netherlands. [5] Physics Department and Center for Optoelectronics and Photonics Paderborn (CeOPP), Universität Paderborn, Paderborn 33098, Germany. [6] College of Optical Sciences, University of Arizona, Tucson, Arizona AZ85721, USA. Correspondence and requests for materials should be addressed to E.D.C. (email: edc25@bath.ac.uk).

Recently, a wide range of new applications for doped polymers has emerged, which include thermoelectrics[1,2], spintronics[3], (opto)electronics[4] and biosensors[5]. This recent progress was mainly driven by the design of robust molecular dopants[6], which when mixed with the semiconductor in controlled amounts can finely tune the electrical characteristics of the material. Despite the increasing interest in device applications, there is only limited understanding of how molecular doping of conjugated polymers occurs. Doping organic semiconductors is different in nature with respect to the similar concept applied in inorganic semiconductor technology. While p- and n-type doping of silicon, for example, by boron or phosphor, respectively, means the substitution of atoms in a covalently bound lattice, molecular doping of conjugated polymers generally refers to charge transfer occurring between molecular components in a film. The molecules form a van der Waals solid and each molecule retains its chemical identity. This intermolecular type of doping opens the possibility for many different geometrical configurations, exhibiting different degrees of electronic interaction and resulting in a variation in doping efficiency as we demonstrate in this article. In our work, we discuss the doping efficiency referring to the amount of charge transferred between the dopant and the conjugated polymer.

To achieve p- or n-type molecular doping, highly electronegative or highly electron donating molecules are mixed in low concentration with an organic semiconductor[6]. The most striking success of this approach is the realization of organic field effect transistors with improved operational stability[4,7], highly efficient organic light emitting diodes[8,9] and solar cells with improved performance[10,11]. We focus on the case of p-type doping, that is, the introduction of excess positive charge carriers (holes) in the semiconductor. In this respect, the most commonly presented picture is the ground-state transfer of one electron from the highest occupied molecular orbital (HOMO) of the polymer to the lowest unoccupied molecular orbital (LUMO) of the electronegative dopant molecule[6,12]. Holes in the semiconductor increase the carrier density, leading to an enhancement of the electrical conductivity. Furthermore, it has been recently reported by several groups that doping can fill trap states, resulting in improved carrier mobility in different types of device architectures[7,10,13,14]. However, these beneficial effects are difficult to reliably control. The density of free carriers and the dopant density in the semiconductor, thus the efficacy of the charge transfer process, are the most discussed variables in the parameters space[12,15]. Particularly interesting are the recent observations showing evidence that the effect of doping on conductivity enhancement in donor–acceptor (D–A) copolymers is lower than that for homopolymers[16].

D–A copolymers have revolutionized the field of organic electronics by showing single-junction solar cells reaching close to 10% power conversion efficiency[17], carrier mobility $>10\,cm^2\,V^{-1}\,s^{-1}$ in field effect transistors[18] and bipolar transport[19]. The most important feature of D–A copolymers is the possibility of finely tuning the energy bandgap via the selection of the two moieties[20]. The intrinsically more complex structure of the repeat unit of D–A copolymers, however, brings more difficulties to the microscopic description of doping in these systems. Studies aiming for a microscopic description of doping have appeared recently mainly focusing on homopolymers[12,21–25], leaving the challenge of describing the interaction between dopants and D–A alternating copolymers largely unaddressed. A detailed understanding of the mechanism of doping is needed in order to shed light on the very low amount of free charges per dopant ($\sim$4 charges donated every 100 dopants) observed in D–A copolymers[26], and offer a solid understanding for future materials development.

In this article, we provide a microscopic description of doping in the D–A copolymer (poly[2,6-(4,4-bis(2-ethylhexyl)-4H-cyclopenta[2,1-b;3,4-b′′]dithiophene)-*alt*-4,7-(2,1,3-benzothiadiazole)] (PCPDT-BT) mixed at different concentrations with the dopant 2,3,5,6-tetrafluoro-7,7,8,8-tetracyanoquinodimethane (F4-TCNQ). In PCPDT-BT, the cyclopenta-dithiophene (CPDT) moiety is D and the BT moiety is A. We used infrared spectroscopy to study microscopic changes induced by doping, as this technique is known to be sensitive to the presence of charged species in conjugated polymers through molecular vibrations[27–29]. An advantage of looking at vibrations is that their absorption resonances are less affected by inhomogeneous broadening, an effect which is instead markedly impacting the amount of information possibly extracted from electronic transitions in conjugated polymers[30,31]. In contrast to previous studies looking at the vibrational absorption bands of the dopant[21,32], our work is concentrating on the modes of the conjugated polymer backbone. This distinctive approach is motivated by the following two reasons: (i) the much higher sensitivity of these bands in witnessing charge carriers and thus the possibility to study the low doping concentration regime of 1% molar ratio, and (ii) a more detailed understanding of the role of polymer-dopant geometrical structure on doping, which we achieve by ab initio simulations despite the demanding computational effort in reproducing the experimental spectra. We demonstrate that if the dopant molecule is close to the A moiety of the copolymer, there is no efficient charge transfer. This can, therefore, be considered as an inactive site, lowering the overall efficiency of doping in the semiconductor film. Efficient charge transfer is instead observed for F4-TCNQ close to D. The critical aspect of intermolecular geometrical disorder is further demonstrated by a series of experiments with the homopolymer PCPDT, which contains only D in the repeat unit. As expected in the case of more efficient doping, this homopolymer exhibits the characteristic spectroscopic signals of charges on the conjugated chain at lower doping concentrations.

Results

FTIR spectroscopy on doped polymer films. In Fig. 1a, the chemical structures of the copolymer PCPDT-BT, the homopolymer PCPDT and the dopant F4-TCNQ are shown. Figure 2a shows the Fourier transform infrared (FTIR) spectra of PCPDT-BT in the pristine form (0%) and doped with F4-TCNQ at different % molar ratios. Each spectrum is normalized to the absorbance of the band peaked at $1{,}400\,cm^{-1}$. To calculate the % molar ratio, we use the number of moles of F4-TCNQ divided by the number of moles of polymer repeat unit. Using this definition, 4% molar ratio corresponds to 25 polymer repeat units for each F4-TCNQ molecule. The spectra of doped samples with molar ratio >4% exhibit additional infrared active vibrational modes in the region $1{,}000$–$1{,}300\,cm^{-1}$, which are almost undetectable in pristine PCPDT-BT. By zooming this spectral region in the inset, we note a remarkable increase in the absorption intensity of modes at 1,055, 1,080 and $1{,}120\,cm^{-1}$ in comparison with the one at $1{,}190\,cm^{-1}$, as the dopant molar ratio is increased to 6.7%. The high intensity vibrational bands of pristine PCPDT-BT in the region $1{,}360$–$1{,}550\,cm^{-1}$ are present in all samples introduced in this figure and do not exhibit any detectable change in spectral position. We attribute the intensity enhancement of absorption between 1,000 and $1{,}300\,cm^{-1}$ to the presence of dopant-induced hole polarons on the polymer chain. The high oscillator strength for vibrational absorption bands in presence of charged states has been extensively documented in conjugated molecules[27,33,34]. Figure 2b shows the infrared spectra on a larger spectral range up to $6{,}000\,cm^{-1}$ for the same PCPDT-BT

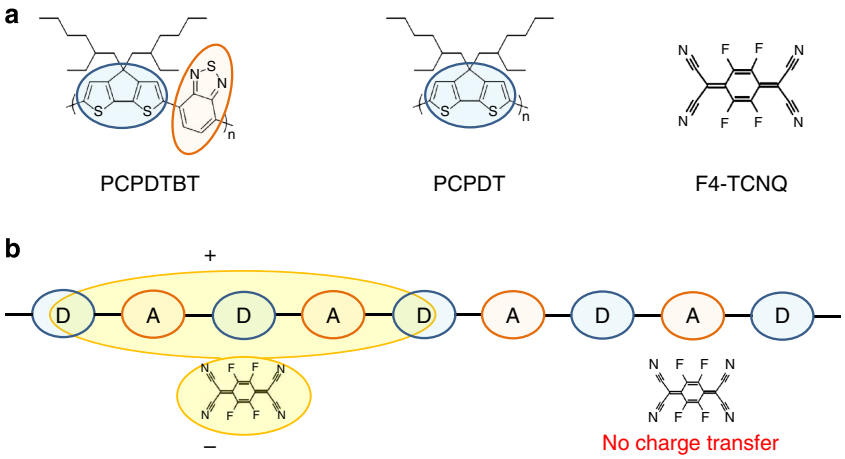

Figure 1 | Chemical structures. (**a**) Structure of the D–A copolymer PCPDT-BT, the homopolymer PCPDT and the dopant F4-TCNQ. The light blue and orange ovals highlight the donor (D) and acceptor (A) moieties of the repeat unit, respectively. (**b**) Scheme showing the dependence of electron transfer efficiency on the position of F4-TCNQ molecules along the D–A chain; when F4-TCNQ is on the *D* moiety, electron transfer is efficient, and when on the A moiety there is no charge transfer.

samples presented above. These cover not only the region of fingerprint molecular vibrations but also the polaronic transitions due to the hole polarons on the conjugated segments of the copolymer. Only at 6.7%, we observe the appearance of a prominent polaron band centred at 3,500 cm^{-1}.

We contrast these results on the copolymer with the spectra for the pristine and doped homopolymer. Figure 2c shows normalized infrared spectra of PCPDT in the same spectral interval and same F4-TCNQ molar concentrations of Figure 2a. The absorption intensity increases in the region from 1,000 to 1,300 cm^{-1} as a function of doping and it is evident at molar percentages lower than those reported above for the copolymer PCPDT-BT. Prominent vibrational bands are at 1,083, 1,108 and 1,182 cm^{-1}, together with a broad structure of bands from 1,225 to 1,335 cm^{-1}. Importantly, here the effect of doping is visible already at 1% F4-TCNQ molar concentration, with a detectable enhancement of the broad band between 1,225 and 1,325 cm^{-1} (inset Fig. 2c). At 2%, the effect becomes more substantial with the enhancement of bands in the region between 1,000 and 1,200 cm^{-1} as well. The spectrum of pristine PCPDT (lower black curve in main panel) is characterized by four intense vibrational bands at 1,165, 1,378, 1,418 and 1,460 cm^{-1}. These four vibrational transitions are present in all the samples that we show. Increasing the dopant concentration in PCPDT films also results in a vibrational band at 1480 cm^{-1} which gains intensity with dopant concentration. This is in contrast to the spectra of doped PCPDT-BT (Fig. 2a), where the 1,350 to 1,600-cm^{-1} part of the spectrum remains almost unchanged upon doping.

Figure 2d shows the enlarged spectral range with the polaronic transition peaking at $\sim$4,100 cm^{-1}. In agreement with the intensity trend in the vibrational bands, also the polaronic transition of PCPDT appears at lower molar concentration with respect to what we observe in the copolymer. Interestingly, the polaronic absorption band of PCPDT can be clearly distinguished only for dopant percentages $>2\%$, whereas signatures of doping enhanced vibrational bands are seen at lower concentrations of 1% as presented above. This latter observation indicates that the enhancement of oscillator strength (intensity) of certain vibrational transitions allows for a more sensitive monitoring of charged states with respect to the polaronic transitions solely.

***Ab initio* simulations of vibrational spectra using DFT**. We now focus on the theoretical description of the infrared spectra in the region of the conjugated backbone vibrations, that is, 800–1,600 cm^{-1}. Spectra are shown as integrated infrared absorption intensity as a function of frequency (see Methods section for details on calculations). Figure 3a shows the computed vibrational spectrum for a polymer strand of PCPDT-BT made of four and a half repeat units (structure in Supplementary Fig. 1) simulated with a continuum model of the surrounding medium defined by the bulk dielectric constant[35]. The computed spectrum (lower black curve) reproduces with a good agreement the experimental features observed in Fig. 2a for pristine PCPDT-BT. We note that there is also a reasonable agreement in the prediction of the relative intensities of the vibrational bands. The peak at 1,397 cm^{-1} is reproduced as the most intense followed by the peaks in the region close to 1,500 cm^{-1} and the one at 1,568 cm^{-1}. Following a standard procedure described in the Methods section, we scaled the calculated frequencies by a factor <1 in the part of the spectra $>$1,280 cm^{-1} (ref. 36). Figure 3a shows also the spectrum of Complex-1, a molecular cluster obtained by energetically optimizing the geometry of F4-TCNQ in proximity of one of the CPDT moieties of PCPDT-BT (Fig. 3c). The computed infrared spectrum has changed markedly compared with the neutral copolymer strand and exhibits intense vibrational bands in the region from 1,000 to 1,200 cm^{-1}. We point out that the band peaked at 1,033 cm^{-1} of Complex-1 carries a 20 times larger intensity than the most intense peak of the neutral copolymer at 1,397 cm^{-1}. This appears to be qualitatively consistent with the charge-induced intensity enhancement that we experimentally observed. In Fig. 3a, we also show the following two additional spectra: the copolymer without F4-TCNQ, but with a positive charge on the chain strand, that is, a cation, and Complex-2, which is a different optimized geometry where the dopant F4-TCNQ is in the vicinity of the A moiety (Fig. 3b). The computed spectrum of the cation resembles Complex-1 in terms of intensity of the bands and similarity of the enhanced modes (Supplementary Figs 2 and 3). Complex-2 has, instead, a spectrum almost identical to the neutral copolymer. Further, the Mulliken analysis of partial charge density (see Methods section) indicates an almost complete charge transfer in Complex-1 (0.93 *e* on the polymer) and almost zero (-0.02 *e* on the polymer) in Complex-2. The similar enhancement of vibrational transitions in the region 800–1,200 cm^{-1} for the cation and Complex-1 spectra, together with the Mulliken charge density distribution, confirms that for F4-TCNQ on the D moiety

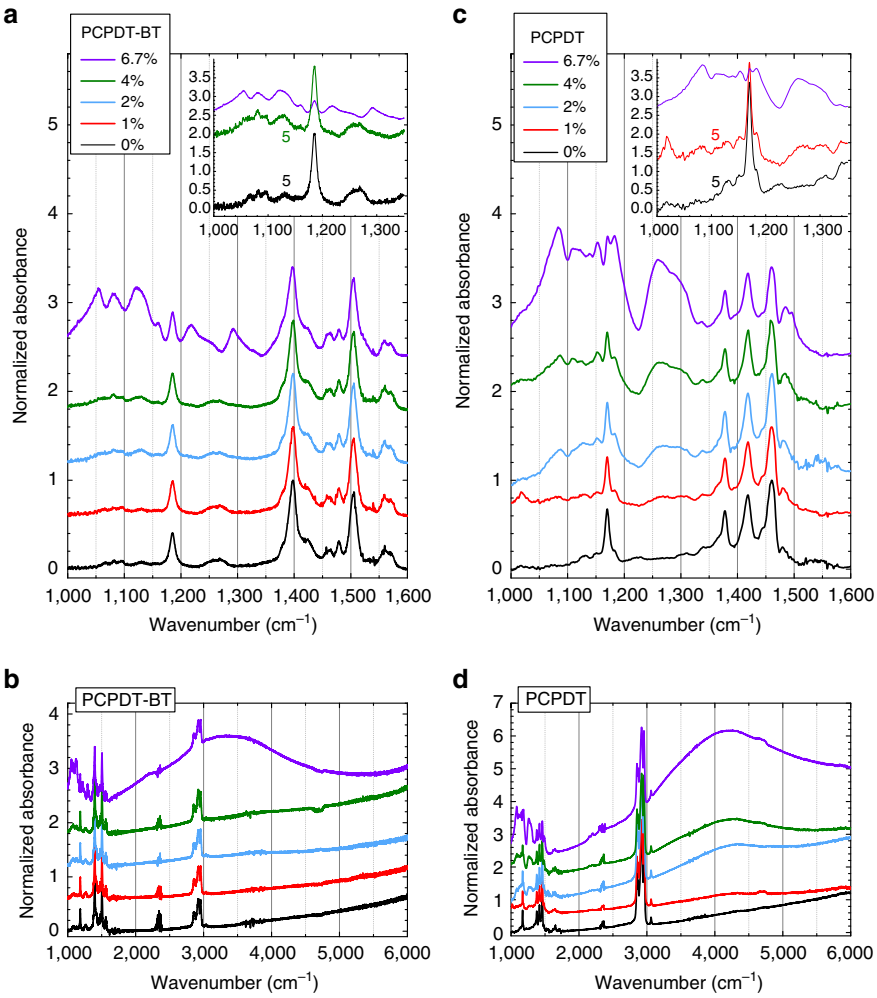

Figure 2 | FTIR absorption spectra of doped thin films. Normalized FTIR absorption spectra in the region of backbone vibrations for (**a**) PCPDT-BT and (**c**) PCPDT spin-coated thin films, pristine and doped with F4-TCNQ in different molar percentages (see legend). The molar percentage is calculated using the number of moles of F4-TCNQ divided by the number of moles of polymer repeat unit. The insets in **a**,**c** are a zoom of the low wavenumber part, with the intensity of neutral and doped samples spectra (4% and 1% for PCPDT-BT and PCPDT, respectively) multiplied five times to better compare the 6.7% samples. (**b**,**d**) Wider wavenumber ranges for PCPDT-BT and PCPDT, respectively. All the spectra are normalized on the band peaked at *ca.* 1,400 cm^{-1} for PCPDT-BT samples and at *ca.* 1,460 cm^{-1} for PCPDT, and offset for clarity. In **b**,**d**, the light scattering contribution to the baseline was not corrected. The vibrational bands in the 2,800–3,000 cm^{-1} region originate from the alkyl side chains of the polymers. F4-TCNQ vibrations, either in neutral or charged state[51], are not apparent due to the low dopant concentrations.

charge transfer occurs and a hole polaron is formed, whereas with the F4-TCNQ on the A moiety charge transfer and polaron formation are hindered.

With a similar approach to the one used for PCPDT-BT, we have computed the infrared spectra for the homopolymer PCPDT. Figure 3d shows a series of spectra for a PCPDT polymer strand of six repeat units in its neutral form, a complex with F4-TCNQ (named Complex-3) and the same strand without the dopant, but with a net positive charge representing a cation. The calculated spectrum for the neutral polymer (lower black curve in Fig. 3d) has the highest intensity bands in the 1,300 to 1,500-cm^{-1} region, similar to the experimental one (Fig. 2c). The spectra of Complex-3 and of the cation show vibrational modes with high intensity in the low wavenumber region (800–1,300 cm^{-1}), with intensities comparable to those of the copolymer PCPDT-BT. As already noted for the PCPDT-BT case, the similarity in spectral evolution of complex and cation testifies the transfer of one electron from the HOMO of the polymer to the LUMO of F4-TCNQ. The illustration of a selection of vibrational modes is shown in the Supplementary Figs 1–4 and 7–9 for PCPDT-BT and PCPDT, respectively. In addition Supplementary Figs 5, 6 and 10, 11 contain the assignment of some of the experimental bands to the calculated vibrational modes. The criteria used in the selection are described in the Supplementary Discussion.

Discussion

The most immediate message that can be drawn from our theoretical results is that the primary step in doping of conjugated copolymers is extremely sensitive to geometrical intermolecular disorder. If F4-TCNQ forms a complex where it is co-facially aligned with the CPDT moiety, D, electron transfer occurs and a segment of the copolymer chain becomes doped with a hole. In contrast, if F4-TCNQ is closer to the BT moiety, A, only a negligible amount of charge transfer occurs. This conclusion is schematically depicted in Fig. 1b and is further supported by the results on the homopolymer; here different geometrical configurations were tested (Supplementary Fig. 13 and the Supplementary Discussion). We found that charge transfer

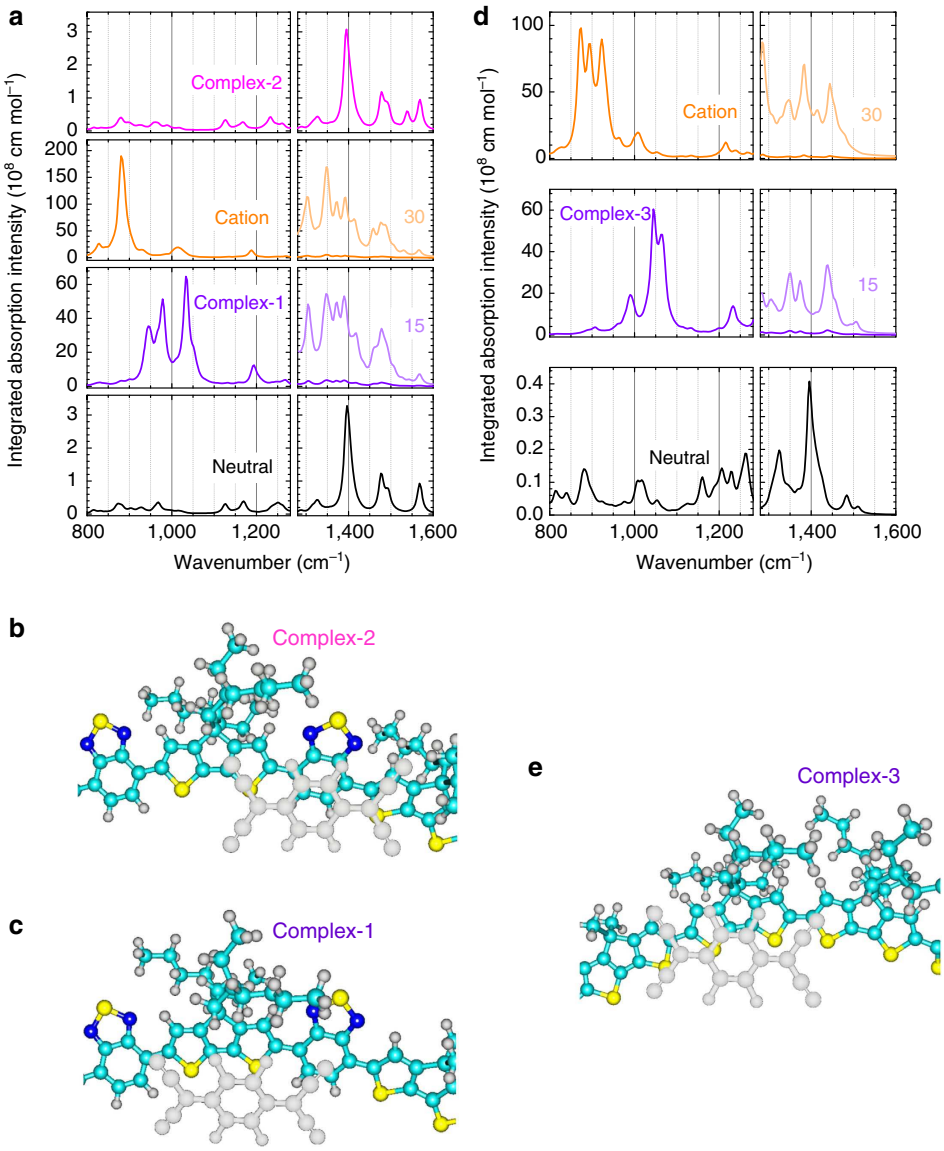

Figure 3 | Vibrational spectra calculated by DFT. Calculated vibrational spectra of (**a**) PCPDT-BT and (**d**) PCPDT in different configurations as indicated by the labels in the graphs. The ordinates are in units of integrated absorption intensity (see Methods section). Each spectrum is divided in the following two parts: for wavenumbers $<1{,}280\,cm^{-1}$ the *x* axis has not been scaled, whereas for wavenumbers $>1{,}280\,cm^{-1}$ a scaling factor of 0.935 has been applied. To show some of the weaker absorption bands on the same scale, part of the spectra of Complex-1 and Complex-3 has been multiplied by 15 and part of the spectra of the cations has been multiplied by 30. (**b**,**c**,**e**) Image cuts of the optimized molecular geometries used to calculate the spectra of Complex-2, Complex-1 and Complex-3, respectively. The F4-TCNQ molecule lies in front of the polymer and is coloured in grey for better visualization.

occurs with similar amounts of transferred charge (>0.90 *e*), independent of the exact position of F4-TCNQ along the polymer backbone and with respect to the repeat unit. From calculations, we have estimated the difference in the total Gibbs energy between Complexes-1 and -2 (Supplementary Table 1). This is ~ 0.22 eV, which is above thermal energy at room temperature. While this could imply an instability of Complex-2 in conditions of thermodynamic equilibrium, we stress that the preparation of films by spin coating is a kinetic out of equilibrium process. Thus, intermolecular arrangements such as the one of Complex-2 are likely to be present, with large potential barriers for reorganization[37]. In addition, this energy estimation is for two molecules, while in the film additional polymer chains in proximity could further stabilize the geometry of Complex-2.

The calculations on PCPDT-BT:F4-TCNQ in Complex-1 geometry can be considered as an idealized realization of an effectively doped copolymer film, where each F4-TCNQ molecule in every four and a half repeat units is accepting an electron and generating a hole. The spectrum of such a hypothetical film should be largely dominated by the bands between 1,000 and $1{,}200\,cm^{-1}$ (Fig. 3a). Furthermore, the region 1,300–$1{,}600\,cm^{-1}$ should show additional vibrational transitions of comparable intensity to the peak at $1{,}400\,cm^{-1}$, which are not present in the neutral copolymer strand. Note that the calculated absorption intensity for modes in this region are very similar for Complex-1 and neutral PCPDT-BT (Fig. 3a). In contrast to these predictions, for all the dopant concentrations that we have used in the PCPDT-BT films (Fig. 2a) we observe only the molecular vibrations characteristic of the pristine copolymer left (1,350–$1{,}600\,cm^{-1}$). Even at the highest molar percentage of 6.7%, the vibrational bands between 1,350 and $1{,}600\,cm^{-1}$ remain the most intense with just an additional background on the red side of the $1{,}400\text{-}cm^{-1}$ peak. This dopant percentage would correspond to one F4-TCNQ every 15 repeat units, which is a

situation comparable to our theoretical simulations of one in every four and half repeat units. This discrepancy between experiments and predictions based on density functional theory (DFT) simulations can be rationalized, considering that the absorption spectra of our doped thin films contain a superimposition of contributions from charged and neutral polymer strands, with the latter dominating. The question is then why a considerable amount of polymer strands (chromophores) appears to be left undoped even when, as argued above, the amount of F4-TCNQ molecules in the 6.7% film should be just a factor of ~ 3 away from what is required for charging a conjugated segment.

In principle, F4-TCNQ could phase segregate in the film. Without being in contact with PCPDT-BT chains, some dopant molecules would be excluded from the doping process. At the low concentrations that we explore here, this is unlikely and dopant segregation would appear as saturation or decrease in the intensity of the polaronic absorption[38], which we do not observe in any of our samples. Our computational investigations suggest a different explanation: even if F4-TCNQ is molecularly dispersed, there are some intermolecular configurations that do not lead to doping. The latter case is theoretically reproduced by the simulations with the dopant on the A unit (Complex-2 in Fig. 3c). On one hand, it is important that doped polymer layers in devices are prepared with molecularly dispersed dopants. On the other hand, it is apparent from our work that even taking care of morphology issues, F4-TCNQ may find a stable configuration close to the A moiety, forming a very weak charge transfer complex that does not contribute to doping. This analysis is supported by the data and simulations on the homopolymer, which has a similar energy of the HOMO with respect to PCPDT-BT (see Methods section), and thus a very similar driving force for charge transfer, but exhibits doping characteristics at much lower F4-TCNQ concentration. Note that the absorption intensities of vibrational modes enhanced by charges are very similar for Complexes-1 and -3, and thus spectral features should appear at equal experimental concentrations if the doping efficiency was the same for both polymers. To summarize, our results reveal that intermolecular geometrical disorder acts as an intrinsic limitation to efficient doping of D–A-conjugated copolymers with F4-TCNQ, even in the case of homogeneous dopant dispersion in the film.

There is a complementary important aspect on which our results can shed light and contribute to the microscopic understanding of doping in conjugated copolymers, that is, the degree of delocalization of the dopant-induced hole on the conjugated polymer. This is intrinsically correlated to the density of free carriers and charge carrier transport characteristics. Holes generated on the polymer backbone may remain localized in the proximity of the ionized dopant and thus exhibit a low probability of escaping from the Coulomb potential generated by the negative charge on the F4-TCNQ. In contrast, delocalized holes should have a larger probability of escaping the Coulomb potential by hopping on nearest neighbour conjugated chains and becoming mobile.

Since the vibrational spectra and their description are particularly sensitive to the length of chemical bonds along the π-conjugated backbone, we could extract information on the polaron delocalization. We analysed the evolution of the C–C bond lengths along the PCPDT-BT copolymer strands in the neutral and charged states, as computed in our DFT calculations. As previously shown, the presence of a polaron on a conjugated polymer backbone is accompanied by an evolution from aromatic to quinoid structure[39]. Figure 4a shows the difference between a selection of C–C bond lengths in the Complex-1 configuration and the same bonds in the neutral PCPDT-BT strand. These are the bonds mostly affected by the presence of a polaron. The convention used for the bond numbering is indicated in

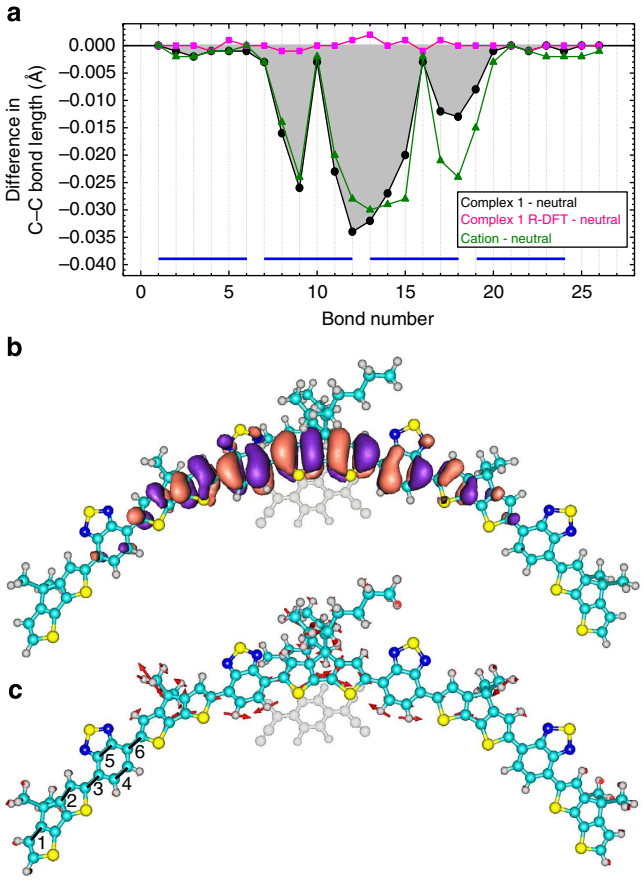

Figure 4 | Bond length alternation and mode visualization for Complex-1 (**a**) Difference between the calculated carbon–carbon (C–C) bond lengths of PCPDT-BT in Complex-1 and the neutral PCPDT-BT strand (black). The bond length difference compared with the neutral strand is shown also for PCPDT-BT in Complex-1 configuration calculated with R-DFT (pink) and for the PCPDT-BT cation (green). The line connecting the symbols is a guide to the eye. The C–C length of bond number 1 in the neutral chain is 1.421 Ångstrom. The bond numbering is defined as indicated by the black bars and labels on the first repeat unit in **c**. The blue horizontal bars indicate the polymer repeat units. (**b**) Molecular orbital of the positive polaron induced on the PCPDT-BT chain by charge transfer to F4-TCNQ. (**c**) Scaled vectors representing the vibrations corresponding to the absorption peaked at 1,033 cm^{-1} (Fig. 3a) as calculated for Complex-1. For visual clarity, in **b**,**c**, the F4-TCNQ molecule lies behind the polymer chain.

Fig. 4c. The change in bond length is up to 0.035 Å and it extends over two repeat units in front of the F4-TCNQ molecule. The main distortion (change in C–C length >0.01 Å) is over ~ 2 nm along the chain. Figure 4b shows the molecular orbital describing the polaron, that is, the singly occupied HOMO. By comparing Fig. 4a and Fig. 4b, the correlation between the change in bond length and the spatial extension of the polaron is apparent. In order to exclude any role of steric hindrance effects due to F4-TCNQ on the copolymer structure, Fig. 4a also shows the bond length change for Complex-1 geometry calculated using a restricted DFT (R-DFT) approach (see Methods section), where no charge is transferred and the C–C distances remain essentially the same as for the neutral copolymer.

We have attempted to visualize the impact of Coulomb interactions on the polaron wavefunction delocalization. This is done by comparing the change in bond lengths of the PCPDT-BT cation to that of the polaron in Complex-1, using the same type of bond length analysis. The results, displayed in Fig. 4a, show how

the distortion in bond length is more extended in the absence of F4-TCNQ, particularly on the right side of the polymer strand centre (bond number >14). It is gratifying to note that electron spin resonance measurements on a similar copolymer yielded a free polaron delocalized over three repeat units[40], very close to our polaron size for the cation. The comparison between cation and Complex-1 indicates that in the latter the negatively charged F4-TCNQ molecule exerts an electrostatic attraction on the positive polaron on the polymer, contributing to confine it. The more delocalized polaron for the cation leads to a red-shift of the most intense vibrational band to 880 cm^{-1} (Fig. 3a). Signatures of this mode in experiments have not been detected, suggesting that most of the holes on the doped copolymer film remain bound to the ionized F4-TCNQ, that is, in a configuration similar to Complex-1. We obtain a similar red-shift of the low-frequency vibrational bands (from *ca.* 1,050 to *ca.* 900 cm^{-1}) between the calculated spectra of Complex-3 and PCPDT cation (Fig. 3d), indicating that also for the homopolymer the polaron is localized by the Coulomb interaction with the negatively charged F4-TCNQ. Figure 4c illustrates with displacement vectors the vibrational mode at 1,033 cm^{-1}, corresponding to the most intense peak in the calculated spectrum of Complex-1 (Fig. 3a). Comparing Fig. 4b,c, it can be seen how the biggest atomic displacements of this mode happen to be in the region where the polaron is located. The enhancement in absorption intensity associated with this mode is consistent with previous results, which have argued that the oscillation of the polaron charge density concomitantly with a vibrational mode can result in an increase in the transition dipole moment[27]. Thus, for the case of PCPDT-BT, while the charge transfer occurs when F4-TCNQ is close to the D moiety, the bond vibrations involving the two nearest neighbours A moieties on which the polaron wavefunction delocalizes give an important contribution to the mode absorption intensity.

Future experiments on charge-sensitive vibrations using infrared near-field microscopy[41] or two-dimensional coherent infrared spectroscopy[42] could provide further important insights on the mesoscopic structure and electronic couplings between dopant and adjacent polymer strands. From the materials point of view, the recently discovered doping via Lewis acids[43,44] offers a new interesting system where the impact of intermolecular disorder needs to be explored.

In conclusion, we studied the microscopic details of the formation of hole polarons induced by the dopant molecule F4-TCNQ on the D–A copolymer PCPDT-BT, showing the crucial influence of intermolecular geometrical disorder on the efficiency of doping. By exploiting the high sensitivity of vibrational spectroscopy to the presence of charged species on the polymer chains, we have probed that polarons are formed only above a molar ratio of 4%. This concentration is rather high compared with what we observed in the homopolymer PCPDT, where the formation of polarons was observed already at 1%. These observations can explain the low doping efficiency previously shown in transport measurements on doped D–A copolymers. Here we were able to pinpoint the intermolecular factors contributing to the low doping efficiency by theoretically simulating infrared spectra. We showed that the efficiency of charge transfer from copolymer to dopant strongly depends on the intermolecular geometry. The design of new dopants with a larger molecular size bridging the entire repeat unit of copolymers could be a strategy to overcome these limitations.

Methods

Materials, thin-film preparation and FTIR. PCPDT-BT ($M_w = 34$ kg mol^{-1}, polydispersity (PD) = 2.1, purity = 99.99%, based on trace metals content) was purchased from 1-Material and used as received. PCPDT ($M_w = 26$ kg mol^{-1}, PD = 1.8) was synthesized in a Yamamoto type polycondensation reaction of 2,6-dibromo-4,4-bis(2-ethylhexyl)-4H-cyclopenta[2,1-b:3,4-b′]dithiophene as described in the literature[45]. The molecular weight of PCPDT was measured on a PSS/Agilent SECurity GPC equipped with MZ Gel SDplus linear columns, a VWD G1329A ALS ultraviolet detector, and a RID C1362A RI detector, using chloroform as eluent. F4-TCNQ (purity ≥98%) was purchased by TCI-europe and used as received. The HOMO levels of PCPDT-BT and PCPDT were measured in film on a Riken Keiki AC-2 spectrometer. We measured the energy of the HOMO levels of PCPDT-BT and PCPDT by photoelectron spectroscopy under ambient conditions, and have obtained values with respect to vacuum of −5.07 and −5.08 eV, respectively. Therefore, we exclude that the difference in doping efficiency observed between the two polymers is owing to a difference in energetics of the two systems. For the LUMO level of F4-TCNQ, we consider the value reported in literature of −5.24 eV (ref. 46). Infrared spectra were recorded in transmission mode on a PerkinElmer Frontier FTIR spectrometer at room temperature.

Thin-film samples for FTIR spectroscopy were fabricated by spin coating polymer and F4-TCNQ dissolved in chlorobenzene. The solutions were prepared as follows: a starting F4-TCNQ solution was prepared (0.875 mg ml^{-1}) and the appropriate amount was added to a separate polymer solution to obtain the desired molar percentages. In the final solutions, the polymer concentration was always 10 mg ml^{-1}. The solutions were spin coated onto pre-cleaned CaF_2 substrates in nitrogen atmosphere. The optimal spin speeds for film homogeneity were found at 900 and 1,500 r.p.m. for PCPDT and PCPDT-BT, respectively.

Quantum chemistry calculations. *Ab initio* molecular orbital calculations were performed using the Gaussian 09 and Firefly suite of programs. Owing to the extremely large number of conformational degrees of freedom, great attention and a large endeavour was devoted to a detailed conformational analysis of the Complexes (Supplementary Figs 12 and 13, and Supplementary Discussion). To reduce the computational cost, alkyl side chains, which are likely to be uninvolved in determining electronic structure of frontier orbitals, have been largely replaced by methyl groups. A conspicuous amount of screening optimization-geometry calculations (Supplementary Tables 1 and 2), as well as Hessian analysis, were carried out. In particular, CAM-B3LYP DFT was used using 6–31G** basis sets giving the best agreement with the experimental vibrational spectra. Calculations on the PCPDT-BT:F4-TCNQ Complexes were run using both R-DFT and spin-unrestricted DFT wavefunctions. Restricted calculations (R-DFT) yield a much more limited intermolecular charge separation, resulting in a Mulliken net charge of 0.04 *e* on F4-TCNQ. As discussed by us[47] and other authors[22], unrestricted calculations are more suitable for describing charge states and R-DFT was used only for control experiments (Fig. 4a). All the calculations were performed without any symmetry constraints (that is, C1 point group symmetry). Aiming to account for the influence of the surrounding condensed phase, the calculations were performed including electrostatic interactions between the polymer or Complex under study and a polarizable continuum medium with relative dielectric constant 3. This was done exploiting the solvation model based on density[35] as implemented in Gaussian 09. The stabilization energies for Complexes-1 and -2 are −0.46 and −0.22 eV, respectively (Supplementary Table 1). For each vibrational mode, the integrated absorption intensity was calculated (units of cm mol^{-1}; ref. 48). To better fit the experimental spectra, we introduced a broadening by multiplying each computed absorption line of wavenumber f_0 with a unitless Lorentzian-like function of the form $\frac{1}{1+\left(\frac{f-f0}{a/2}\right)^2}$, where a is the full-width at half-maximum.

We chose to use $a = 15$ cm^{-1}. Note that, in general, the computed vibrational bands, especially at higher wavenumbers, are blue shifted compared with the experimental ones. This is a well-known effect arising from the parabolic potentials used in calculating the vibrational bands[49]. To account for this, and following standard procedures, we have rescaled the wavenumber axis of the computed spectra by a factor of 0.935 for wavenumbers >1,280 cm^{-1} (refs 36,50). For frequencies <1,280 cm^{-1}, no scaling was applied. Full and unscaled spectra are shown in the Supplementary Discussion (Supplementary Figs 14 and 15).

References

1. Bubnova, O. *et al.* Semi-metallic polymers. *Nat. Mater.* **13,** 190–194 (2014).
2. Glaudell, A. M., Cochran, J. E., Patel, S. N. & Chabinyc, M. L. Impact of the doping method on conductivity and thermopower in semiconducting polythiophenes. *Adv. Energy Mater.* 10.1002/aenm.201401072 (2014).
3. Cox, M., van der Heijden, E. H. M., Janssen, P. & Koopmans, B. Investigating the influence of traps on organic magnetoresistance by molecular doping. *Phys. Rev. B* **89,** 085201 (2014).
4. Lu, G. H. *et al.* Moderate doping leads to high performance of semiconductor/insulator polymer blend transistors. *Nat. Commun.* **4,** 1588 (2013).
5. Yang, S. Y. *et al.* Detection of transmitter release from single living cells using conducting polymer microelectrodes. *Adv. Mater.* **23,** 184–188 (2011).
6. Walzer, K., Maennig, B., Pfeiffer, M. & Leo, K. Highly efficient organic devices based on electrically doped transport layers. *Chem. Rev.* **107,** 1233–1271 (2007).
7. Wei, P., Oh, J. H., Dong, G. F. & Bao, Z. N. Use of a 1H-benzoimidazole derivative as an n-type dopant and to enable air-stable solution-processed

n-channel organic thin-film transistors. *J. Am. Chem. Soc.* **132,** 8852–8853 (2010).
8. Gross, M. *et al.* Improving the performance of doped pi-conjugated polymers for use in organic light-emitting diodes. *Nature* **405,** 661–665 (2000).
9. Reineke, S. *et al.* White organic light-emitting diodes with fluorescent tube efficiency. *Nature* **459,** 234–238 (2009).
10. Tunc, A. V. *et al.* Molecular doping of low-bandgap-polymer:fullerene solar cells: effects on transport and solar cells. *Org. Electron.* **13,** 290–296 (2012).
11. Zhang, Y. *et al.* Molecular doping enhances photoconductivity in polymer bulk heterojunction solar cells. *Adv. Mater.* **25,** 7038–7044 (2013).
12. Pingel, P. & Neher, D. Comprehensive picture of p-type doping of P3HT with the molecular acceptor F(4)TCNQ. *Phys. Rev. B* **87,** 115209 (2013).
13. Olthof, S. *et al.* Ultralow doping in organic semiconductors: evidence of trap filling. *Phys. Rev. Lett.* **109,** 176601 (2012).
14. Zhang, Y., de Boer, B. & Blom, P. W. M. Trap-free electron transport in poly(p-phenylene vinylene) by deactivation of traps with n-type doping. *Phys. Rev. B* **81,** 085201 (2010).
15. Pingel, P., Schwarzl, R. & Neher, D. Effect of molecular p-doping on hole density and mobility in poly(3-hexylthiophene). *Appl. Phys. Lett.* **100,** 143303 (2012).
16. Yim, K. H. *et al.* Controlling electrical properties of conjugated polymers via a solution-based p-type doping. *Adv. Mater.* **20,** 3319–3324 (2008).
17. Dou, L. T. *et al.* 25th Anniversary article: a decade of organic/polymeric photovoltaic research. *Adv. Mater.* **25,** 6642–6671 (2013).
18. Kim, G. *et al.* A Thienoisoindigo-naphthalene polymer with ultrahigh mobility of 14.4 cm(2)/V.s that substantially exceeds benchmark values for amorphous silicon semiconductors. *J. Am. Chem. Soc.* **136,** 9477–9483 (2014).
19. Beaujuge, P. M. *et al.* Synthetic principles directing charge transport in low-band-gap dithienosilole-benzothiadiazole copolymers. *J. Am. Chem. Soc.* **134,** 8944–8957 (2012).
20. Boudreault, P. L. T., Najari, A. & Leclerc, M. Processable low-bandgap polymers for photovoltaic applications. *Chem. Mater.* **23,** 456–469 (2011).
21. Zhu, L. Y., Kim, E. G., Yi, Y. P. & Brédas, J. L. Charge transfer in molecular complexes with 2,3,5,6-tetrafluoro-7,7,8,8-tetracyanoquinodimethane (F-4-TCNQ): a density functional theory study. *Chem. Mater.* **23,** 5149–5159 (2011).
22. Zamoshchik, N. & Bendikov, M. Doped conductive polymers: modeling of polythiophene with explicitly used counterions. *Adv. Funct. Mater.* **18,** 3377–3385 (2008).
23. Burkhardt, S. E. *et al.* Theoretical and electrochemical analysis of poly(3,4-alkylenedioxythiophenes): electron-donating effects and onset of p-doped conductivity. *J. Phys. Chem. C* **114,** 16776–16784 (2010).
24. Gao, J., Niles, E. T. & Grey, J. K. Aggregates promote efficient charge transfer doping of poly(3-hexylthiophene). *J. Phys. Chem. Lett.* **4,** 2953–2957 (2013).
25. Gao, J. *et al.* The effect of 2,3,5,6-tetrafluoro-7,7,8,8-tetracyanoquinodimethane charge transfer dopants on the conformation and aggregation of poly(3-hexylthiophene). *J. Mater. Chem. C* **1,** 5638–5646 (2013).
26. Zhang, Y. A. & Blom, P. W. M. Electron and hole transport in poly(fluorene-benzothiadiazole). *Appl. Phys. Lett.* **98** (2011).
27. Zamadar, M., Asaoka, S., Grills, D. C. & Miller, J. R. Giant infrared absorption bands of electrons and holes in conjugated molecules. *Nat. Commun.* **4,** 2818 (2013).
28. Neugebauer, H. Infrared signatures of positive and negative charge carriers in conjugated polymers with low band gaps. *J. Electroanal. Chem.* **563,** 153–159 (2004).
29. Osterbacka, R., Jiang, X. M., An, C. P., Horovitz, B. & Vardeny, Z. V. Photoinduced quantum interference antiresonances in pi-conjugated polymers. *Phys. Rev. Lett.* **88,** 226401 (2002).
30. Thiessen, A. *et al.* Unraveling the chromophoric disorder of poly(3-hexylthiophene). *Proc. Natl Acad. Sci. USA* **110,** E3550–E3556 (2013).
31. Walter, M. J. *et al.* Simultaneous Raman and fluorescence spectroscopy of single conjugated polymer chains. *Phys. Rev. Lett.* **98,** 137401 (2007).
32. Ghani, F. *et al.* Charge transfer in and conductivity of molecularly doped thiophene-based copolymers. *J. Polym. Sci. B Polym. Phys.* **53,** 58–63 (2015).
33. Horovitz, B. Infrared activity of Peierls systems and application to polyacetylene. *Solid State Commun.* **41,** 729–734 (1982).
34. Österbacka, R., An, C. P., Jiang, X. M. & Vardeny, Z. V. Two-dimensional electronic excitations in self-assembled conjugated polymer nanocrystals. *Science* **287,** 839–842 (2000).
35. Marenich, A. V., Cramer, C. J. & Truhlar, D. G. Universal solvation model based on solute electron density and on a continuum model of the solvent defined by the bulk dielectric constant and atomic surface tensions. *J. Phys. Chem. B* **113,** 6378–6396 (2009).
36. Girlando, A. Charge Sensitive vibrations and electron-molecular vibration coupling in bis(ethylenedithio)-tetrathiafulvalene (BEDT-TTF). *J. Phys. Chem. C* **115,** 19371–19378 (2011).
37. Sherwood, J. N. *The Plastically Crystalline State (Orientationally-Disordered Crystals)* (John Wiley & Sons, 1979).
38. Duong, D. T., Wang, C. C., Antono, E., Toney, M. F. & Salleo, A. The chemical and structural origin of efficient p-type doping in P3HT. *Org. Electron.* **14,** 1330–1336 (2013).
39. Brédas, J. L., Themans, B., Fripiat, J. G., Andre, J. M. & Chance, R. R. Highly conducting polyparaphenylene, polypyrrole and polythiophene chains- an ab-initio study of the geometry and electronic structure modifications upon doping. *Phys. Rev. B* **29,** 6761–6773 (1984).
40. Niklas, J. *et al.* Highly-efficient charge separation and polaron delocalization in polymer-fullerene bulk-heterojunctions: a comparative multi-frequency EPR and DFT study. *Phys. Chem. Chem. Phys.* **15,** 9562–9574 (2013).
41. Westermeier, C. *et al.* Sub-micron phase coexistence in small-molecule organic thin films revealed by infrared nano-imaging. *Nat. Commun.* **5,** 4101 (2014).
42. Kuroda, D. G. *et al.* Snapshot of the equilibrium dynamics of a drug bound to HIV-1 reverse transcriptase. *Nat. Chem.* **5,** 174–181 (2013).
43. Zalar, P. *et al.* Increased mobility induced by addition of a Lewis acid to a Lewis basic conjugated polymer. *Adv. Mater.* **26,** 724–727 (2014).
44. Poverenov, E., Zamoshchik, N., Patra, A., Ridelman, Y. & Bendikov, M. Unusual doping of donor-acceptor-type conjugated polymers using Lewis acids. *J. Am. Chem. Soc.* **136,** 5138–5149 (2014).
45. Asawapirom, U. & Scherf, U. Dialkylcyclopentadithiophene polymers and copolymers. *Macromol. Rapid Commun.* **22,** 746–749 (2001).
46. Djurovich, P. I., Mayo, E. I., Forrest, S. R. & Thompson, M. E. Measurement of the lowest unoccupied molecular orbital energies of molecular organic semiconductors. *Org. Electron.* **10,** 515–520 (2009).
47. Wiebeler, C. *et al.* Spectral signatures of polarons in conjugated co-polymers. *J. Phys. Chem. B* **117,** 4454–4460 (2013).
48. Hess, B. A., Schaad, L. J., Carsky, P. & Zahradnik, R. Ab initio calculations of vibrational-spectra and their use in the identification of unusual molecuLES. *Chem. Rev.* **86,** 709–730 (1986).
49. Andersson, M. P. & Uvdal, P. New scale factors for harmonic vibrational frequencies using the B3LYP density functional method with the triple-xi basis set 6-311 + G(d,p). *J. Phys. Chem. A* **109,** 2937–2941 (2005).
50. Irikura, K. K., Johnson, R. D. & Kacker, R. N. Uncertainties in scaling factors for ab initio vibrational frequencies. *J. Phys. Chem. A* **109,** 8430–8437 (2005).
51. Meneghetti, M. & Pecile, C. Charge-transfer organic crystals: Molecular vibrations and spectroscopic effects of electron-molecular vibration coupling of the strong electron acceptor $TCNQF_4$. *J. Chem. Phys.* **84,** 4149–4162 (1986).

Acknowledgements

We thank the Royal Society for the Wolfson Lab Refurbishment Grant and the Deutsche Forschungsgemeinschaft (DFG) for support through the SPP1355. The work in Paderborn was supported by the DFG within the GRK1464. We appreciate the technical support from W.A. Lambson and H. Bone.

Author contributions

D.D.N., E.v.H. and E.D.C. designed the research. D.D.N. and R.J. fabricated the thin films and performed the infrared spectroscopy experiments. D.D.N. analysed the data and compared with the DFT calculations performed by C.F. and S.S. S.A., I.D. and U.S synthesized the polymers and performed photoelectron spectroscopy. D.D.N. and E.D.C. wrote the paper with all the authors contributing in the discussion and preparation.

Additional information

Supplementary Information accompanies this paper at http://www.nature.com/naturecommunications

Competing financial interests: The authors declare no competing financial interests.

Reprints and permission information is available online at http://npg.nature.com/reprintsandpermissions/

How to cite this article: Di Nuzzo, D. *et al.* How intermolecular geometrical disorder affects the molecular doping of donor–acceptor copolymers. *Nat. Commun.* 6:6460 doi: 10.1038/ncomms7460 (2015).

Supplementary Figures

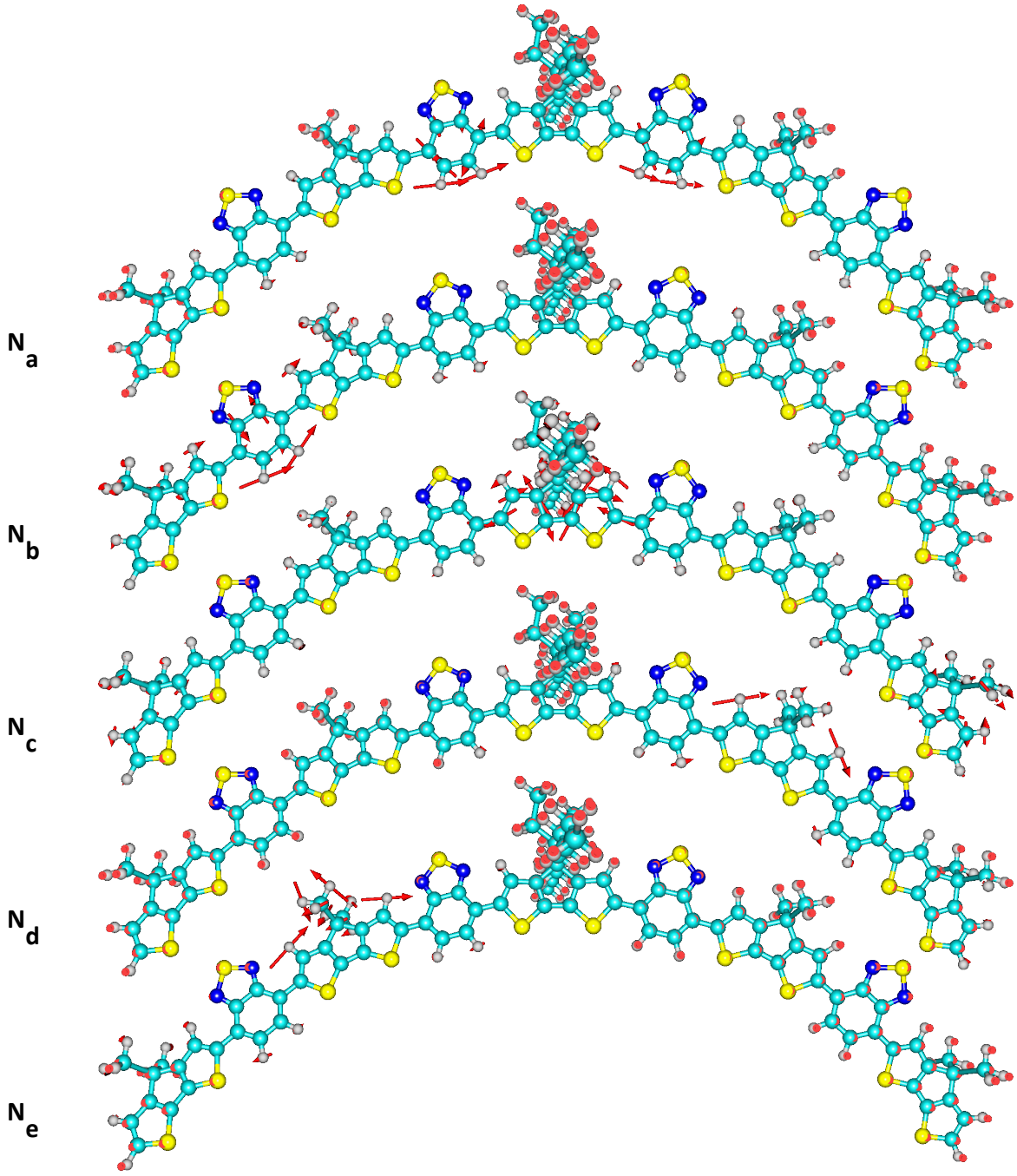

Supplementary Figure 1. Vibrational modes of PCPDT-BT "Neutral" corresponding to frequencies at 1567.6 cm^{-1} (mode labelled N_a), 1477.6 cm^{-1} (N_b), 1395.1 cm^{-1} (N_c), 1252.1 cm^{-1} (N_d), 1169.8 cm^{-1} (N_e). See Figure S5(b) for the corresponding spectrum.

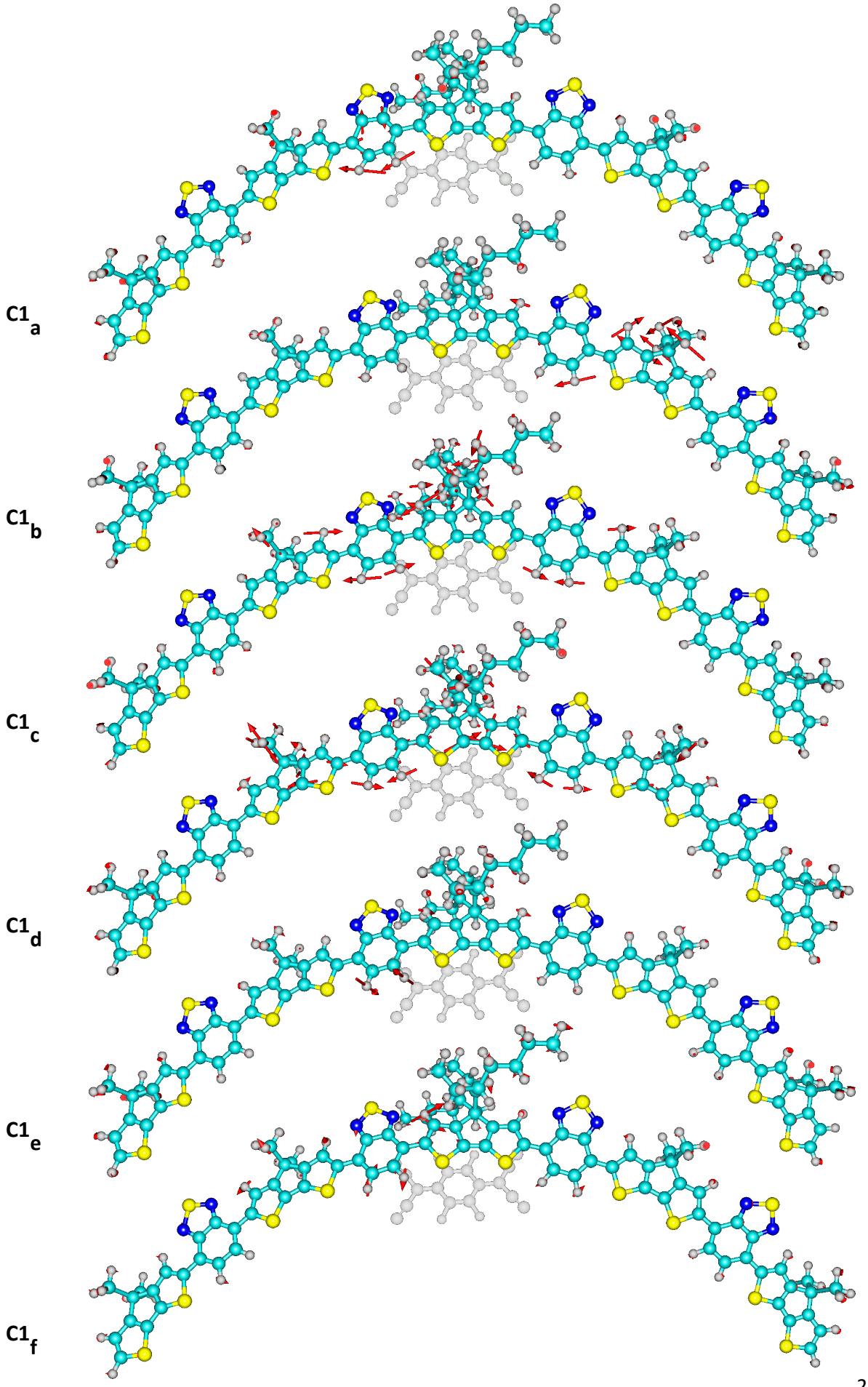
C1a
C1b
C1c
C1d
C1e
C1f

Supplementary Figure 2. Vibrational modes of PCPDT-BT:F4-TCNQ in "Complex-1" conformation, corresponding to frequencies at 1476.5 cm^{-1} (mode labelled $C1_a$), 1388.8 cm^{-1} ($C1_b$), 1194.2 cm^{-1} ($C1_c$), 1033.1 cm^{-1} ($C1_d$), 979.6 cm^{-1} ($C1_e$), 941.8 cm^{-1} ($C1_f$). The F4-TCNQ molecule is coloured in grey and lies behind the polymer. See Figure S6(b) for the corresponding spectrum. $C1_d$ is the mode displayed in Figure 4c of the manuscript.

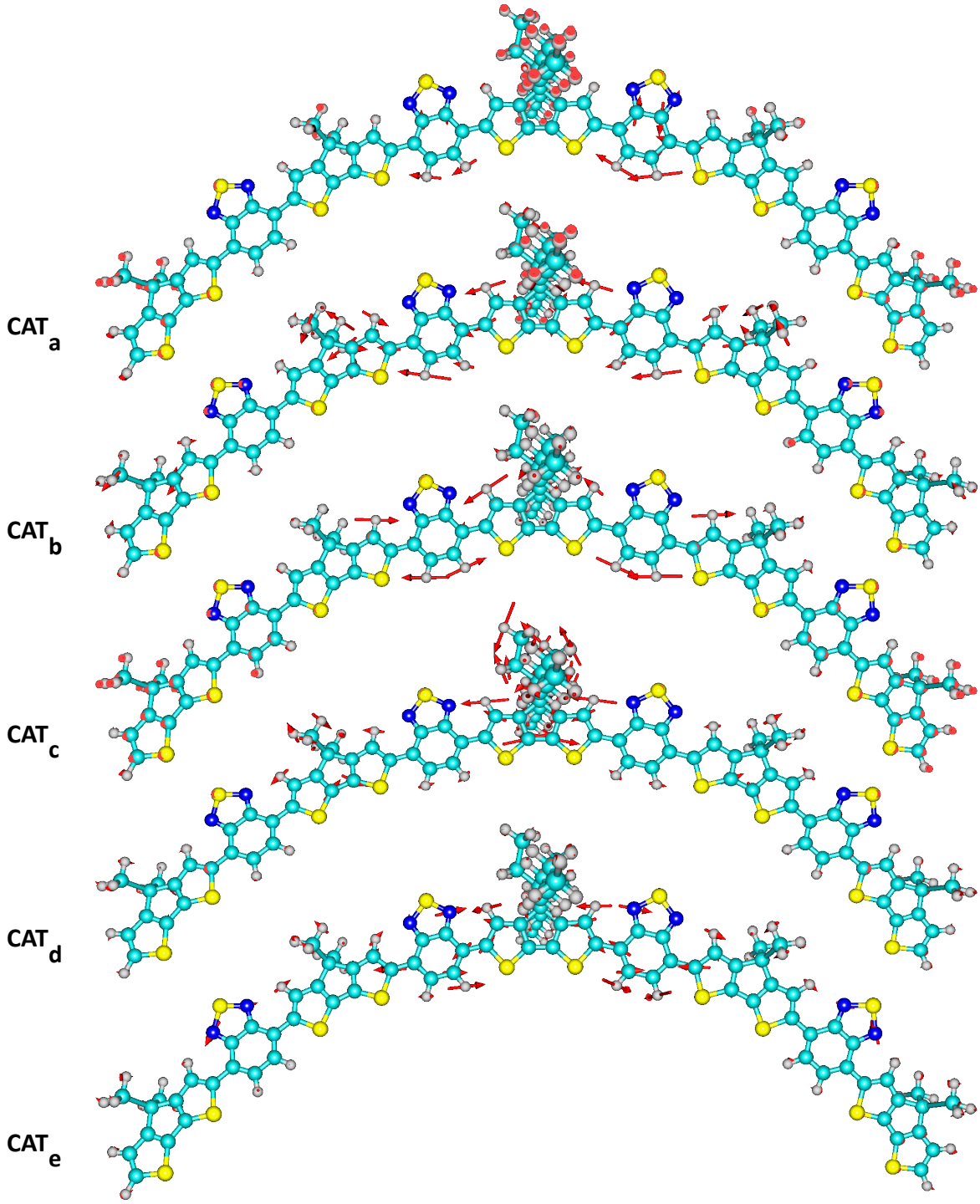

Supplementary Figure 3. Vibrational modes of PCPDT-BT^{+} "Cation", corresponding to frequencies at 1475.4 cm^{-1} (mode labelled CAT$_a$), 1391.9 cm^{-1} (CAT$_b$), 1187.8 cm^{-1} (CAT$_c$), 1005.7 cm^{-1} (CAT$_d$), 880.3 cm^{-1} (CAT$_e$).

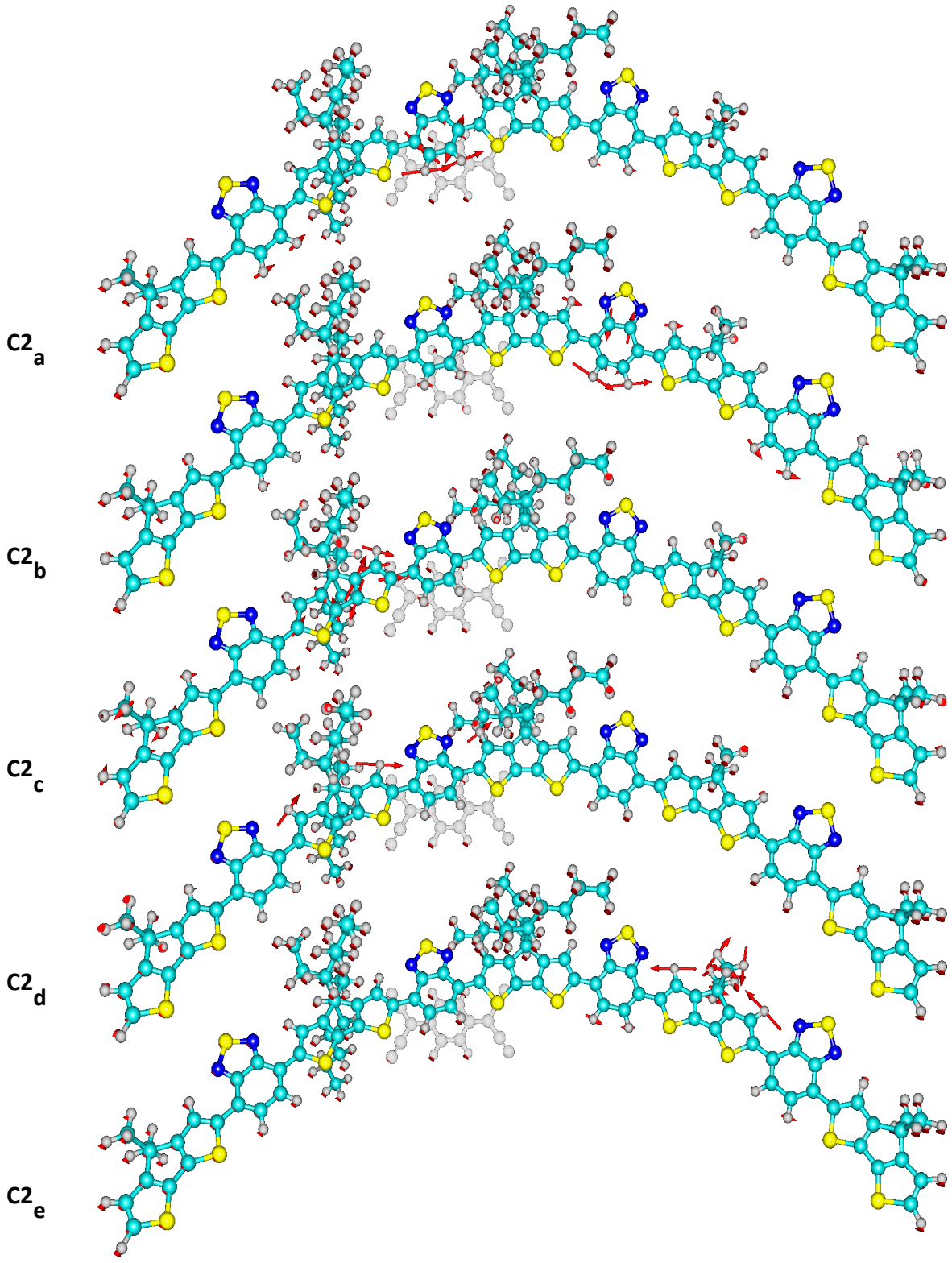

Supplementary Figure 4. Vibrational modes of PCPDT-BT:F4-TCNQ in "Complex-2" conformation, corresponding to frequencies at 1567.9 cm^{-1} (mode labelled $C2_a$), 1478.1 cm^{-1} ($C2_b$), 1393.3 cm^{-1} ($C2_c$), 1232.8 cm^{-1} ($C2_d$), 1169.4 cm^{-1} ($C2_e$). The F4-TCNQ molecule is coloured in grey and lies behind the polymer.

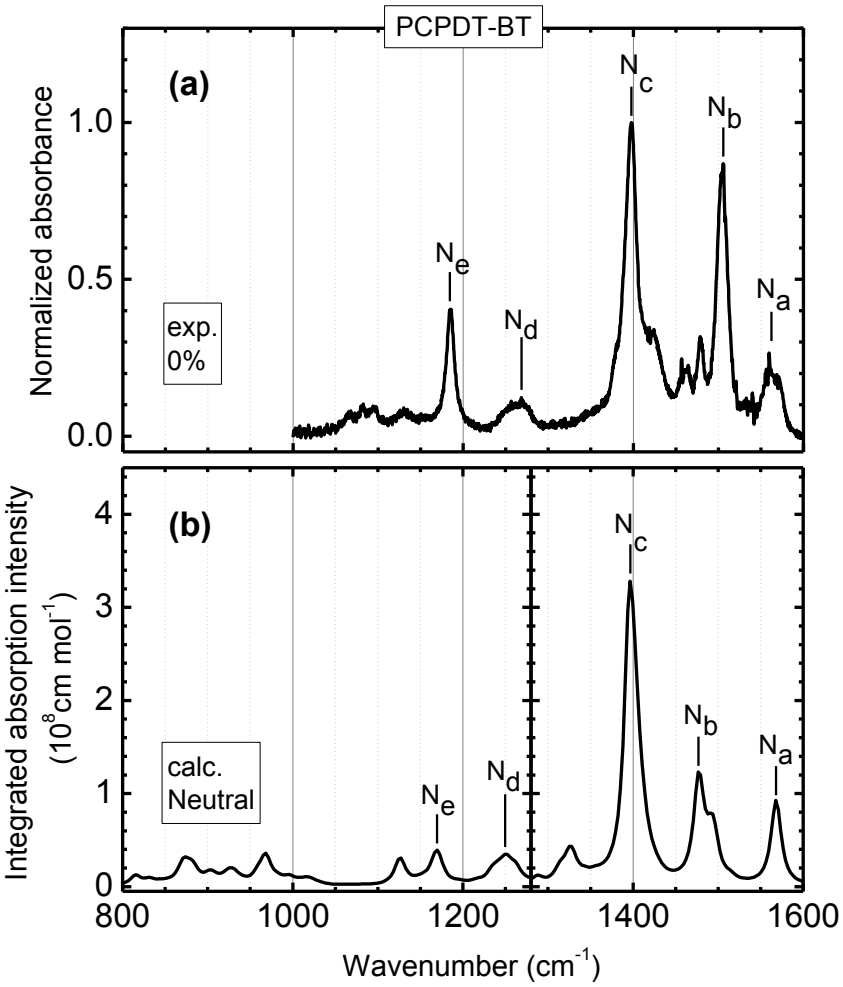

Supplementary Figure 5. **a**, Normalized FTIR absorption spectrum of a pristine PCPDT-BT film, as shown in Figure 2a of the manuscript. Some of the experimental bands are assigned to calculated vibrational transitions by comparing with the calculated spectrum of PCPDT-BT in "Neutral" conformation, displayed in panel **b** (as in in Figure 3a of the manuscript). The labels used for the assignment correspond to the frequencies of the modes visualized in Figure S1.

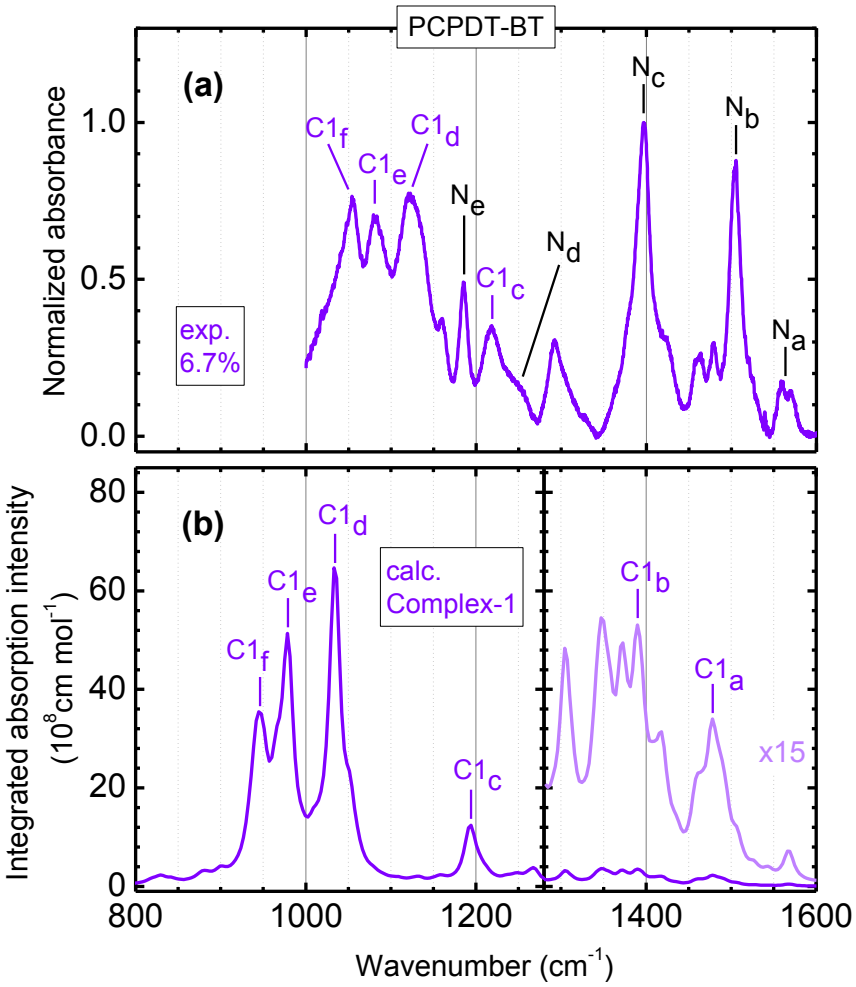

Supplementary Figure 6. a, Normalized FTIR absorption spectrum of a PCPDT-BT film doped with F4-TCNQ in 6.7% molar ratio, as shown in Figure 2a of the manuscript, with no vertical scale offset. Some of the experimental bands are assigned to calculated vibrational transitions by comparing with the calculated spectrum of PCPDT-BT in "Complex-1" conformation, displayed in panel **b** (as in in Figure 3a of the manuscript, including the 15-fold magnification of the 1280-1600 cm^{-1} part of the spectrum). The bands assigned to neutral polymer chains are also indicated, labelled as in Figure S1. The labels used for the assignment correspond to the frequencies of the modes visualized in Figures S1-S2. Due to dominant contribution of neutral chains to absorption in the 1350-1600 cm^{-1} region of the experimental spectrum, we did not attempt to assign the $C1_a$ and $C1_b$ calculated modes.

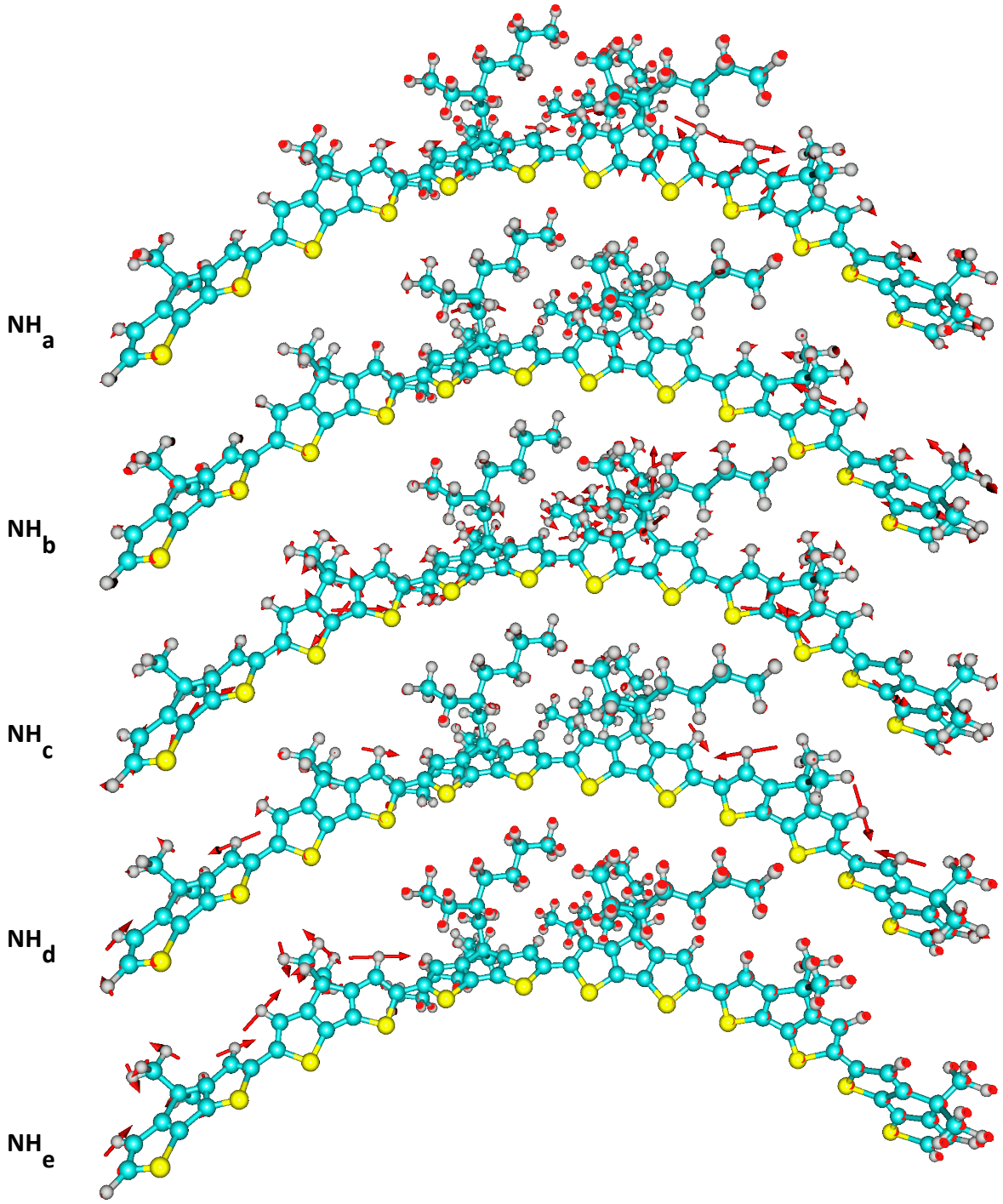

Supplementary Figure 7. Vibrational modes of PCPDT "Neutral", corresponding to frequencies at 1484.7 cm^{-1} (mode labelled NH_a), 1394.7 cm^{-1} (NH_b), 1320.6 cm^{-1} (NH_c), 1206.6 cm^{-1} (NH_d), 1158.7 cm^{-1} (NH_e). See Figure S10(b) for the corresponding spectrum.

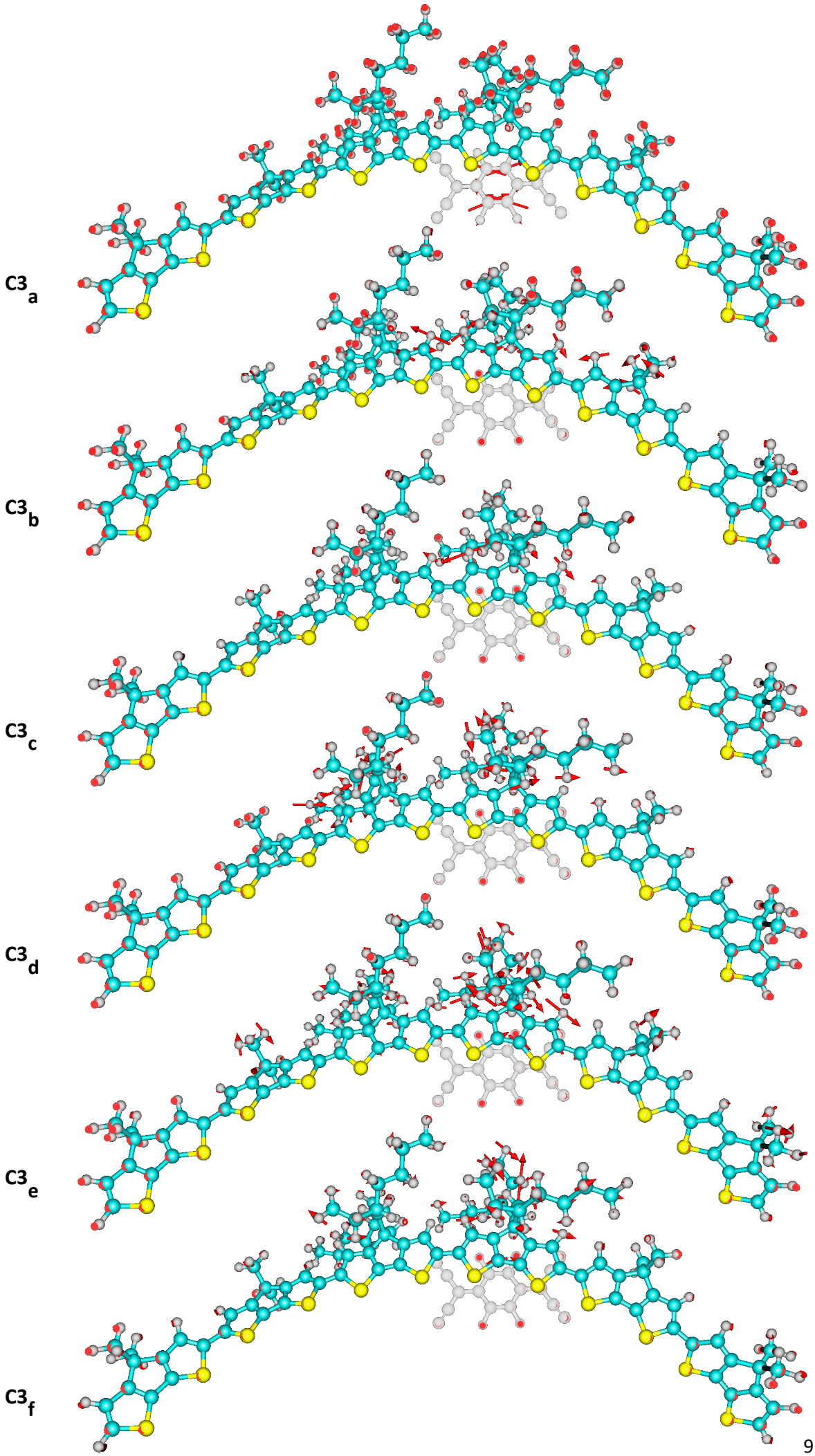
C3a
C3b
C3c
C3d
C3e
C3f

Supplementary Figure 8. Vibrational modes of PCPDT:F4-TCNQ in conformation "Complex-3", corresponding to frequencies at 1507.7cm^{-1} (mode labelled C3$_a$), 1439.2 cm^{-1} (C3$_b$), 1234.2 cm^{-1} (C3$_c$), 1068.4 cm^{-1} (C3$_d$), 1044.8 cm^{-1} (C3$_e$), 990.8 cm^{-1} (C3$_f$). The F4-TCNQ molecule is coloured in grey and lies behind the polymer. See Figure S11(b) for the corresponding spectrum.

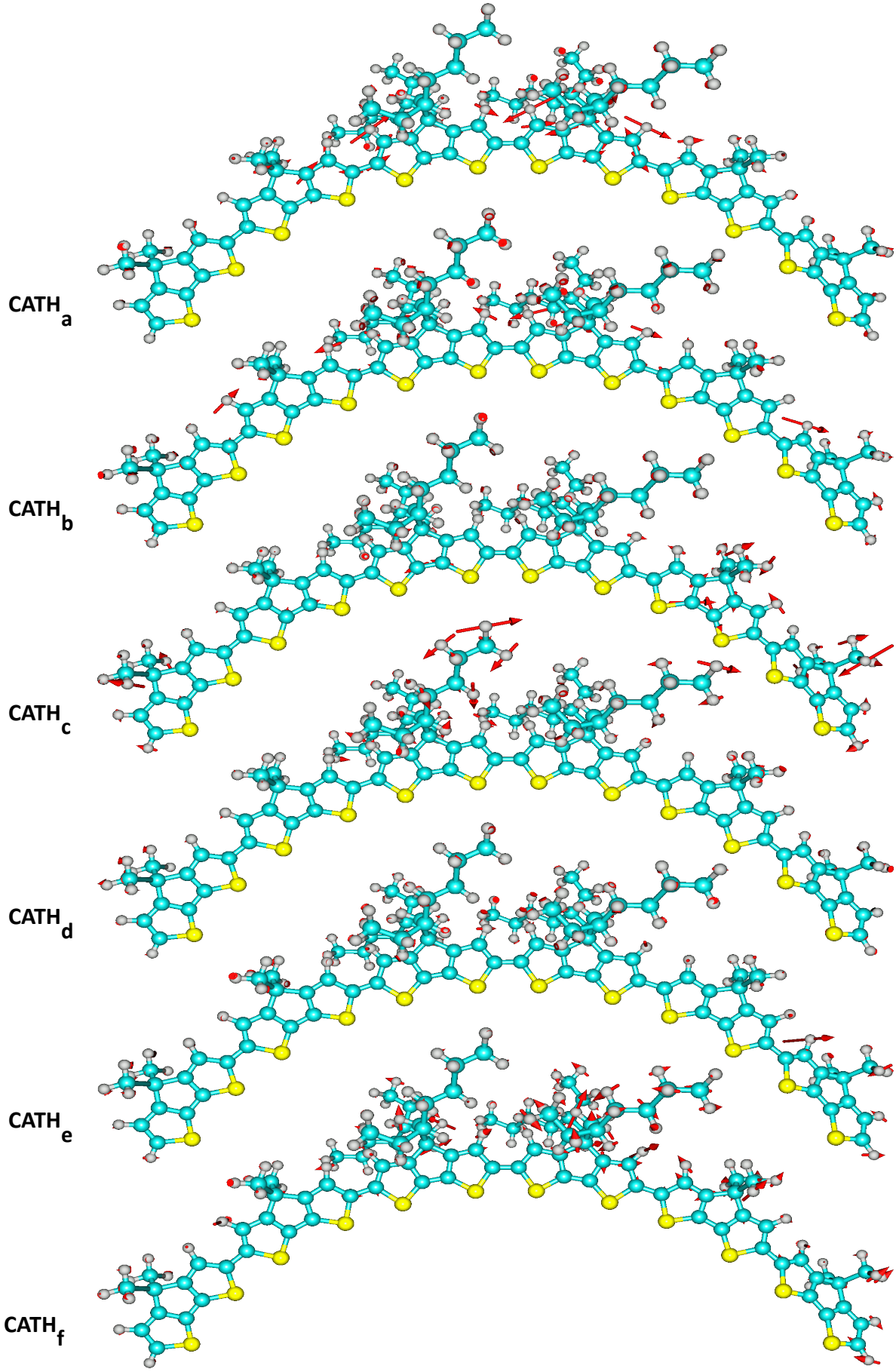
CATH a
CATH b
CATH c
CATH d
CATH e
CATH f

Supplementary Figure 9. Vibrational modes of $PCPDT^{+}$ "Cation", corresponding to frequencies at 1444.1 cm^{-1} (mode labelled $CATH_a$), 1216.0 cm^{-1} ($CATH_b$), 1011.0 cm^{-1} ($CATH_c$), 920.9 cm^{-1} ($CATH_d$), 892.1 cm^{-1} ($CATH_e$), 870.2 cm^{-1} ($CATH_f$).

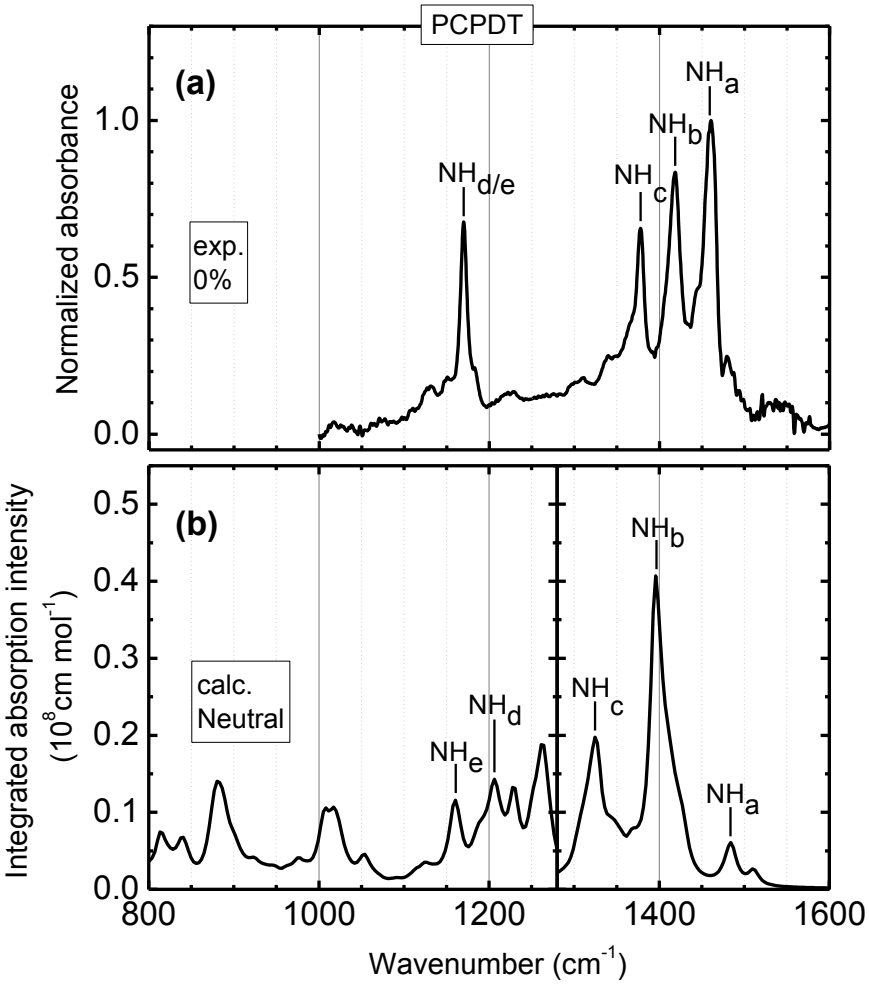

Supplementary Figure 10. a, Normalized FTIR absorption spectrum of a pristine PCPDT film, as shown in Figure 2c of the manuscript. Some of the experimental bands are assigned to calculated vibrational transitions by comparing with the calculated spectrum of PCPDT in "Neutral" conformation, displayed in panel **b** (as in in Figure 3d of the manuscript). The labels used for the assignment correspond to the frequencies of the modes visualized in Figure S7. For the band peaked at 1170 cm^{-1} in the experimental spectrum we indicate two possible assignments, to the calculated modes NH_d and NH_e.

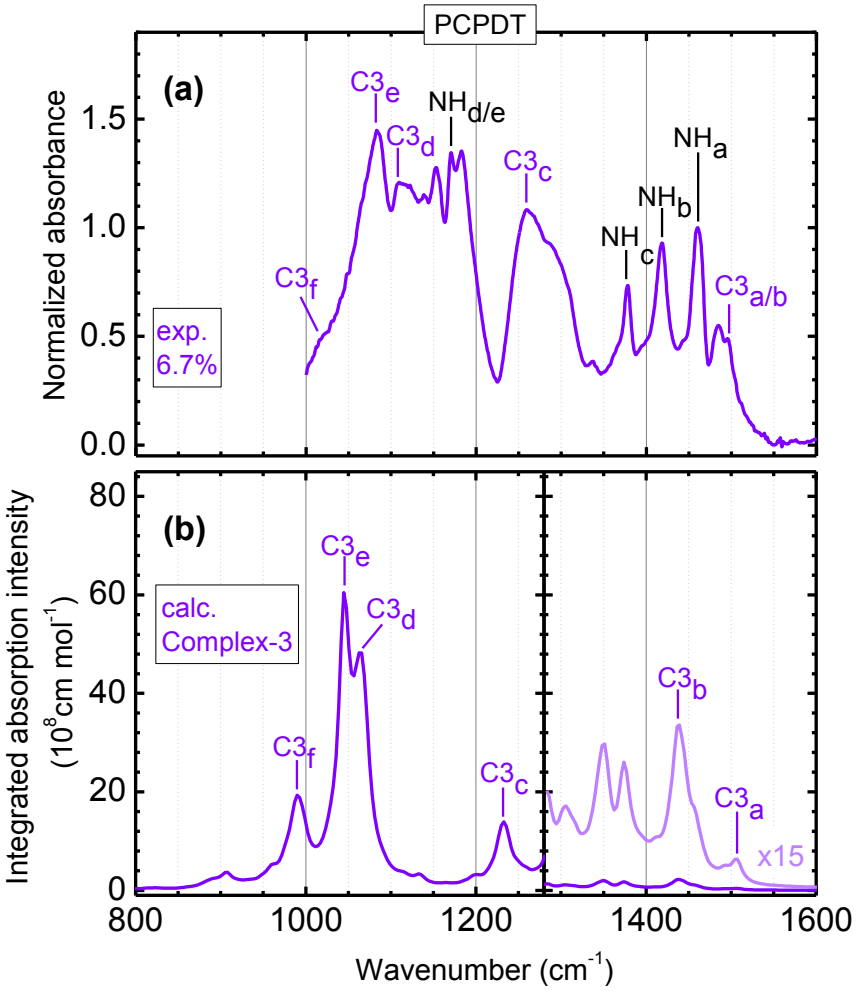

Supplementary Figure 11. a, Normalized FTIR absorption spectrum of a PCPDT film doped with F4-TCNQ in 6.7% molar ratio, as shown in Figure 2c of the manuscript, with no vertical scale offset. Some of the experimental bands are assigned to calculated vibrational transitions by comparing with the calculated spectrum of PCPDT in "Complex-3" conformation, displayed in panel **b** (as in in Figure 3d of the manuscript, including the 15-fold magnification of the 1280-1600 cm^{-1} part of the spectrum). The bands assigned to neutral polymer chains are also indicated, labelled as in Figure S7. The labels used for the assignment correspond to the frequencies of the modes visualized in Figures S7-S8. For the band peaked at 1496 cm^{-1} in the experimental spectrum we indicate two possible assignments, to the calculated modes $C3_a$ and $C3_b$.

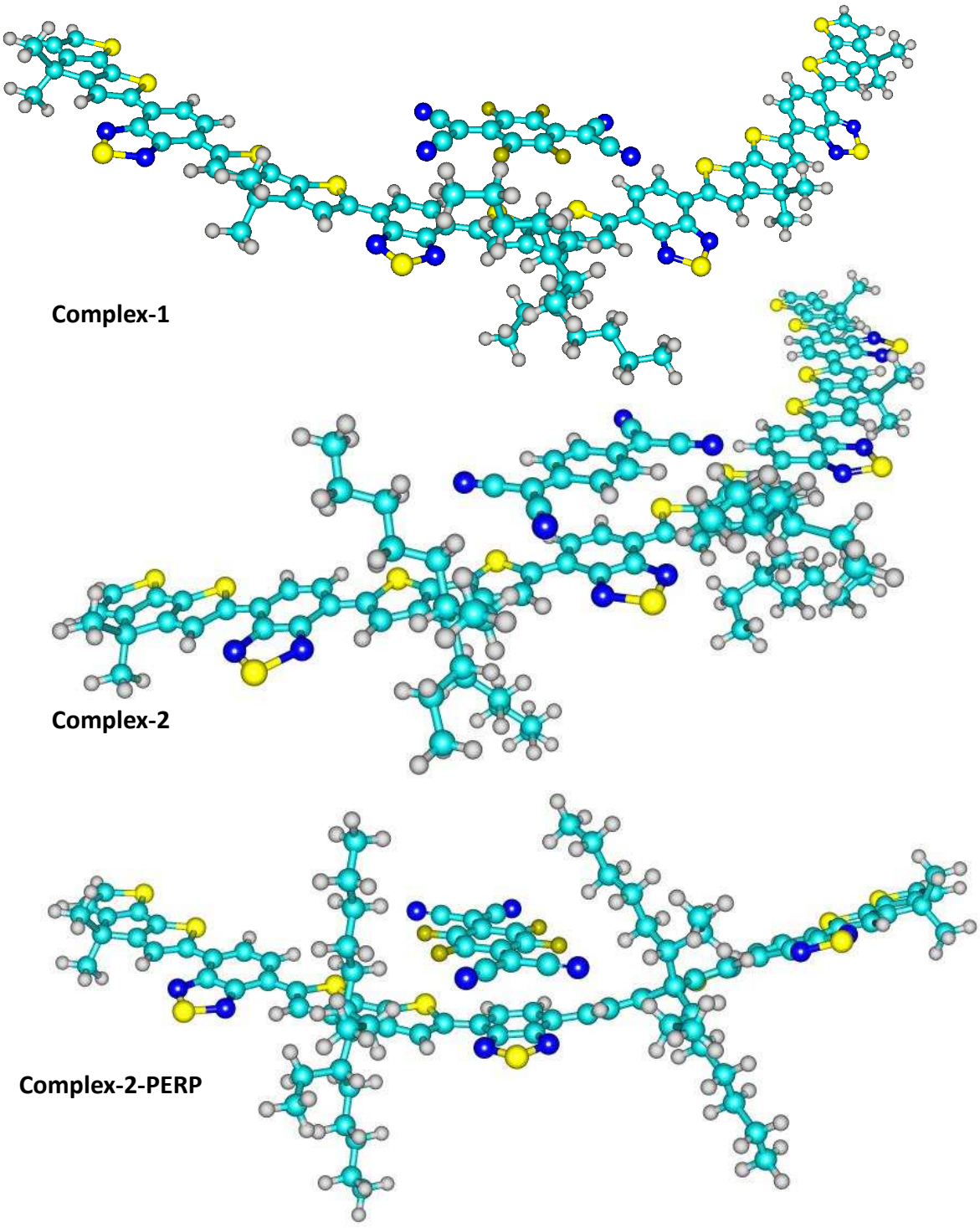

Supplementary Figure 12. Optimized molecular geometries corresponding to PCPDT-BT:F4-TCNQ in the conformations Complex-1, Complex-2 and Complex-2-PERP.

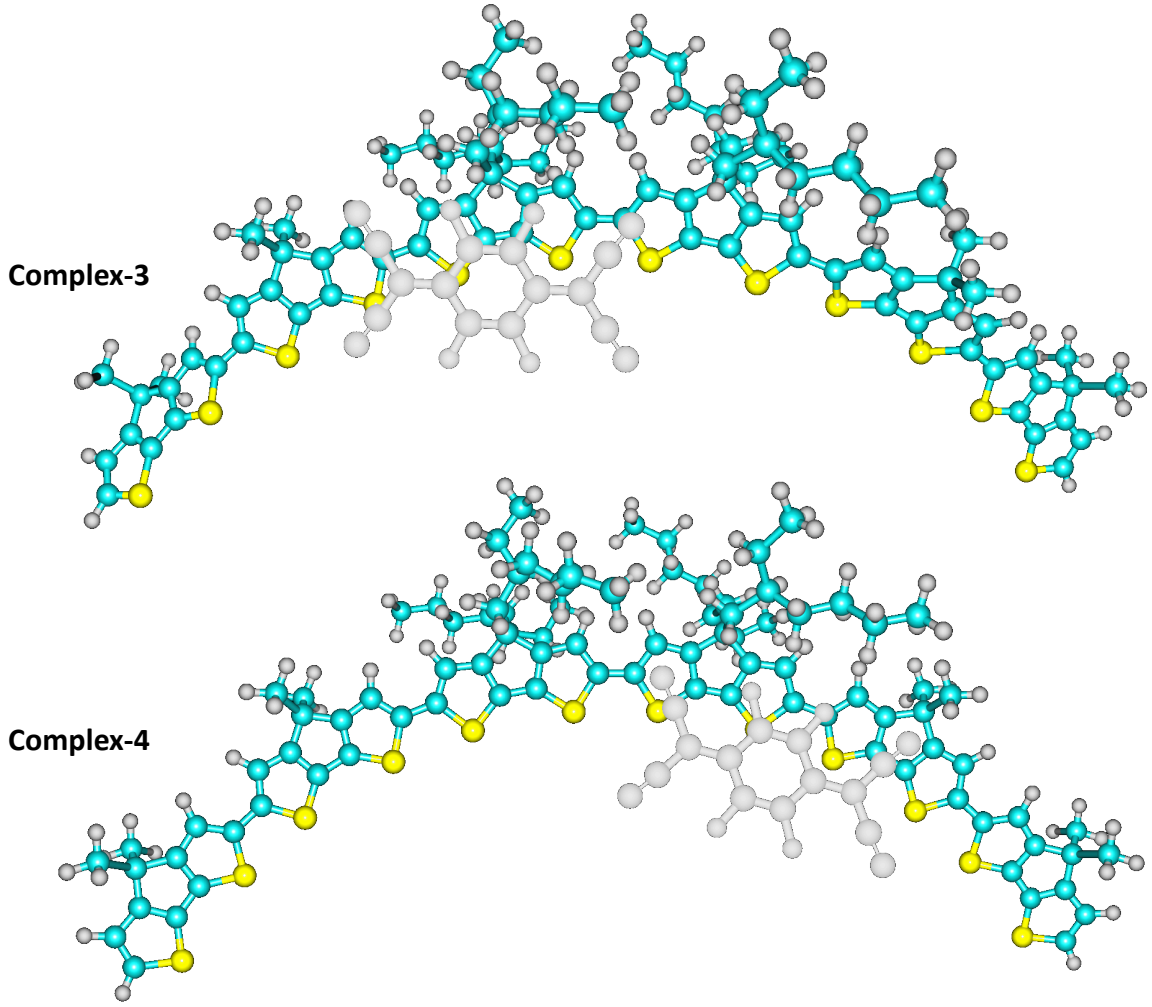

Supplementary Figure 13. Optimized molecular geometries corresponding to PCPDT:F4-TCNQ in the conformations Complex-3 and Complex-4. The F4-TCNQ molecule lies in front of the polymer and is coloured in grey for better visualization.

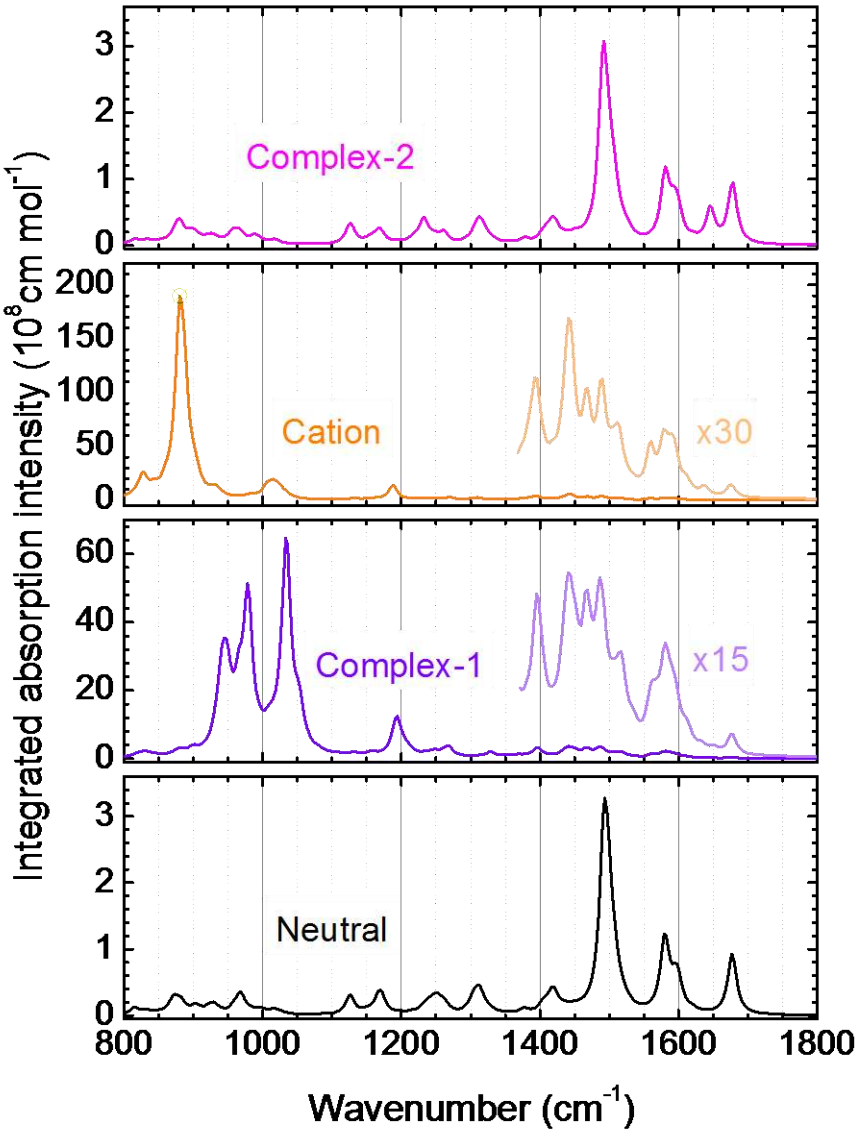

Supplementary Figure 14. Calculated vibrational absorption spectra of PCPDT-BT in different conformations, without frequency scaling: single polymer strand without F4-TCNQ (Neutral), with an F4-TCNQ molecule localized close to the CPDT moiety (Complex-1), without F4-TCNQ molecule and one electron less on the HOMO (Cation), and with an F4-TCNQ molecule localized close to the BT moiety (Complex-2). For Complex-1 and Cation, a magnified part of the spectrum is also shown, with intensity multiplied 15 and 30 times respectively.

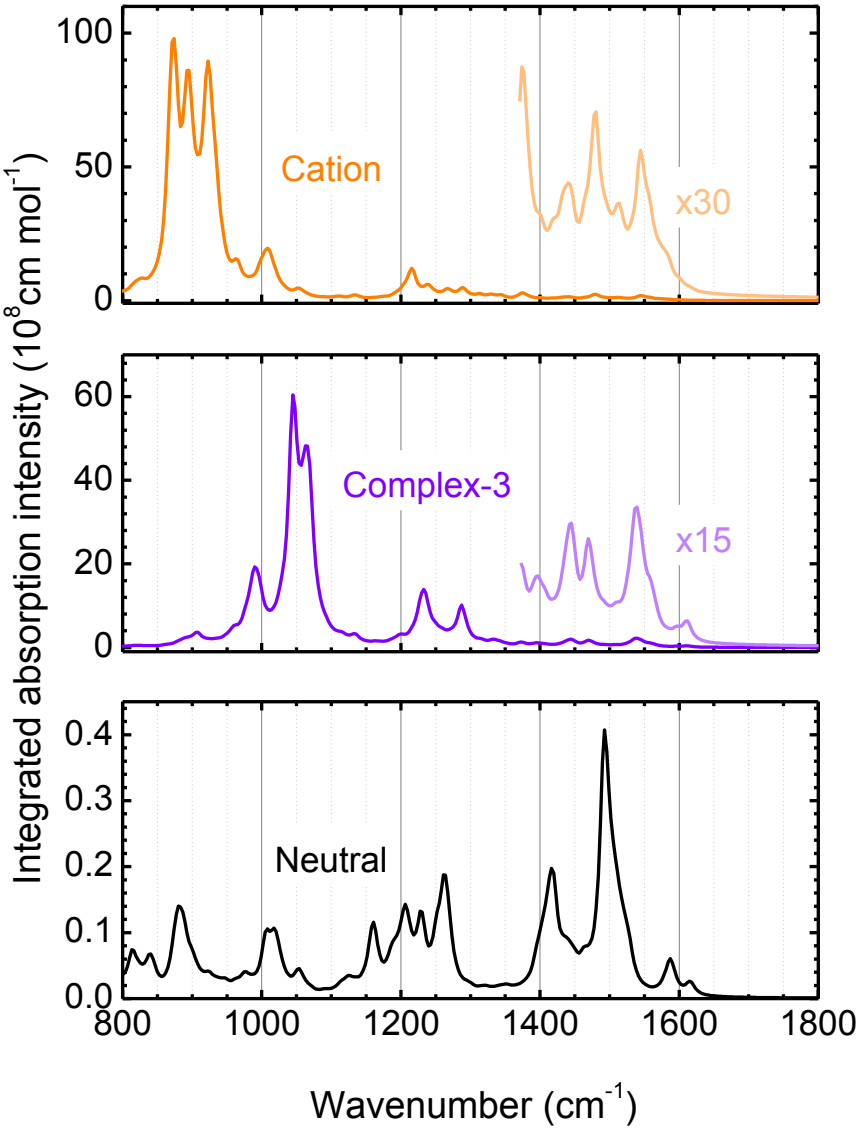

Supplementary Figure 15. Calculated vibrational absorption spectra of PCPDT in different conformations, without frequency scaling: single polymer strand without F4-TCNQ (Neutral), with F4-TCNQ (Complex-3), without F4-TCNQ molecule and one electron less on the HOMO (Cation). For Complex-3 and Cation, a magnified part of the spectrum is also shown, with intensity multiplied 15 and 30 times respectively.

Supplementary Tables

Supplementary Table 1. Summary of stabilization energies ΔG and amount of charge present on the polymer in different conformations of the complex PCPDT-BT:F4-TCNQ.

Conformation	**ΔG (eV)** [*]	**Charge on polymer (*e*) ****
Complex-1	-0.46	0.93
Complex-2	-0.22	-0.02
Complex-2-PERP	-0.43	-0.06

[*] The stabilization energy ΔG is calculated as: $\Delta G = G_{complex} - (G_{polymer} + G_{F4\text{-}TCNQ})$, where G_x are the Gibbs energies of the complex, the polymer strand and the F4-TCNQ molecule.
[**] According to Mulliken analysis.

Supplementary Table 2. Summary of stabilization energies ΔG and amount of charge present on the polymer in different conformations of the complex PCPDT:F4-TCNQ.

Conformation	**ΔG (eV)** [*]	**Charge on polymer (*e*)** [**]
Complex-3	-0.60	0.92
Complex-4	-0.58	0.93

[*] The stabilization energy ΔG is calculated as: $\Delta G = G_{complex} - (G_{polymer} + G_{F4\text{-}TCNQ})$, where G_x are the Gibbs energies of the complex, the polymer strand and the F4-TCNQ molecule.
[**] According to Mulliken analysis.

Supplementary Discussion

1. Visualization of vibrational modes and assignment to the experimental IR bands

For each of the different conformations considered in the calculations presented in Figure 3 of the manuscript, we display a selection of the computed vibrational normal modes (Supplementary Figures 1-4 for PCPDT-BT and 7-9 for PCPDT). For each mode the displacement vectors have been normalized in length, to visualize which parts of the molecule move the most. We indicate the frequency of each selected mode after the application of the same scaling factors used in Figure 3 of the manuscript. Note that we were forced to apply a selection, due to the great amount (>100) of calculated modes having a non-negligible IR absorption intensity in the spectral region of interest. In particular, in some cases more than one mode is present under the same broadened peak: in these cases we have selected for display the most intense one. We label each of the selected modes and we use the same labels in Supplementary Figures 5 and 6, where we make a tentative assignment of the vibrational bands observed in the experiments on pristine and 6.7% doped films of PCPDT-BT (Figure 2 of the manuscript) by comparing with the calculated spectra ("Neutral" and "Complex-1" respectively). The same is done in Supplementary Figures 10 and 11 for the homo-polymer PCPDT, using the calculations on conformations "Neutral" and "Complex-3" respectively.

2. Conformational analysis of the complexes

In addition to Complex-1, -2, -3 discussed in the manuscript, we investigated a number of other energetically stable conformations in which the polymer:F4-TCNQ complexes can arrange. To be as close as possible to the real system, we focused on conformations where the F4-TCNQ molecule is in front of repeat units which are attached to alkyl side-chains. For PCPDT-BT:F4-TCNQ we show here one optimized conformation, which we call Complex-2-

PERP, and compare it to Complex-1 and Complex-2 (Supplementary Figure 12). The only conformation resulting in efficient transfer of charge is Complex-1. For PCPDT:F4-TCNQ we show one additional optimized structure, called Complex-4, and compare it to Complex-3 (Supplementary Figure 13). In Complex-4 the F4-TCNQ molecule is in front of a different repeat unit than in Complex-3. Furthermore, its position with respect to the repeat unit itself is different than in Complex-3. Both conformations give efficient charge transfer. The stabilization energies and the amount of charge transferred (from Mulliken analysis) in the different conformations involving PCPDT-BT:F4-TCNQ and PCPDT:F4-TCNQ are summarized in Supplementary Tables 1 and 2, respectively.

As for Complex-1, -2, -3, all the additional conformations were calculated using CAM-B3LYP/6-31G** density functional theory, with spin-unrestricted wave functions and including a polarizable continuum medium (ε_r = 3) which exploits SMD ("Solvation Model based on Density", see Methods section of the manuscript). Cartesian coordinates of the presented complexes are available upon request to the authors.

"Giant IR signature" in doped polythiophenes: electronic/structural effects

In this section, it is assessed, in a detailed study, the influence of both structural (i.e. size and conformation) and "level of the theory" factors on IR calculated spectra of the PCPDT-BT cation species (it is also both hoped and thought that these results could be extended to the interpretation of experimental data concerning the broader class of conducting organic polymers [85,86]). The aim is to infer the physical properties underlying the experimental observation of the "Giant IR polaron signature". In the following the theoretical results are obtained by using ab-initio molecular orbital calculations: using the Gaussian [87], GAMESS [88] and Firefly [89] suite of programs. To reduce the computational cost, alkyl side chains, which are likely to be uninvolved in determining electronic structure of frontier orbitals, have been replaced by methyl groups[1], this is a widely followed strategy compare for instance Da Como [22], Bredas [35] and Miller [48]. Thus, the dependence of the vibrational spectra has been systematically studied as a function of the length of the oligomers (that is, as a function of the number of the polymer repeating units): elementary polymer units here considered are the BT (benzothiazole) and T2 (bithiophene) moieties. The level of the theory was checked too considering different theoretical paradigms: HF[2] and DFT[3], hybrid B3LYP and CAMB3LYP hybrid functional have been used too.

Vibrational IR spectra have been calculated for different oligomers as a function of the number of repeating units, as well as for different levels of the theory. Only the results concerning the PCPDT-BT monomer, T2-BT, and trimer, BT-$(T2\text{-}BT)_3$, elementary units sequence) are shown in the following. In each graph the relevant "ball and stick" model is displayed as an inset.

Figure 7 shows the IR calculated spectra, HF and UHF (radical cation) 6-31G(d,p) basis set, of the monomer and trimer, neutral and cation oxidation states. The spectrum of the cation features a low-

[1] Anyhow, the impact of this quite rude approximation was cross-checked by performing the calculation of the IR spectrum for the "true" trimer oligomer featuring all of the lateral side chains. *Vide infra* Figure 11.
[2] Restricted RHF, restricted open-shell ROHF methods have the same spatial part for the α and β electrons molecular orbital; unrestricted UHF method allows for a different spatial part (and energies) for the α and β electrons molecular orbital.
[3] LDA (Localized Density Approximation) pure VWN (Vosko-Wilk-Nusair).

er number of prominent peaks, the maximum intensity is eight times larger for the monomer cation with respect to the neutral, whilst for the trimer the maximum intensity remains roughly the same when comparing the neutral and cation oxidized states. Indeed, in the case of the cation, the $<S^2>$ (indicated as <S**2> in the graphs) eigenvalue is significantly different from 0.75 which is the expected value for a doublet state. Such a large difference is in general a symptom of large spin contamination (i.e., the presence of a manifold of electronic excited states of low and comparable energy, a limitation due to the mono-determinantal approach [90,68,91]).

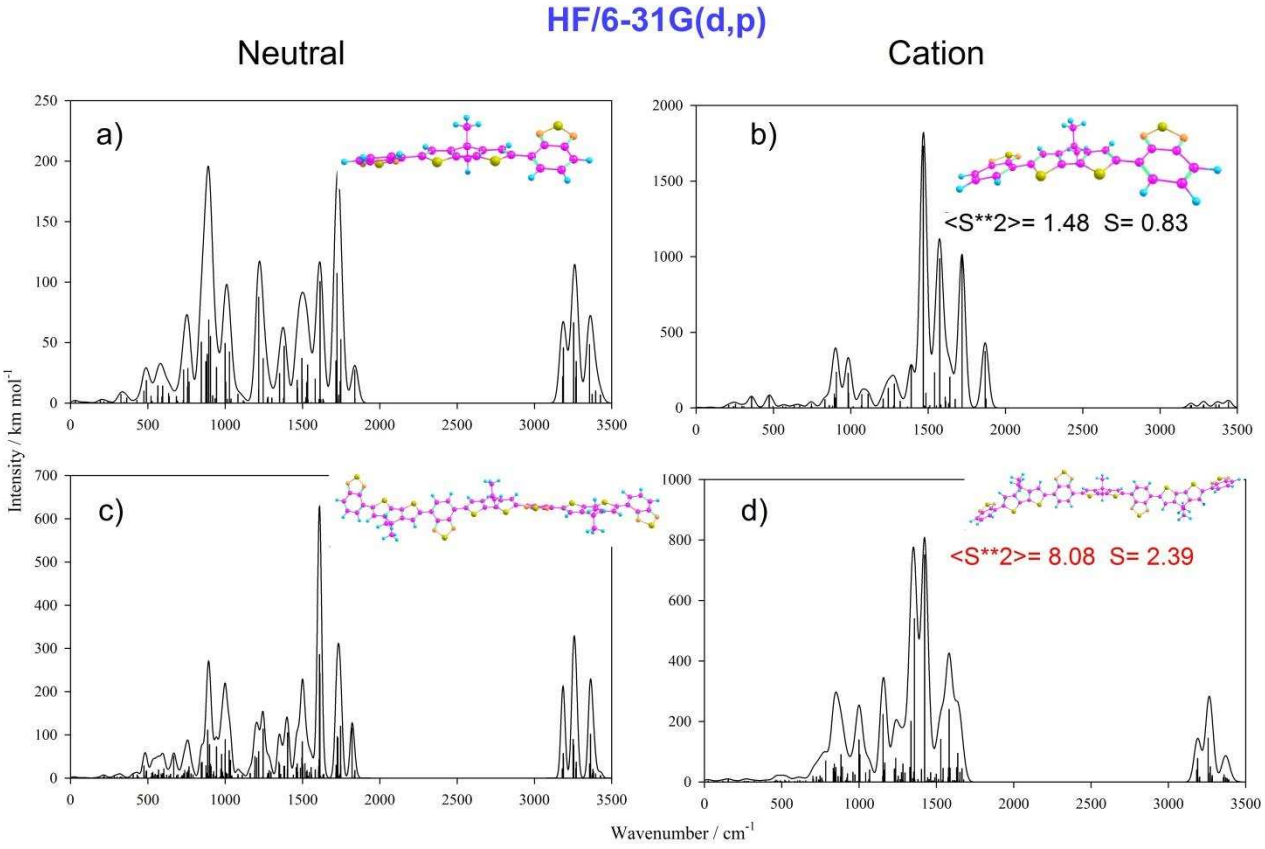

Figure 7. Calculated IR spectra, "pure" Hartree-Fock, 6-31G(d,p) basis set. Monomer species: a) neutral b) cation. Trimer species: c) neutral d) cation.

Figure 8 shows the same type of results as just above discussed, but the calculations are carried out by using the DFT Slater exchange VWN [92], correlation functional (SVWN). The overall picture is just a little worse than the HF one, the difference between neutral and cation species is not so evident, both peaks intensity and frequency range remain almost the same, not any hint of any "Giant

polaron signature". The unique reasonable result is the $<S^2>$ value, coincident with that of a pure doublet state.

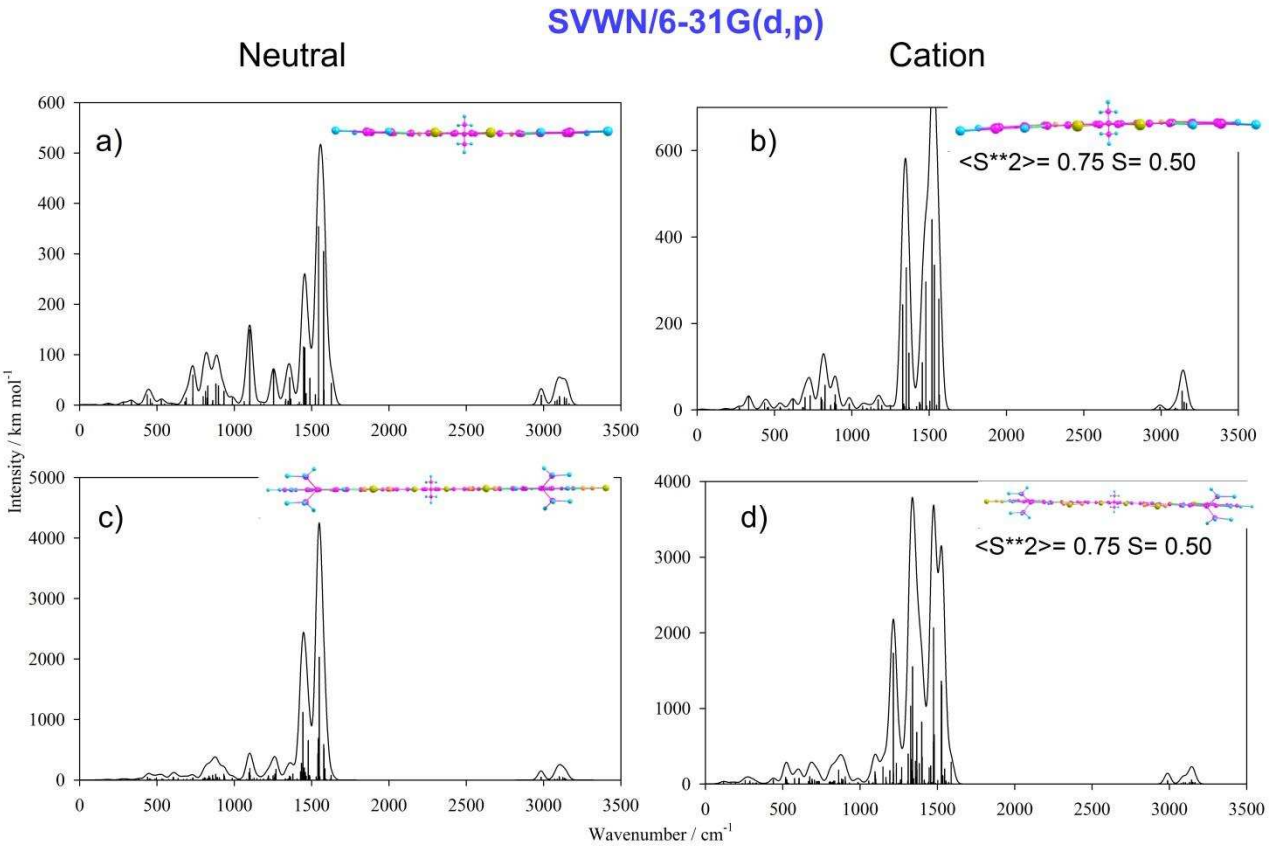

Figure 8. Calculated IR spectra, "pure" DFT Local Spin Density Approximation (LSDA), which is implemented in Gaussian as: Slater exchange VWN correlation functional (SVWN). 6-31G(d,p) basis set. Monomer species: a) neutral b) cation. Trimer species: c) neutral d) cation.

Figure 9, again, shows the results obtained pursuing the same type of analysis. The comparison between the IR spectra of the neutral and charged species shows a marked tendency for the most prominent peak to shift to a lower wavenumber: 1500 cm^{-1} for both the monomer and trimer neutral species (Figure 9a,c), about 1360 cm^{-1} for the monomer and 1220 cm^{-1} / 1310 cm^{-1} the two main peaks for the trimer. Notably, the trimer cation intensity is 10 times that one of the neutral species. While for the monomer, what is more, the intensity remains almost the same.

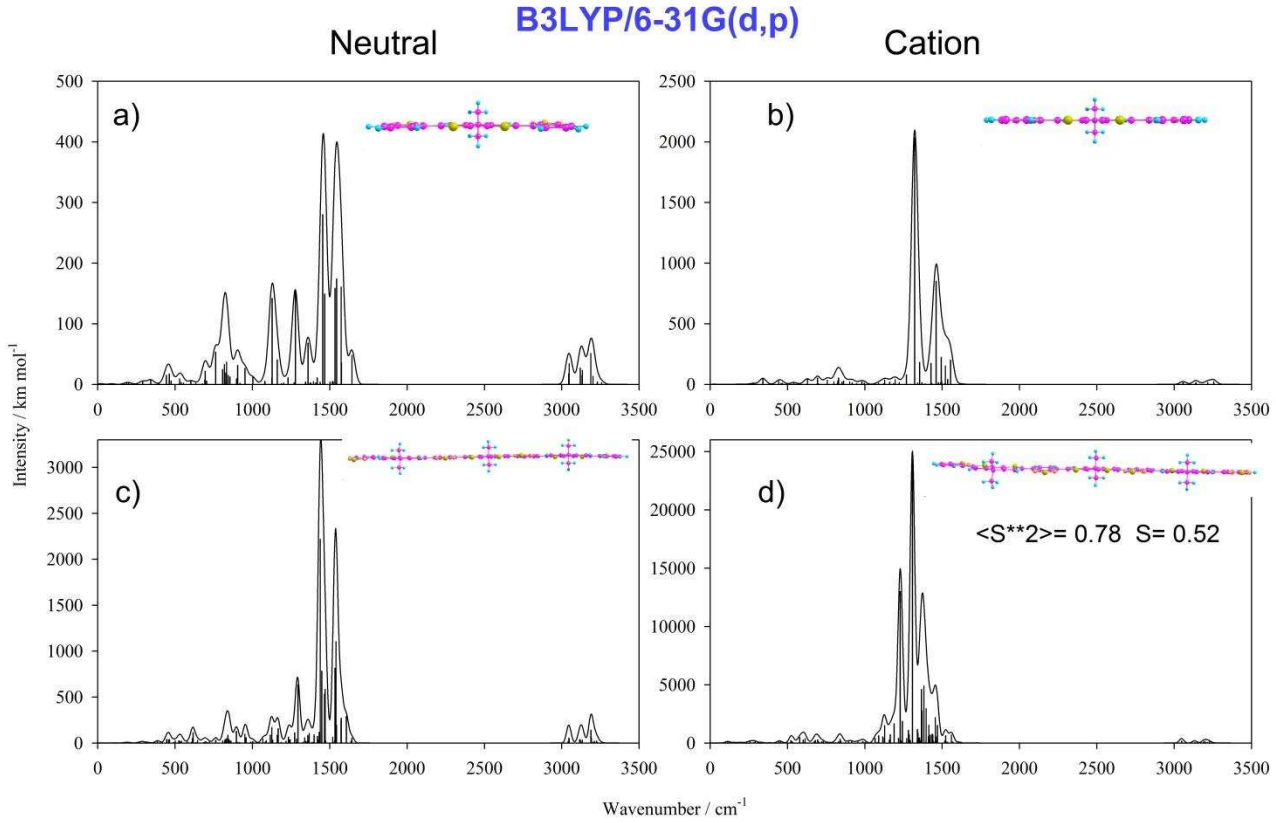

Figure 9. Calculated IR spectra, "hybrid" DFT/HF, B3LYP functional, 6-31G(d,p) basis set. Trimer species: a) neutral b) cation.

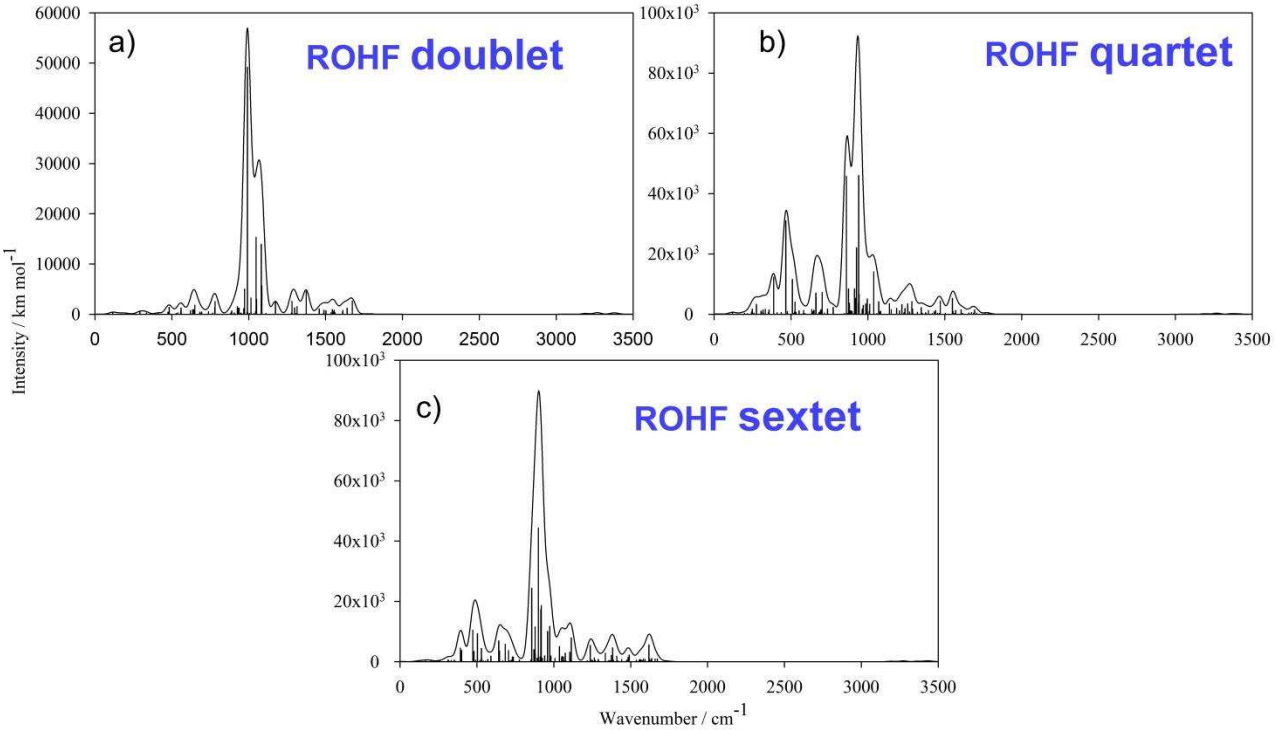

Figure 10. Calculated IR spectra, ROHF/6-31G(d,p) basis set. **Trimer cation** species only, different spin multiplicity, as reported: a) doublet, "spin multiplicity" = 2 b) quartet, "spin multiplicity" = 4 c) sextet, "spin multiplicity" = 6.

Figure 10 shows the IR spectra calculated using the Restricted Open-Shell HF method. Data calculated for the trimer species only. Here the intensity is much larger than the neutral one (600 km mol^{-1}, compare Figure 7c), ROHF doublet cation 60000 km mol^{-1} (compare Figure 10a); it means about 100 times larger. What is more, there is a substantial change in the spectrum appearance: the spectrum of the cation shows a well-defined single prominent peak centered around 1000 cm-1, which is the wavenumber range where the "Giant polaron signature" is found in IR spectra [31,42,43].

Figure 11 shows the IR calculated spectra (CAMB3LYP/6-31G(d,p)) for the trimer species only, but in this case all of the alkyl side chains are included in the calculation (which means much longer computation times, roughly speaking a factor of about 7). By and large the comparison between the neutral and cations species tightly resembles the results obtained neglecting the alkyl side chains. Thus giving due reason to the simplification adopted by using only methyl groups as "surrogate" of the complete unsaturated long chain, which in the very end scarcely affects the electronic properties probed by vibrational (as well as electronic) spectroscopy.

Figure 12 shows CAMB3LYP/6-31G(d,p) IR spectra calculated for the neutral and cation species, trimer only, but two vicinal ter–butyl (ter-butyl substituent is a bulky, and almost spherical, alkyl type moiety: $-C(CH_3)_3$) groups are bound to the bithiophene moieties, so to induce a large distortion, close to orthogonality, in the planarity of the conjugated thiophene backbone (in general π electrons conjugation efficiency decays rapidly with increasing the dihedral angle, from 0 to 90 degrees, between aromatic rings, save a few class of compounds [93]). Note that, the most prominent peak in the spectrum of the cation species is found at a larger wavenumber, about 1300 cm^{-1}, and with a lower intensity with respect to the results of the trimer featuring an almost planar thiophene backbone (Figure 11 and ref [31]).

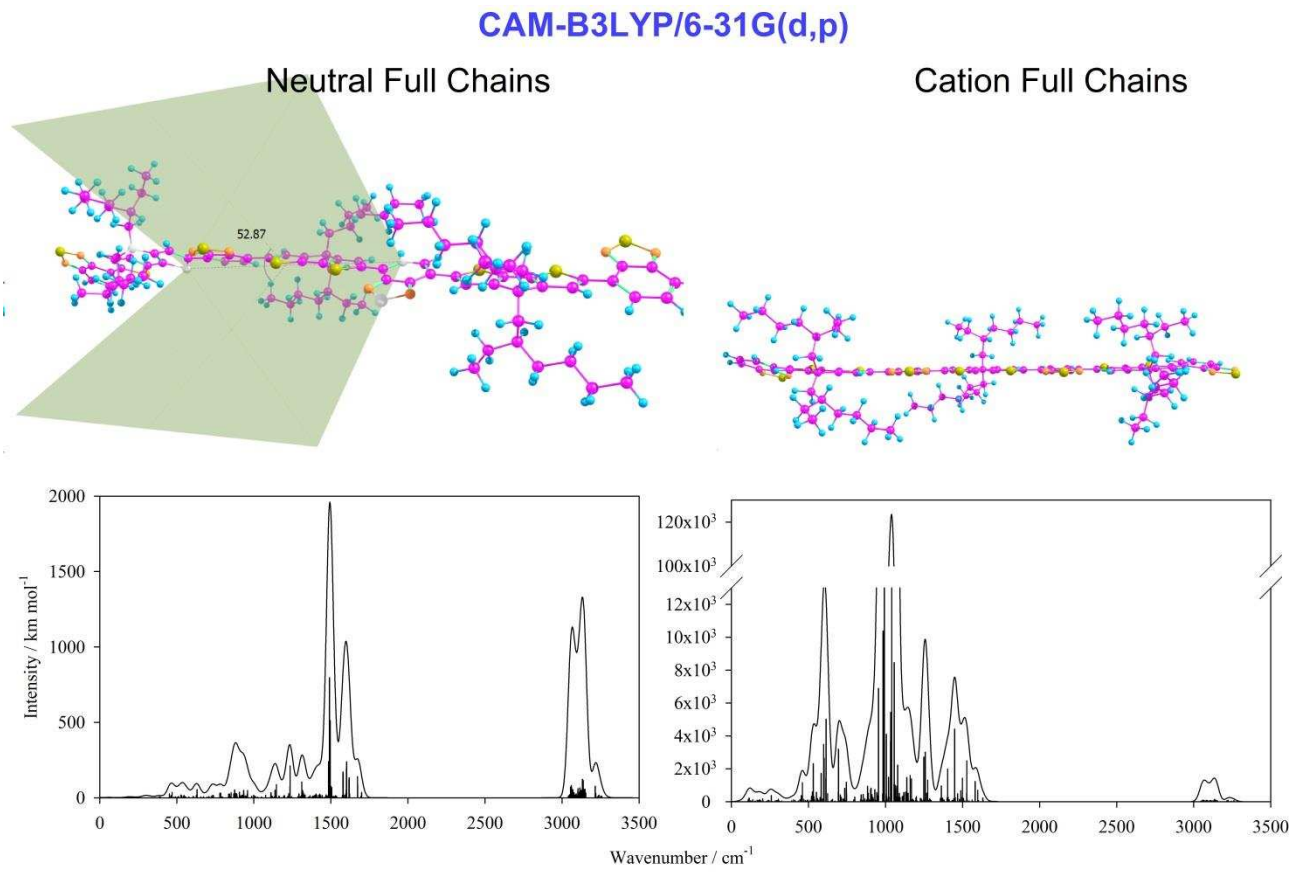

Figure 11. Calculated IR spectra, "hybrid" DFT/HF, CAMB3LYP functional, 6-31G(d,p) basis set. Trimer species inclusive of **all** the side branch alkyl chains: **left** panel neutral, **right** panel cation.

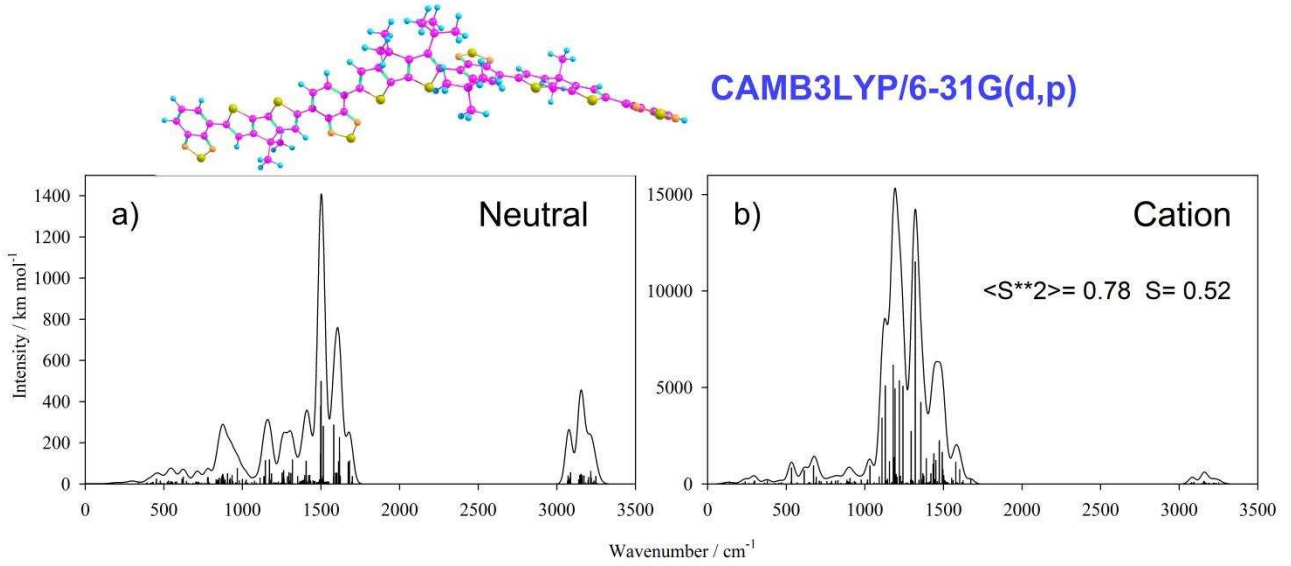

Figure 12. Calculated IR spectra, "hybrid" DFT/HF CAMB3LYP functional, 6-31G(d,p) basis set. Hypothetical trimer species featuring two suitable ter-butyl groups so to obtain a distorted othogonal two planes species: **a)** neutral b) cation. To be compared with ref [31] and Figure 9 results.

Table I. Frontier orbital energies, HOMO, LUMO, SOMO† and total spin, S, and $<S^2>$ eigenvalues for the trimer species, BT-(T2-BT)$_3$. Values reported for the closed-shell neutral and open-shell doublet species

BT-_T2-BT_3 Trimer NO CHAINS	HOMO / eV	HOMO LUMO / eV		SOMO / eV	SOMO LUMO / eV	S	$<S^2>$
	Neutral			Cation			
PM3	-8.2434	6.0284		-10.0737	4.3005	1.9213	5.6126
ROHF				-4.3671	1.9956		
HF / UHF	-6.6627	7.2546		-9.4745	5.5574	2.3865	8.0821
LDA SVWA	-4.7389	0.7292		-6.6622	0.0767	0.7510	0.5005
B3LYP	-4.5486	1.6408		-6.6559	0.6378	0.7802	0.5150
CAM-B3LYP	-5.7601	3.9682		-7.6872	2.4177	0.6233	1.0119

† Singly Occupied Molecular Orbital

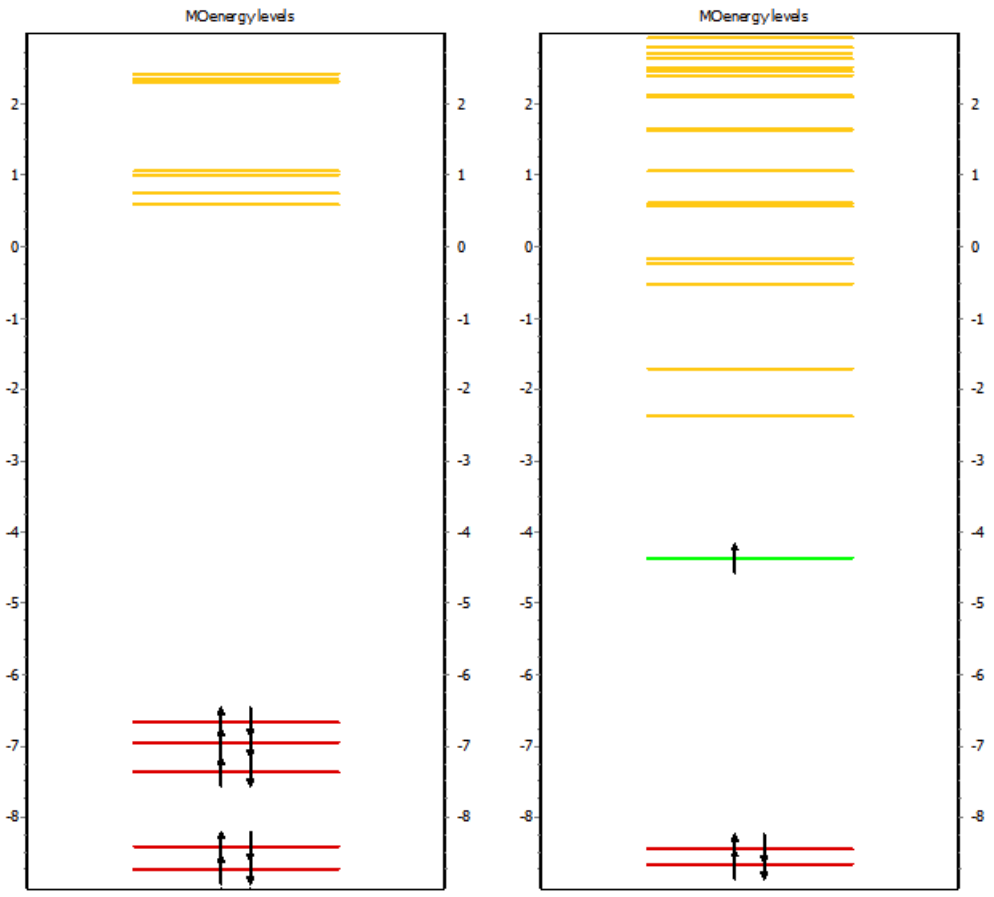

Figure 13. MOs energy diagram. Trimer species, BT-(T2-BT)$_3$, 6-31G(d,p) basis set. **Left:** neutral species, UHF results (note that UHF looks like exactly as a RHF calculation, as it must be for the equilibrium geometrical configuration, in the case of a closed shell system). **Right:** cation species ROHF calculation.

The data shown in this section clearly show how a number of issues are tightly interrelated in the calculation of theoretical IR spectra of charged π conjugated thiophene-based polymers: i) the length and "ordering" [94–96] of the thiophene back-bone (in a word the "effective spatial extension" of the π electron conjugated system)[4] ii) the level of the theory.

It is evident that the "size" of the system, meant to simulate the properties of a virtually infinite 1D polymer, is of paramount importance. The IR spectra here reported clearly show that for oligomers of the size of the trimer (and longer) the "Giant IR polaron signature" essential features, both wave-number position shift and maximum peak intensity relative to the neutral species, are qualitatively correctly foreseen.

The effect of the "level of the theory" is a much more complex topic to tackle. Unrestricted HF based approach is clearly a failure, signaled by the very large SOMO/LUMO (5.5574 eV) energy difference and not realistic $<S^2>$ = 8 eigenvalue (a totally reasonable outcome, coded as a limit of the single determinant calculation nature of the HF method). The same outcome is obtained by using a pure DFT functional (SVWN), the IR polaron signature is totally missing, with a small SOMO/LUMO gap (about 0.1 eV) and a correct $<S^2>$ = 0.75 value (compare Table I).

Notably B3LYP, ROHF and CAMB3LYP results, which show the best qualitative description of the IR polaron signature, feature comparable (intermediate to HF and DFT results) SOMO/LUMO energy gap and the $<S^2>$ values are rather close to 0.75 (compare Table I).

These results seem to indicate that the physics underlying the IR polaron signature is related to electron/vibrational interaction (vibronic coupling).

Eventually, the electron-phonon coupling constant, λ, is estimated on the basis of the approach shown in Chapert 2 (section b): $(a_0)^{-1} = \hbar^2 B/m\lambda^2$. Assuming a polaron size of 1.0 nm[5] electron-phonon constant of 0.9 and 0.6 eV are found for bulk modulus values of 1 and 2 GPa [97], respectively.

Moreover, recent theoretical work, recently developed within Enrico Da Como's group, seem to indicate a much more complex situation [98].

[4] The spatial extention possibly spanned by the electron plays a crucial role in determining the polaron state, compare Chapter 2 subsections a) and b).
[5] Which is roughly the length of the dithiophene-benzothiadiazole repeat unit in PCPDT-BT.

4.2) *Molecules* 2016, 21, 110 [26]

Preamble

The study underlying this paper is in tight connection with the subject analysed and assessed in the previous paper on doped thiophene based homo/co-polymers. Here the electronic features of 8 rather different poly-thiophenes are theoretically investigated. The main objective is to understand if some of the properties, peculiar of the doped polythiophenes system, can be foreseen on the basis of the properties of the pristine system. From the operational point of a view simple relationship between experimental observables (UV/Vis onset and reduction/oxidation potentials, i.e. quantities widely used to rationalize the use of polythiophenes in actual devices: photovoltaics or organic electronics) and the HOMO/LUMO energy gap has been examined (with particular attention devoted highlight the different physical processes probed by the UV/Vis spectroscopic and electrochemical measurements). Moreover, calculated data where used to compare i) HOMO/LUMO energy gap reckoned at the HF and DFT level of the theory ii) its dependence on the oligomer length and conformational arrangement (unexpectedly, the theoretical results showed to be almost converged already with two repeating units, no appreciable different is found between the 2 or 3 repeating units oligomers) iii) the dependence, of TDDFT electronic absorption spectra, on the number of repeating units in the oligomer. Notably, here only **neutral** systems are considered. A clear-cut point is made concerning the difference between HOMO/LUMO gap and electronic absorption spectra. Summarizing, the main outcome of this work: a systematic difference between spectroscopic and electrochemical experimental results is highlighted and discussed both in the light of HF and DFT results, as well as with respect to the application of these concepts in the rationalization of the experimental behaviour of photovoltaic devices, giving a rather detailed explanation why spectroscopic and electrochemical results show systematic differences. Finally, the exciton stabilization energy is estimated and discussed, even if based on simple/phenomenological evidence. Please note that the experimental data used as reference in this study are obtained from i) electronic absorption spectra in bulk solution ii) redox potentials from “thin” (in the μm range thickness) drop-casted films.

The candidate contribution concerned the design of the research, the electrochemical measurements, theoretical calculations and critical assembly of the global outcome leading to the final manuscript.

Statement of Authorship

<table>
<tr><td colspan="5">This declaration concerns the article entitled:

An Integrated Experimental/Theoretical Study of Structurally Related Poly-Thiophenes Used in Photovoltaic Systems</td></tr>
<tr><td colspan="5">Publication status (tick one)</td></tr>
<tr><td>draft manuscript</td><td>Submitted</td><td>In review</td><td>Accepted</td><td>Published X</td></tr>
<tr><td colspan="5">Publication details (reference): Molecules 2016, 21, 110</td></tr>
<tr><td colspan="2">Candidate's contribution to the paper (detailed, and also given as a percentage).</td><td colspan="3">The candidate contributed to the design of the research, theoretical interpretation and actual calculations (vide supra).

Formulation of ideas: 75 %

Design of methodology: 90 %

Experimental work: 50 %

Presentation of data in journal format: 70 %</td></tr>
<tr><td colspan="2">Statement from Candidate</td><td colspan="3">This paper reports on original research I conducted during the period of my Higher Degree by Research candidature.</td></tr>
<tr><td colspan="2">Signed  </td><td colspan="3">Date 15 May 2017</td></tr>
</table>

Open AccessArticle An Integrated Experimental/Theoretical Study of Structurally Related Poly-Thiophenes Used in Photovoltaic Systems
by Davide Vanossi, Luigi Cigarini, Andrea Giaccherini, Enrico da Como and Claudio Fontanesi
Molecules **2016**, *21*(1), 110; doi:10.3390/molecules21010110
Received: 24 December 2015 / Revised: 12 January 2016 / Accepted: 14 January 2016 / Published: 19 January 2016

Terms and Conditions

§ 1
Scope

1.1

These Business Terms and Conditions apply to the purchase of contracts concluded through the website of www.mdpi.com and all subdomains (hereinafter referred to as "Website") or through related e-mail communication, and to all related services provided by MDPI AG, St. Alban-Anlage 66, CH-4052 Basel, Switzerland (hereinafter referred to as "MDPI").

1.2

Any user of the website or buyer of services shall be referred to as "Customer" throughout these Terms and Conditions.

1.3

Any business terms by the Customer which diverge from these Terms and Conditions shall not apply, unless expressly confirmed by MDPI in written form.

1.4

The Terms of Use of the Website (http://www.mdpi.com/about/termsofuse) constitute an integral part of the present Terms and Conditions.

§ 2
Offering of MDPI

MDPI offers scientific publication and editorial services, which can be ordered by the Customer through the Website.

§ 3
Ordering and Purchasing of Services from MDPI

3.1

To order a publication service through the Website, the Customer must first register with the Website.

3.2

The requirements for registering with the Website are that the Customer is of full age and has full legal capacity.

3.3

The Customer asks for contracting publication and editorial services with MDPI the moment she/he submits an original scientific article ("Article") for evaluation through peer-review and possible publication by MDPI.

3.4

The Customer agrees to support open access publishing, which allows unlimited access to his/her published paper. In addition, the Customer agrees to the publishing fee (APC) and is bound to pay the APC after acceptance of the paper for publication.

3.5

When purchasing services from MDPI, the Customer has the following cancellation right: The Customer can withdraw her/his Article and cancel the declared intention to conclude the contract anytime during the evaluation of the Article, unless the Article has been accepted for publication by MDPI, but at least for a period of 14 days. Any benefits or interests received by the Customer up to the cancellation have to be restituted to MDPI. Any service prices paid before the cancellation will be refunded to the Customer minus the payment transfer charges.

3.6

When offering services to the Customer, MDPI has the following cancellation right: MDPI may turn down or reject the Article anytime without specifying any reason and thus cancel the conclusion of the contract. After the cancellation through MDPI, both parties are freed from any previous commitments of these Terms and Conditions. The customer shall be fully refunded if any service fees were already paid before the cancellation of the contract, with the exception of English editing charges.

3.7

In case a Customer pays more than invoiced by MDPI, any bank or transaction charges will be deduced from a partial refund of the overpaid amount.

3.8

Once an article is published, MDPI will refund authors in exceptional circumstances only and a decision will be made on a case-by-case basis.

§ 4
Manuscript and Copyright Issues

4.1

If material from other publications is reproduced in your manuscript, please provide proof that you have obtained the necessary copyright permission. Please refer to our Rights & Permissions website: http://www.mdpi.com/authors/rights/.

4.2

Your manuscript is accepted for processing on the understanding that it has not been published elsewhere (or submitted to another journal). Exceptions to this rule are papers containing material disclosed at conferences, however please inform us if this is the case. For papers with multiple authors, please also confirm that all authors are familiar with, and agree with, the contents of the manuscript. We reserve the right to contact all authors to confirm this in case of doubt. Please provide e-mail addresses for all authors and at least one institutional email address for one of the co-authors, and specify the name, address and E-mail for invoicing purposes.

4.3

This article, if accepted, will be an open access article distributed under the terms and conditions of the Creative Commons Attribution License (http://creativecommons.org/licenses/by/4.0/). MDPI will insert the following note at the end of the published text: © 2017 by the authors; licensee MDPI AG, Basel, Switzerland. This article is an open-access article distributed under the terms and conditions of the Creative Commons Attribution License (http://creativecommons.org/licenses/by/4.0/).

§ 5
Prices, Terms of Payment

5.1

Prices are stated at the following page: http://www.mdpi.com/about/apc. The applicable price for the publication service regarding an accepted Article is based on the date of the original submission of the Article to MDPI.

5.2

Discounts on the service price apply for established institutional memberships and may be granted to reviewers. Furthermore, MDPI may grant discounts and waivers in exceptional cases, however, reserves the right to decline such discounts and waivers without specifying a reason.

5.3

Payments to MDPI are due within 5 days of sending the invoice to the Customer. Longer payment terms up to a maximum of 60 days can be granted by MDPI in written form by e-mail on the request of the Customer. If requested, MDPI will issue a revised invoice for purpose of restating the new payment term.

5.4

Invoices are sent by e-mail to the payment contact person provided by the Customer soon after acceptance of an Article for publication.

§ 6
Contract Document

MDPI makes no provision for a separate contract document based on these Terms and Conditions. However, the Customer may check at any time the ordered services and status of the Article through her/his personal account on the Website.

§ 7
Miscellaneous

7.1

Basel, Switzerland shall be the place of jurisdiction for all legal disputes arising of these Terms and Conditions, even if the Customer has her/his domicile outside of Switzerland.

7.2

Swiss law applicable at the place of jurisdiction of MDPI shall apply exclusively.

7.3

If any provisions of the Terms and Conditions should be found invalid, this shall not affect the validity of the remaining provisions. In any such case, the contracting parties shall negotiate on the invalid clause to substitute by a valid arrangement as close as possible to the original provision.

7.4

MDPI reserves the right to change these Terms and Conditions at any time by posting changes to this page of the website without prior notice. Please check these Terms and Conditions periodically for any modifications. Your continued use of any Service following the post-ing of any changes will mean that you have accepted and agreed to the changes.

Business Terms and Conditions MDPI AG

Standard Terms and Conditions of Business of MDPI AG (pdf)

These Terms and Conditions were last updated on 1 March 2017

Publication title:
An Integrated Experimental/Theoretical Study of Structurally Related Poly-Thiophenes Used in Photovoltaic Systems

the thesis page numbers that it spans:
62 to 71

molecules

MDPI

Article

An Integrated Experimental/Theoretical Study of Structurally Related Poly-Thiophenes Used in Photovoltaic Systems

Davide Vanossi [1], Luigi Cigarini [2], Andrea Giaccherini [3], Enrico da Como [4] and Claudio Fontanesi [4,5,*]

Received: 24 December 2015 ; Accepted: 14 January 2016 ; Published: 19 January 2016
Academic Editors: Nicola Cioffi, Antonio Monopoli and Massimo Innocenti

1 Department of Geological and Chemical Sciences, University of Modena and Reggio Emilia, Via G. Campi 183, Modena 41125, Italy; davide.vanossi@unimore.it
2 Department of Physics, University of Modena and Reggio Emilia, Via G. Campi 213, Modena 41125, Italy; luigi.cigarini@unimore.it
3 Department of Chemistry, University of Florence, Via della Lastruccia 3, Sesto Fiorentino 50019, Italy; andrea.giaccherini@unifi.it
4 Department of Physics, University of Bath, Claverton Down Bath BA2 7AY, UK; E.Da.Como@bath.ac.uk
5 Department of Engineering "Enzo Ferrari", University of Modena and Reggio Emilia, Via Vivarelli 10, Modena 41125, Italy
* Correspondence: claudio.fontanesi@unimore.it; Tel.: +39-059-250-6170

Abstract: In this work, a series of eight thiophene-based polymers (exploited as "donors" in bulk heterojunction photovoltaics cells), whose structures were designed to be suitably tuned with the electronic characteristics of the [6,6]-Phenyl C61 butyric acid methyl ester (PCBM), is considered,. The electronic properties of the mono-, di-, trimeric oligomers are reckoned (at the Hartree-Fock and DFT level of the theory) and compared to experimental spectroscopic and electrochemical results. Indeed, electrochemical and spectroscopic results show a systematic difference whose physical nature is assessed and related to the exciton (electron-hole) binding energy ($J_{e,h}$). The critical comparison of the experimental and theoretical band gaps, *i.e.*, the HOMO-LUMO energy difference, suggests that electrochemical and DFT values are the most suited to being used in the design of a polythiophene-based p-n junction for photovoltaics.

Keywords: polythiophenes; band gap; DFT; HF; exciton

1. Introduction

The electronic properties of eight thiophene-based polymers (Figure 1 shows the relevant structures), with a particular focus on the interfacial behavior, are rationalized within a "Lego-like sum approach": the electronic properties of the mono-, di-, trimeric species are calculated, and eventually the trimer results are selected (the differences between the dimer and trimer oligomers are almost negligible) and shown, in the following figures, to represent the electronic features of the polymer system well. Such a general modelistic approach spans extremely different worlds: from the Mott-Schottky barrier to Tafel plots in electrochemical systems [1–3]. It is noteworthy that when the field of linear conjugated polymers is considered, a number of non-linear effects concur to determine the final observed electronic properties (with a particular focus on conductivity), leaving this research topic still open to discussion and further development, because low dimensional structures such as polymers (polymers can be considered as electron one-dimensional conductive wires) are unstable, and, in these systems, the coupling between electrons and phonons wavefunctions (leading to the definition of the polaron [4,5]) determines a more tight localization of single- and double-bonds which

lifts molecular orbitals' degeneracy and finally induces the localization of π-electrons, leaving both the experimental and theoretical work a still-challenging field [4–8]. Within this field, the up-to-date frontier hot topic is the estimation and calculation of the so-called polaron dimension [9], which is thought to play a prominent role in determining the polymer electronic conduction.

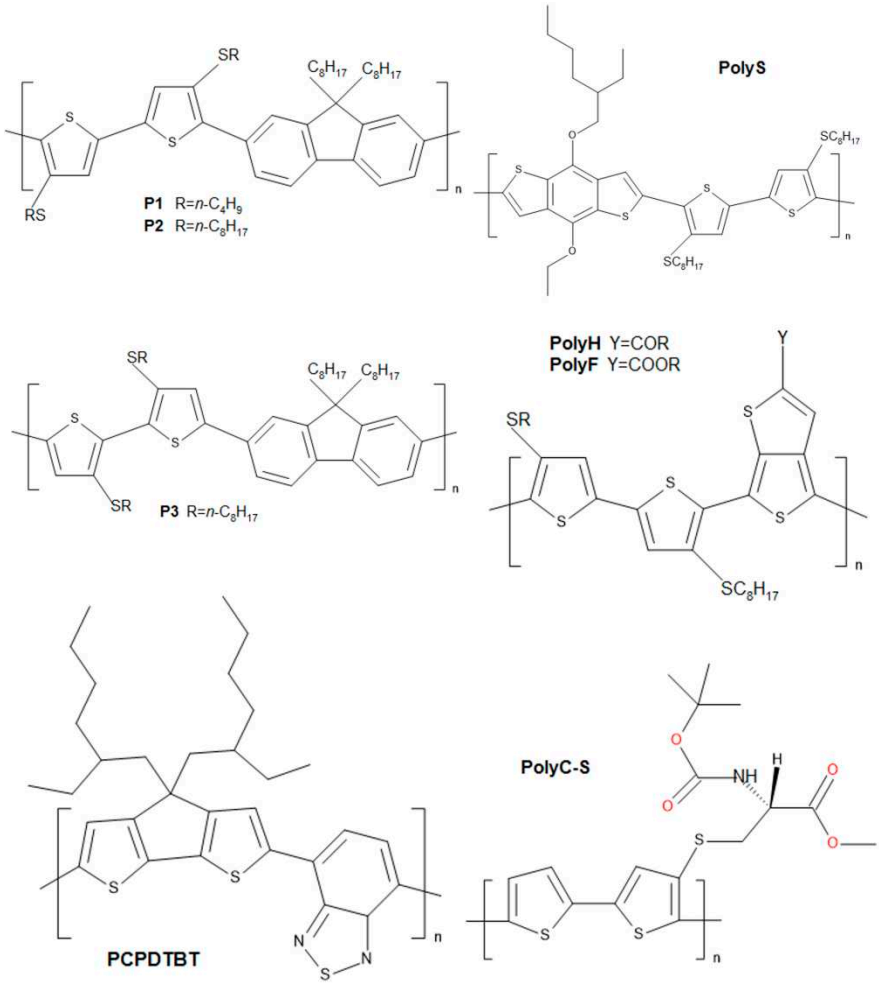

Figure 1. Polymer structures studied in this work.

Furthermore, a field of extremely relevant interest and expectations concerns thin-film polymer semiconductors exploited in hybrid systems, such as organic-based light-emitting diodes, photovoltaic cells and thin-film transistors, where the influence of the degree of order in the solid state plays a major role [10,11]. Indeed, the understanding of the interplay and relationship between the film morphology/electronic-structure and charge transport is of key importance for improving the performance of thin-film transistors [8].

In particular, in the field of organic semiconductors exploited to assemble photovoltaic devices, the open circuit potential is rationalized on the basis of the reciprocal HOMO-LUMO energy differences between the donor and the acceptor partners [11–13]. Although such an approach seems by far much too crude in its strategy, the straight comparison of HOMO-LUMO MOs energy levels, of the donor and acceptor building blocks, is still the most widespread tool exploited in the modelization of photovoltaic organic-based systems [14,15]. The electronic properties of the mono-, di-, trimeric oligomer species are considered and compared to the experimental spectroscopic and electrochemical results [16–19]. Among the different polythiophene structures investigated here, the peculiar characteristics of the chiral PolyC-S made it suitable for the realization of hybrid interfaces [20] exploited in the recently established field of "spin-dependent electrochemistry" [21,22].

2. Semiconductive Polythiophene Structures

In this work, a series of eight thiophene-based polymers (donors) are considered. Their structures were designed (both by the introduction of ring structures of various chemicals in the polymeric backbone structure—heteropolymers—and also by various lateral alkyl chains) to suitably tune the electronic properties of the PCBM (acceptor). The structures of the polymers studied here, are shown in Figure 1. PCPDTBT was purchased by Sigma-Aldrich (St. Louis, MO, USA) (754005 Aldrich, CAS Number 920515-34-0), while all of the other compounds are of original synthesis [16–19].

3. Experimental Setup

UV-vis spectra were recorded in ambient air at room temperature (25 °C), by means of a Perkin Elmer Lambda 900 spectrophotometer (Perkin Elmer, Waltham, MA, USA). Cyclic voltammetry (CV) measurements were performed both with a CHI 660A Electrochemical Workstation (CH Instruments, Inc., Austin, TX, USA) and an AUTOLAB PGSTAT20 (Metrohm Autolab B.V., Utrecht, The Netherlands). A three-electrode electrochemical cell configuration was adopted. A 0.1 mol/L *n*-tetrabutyl ammonium hexa fluorophosphate ($TBAPF_6$ > 99.9%, Sigma-Aldrich Chemie B.V., Zwijndrecht, The Netherlands) in acetonitrile (ACN) solution was used as the base electrolyte. The working electrode is obtained by drop-casting of polythiophene/CH_2Cl_2 solution applied on freshly polished Glassy Carbon (GC) electrodes (Metrohm Schweiz AG, Zofingen, Switzerland) and HTW Sigradur (HTW Hochtemperatur-Werkstoffe GmbH, Thierhaupten, Germany). Prior to polymer drop-casting, the GC surface was mechanically polished with emery paper, then with 0.05 µm alumina (Buheler, Lake Bluff, IL, USA), finally followed by a 5 min sonication cleaning in water. The GC surface was polymer-coated by casting one drop of a 0.1 mg/mL, in CH_2Cl_2, polymer solution on top of the GC surface and allowing it to dry [16]. A platinum wire was used as the counter electrode. A silver wire was used as a quasi-reference electrode, whose stability was checked (at the end of each measurement session) with respect to the ferrocene/ferrocenium reversible redox couple. In the following all potential values are referred to the Ag/Ag^+ couple. A large number of screening experiments were carried out, varying both the dose of the drop-casting as well as the drying time. Films obtained on repeating the sequence of a single drop-cast application three times, followed by 15 min drying, allowed for the best CV reproducibility. We estimate that our reduction and oxidation potentials are affected by a 30 mV absolute error (±15 mV error). The electrochemical cell was de-aerated with argon for 15 min before any measurement session. Figure 2 shows two examples of the cyclic voltammetry data treatment, in order to show in detail how the electrochemical onset potentials were determined. Two completely different experimental behaviors are considered: Poly H characterized by a rather hill-defined/sluggish cyclic voltammetry pattern (with particular reference to the positive potential range: polymer film oxidation), Figure 2a, and Poly F which shows a rather well-defined and neat cyclic voltammetry pattern, Figure 2b.

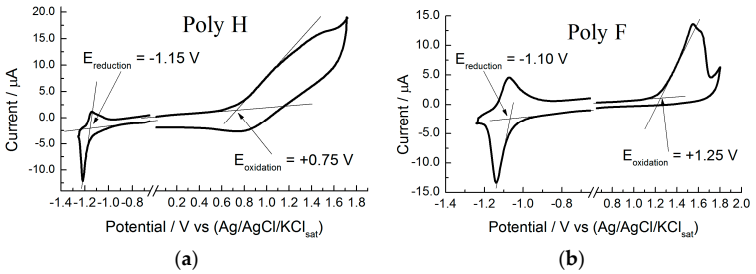

Figure 2. Cyclic voltametries (**a**,**b**) of the Poly H and Poly F polymer films on GC surfaces (obtained by drop-casting procedure), respectively. Showing the method adopted to determine the reduction and oxidation onset potentials, which are used to calculate the so-called electrochemical band gap (ΔE_{EC}). Onset values are obtained by the intercept of the lines interpolating the baseline and redox peak currents.

Figure 3 shows, as an example, the treatment of the UV-vis spectrum of Poly F, in order to show in detail how the onset wavelength is determined, which eventually leads to the calculations of the ΔE_{OPT} value.

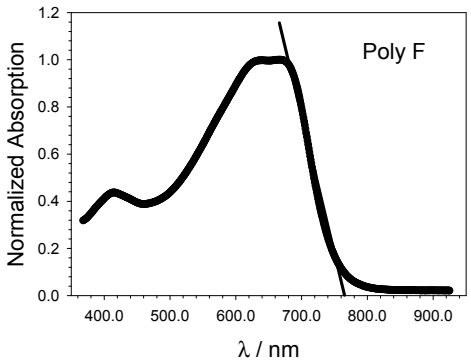

Figure 3. Poly F UV-vis spectrum, the line used to determine the onset wavelength is shown. The intercept with the absissa allows us to determine the optical band gap (ΔE_{OPT}).

4. Computational Details

In the present work, the overall calculations were performed in the framework of *ab initio* methods using the Gaussian and Firefly [23] QC packages, which are partially based on the GAMESS (US) source code. All calculations, unless otherwise indicated, were performed using C_1 symmetry and are of restricted nature. The results presented in this paper are obtained both at the very basic Hartree-Fock (HF) and Becke, three-parameter, Lee-Yang-Parr (B3LYP) exchange-correlation density functional levels of the theory; the all-electron split valence plus polarization basis set 6-31G(d) was used in both HF and DFT calculations. Preliminary screening calculations were carried out using less accurate basis sets: LanL2DZ, 3-21G*, with focus on the influence of the geometry optimization as well as of the number of repetitive units in the oligomer on the variation of the HOMO-LUMO energies and band gap. Moreover, periodic boundary condition (PBC) calculations were performed, the latter results well compare with the HOMO-LUMO band gap relevant to the dimeric and trimeric species, together with the systematic calculation (again involving the mono-, di-, trimer species) of TDDFT electronic spectra [24].

5. Theoretical Background

5.1. Orbital Energies: DFT vs. HF

It is well established [25] that the Kohn-Sham orbitals, $\varphi_i(\boldsymbol{r})$, do not have any particular physical meaning; they only serve as a tool to construct the exact (at least in principle) ground-state density for the actual system of interacting electrons. The same consideration is clearly also directed for the Kohn-Sham eigenvalues, ε_i, which, from a formal point of view, are simply lagrangian multipliers inserted "*ad hoc*" to perform the constrained variational minimization. Nevertheless, there is one important exception to this statement when the energy ε_N of the highest occupied orbital, for a finite system of N electrons, is considered: minus ε_N depicts, in fact (at least in the case of an exact exchange-correlation functional [25,26]), the ionization potential $I_p(N)$ of the system, *i.e.*,:

$$\varepsilon_N(N) = E(N) - E(N-1) = -I_p(N) \quad (1)$$

where $E(N)$ and $E(N-1)$ are the total ground-state energies for the system with N and $N-1$ electrons. On the contrary, all the Hartree-Fock mono-electronic energies, thanks to the Koopmas theorem [27], correspond to electron removal energies once correlation and orbital relaxation effects are neglected.

It is also possible to write down an exact and equivalent relation to Equation (1) starting from the Kohn-Sham energy ε_{N+1} of the highest occupied orbital for a system with $N + 1$ electrons:

$$\varepsilon_{N+1}(N+1) = E(N+1) - E(N) = -I_a(N) \quad (2)$$

Equations (1) and (2) can be considered the DFT Koopmans theorem, which, however, in comparison to the Hartree-Fock version, is exact because ε_N is endowed with a many-bodies nature. Equation (2) shows that minus ε_{N+1} is equal to the electron affinity $I_a(N)$ for the N-electron system (being $E(N+1)$, the total ground-state energy for the system with $N + 1$ electrons).

Despite the soundness of Equations (1) and (2), differences in Kohn-Sham energy eigenvalues do not correspond, in general, to the exact excitation energies for the interacting N-electron system but, sometimes, they can be used as first, rather fairly acceptable approximations [28].

5.2. Computing the Band Gaps

When different types and states of matter are considered, it is well known [26,28,29] that energy band gaps may or may not occur. A gap is the direct manifestation of the existence of a finite energetic difference between two states of the system. In physics there are several type of gaps: the particle (or quasi-particle) gap, optical gap, superconducting gap [28]. For each one of these gaps, different experimental characterization methods exist. For example, the optical gap, which is related to the energy difference between the electronic ground state and the first excited state for a system with a fixed particle number N (neutral excitation), can be addressed by means of optical spectroscopy. Otherwise, the particle gap (which is of fundamental importance in an insulating periodic solid) is related to the ground-state energies of systems with different particle numbers (charged excitation) and can be typically probed using photoelectron spectroscopy. The particle gap is defined as [26,28]:

$$E_g(N) = I_p(N) - I_a(N) \quad (3)$$

In terms of KS energies, Equations (1) and (2) can be rearranged as:

$$E_g(N) = \varepsilon_{N+1}(N+1) - \varepsilon_N(N) \quad (4)$$

Equation (4) involves the energies of the highest occupied orbitals of two systems with a different number of electrons, so we are dealing with an excitation which does not conserve the number of electrons. Equation (4) can be clearly used when a finite system (such as a molecule) is considered, but becomes quite impractical when referring to a solid. In this last situation it is necessary to define a different particle gap, also known as a Kohn-Sham gap, by means of the following equation:

$$E_g^{KS}(N) = \varepsilon_{N+1}(N) - \varepsilon_N(N) \equiv \Delta E_{DFT} \quad (5)$$

in which the lowest unoccupied (LUMO) and the highest occupied (HOMO) orbital energies, for the system with N electrons (neutral excitation), are considered. It is worthwhile to note that a relation formally equivalent to Equation (5) is commonly also adopted in the Hartree-Fock framework (even for finite systems):

$$E_g^{HF}(N) = \varepsilon_{N+1}^{HF}(N) - \varepsilon_N^{HF}(N) \equiv \Delta E_{HF} \quad (6)$$

Equations (4) and (5) can be related to one another in this way:

$$E_g(N) = E_g^{KS}(N) + \Delta_{xc} \quad (7)$$

where Δ_{xc}, the many-bodies correction to the Kohn-Sham particle gap, can be casted as [28]:

$$\Delta_{xc} = \varepsilon_{N+1}(N+1) - \varepsilon_{N+1}(N) \quad (8)$$

5.3. Optical and Electrochemical Band Gaps

Absorption of a photon with energy equal to or greater than the band gap results in the excitation of an electron from the valence to the conduction band, leaving a hole in the valence band. Such an electron hole pair, or exciton, is bound by the electrostatic attraction between the collective state's electron in the conductive band and the hole in valence band. By means of optical excitation, four basic types of charge-transfer processes are proposed by Credi *et al*. [30], and we proposed them also for semiconducting polymers: electron injection into a neutral molecule (Figure 4a), electron extraction from a neutral molecule (or hole injection, Figure 4b), removal of an electron from one molecule and placing it into an identical molecule at a infinite distance, (Figure 4c), and generation of an electron-hole pair within the same molecule (Figure 4d).

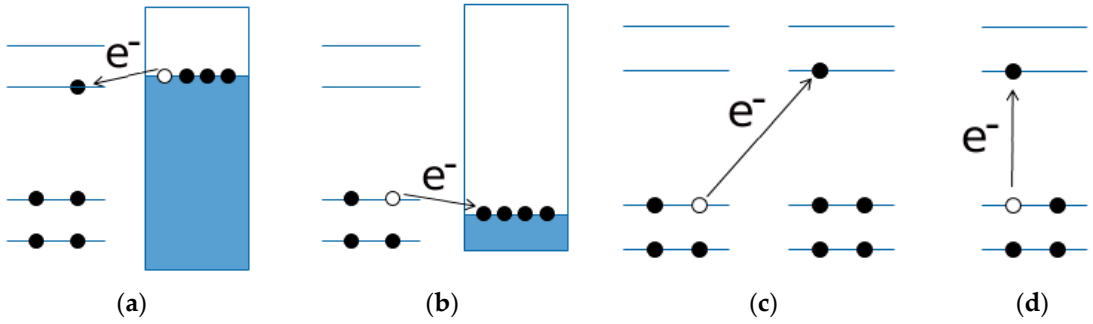

Figure 4. The white circles represent holes and the black circles electrons. In (**a**,**b**) the pseudo-fermi level of the polarized electrode is represented by the line on top of the dark rectangle representing the conduction band of the solid; (**c**,**d**) depicts the intermolecular and intramolecular electronic transitions, respectively. The other lines represent the orbitals in the polymer molecules while the arrows represent the electron transfer.

The electrochemically determined band gap (ΔE_{EC}) is operatively defined as the difference in energy between the first reduction and the first oxidation processes of the molecule, respectively, corresponding to the process in Figure 4a,b. Thus is equivalent to the energy required to produce a noninteracting electron-hole pair (quasi-particle gap). The optical band gap ΔE_{OPT} corresponds to the process in Figure 4d. In the ground of this theoretical model, the two band gaps are related by Equation (9):

$$\Delta E_{OPT} = \Delta E_{EC} + J_{e,h} \quad (9)$$

where $J_{e,h}$ is the binding energy of the exciton. Hence, for any given semiconducting molecule, the electrochemical energy gap is expected to be larger than the optical energy gap.

6. Results

Figure 5a shows the ΔE_{EC} *vs.* ΔE_{OPT} graph, obtained by the experimental band gap values. The latter are obtained (i) by means of spectroscopical measurements, ΔE_{OPT} (optical band gap, calculated by the onset of the absorption peak determined from the UV/Vis spectra), and (ii) by means of CV curves, ΔE_{EC} (note that the difference in the onset of potentials, V, relevant to the reduction and oxidation current peaks is straight transformed in a band gap energy, eV, on the basis of the work of Trasatti [31]).

All the points in this dataset are more positive than the "equivalence line": the electrochemical band gap is systematically larger than the optical band gap (about 0.45 eV), suggesting a bias in the difference between the two band gaps. In Figure 5b, the LUMO/HOMO energy difference, the HF band gap (ΔE_{HF}) has been compared with the DFT band gap (ΔE_{DFT}). Note the systematic large difference between ΔE_{HF} and ΔE_{DFT} values. Figure 5c,e patterns demonstrate that ΔE_{HF} are overestimated with respect to both the optical and electrochemical band gap, while in Figure 5d a comparison between the

DFT band gap and the optical band gap shows that DFT systematically overestimates the optical band gap. Eventually, the electrochemical band gap is compared with the DFT gap (Figure 5f), and ΔE_{DFT} values semi-quantitatively match the electrochemical band gap: the equivalence line is almost exactly placed in the middle of the dataset. Figure 6 shows the difference between the DFT, electrochemical and optical band gap values (*i.e.*, ($\Delta E_{DFT} - \Delta E_{EC}$), ($\Delta E_{EC} - \Delta E_{OPT}$) and ($\Delta E_{DFT} - \Delta E_{OPT}$) differences). Notably, the difference between electrochemical and DFT band gaps ($\Delta E_{DFT} - \Delta E_{EC}$) is scattered homogenously around zero, and the maximum deviation is 0.28 eV. However, the discrepancy between electrochemical and optical results is the same as the DFT and optical one: both ranging between 0.2 and 0.9 eV, highlighting that the DFT and electrochemical band gaps have the same quantitative trend.

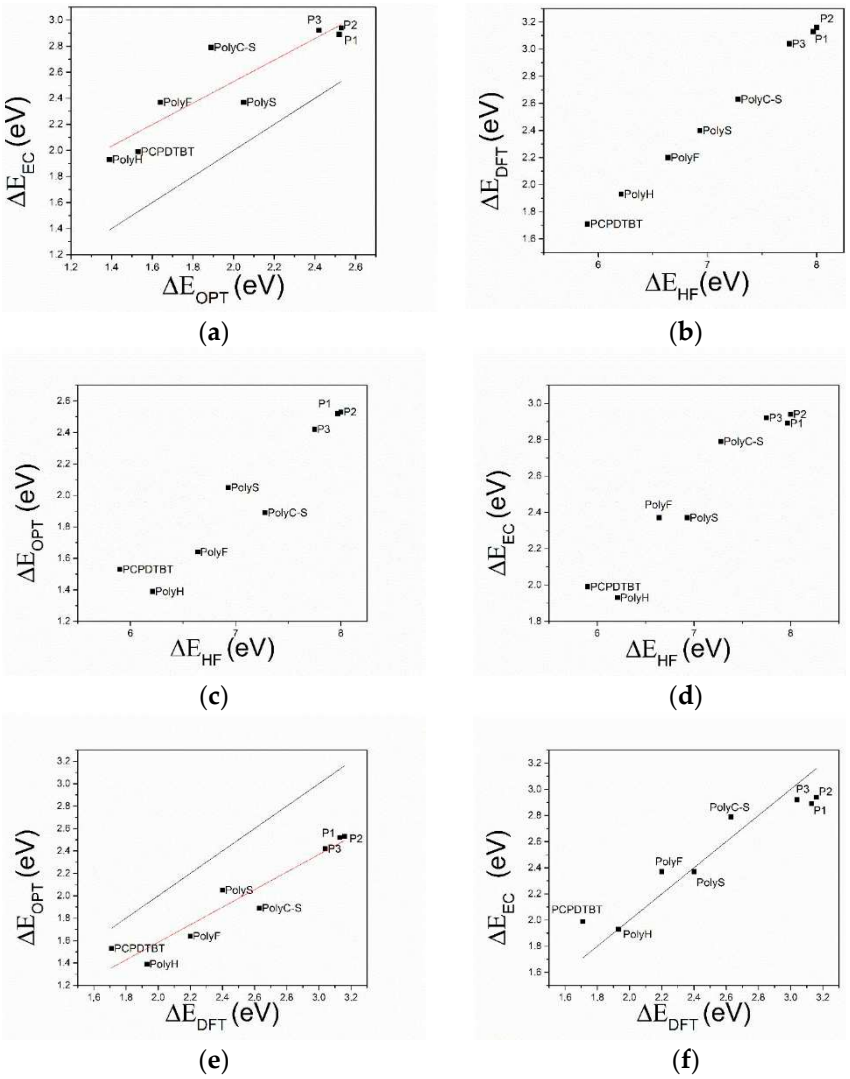

Figure 5. Comparison between (**a**) electrochemically determined and spectroscopically determined band gap; (**b**) band gap computed by means of DFT and HF methods; (**c**) band gap spectroscopically determined and computed by means of HF method; (**d**) band gap electrochemically determined and computed by means of HF method; (**e**) band gap spectroscopically determined and computed by means of DFT method; (**f**) band gap electrochemically determined and computed by means of DFT method. All data are reported in eV. The "equivalence line" shows the ideal line featuring slope = 1 and intercept = 0.

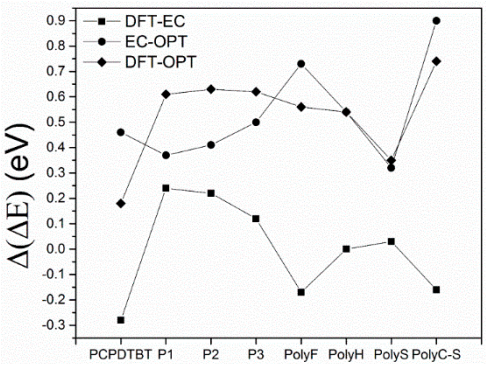

Figure 6. Discrepancies between band gaps computed by means of DFT method and electrochemically determined; band gaps electrochemically and spectroscopically determined; band gaps computed by means of DFT method and spectroscopically determined.

7. Conclusions

The electronic characteristics, with a focus on the band gap, of eight thiophene-based semiconducting polymers have been determined both experimentally (electrochemically, spectroscopically) and theoretically (at the Hartree/Fock and DFT level of the theory). Careful comparison between theoretical and experimental results allows us to draw some main line of action that is useful when dealing with problems of reciprocal coupling of hybrid donor/acceptor systems, where band gap features are thought to determine the ultimate performances of a system/device.

(1) The comparison of HF and DFT theoretical data, with both electrochemical and spectroscopic experimental band gap values, shows that the HF approach provides a dramatic overestimation of the band gap. The exchange-correlation and electron-correlation cannot be neglected; they have to be taken into account to assess the correct band gap energy. Indeed, ΔE_{DFT} values definitively show a better quantitative match with both the electrochemical and spectroscopic band gap values, as it is shown in Figures 5 and 6.

(2) Arguments, based both on the purely modelistic (Figure 4) and on the comparison between DFT and experimental data (Figures 5 and 6), show that the most effective approach to be used when assessing the band gap characteristics for photovoltaic materials is to make a reference to both the DFT and electrochemical methods to determine the HOMO-LUMO band gap.

(3) Eventually, an empirical quantitative value can be determined for the exciton stabilization energy ($J_{e,h}$), *vide infra* relation 8. The close comparison of the physics underlying absorption in electronic spectra (Figure 4d) and reduction/oxidation current peaks in cyclic voltammetry measurements (Figure 4a,b) together with the systematic difference observed in Figure 5a (the least square fit yields $\Delta E_{EC} = 0.53 + 0.99\ \Delta E_{OPT}$) allow us to propose a value of about 0.5 eV (the intercept of the least square fit) as an average value for the exciton stabilization energy [30,32]. Such an estimate is further supported by the systematic shift observed in Figure 6 between the ΔE_{OPT} *vs.* ΔE_{DFT} pattern (red line represents the least square fitting of the ΔE_{OPT} *vs.* ΔE_{DFT} data) and the relevant equivalence line.

As a whole, the results presented in this paper strongly support the view of a tight equivalence between the DFT and electrochemically determined band gap values (a result consistent both in terms of the physics underlying the different processes involving electrons and of the purely measured and computed values). The electrochemical measurements, giving an insight in the relative energy of HOMO and LUMO in different systems, seem to provide the values best suited for designing and selecting optimum candidates for organic/hybrid photovoltaic systems.

Acknowledgments: DIEF (UniMORE), Department of Chemistry (UniFI) and Department of Physics (UniBATH) are kindly acknowledged.

Author Contributions: Davide Vanossi and Claudio Fontanesi conceived and designed the experiments; Luigi Cigarini and Andrea Giaccherini performed the calculations and analyzed the data; Enrico da Como contributed materials; Enrico da Como, Davide Vanossi and Claudio Fontanesi wrote the paper.

Conflicts of Interest: The authors declare no conflict of interest.

References and Notes

1. Tung, R.T. Chemical Bonding and Fermi Level Pinning at Metal-Semiconductor Interfaces. *Phys. Rev. Lett.* **2000**, *84*, 6078–6081. [CrossRef] [PubMed]
2. Mohilner, D.M. The electrical double layer, part I: Elements of double-layer theory. In *Electroanalytical Chemistry: A Series of Advances*; Bard, A.J., Ed.; CRC Press: Boca Raton, FL, USA, 1996; Volume 1.
3. Bard, A.J.; Faulkner, L.R. *Electrochemical Methods: Fundamentals and Applications*, 2nd ed.; Wiley: New York, NY, USA, 1980.
4. Bredas, J.L.; Street, G.B. Polarons, bipolarons, and solitons in conducting polymers. *Acc. Chem. Res.* **1985**, *18*, 309–315. [CrossRef]
5. Brédas, J.L.; Wudl, F.; Heeger, A.J. Polarons and bipolarons in doped polythiophene: A theoretical investigation. *Solid State Commun.* **1987**, *63*, 577–580. [CrossRef]
6. Roncali, J. Synthetic Principles for Bandgap Control in Linear π-Conjugated Systems. *Chem. Rev.* **1997**, *97*, 173–206. [CrossRef] [PubMed]
7. Pesant, S.; Boulanger, P.; Côté, M.; Ernzerhof, M. Ab initio study of ladder-type polymers: Polythiophene and polypyrrole. *Chem. Phys. Lett.* **2008**, *450*, 329–334. [CrossRef]
8. Lan, Y.-K.; Yang, C.H.; Yang, H.-C. Theoretical investigations of electronic structure and charge transport properties in polythiophene-based organic field-effect transistors. *Polym. Int.* **2010**, *59*, 16–21. [CrossRef]
9. Rawson, J.; Angiolillo, P.J.; Therien, M.J. Extreme electron polaron spatial delocalization in π-conjugated materials. *PNAS* **2015**, *112*, 13779–13783. [CrossRef] [PubMed]
10. Joseph Kline, R.; McGehee, M.D.; Toney, M.F. Highly oriented crystals at the buried interface in polythiophene thin-film transistors. *Nat. Mater.* **2006**, *5*, 222–228. [CrossRef]
11. Di Nuzzo, D.; Fontanesi, C.; Jones, R.; Allard, S.; Dumsch, I.; Scherf, U.; von Hauff, E.; Schumacher, S.; da Como, E. How intermolecular geometrical disorder affects the molecular doping of donor-acceptor copolymers. *Nat. Commun.* **2015**, *6*. [CrossRef] [PubMed]
12. Hallermann, M.; Como, E.D.; Feldmann, J.; Izquierdo, M.; Filippone, S.; Martín, N.; Jüchter, S.; von Hauff, E. Correlation between charge transfer exciton recombination and photocurrent in polymer/fullerene solar cells. *Appl. Phys. Lett.* **2010**, *97*, 023301. [CrossRef]
13. Veysel Tunc, A.; de Sio, A.; Riedel, D.; Deschler, F.; da Como, E.; Parisi, J.; von Hauff, E. Molecular doping of low-bandgap-polymer:fullerene solar cells: Effects on transport and solar cells. *Org. Electron.* **2012**, *13*, 290–296. [CrossRef]
14. Li, Y. Molecular Design of Photovoltaic Materials for Polymer Solar Cells: Toward Suitable Electronic Energy Levels and Broad Absorption. *Acc. Chem. Res.* **2012**, *45*, 723–733. [CrossRef] [PubMed]
15. Li, Y.; Calder, S.; Yaffe, O.; Cahen, D.; Haick, H.; Kronik, L.; Zuilhof, H. Hybrids of Organic Molecules and Flat, Oxide-Free Silicon: High-Density Monolayers, Electronic Properties, and Functionalization. *Langmuir* **2012**, *28*, 9920–9929. [CrossRef] [PubMed]
16. Parenti, F.; Morvillo, P.; Bobeico, E.; Diana, R.; Lanzi, M.; Fontanesi, C.; Tassinari, F.; Schenetti, L.; Mucci, A. (Alkylsulfanyl)bithiophene-alt-Fluorene: π-Conjugated Polymers for Organic Solar Cells. *Eur. J. Org. Chem.* **2011**, *2011*, 5659–5667. [CrossRef]
17. Morvillo, P.; Parenti, F.; Diana, R.; Fontanesi, C.; Mucci, A.; Tassinari, F.; Schenetti, L. A novel copolymer from benzodithiophene and alkylsulfanyl-bithiophene: Synthesis, characterization and application in polymer solar cells. *Sol. Energy Mater. Sol. Cells* **2012**, *104*, 45–52. [CrossRef]
18. Morvillo, P.; Diana, R.; Fontanesi, C.; Ricciardi, R.; Lanzi, M.; Mucci, A.; Tassinari, F.; Schenetti, L.; Minarini, C.; Parenti, F. Low band gap polymers for application in solar cells: Synthesis and characterization of thienothiophene-thiophene copolymers. *Polym. Chem.* **2014**, *5*, 2391–2400. [CrossRef]
19. Parenti, F.; Ricciardi, R.; Diana, R.; Morvillo, P.; Fontanesi, C.; Tassinari, F.; Schenetti, L.; Minarini, C.; Mucci, A. Polymers for application in organic solar cells: Bithiophene can work better than thienothiophene when coupled to benzodithiophene. *J. Polym. Sci. A Polym. Chem.* **2015**. [CrossRef]

20. Fontanesi, C.; Tassinari, F.; Parenti, F.; Cohen, H.; Mondal, P.C.; Kiran, V.; Giglia, A.; Pasquali, L.; Naaman, R. New One-Step Thiol Functionalization Procedure for Ni by Self-Assembled Monolayers. *Langmuir* **2015**, *31*, 3546–3552. [CrossRef] [PubMed]
21. Mishra, D.; Markus, T.Z.; Naaman, R.; Kettner, M.; Gohler, B.; Zacharias, H.; Friedman, N.; Sheves, M.; Fontanesi, C. Spin-dependent electron transmission through bacteriorhodopsin embedded in purple membrane. *Proc. Natl. Acad. Sci. USA* **2013**, *110*, 14872–14876. [CrossRef] [PubMed]
22. Mondal, P.C.; Kantor-Uriel, N.; Mathew, S.P.; Tassinari, F.; Fontanesi, C.; Naaman, R. Chiral Conductive Polymers as Spin Filters. *Adv. Mater.* **2015**, *27*, 1924–1927. [CrossRef] [PubMed]
23. Granovsky, A.A. Firefly Version 8.0.0. Available online: http://classic.chem.msu.su/gran/firefly/index.html (accessed on 18 January 2016).
24. Data available upon request to the corresponding author.
25. Koch, W.; Holthausen, M.C. *A Chemist's Guide to Density Functional Theory*, 2nd ed.; Wiley-VCH: New York, NY, USA, 1989.
26. Martin, R.M. *Electronic Structure: Basic Theory and Practical Methods*; Cambridge University Press: Cambridge, UK, 2004.
27. Szabo Ostlund Modern Quantum Chemistry Intro to Advanced Electronic Structure Theory 481s. Available online: http://www.scribd.com/doc/38501522/Szabo-Ostlund-Modern-Quantum-Chemistry-Intro-to-Advanced-Electronic-Structure-Theory-481s (accessed on 15 July 2013).
28. Ullrich, C.A. *Time-Dependent Density-Functional Theory: Concepts and Applications*; Oxford University Press: Oxford, UK, 2011.
29. Giuliani, G.; Vignale, G. Quantum Theory of the Electron Liquid. Available online: http://www.cambridge.org/us/academic/subjects/physics/condensed-matter-physics-nanoscience-and-mesoscopic-physics/quantum-theory-electron-liquid?format=PB (accessed on 22 December 2015).
30. Amelia, M.; Lincheneau, C.; Silvi, S.; Credi, A. Electrochemical properties of CdSe and CdTe quantum dots. *Chem. Soc. Rev.* **2012**, *41*, 5728–5743. [CrossRef] [PubMed]
31. Trasatti, S. The "absolute" electrode potential—The end of the story. *Electrochim. Acta* **1990**, *35*, 269–271. [CrossRef]
32. Strinati, G. Application of the Green's functions method to the study of the optical properties of semiconductors. *Riv. Nuovo Cim.* **2008**, *11*, 1–86. [CrossRef]

Sample Availability: Samples of the compounds are not available from the authors.

TDDFT UV/Vis spectra. A way to assess the minimum oligomer length to be considered in the calculation of the optical band gap.

Figure 14 sets out the comparison between UV/Vis spectra (solid line) recorded in chloroform bulk solution and TDDFT calculated spectra (bar graph), P1 polymer only ref [26]. This because all the other examined polyhiophenes show the same trend. Figure 14 a, b, c shows the TDDFT (bar plot of the oscillator strength) results concerning the monomer, dimer and trimer oligomers, respectively. TDDFT results are obtained at the B3LPY/6-31G(d,p) level of the theory, following full geometry optimization at the same level of the theory. All the experimental UV/Vis spectra as well as the theoretical calculations concern the neutral species. Note that the TDDFT calculated of the monomer is characterized by a prominent absorption peak found at 369.2 nm, whilst the experimental main peak is roughly centred at 434 nm.

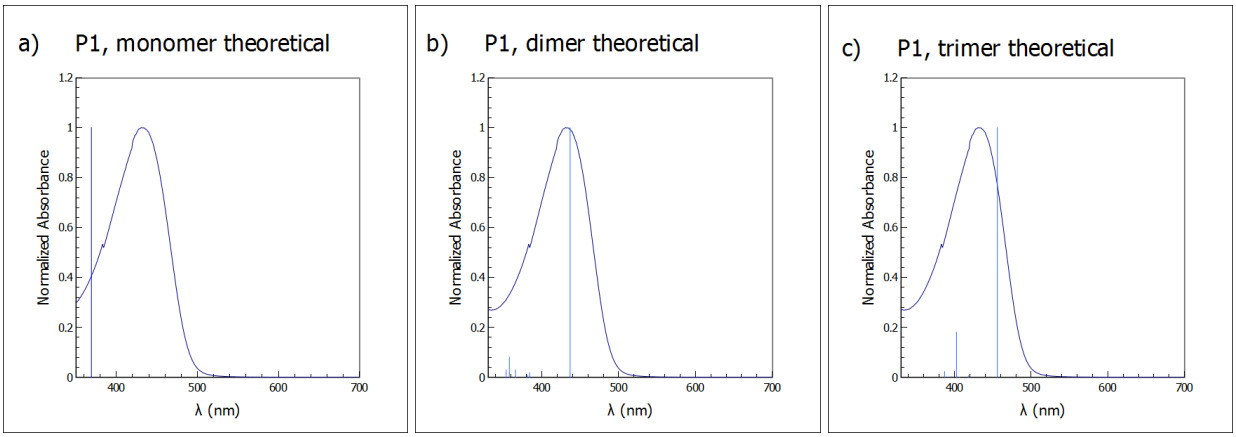

Figure 14. UV-vis spectrum for the P1 polythiophene species in chloroform. Normalized oscillator strength values, TDDFT B3LYP/6-31G(d,p) level of the theory, are represented by turquoise bars: a) monomer b) dimer c) trimer. The explicit molecular structure of P1 can be found in ref [26].

Thus, a difference of 65 nm is found, a rather poor agreement between experimental and theoretical results. A much more satisfactory behaviour is observed when the dimer (main peak found at 437 nm) and trimer (main peak found at 455 nm) species are considered, Figure 14 b and c, respectively. Notably, passing from the dimer to the trimer yields a difference of 18 nm in the theoretical TDDFT "main" peak. These results led to the assumption that theoretical quantities (with particular reference to the electronic and optical band gap, i.e. the ubiquitous used HOMO/LUMO gap) calculated for the trimer oligomer could be assumed to be "reasonably" representative of the polymer ones.

*4.2 Organic Crystals: Coronene polymorphs, Perylene/*TCNQ-F_x co-crystals

Our attention is here focused on the interplay between electronic properties and structural arrangement in the crystalline phase of two PAHs based systems: polymorphs of coronene molecular crystals and perylene/TCNQ-F_x co-crystals. The definition of co-crystal is still a matter of discussion, there is a general agreement on "solids that are crystalline single phase materials composed of two or more different molecular and/or ionic compounds generally in a stoichiometric ratio which are neither solvates nor simple salts" [99].

4.2.1 *Nat. Commun.* 7 (2016) 11555 [32]

Preamble

This work deals with the study of the electronic properties of coronene molecular crystals. In particular, the experimental part of this paper deals with the characterization of the physical properties of two coronene crystal polymorphs γ phase (natural occurring) and β phase (obtained by crystallization under application of a magnetic field). Coronene is an appealing material for possible organic electronics applications, because this organic semiconductor seems to show superconductivity at ~ 7 K upon doping with potassium [100]. In this paper the theoretical work deals with i) the rationalization of the electronic properties, in particular the electronic band diagram dispersion curves for the two polymorphs and band gap ii) shed light on the stability of the new β polymorph, i.e. the theoretical estimation of the difference in energy between the two polymorphs. Theoretical results reported in this paper are obtained by using PBE [101,102] plane waves basis-set at the DFT level of the theory, as implemented in the two different suite of programs: VASP and CASTEP [103]. Indeed, X-ray data are known for both the polymorphs, thus periodic boundary conditions can be exploited in the calculations. Full geometry cell optimization has been performed: ion positions, volume and cell shape (lattice vectors) are, in steps, fully optimized. Calculations including van der Waals dispersion energy interactions, following both the Grimme [104] and Tkatchenko-Scheffler [105,106] methods, have been performed. The theoretical results support the stability of the unforeseen new β polymorph. It is worth mentioning that a number of different possible complicating effects (results not reported in the paper) were considered too i) the influence of the magnetic field on molecular properties (in terms of "simple" magnetic moment interaction energies, due to induced magnetic moments - ring currents) was thoroughly analysed, but without reaching any positive outcome ii) calculation of phonon dispersion curves. Please note that some topics tackled in this paper, and not fully developed, are just dawning in science: the interaction between magnetic fields and matter is involved in spintronics applications, as well as in the electron spin control within condensed matter.

The candidate contribution concerned the critical assessment of the crystal structure stability of the γ phase and β phase polymorphs of coronene. The calculations were carried out by using plane wave and localized orbitals (not reported in ref [32]) methods, with the critical use of dispersion energy corrections.

Statement of Authorship

<table>
<tr><td colspan="5">This declaration concerns the article entitled:

An unforeseen polymorph of coronene by the application of magnetic fields during crystal growth</td></tr>
<tr><td colspan="5">Publication status (tick one)</td></tr>
<tr><td>draft manuscript</td><td>Submitted</td><td>In review</td><td>Accepted</td><td>Published X</td></tr>
<tr><td colspan="5">Publication details (reference): Nat. Commun. 7 (2016) 11555</td></tr>
<tr><td colspan="2">Candidate’s contribution to the paper (detailed, and also given as a percentage).</td><td colspan="3">The candidate contributed to the theoretical interpretation and actual calculations (vide supra).

Formulation of ideas: 40 %

Design of methodology: 50 %

Experimental work: 0 %

Presentation of data in journal format: 25 %</td></tr>
<tr><td colspan="2">Statement from Candidate</td><td colspan="3">This paper reports on original research I conducted during the period of my Higher Degree by Research candidature.</td></tr>
<tr><td colspan="2">Signed  </td><td colspan="3">Date 15 May 2017</td></tr>
</table>

Title:	An unforeseen polymorph of coronene by the application of magnetic fields during crystal growth
Author:	Jason Potticary, Lui R. Terry, Christopher Bell, Alexandros N. Papanikolopoulos, Peter C. M. Christianen et al.
Publication:	Nature Communications
Publisher:	Nature Publishing Group
Date:	May 10, 2016

Author Use

Authors of NPG articles do not require permission to use content from their article in most cases as stated in the author's guidelines.

Authors wishing to use their article for commercial purposes must request permission in the normal way.

For further questions, please contact NPG's permissions department: permissions@nature.com

BACK CLOSE WINDOW

Publication title:
An unforeseen polymorph of coronene by the application of magnetic fields during crystal growth

the thesis page numbers that it spans:
91 to 106

nature COMMUNICATIONS

ARTICLE

Received 1 Dec 2015 | Accepted 7 Apr 2016 | Published 10 May 2016

DOI: 10.1038/ncomms11555 OPEN

An unforeseen polymorph of coronene by the application of magnetic fields during crystal growth

Jason Potticary[1], Lui R. Terry[1], Christopher Bell[2], Alexandros N. Papanikolopoulos[3], Peter C.M. Christianen[3], Hans Engelkamp[3], Andrew M. Collins[4], Claudio Fontanesi[5,6], Gabriele Kociok-Köhn[7], Simon Crampin[5], Enrico Da Como[5] & Simon R. Hall[1]

The continued development of novel drugs, proteins, and advanced materials strongly rely on our ability to self-assemble molecules in solids with the most suitable structure (polymorph) in order to exhibit desired functionalities. The search for new polymorphs remains a scientific challenge, that is at the core of crystal engineering and there has been a lack of effective solutions to this problem. Here we show that by crystallizing the polyaromatic hydrocarbon coronene in the presence of a magnetic field, a polymorph is formed in a β-herringbone structure instead of the ubiquitous γ-herringbone structure, with a decrease of 35° in the herringbone nearest neighbour angle. The β-herringbone polymorph is stable, preserves its structure under ambient conditions and as a result of the altered molecular packing of the crystals, exhibits significant changes to the optical and mechanical properties of the crystal.

[1] Complex Functional Materials Group, School of Chemistry, University of Bristol, Bristol BS8 1TS, UK. [2] School of Physics, HH Wills Physics Laboratory, Tyndall Avenue, Bristol BS8 1TL, UK. [3] High Field Magnet Laboratory (HFML-EMFL), Radboud University, Toernooiveld 7, 6525 ED Nijmegen, The Netherlands. [4] Bristol Centre for Functional Nanomaterials, HH Wills Physics Laboratory, Tyndall Avenue, Bristol BS8 1TL, UK. [5] Department of Physics, University of Bath, Claverton Down, Bath BA2 7AY, UK. [6] Dipartimento di Ingegneria Enzo Ferrari, Universita' di Modena e Reggio Emilia, Via Vivarelli 10, 41125 Modena, Italy. [7] Department of Chemistry, University of Bath, Claverton Down, Bath BA2 7AY, UK. Correspondence and requests for materials should be addressed to S.R.H. (email: simon.hall@bristol.ac.uk).

The ability to discover new phenomena and properties in materials depends on our ability to synthesize new structures. The discovery of new structures, however, should rely on variables that transcend the typical thermodynamic parameters of temperature and pressure. In the field of functional molecular materials, polymorphism, the presence of different crystal structures of the same molecular system, can be an opportunity to discover novel phenomena[1] and tune properties[2]. For example, charge carrier mobility in organic semiconductors can be increased by crystallizing molecules under pressure, resulting in shorter intermolecular distances favourable for transport[3]. One successful tool at the scientist's disposal to control crystal structure has been to perform crystallization in the presence of electric fields. This is a well-known process and is used extensively to prepare nonlinear optical materials through electric poling. Crystal growth in the presence of an external magnetic field is much less explored, although it has been proven to be efficacious in the melt texturing of alloys[4] or in cases where controlled convection of the crystallizing solution is required, for example, in the growth of high-quality protein crystals[5], chiral aggregates[6] or in the alignment of liquid crystal and block copolymer arrays[7,8]. A magnetic field has even been demonstrated to be able to separate polymorphs of crystals post-synthetically[9] and in one case to preferentially nucleate a monoclinic form of terpyridine[10]. Although it is known that magnetic forces can have an effect on solidification and subsequent physical behaviour in crystals, their use to create previously unknown polymorphs in single crystals has never been reported.

Polyaromatic hydrocarbons (PAHs) are commonly researched molecules due to their rigid planar structure, high stabilities and characteristic optical and electronic behaviour[10,11]. As molecular solids, PAHs crystallize in four basic structure types according to well-defined geometric and energetic considerations[12]. These are the herringbone structure, the gamma-herringbone (γ-) structure, the sandwich-herringbone (SHB) structure and the beta-herringbone (β-) structure (Supplementary Fig. 1). Comprehensive studies of PAHs have shown that the adoption of one of the four structure types depends ultimately on the relative strength of nonbonded C···C and C···H interactions[12–14]. Polymorphism in PAHs has been demonstrated previously by growing thin films on substrates, where variations in processing conditions direct the formation of different polymorphs[15,16], although in single crystals at ambient pressure, polymorphism in PAHs is rare with perylene and pyrene being two notable cases exhibiting both herringbone and SHB polymorphs[17]. In terms of applications, single crystals of PAHs are to be desired, however, as they have distinct physical advantages over thin-film versions of the same material. Most importantly, for conductive applications such as transistors, or optical applications in solar cells, single crystals typically have higher carrier mobilities than their thin-film analogues[18,19], which have to be defect free to achieve mobilities of the same order of magnitude.

Here we show that by crystallizing the PAH coronene in the presence of a magnetic field, it can be made to form as a new β-herringbone polymorph instead of the ubiquitous γ-herringbone form, with a change as large as 35° to the herringbone nearest neighbour angle. The β polymorph is stable and can preserve its structure in ambient conditions and zero magnetic field. Dispersion corrected density functional theory (DFT-D) calculations indicate that the new form is energetically favoured at low temperature. Furthermore, we demonstrate how the new supramolecular structure generates remarkable changes of the electronic, optical and mechanical properties in the crystal.

Results

Crystal growth of a new polymorph. Coronene is a PAH composed of six aromatic rings arranged in a planar discoidal geometry (Supplementary Fig. 2). The high molecular symmetry (D_{6h}) and 24 electron π-system has made coronene an ideal model system for the study of graphene, due to it being large enough to display exotic electronic behaviour, but not so large that contortion becomes a complicating factor[20]. Centimetre-long crystals of coronene (typically ∼0.75 cm) were grown from a supersaturated solution of the molecules in toluene cooled slowly (0.04 K min^{-1}) from 328 K to 298 K over a period of 12 h (Fig. 1a, yellow crystal labelled 'γ'). The very slow cooling rate was chosen to eliminate changes in solution shearing which have been shown to influence nucleation and growth with concomitant changes to the resultant crystal structure[21]. Single crystal X-ray diffraction (XRD) of these crystals indicated that the structure is the conventional γ-polymorph; $a = 10.02$ Å, $b = 4.67$ Å, $c = 15.60$ Å, $\beta = 106.7°$, $Z = 2$, space group $P2_1/n$, with an inter-planar distance (d_π) of 3.43 Å, which is consistent with parallel π-stacking[12] (Fig. 2a,b,e,g).

In the presence of an external magnetic field of 1 Tesla, however, significantly longer (typically ∼2.5 cm) coronene crystals were grown from the same supersaturated solution and exhibit a different colour to normal γ-coronene crystals (Fig. 1a orange crystal labelled 'β'). Single crystal XRD indicates that the unit cell of these crystals are consistent with a new β-coronene structure; $a = 10.39$ Å, $b = 3.84$ Å, $c = 17.23$ Å, $\beta = 96.24°$, $Z = 2$, space group $P2_1/n$ and an inter-planar distance (d_π) of 3.48 Å (Fig. 2c,d,f,h). As a previously unreported polymorph of coronene, the crystallographic data has been lodged with the Cambridge Crystallographic Data Centre (deposition number CCDC 1409823).

By comparing the two crystal forms in Fig. 2c, it can be seen that the short axis, *b*, is substantially decreased in length for the β-coronene crystallized in the magnetic field when compared with the γ-coronene. This new polymorph also has a significantly smaller nearest neighbour herringbone angle of 49.71° compared with 95.86° in γ-coronene. The identification of the new crystal polymorph as a β-structure can be made by reference to a plot of the inter-planar angle of nearest neighbour molecules versus the unit cell short axis[12] (Fig. 3). From this, it can be seen that the new polymorph sits squarely with other PAHs identified as

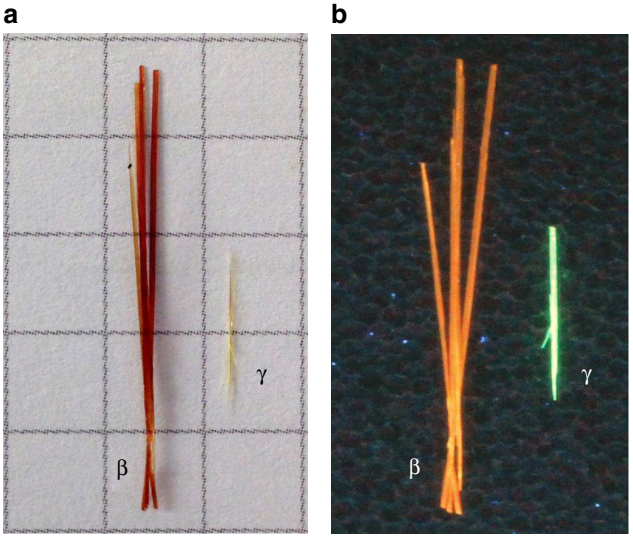

Figure 1 | Optical images of the β- and γ- polymorphs of coronene. (**a**) in daylight and (**b**) under ultraviolet ($\lambda = 365$ nm) illumination to show fluorescence. The squares on the grid in **a** are 0.5 × 0.5 cm^2.

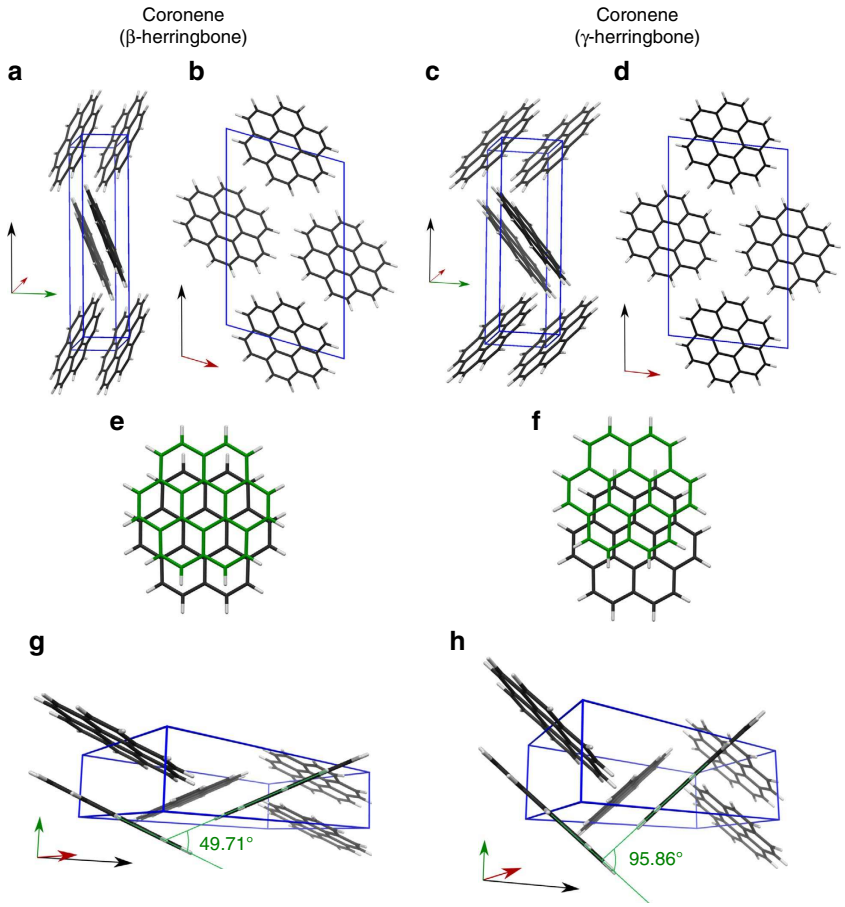

Figure 2 | Representation of the β- and γ- polymorphs of coronene. Differing perspectives of both unit cells (blue boxes) viewed slightly offset from along the *a*-axis (**a** and **c**) and along the *b*-axis (**b** and **d**). The relative shift of the molecules along the stacks are shown for β- (**e**) and γ- (**f**). (**g**) and (**h**) show an orientation of the unit cell clearly demonstrating the difference in nearest neighbour angle between the two polymorphs. Red green and black arrows indicate the direction of the *a*-, *b*- and *c*-axis respectively.

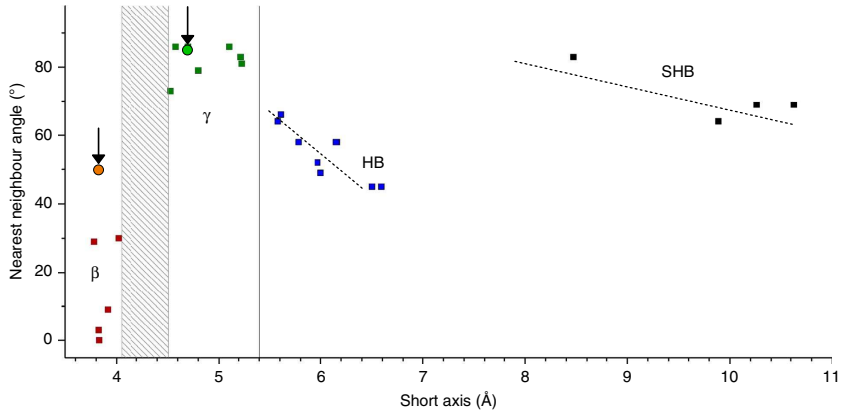

Figure 3 | Grouping of PAHs into structure types. Plotted on the graph are PAHs that adopt the herringbone structure (blue squares), the gamma-herringbone (γ-) structure (green squares), the SHB structure (black squares) and the beta-herringbone (β-) structure (red squares), according to the crystallographic short axis and nearest neighbour herringbone angle. The positions of both γ- and β-coronene polymorphs are indicated by circles and marked with arrows. Adapted from Desiraju and Gavezzotti[12], in which the names of the crystals corresponding to all of the marked squares can be found. Reproduced with permission of the International Union of Crystallography, http://journals.iucr.org/.

having the β-herringbone structure. Under an applied magnetic field of 1 T, the new β-coronene polymorph grows exclusively, is reproducible (>10 times to-date), stable under ambient conditions and also forms in the non-aromatic solvent hexane.

To determine the mechanism of crystal growth, we followed the inception of crystallization of coronene at 1 T and 0 T via *in situ* UV–vis spectrometry. At 358 nm, there are no peaks due to molecules of coronene in solution, nor in the solid state (as crystals). However, a peak will be observed due to the formation of nucleation clusters, which we determined via a single-point energy calculation using time-dependent self-consistent field density functional theory, using basis set

6-31G(D). Supplementary Figure 3 shows that there is a stark difference between the growth of coronene crystals under 1 T of applied field and at 0 T. At 1 T, there is suppression of nucleation which results in the crystallization of the least stable polymorph, that is, beta-coronene. This is entirely consistent with previously published work on the formation of meta-stable polymorphs and is epitomized in Ostwald's rules of stages[22]. Our experimental data therefore demonstrates that the magnetic field is achieving the effect of polymorphic control through suppression of nucleation.

As to the question of why an applied magnetic field of 1 T is having this effect in coronene and not in other molecules at this field strength, it is likely to be intimately linked to the magnetic susceptibility of the molecule. Based on inductively coupled plasma atomic absorption spectroscopy, we note that the level of magnetically active impurities such as cobalt, iron and nickel are at the parts per billion level ($Co = 0.138 \pm 0.98$ ppb; $Fe = 33.81 \pm 0.56$ ppb; and $Ni = 13.46 \pm 0.65$ ppb), and so are unlikely to play any role in polymorph selection. Instead we note that coronene has a very high diamagnetic susceptibility (χ) of -243×10^{-6} emu mol^{-1} (refs 23,24). Crystal growth performed at weaker field strengths of 0.2, 0.5 and 0.8 T resulted in crystals of the $\gamma-$polymorph (Supplementary Fig. 4), suggesting that 1 T is close to a threshold for energetic selection between the two forms. In the case of other PAHs such as pyrene, which do not have such a strong diamagnetic susceptibility, our attempts to control polymorphism at 1 T were unsuccessful. It would appear that for molecules with lower diamagnetic susceptibilities, higher fields would be required. Indeed, work reported in a thesis in 2013 has shown that a simple organic dye molecule with a lower diamagnetic susceptibility than coronene, namely an isoxazolone derivative, can be crystallized in a different known polymorph at fields >2.5 T (ref. 25).

Optical behaviour. Figure 1b shows optical images of the two different polymorphs taken under UV irradiation ($\lambda = 365$ nm). The remarkably different colours of the fluorescence of γ-coronene and β-coronene crystals is further confirmation that the molecular packing in the crystal has been transformed, leading to altered electronic behaviour. To quantify this, we measured the absorption spectrum of two single crystals of the two polymorphs by shining unpolarized light perpendicular to the *a*–*b* plane of the crystals, that is, light propagation parallel to [001]. As shown in Fig. 4a (green plot), the γ-coronene single crystal is characterized by a first absorption resonance at 468 nm assigned to the free exciton in coronene, in agreement with previous studies[26]. The β-coronene spectrum is by stark contrast almost featureless, with an absorption onset at 780 nm and a maximum at ~500 nm (Fig. 4a, orange plot). This is a remarkable change in the optical properties of this material. These data can be plotted as the extinction molar coefficient

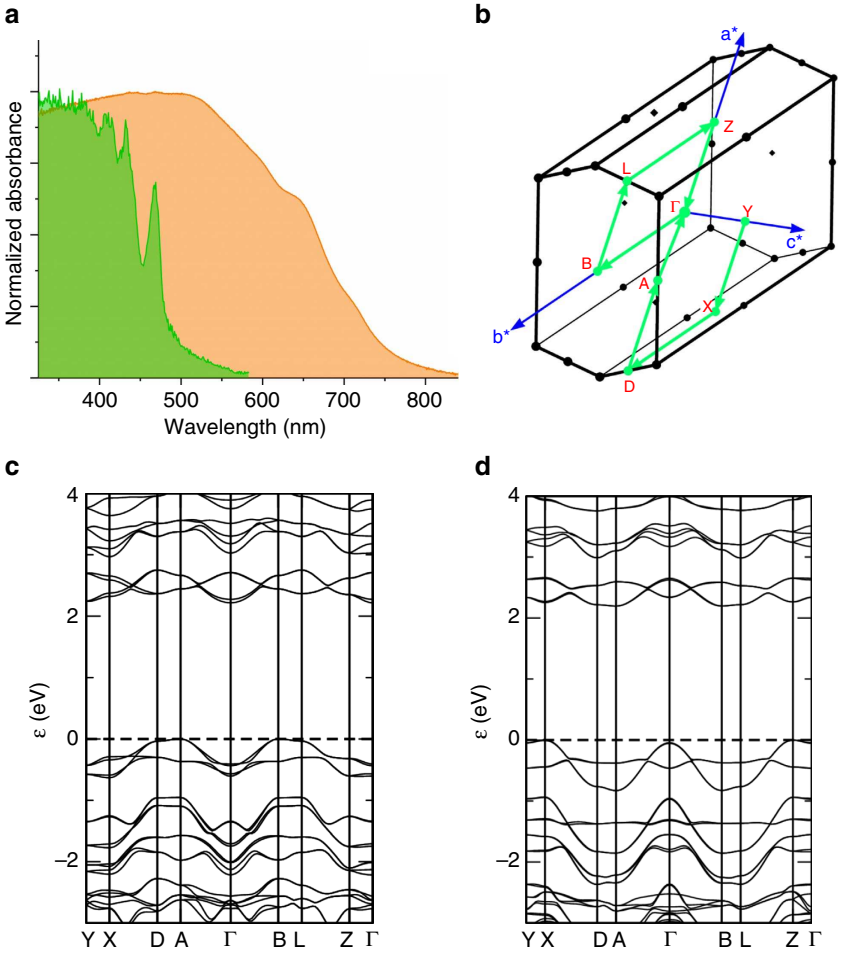

Figure 4 | Electronic structure of γ- and β-coronene. (**a**) Absorption spectra of γ-coronene (green) and β-coronene (orange) single crystals. Unpolarized light was irradiated perpendicular to the *a*–*b* plane at room temperature; (**b**) Brillouin zone with reciprocal lattice vectors and high symmetry points; (**c**) and (**d**) band dispersion along high symmetry points in γ- and β-coronene, respectively.

versus wavelength, to decouple any effects due to differences in the thickness of the crystals of the two polymorphs (50 microns and 76 microns for γ-coronene and β-coronene, respectively; Supplementary Fig. 5). From these spectra, it can be seen clearly that β-coronene is a more strongly absorbing polymorph than γ-coronene. Organic materials tend to be sensitive to a particular range of wavelengths, which can be seen in the features of the γ-coronene absorption spectrum and the lack of absorption of wavelengths >583 nm. In β-coronene, however, the crystal strongly absorbs over a wide band of radiation, from the UV into the near-IR (320–847 nm).

DFT-D calculations correctly describe the existence of the new stable polymorph and indicate that no appreciable difference in the indirect bandgap (Fig. 4b–d) exists between the two polymorphs, suggesting that the large shift in the light absorption onset is instead related to a change in the fundamental photoexcitations in the two structures[27,28]. In β-coronene it is difficult to identify sharp resonances from Frenkel excitons as observed for the γ-polymorph. Instead, the structureless absorption band of the $\beta-$polymorph originates from charge transfer excitons that are favoured by the larger overlap between the molecular π orbitals. Moreover, the transition dipole moment of a charge transfer exciton is likely to be oriented parallel to the *a*–*b* plane, which would ensure optimal coupling with the electromagnetic radiation in our experiment.

Structural stability. The new β-polymorph structure is notable for the large change in the herringbone angle. We can gain insights into the relative stability of the β-coronene structure when compared with the γ-polymorph, by consideration of these changes in the CH$\cdots\pi$ hydrogen bonding motif. It is known that the stronger the hydrogen bond, the stronger the trend for linearity[29,30] depending on the strength of the proton donor. From XRD, we can see that the CH$\cdots\pi$ angle in γ-coronene of 95.86° suggests a strong, almost linear CH$\cdots\pi$ hydrogen bond, whereas in β-coronene, this angle becomes 49.71° (viz. Fig. 2). This change in angle would suggest a weakening of the hydrogen bonding in β-coronene, which is concomitant with the change in estimated CH$\cdots\pi$ hydrogen bond length[31] that increases from 2.5 Å in the γ-polymorph to 3.0 Å in the β-polymorph. This weakening of the CH$\cdots\pi$ hydrogen bonding should therefore manifest itself as a diminution of the physicomechanical properties of β-coronene. To confirm this, we have determined the melting point (T_M) and elastic modulus (E—the modal value measured on the $(\bar{1}0\underline{11}$ and $10\overline{\underline{11}}$ crystal faces) of both polymorphs and find that in γ-coronene, $T_M = 436.14 \pm 0.01$ °C and $E = 227$ GPa, whereas for β-coronene $T_M = 435.48 \pm 0.01$ °C and $E = 92$ GPa (Supplementary Figs 6 and 7). These data suggest weaker intermolecular forces in β-coronene at room temperature.

DFT-D calculations show that β-coronene is actually the more stable of the two polymorphs at 0 K, by 3.8 kJ mol^{-1} based on lattice energy differences (Supplementary Table 1). Confirmation that this is the case comes from powder XRD of polycrystalline γ-coronene recorded through a temperature cycle from room temperature to 12 K. On cooling through a temperature of 150 K, three new peaks emerge which cannot be indexed to the $\gamma-$polymorph (JCPDS card number 12-1611; Supplementary Fig. 8). These emergent peaks correspond to the (002), (101) and (112; $2\theta = 10.55°$, 10.67° and 27.72° respectively) reflections of the new polymorph, β-coronene. Thus β- and γ-coronene are enantiotropic polymorphs, with a critical temperature between 100 K and 150 K (Fig. 5). In general, in an enantiotropic pair of polymorphs, the more intrinsically stable member will have the greater specific enthalpy of fusion. As the differential scanning calorimetry (DSC) experiment to determine melting point (Supplementary Fig. 6) is conducted at far higher temperatures than 150 K, it is the γ-coronene polymorph which will be the more stable at these temperatures and therefore be expected to have the greater specific enthalpy of fusion. From Supplementary Fig. 5, we can calculate the values for the heat of fusion for each of the polymorphs as 20.78 kJ mol^{-1} and 25.26 kJ mol^{-1} for β- and γ-coronene, respectively, confirming that these are enantiotropic polymorphs.

In summary, through judicious application of a magnetic field, we have demonstrated that a well-studied PAH can be grown as a new polymorph and confirmed that a range of physical properties have been significantly altered. The optical properties of the β-coronene crystal have been transformed to such an extent that it absorbs panchromatically from the UV into the near-IR. This new single crystal may therefore be of great interest in organic optoelectronics and photovoltaics.

Methods

Coronene. Coronene crystals (Sigma Aldrich, purity 97%) were recrystallized from toluene and purity assayed by nuclear magnetic resonance (C^{13} and H^+). Trace metals were tested for using inductively coupled plasma—atomic emission spectroscopy (Agilent 710 ICP-AES) after digestion in 3% nitric acid (Sigma Aldrich, ≥99.999%, trace metal basis). Structural analysis was conducted by optical microscopy and single crystal XRD. Analysis of the single crystal data of non-magnetic field grown crystals suggests favourable growth along the *b*-axis, which form the characteristic needle shaped crystals.

Crystal growth under 1 T of magnetic field. A supersaturated solution of coronene (2.5 mg ml^{-1}) in toluene was prepared and stored in an oven at 93 °C. The solution was then passed through a 0.22-μm PTFE filter directly into a 5-mm quartz cuvette with a stopper. Once sealed, the cuvette was placed in the magnetic cavity (Supplementary Fig. 9) and the whole system maintained at 93 °C for 4 h post cuvette insertion. The oven was then programmed to cool to 83, 73 and 63 °C then finally 50 °C, with a 24-h dwell at each temperature, before cooling to room temperature. Crystals of β-coronene are the sole polymorph to grow under the magnetic field and to-date the experiment has been repeated >10 times.

Single crystal X-ray crystallography. Intensity data for all coronene structures were collected at different temperatures on an Agilent SuperNova-E Dual diffractometer equipped with an Oxford Cryosystem, using CuKα radiation ($\lambda = 1.5418$ Å). Data were processed using the CrysAlisPro software (CrysAlisPro, Agilent Technologies, Version 1.171.37.35 (release 13-08-2014 CrysAlis171 .NET; compiled on 13 Aug 2014). For all structures a symmetry-related (multi-scan) absorption correction was applied. Crystal parameters are provided in Supplementary Table 2. See also Supplementary Data 1 and 2. Structure solution, followed by full-matrix least squares refinement was performed using the WINGX-v2014.1 suite of programs throughout.

Physical characterization. Optical absorption spectra were recorded with a ultraviolet–visible–near infrared spectrometer Agilent Cary 5000 measuring in transmission configuration. The spectrometer can measure absorbance up an optical density of 10. Single crystals of β- or γ-coronene were suspended in the sample beam path. Unpolarized light was shone perpendicular to the *a*–*b* plane of the unit cells. High-quality crystals with flat surfaces were carefully selected to avoid light scattering effects. The beam size was narrowed to half the lateral size of crystals. All absorption spectra were recorded at room temperature in air. Elastic moduli were determined using an Asylum Research MFP-3D Infinity AFM operating in AMFM viscoelastic imaging mode, using an AC160TS-R3 silicon tip (9 ± 2 nm radius). Freshly cleaved mica was used as a calibration standard (measured at 178 GPa). Melting point determination was done using a TA-Instruments Q100 DSC with temperature ramp of 1 °C min^{-1} between 35 and 460 °C with 2.2 mg of coronene hermetically sealed under a nitrogen atmosphere in an aluminium pan.

Computational calculations. Computational calculations have been performed with density functional codes CASTEP (ref. 32) and VASP (ref. 33), using the Perdew–Burke–Enzerhof exchange correlation functional with semi-empirical dispersion corrections (DFT-D) to account for van der Waals interactions. CASTEP calculations (version 7.03) used in-built ultra-soft pseudopotentials for C and H atoms, a plane wave cutoff of 600 eV, and Monkhorst-Pack[34] k-point samplings of $3 \times 4 \times 2$. Cell parameters and atomic coordinates were fully relaxed using the Broyden–Fletcher–Goldfarb–Shanno (BFGS) method, halting when residual forces fell below 1 meV Å^{-1}. Changing the cutoff energy from 450 to 600 eV caused structural parameters to change by <0.001 nm or $<0.01°$. Increasing k-point sampling to $6 \times 8 \times 4$ changed energies by <1 meV. Robustness

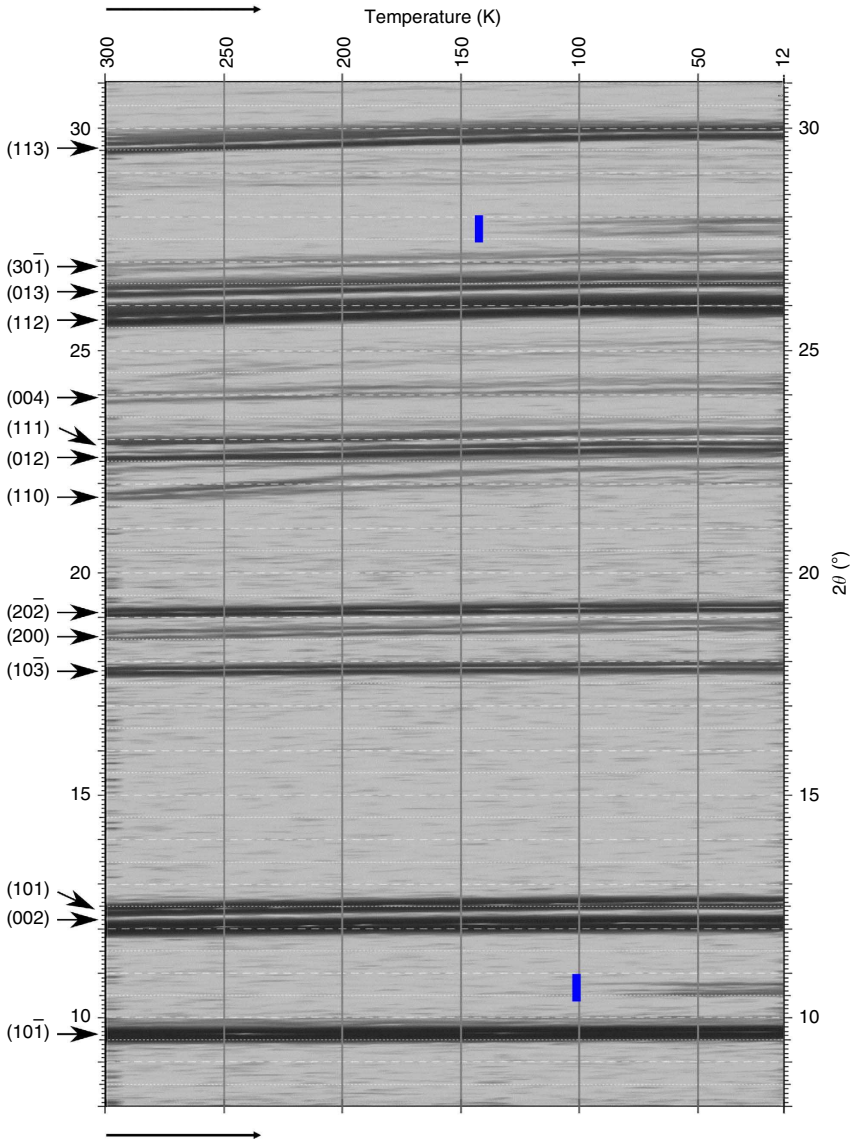

Figure 5 | 2D map of XRD peak shifts as a function of temperature in γ-coronene. Temperature is decreased from 300 to 12 K (left to right). Blue markers indicate the emergence of the new peaks due to β-coronene formation. The blue line near 10° 2θ encompasses two emergent peaks.

of results to choice of semi-empirical dispersion correction was assessed through the use[35] of using the Grimme scheme[36] with both default vdW radii ($R_H = 1.001$, $R_C = 1.452$) and experimental ($R_H = 1.090$, $R_C = 1.750$), as previously employed by Fedorov *et al.*[37] for γ-coronene. VASP calculations (version 5.3.3) use PAW potentials[38] with 500 eV energy cutoff, $3 \times 4 \times 2$ k-point sampling and the Tkatchenko-Scheffler[39,40] dispersion correction. Geometry optimization was performed starting from experimental cell parameters and atom coordinates, aboth with and without symmetry constraint. Stability of optimized geometries was verified by re-optimizing after randomly displacing atoms by 0.05 Å in *x*, *y* and *z*.

Data Availability. Original optical images and raw data from XRD, AFM and DFT-D calculations pertaining to all materials in this manuscript have been placed in the University of Bristol Research Data Repository (https://data.bris.ac.uk/):
Windows path: \\rdsfcifs.acrc.bris.ac.uk\Polymorphism_in_coronene
Linux path: smb://rdsfcifs.acrc.bris.ac.uk/Polymorphism_in_coronene
Mac OSX path: smb://rdsfcifs.acrc.bris.ac.uk/Polymorphism_in_coronene.

References

1. Ganin, A. Y. *et al.* Polymorphism control of superconductivity and magnetism in Cs_3C_{60} close to the Mott transition. *Nature* **466,** 221–225 (2010).
2. Bernstein, J. *Polymorphism in Molecular Crystals* (Oxford University Press, 2002).
3. Giri, G. *et al.* Tuning charge transport in solution-sheared organic semiconductors using lattice strain. *Nature* **480,** 504–508 (2011).
4. Beaugnon, E. *et al.* Material processing in high static magnetic field. A review of an experimental study on levitation, phase separation, convection and texturation. *J. Phys. I France* **3,** 399–421 (1993).
5. Nakamura, A. *et al.* Improvement in quality of protein crystals grown in a high magnetic field gradient. *Cryst. Growth Des.* **12,** 1141–1150 (2012).
6. Micali, N. *et al.* Selection of supramolecular chirality by application of rotational and magnetic forces. *Nat. Chem.* **4,** 201–207 (2012).
7. Boamfa, M. I., Lazarenko, S. V., Vermolen, E. C. M., Kirilyuk, A. & Rasing, T. Magnetic field alignment of liquid crystals for fast display applications. *Adv. Mater.* **17,** 610–614 (2005).
8. Gopinadhan, M. *et al.* Thermally switchable aligned nanopores by magnetic-field directed self-assembly of block copolymers. *Adv. Mater.* **26,** 5148–5154 (2014).
9. Atkinson, M. B. J. *et al.* Using magnetic levitation to separate mixtures of crystal polymorphs. *Angew. Chem. Int. Ed.* **52,** 10208–10211 (2013).
10. Honjo, S., Yokota, M., Doki, N. & Shimizu, K. Magnetic field influence on the crystal structure of 2,2':6',2"-terpyridine. *Kagaku Kogaku Ronbun.* **34,** 383–387 (2008).
11. Rieger, R. & Müllen, K. Forever young: polycyclic aromatic hydrocarbons as model cases for structural and optical studies. *J. Phys. Org. Chem.* **23,** 315–325 (2010).
12. Desiraju, G. R. & Gavezzotti, A. Crystal structures of polynuclear aromatic hydrocarbons. Classification, rationalization and prediction from molecular structure. *Acta Crystallogr. Sect. B Struct. Sci.* **45,** 473–482 (1989).
13. Loots, L. & Barbour, L. J. A simple and robust method for the identification of π–π packing motifs of aromatic compounds. *CrystEngComm* **14,** 300–304 (2014).

14. Schatschneider, B., Phelps, J. & Jezowski, S. A new parameter for classification of polycyclic aromatic hydrocarbon crystalline motifs: a Hirshfeld surface investigation. *CrystEngComm* **11,** 7216–7223 (2011).
15. Mattheus, C. C. *et al.* Identification of polymorphs of pentacene. *Synth. Metals* **138,** 475–481 (2003).
16. Hiszpanski, A. M. *et al.* Tuning polymorphism and orientation in organic semiconductor thin films via post-deposition processing. *J. Am. Chem. Soc.* **136,** 15749–15756 (2014).
17. Botoshansky, M., Herbstein, R. H. & Kapon, M. Towards a complete description of a polymorphic crystal: the example of perylene redetermination of the structures of the (Z = 2 and 4) polymorphs. *Helv. Chim. Acta* **86,** 1113–1128 (2003).
18. Hu, W.-S., Weng, S.-Z., Tao, Y.-T., Liu, H.-J. & Lee, H.-Y. Oriented growth of rubrene thin films on aligned pentacene buffer layer and its anisotropic thin-film transistor characteristics. *Org. Electron.* **9,** 385–395 (2008).
19. Hamaguchi, A. *et al.* Single-crystal-like organic thin-film transistors fabricated from dinaphtho[2,3- b :2′,3′- f]thieno[3,2- b]thiophene (DNTT) precursor–polystyrene blends. *Adv. Mater.* **27,** 6606–6611 (2015).
20. Zhao, Y. & Truhlar, D. A prototype for graphene material simulation: structures and interaction potentials of coronene dimers. *J. Phys. Chem. C* **112,** 4061–4067 (2008).
21. Giri, G. *et al.* Effect of solution shearing method on packing and disorder of organic semiconductor polymers. *Chem. Mater.* **27,** 2350–2359 (2015).
22. Ostwald, W. Studien über die bildung und umwandlung fester körper. *Z. Phys. Chem.* **22,** 289–330 (1897).
23. Steiner, E., Fowler, P. W. & Jenneskens, L. W. Counter-rotating ring currents in coronene and corannulene. *Angew. Chem. Int. Ed.* **40,** 362–366 (2001).
24. Rogers, F. M. T. The magnetic anisotropy of coronene, naphthazarin, and other crystals. *J. Am. Chem. Soc.* **69,** 1506–1508 (1947).
25. Aret, E. Growth of Organic Dye Crystals, PhD Thesis, University of Radboud, Nijmegen. http://repository.ubn.ru.nl/handle/2066/112754 (2013).
26. Yamamoto, T. *et al.* Exciton-phonon coupling and pressure-induced structural phase changes in coronene crystals. *Chem. Phys.* **184,** 247–254 (1994).
27. Hummer, K., Puschnig, P. & Ambrosch-Draxl, C. Lowest optical excitations in molecular crystals: bound excitons versus free electron-hole pairs in anthracene. *Phys. Rev. Lett.* **92,** 147402 (2004).
28. Cudazzo, P., Sottile, F., Rubio, A. & Gatti, M. Exciton dispersion in molecular solids. *J. Phys.-Condes. Matter* **27,** 113204 (2015).
29. Nishio, M., Umezawa, Y., Suezawa, H. & Tsuboyama, S. in *The Importance of Pi-Interactions in Crystal Engineering: Frontiers in Crystal Engineering* 2nd edn (eds Tiekink, E. R. T. & Zukerman-Schpector, J.) 1-39 (Wiley (2012).
30. Steiner, T. & Desiraju, G. R. Distinction between the weak hydrogen bond and the van der Waals interaction. *Chem. Comm.* **8,** 891–892 (1998).
31. Allen, F. H. A systematic pairwise comparison of geometric parameters obtained by X-ray and neutron diffraction. *Acta Crystallogr. B* **42,** 515–522 (1986).
32. Clark, S. *et al.* First principles methods using CASTEP. *Z. Kristallogr.* **220,** 567 (2005).
33. Kresse, G. & Furthmüller, J. Efficient iterative schemes for ab initio total-energy calculations using a plane-wave basis set. *Phys. Rev. B.* **54,** 11169 (1996).
34. Monkhorst, H. J. & Pack, J. D. Special points for Brillouin-zone integrations. *Phys. Rev. B* **13,** 5188 (1976).
35. McNellis, E. R., Meyer, J. & Reuter, K. Azobenzene at coinage metal surfaces: role of dispersive van der Waals interactions. *Phys. Rev. B.* **80,** 205414 (2009).
36. Grimme, S. Semi-empirical GGA-type density functional constructed with a long-range dispersion correction. *J. Comput. Chem.* **27,** 1787 (2006).
37. Fedorov, I., Zhuravlev, Y. & Berveno, V. Properties of crystalline coronene: dispersion forces leading to a larger van der Waals radius for carbon. *Phys. Status Solidi B* **249,** 1438–1444 (2012).
38. Blöchl, P. E. Projector augmented-wave method. *Phys. Rev. B.* **50,** 17953 (1994).
39. Tkatchenko, A. & Scheffler, M. Accurate molecular Van der waals interactions from ground-state electron density and free-atom reference data. *Phys. Rev. Lett.* **102,** 073005 (2009).
40. Bučko, T., Lebègue, S., Hafner, J. & Ángyán, J. G. Tkatchenko-Scheffler van der Waals correction method with and without self-consistent screening applied to solids. *Phys. Rev. B.* **87,** 064110 (2013).

Acknowledgements

S.R.H. and J.P. acknowledge the Engineering and Physical Sciences Research Council (EPSRC), UK (grant EP/G036780/1) and the Bristol Centre for Functional Nanomaterials for project funding. The work at Nijmegen was performed as part of the research programme of the 'Stichting voor Fundamenteel Onderzoek der Materie (FOM)', which is financially supported by the 'Nederlandse Organisatie voor Wetenschappelijk Onderzoek (NWO)'. In addition, S.R.H. and J.P. thank Stasja Stanišić for discussions on low-temperature X-ray crystallography and Spartacus Mills for estimations of magnitude. E.D.C. and S.R.H. are grateful to the GW4 for funding through an accelerator grant and L.R.T. is supported in part by a grant from the USAF European Office of Aerospace Research and Development (FA8655-12-1-2078). All authors thank Prof. John Evans and Liana Vella-Zarb of the University of Durham for low-temperature powder XRD, and Dr Chung Choi and Dr George Whittell of the University of Bristol for ICP-AES and DSC, respectively.

Author contributions

S.R.H. initiated and supervised the project. J.P. performed the crystallization experiments at Bristol and characterized the samples optically and with C.B. undertook magnetic characterizations. J.P., A.N.P., P.C.M.C and H.E. performed the crystallization experiments at Nijmegen and undertook ultraviolet–visible characterizations. L.R.T. performed DSC experiments, E.D.C. and C.F. absorbance spectra experiments, G.K.K. single crystal X-ray characterization. S.C and C.F. undertook DFT-D calculations. A.M.C. performed elastic moduli experiments. All authors contributed to the discussion of the results, analysis of the structures and to manuscript preparation.

Additional information

Accession codes: The X-ray crystallographic coordinates for structures reported in this Article have been deposited at the Cambridge Crystallographic Data Centre (CCDC), under deposition number CCDC 1409823. These data can be obtained free of charge from The Cambridge Crystallographic Data Centre via www.ccdc.cam.ac.uk/data_request/cif.

Supplementary Information accompanies this paper at http://www.nature.com/naturecommunications

Competing financial interests: The authors declare no competing financial interests.

Reprints and permission information is available online at http://npg.nature.com/reprintsandpermissions/

How to cite this article: Potticary, J. *et al.* An unforeseen polymorph of coronene by the application of magnetic fields during crystal growth. *Nat. Commun.* 7:11555 doi: 10.1038/ncomms11555 (2016).

Supplementary Information

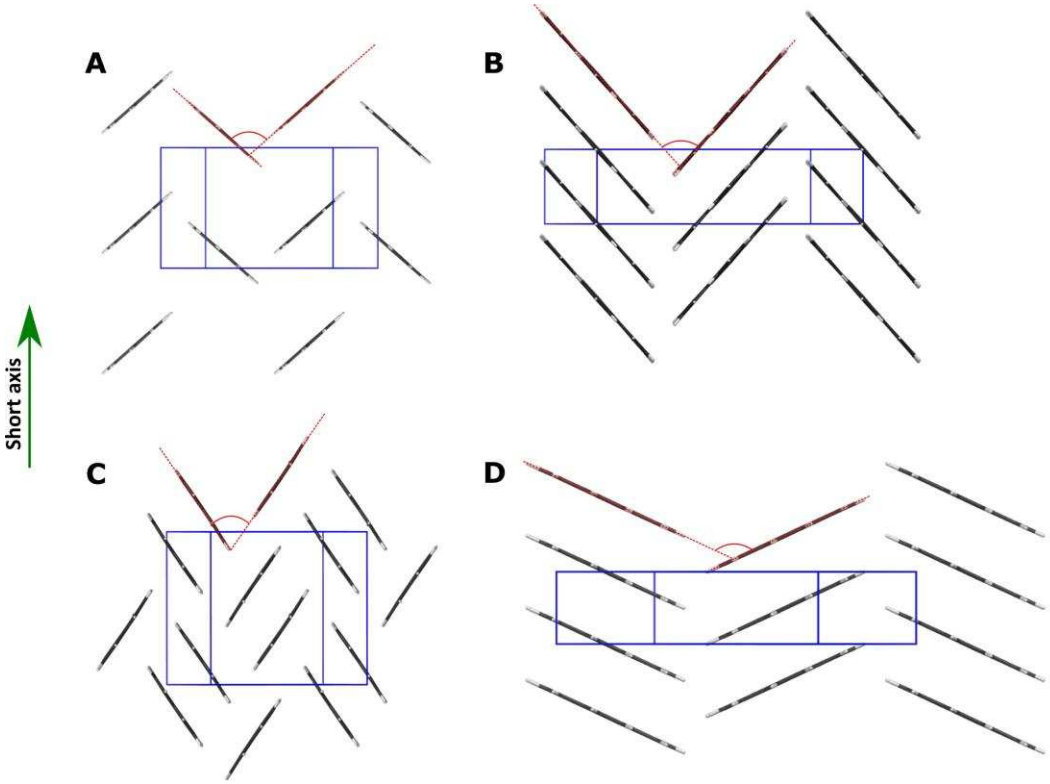

Supplementary Figure 1. The four classes of crystal packing in polyaromatic hydrocarbons. (A) is the herringbone (HB) structure, (B) the gamma-herringbone (γ-) structure, (C) the sandwich-herringbone (SHB) structure and (D) the beta-herringbone (β-) structure.

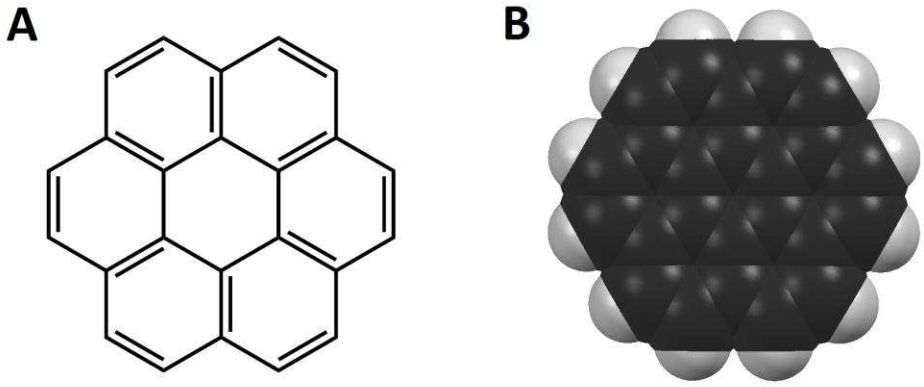

Supplementary Figure 2. The molecular structure of coronene shown as (A) skeletal and (B) space-filling models.

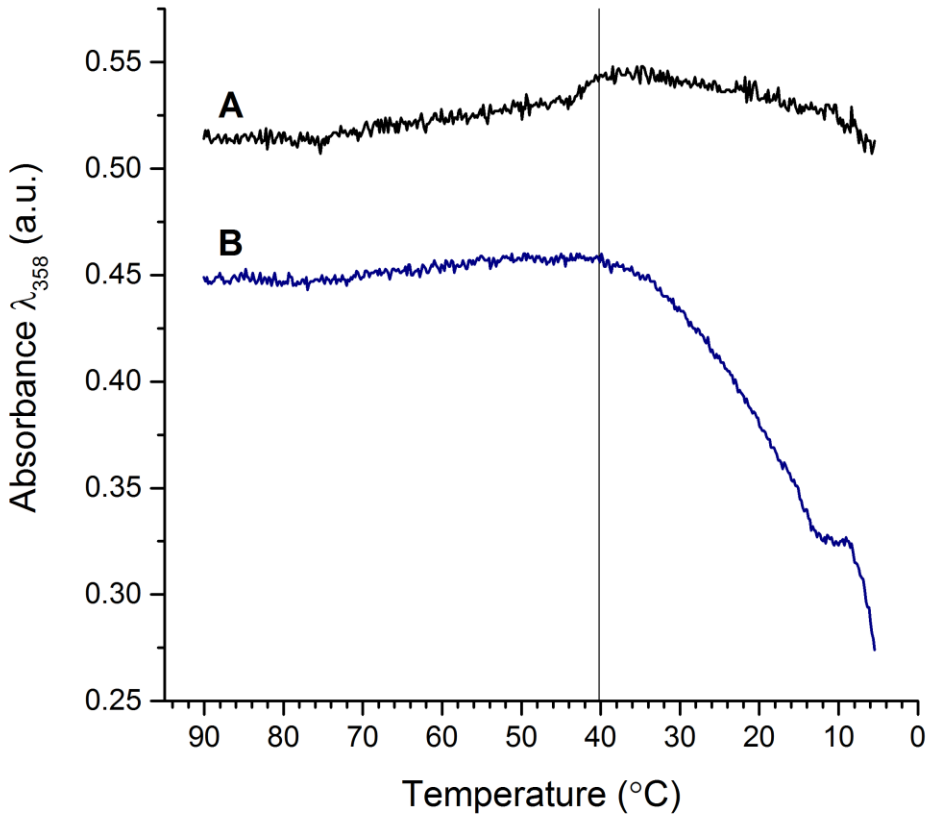

Supplementary Figure 3. UV-vis absorbance at 358 nm as a function of temperature for coronene crystallising under (A) 1 T and (B) 0 T. The clear decrease in absorbance at 40 °C in the 0 T experiment is indicative of crystal growth at this temperature.

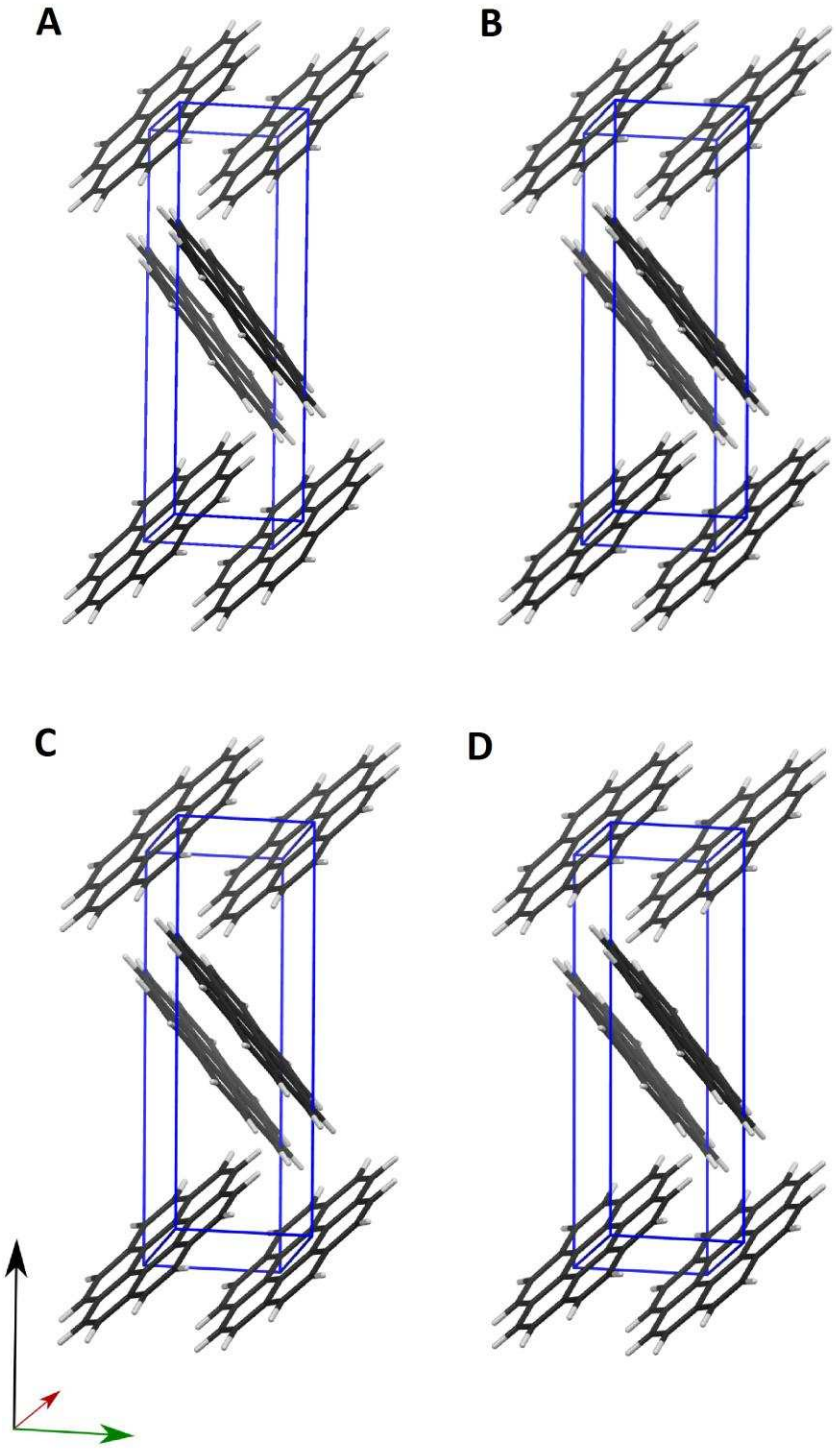

Supplementary Figure 4. X-Ray diffraction crystal structures of coronene grown under a range of applied fields. In (A) the applied field was 0 T; in (B) 0.2 T; in (C) 0.5 T and in (D) 0.8 T. Red green and black arrows indicate the direction of the *a*-, *b*- and *c*-axis respectively.

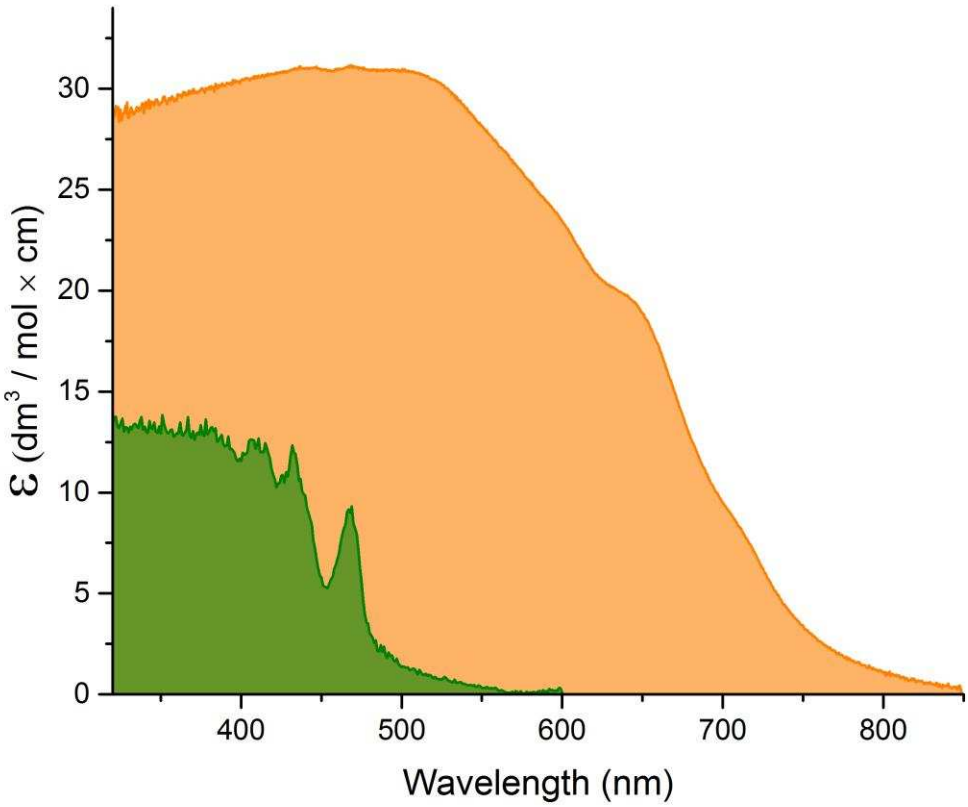

Supplementary Figure 5. Absorption spectra of γ-coronene (green) and β-coronene (orange) single crystals plotted as the extinction molar coefficient (epsilon) vs wavelength. Unpolarized light was irradiated perpendicular to the *a*-*b* plane at room temperature.

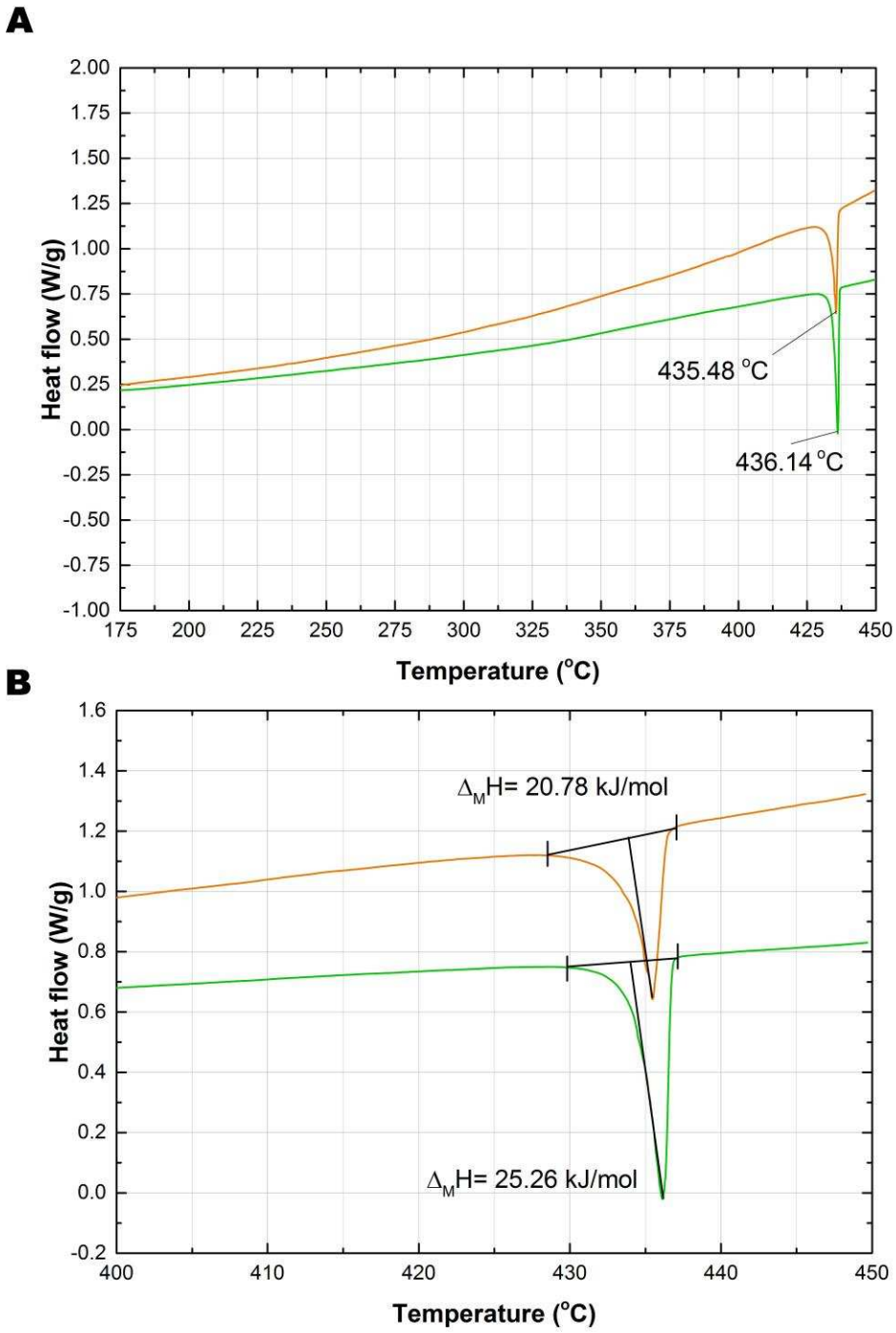

Supplementary Figure 6. DSC curves showing the melting profile of β-coronene (orange) and γ-coronene (green). In (A) the melting points are highlighted and in (B) the values of enthalpy of fusion.

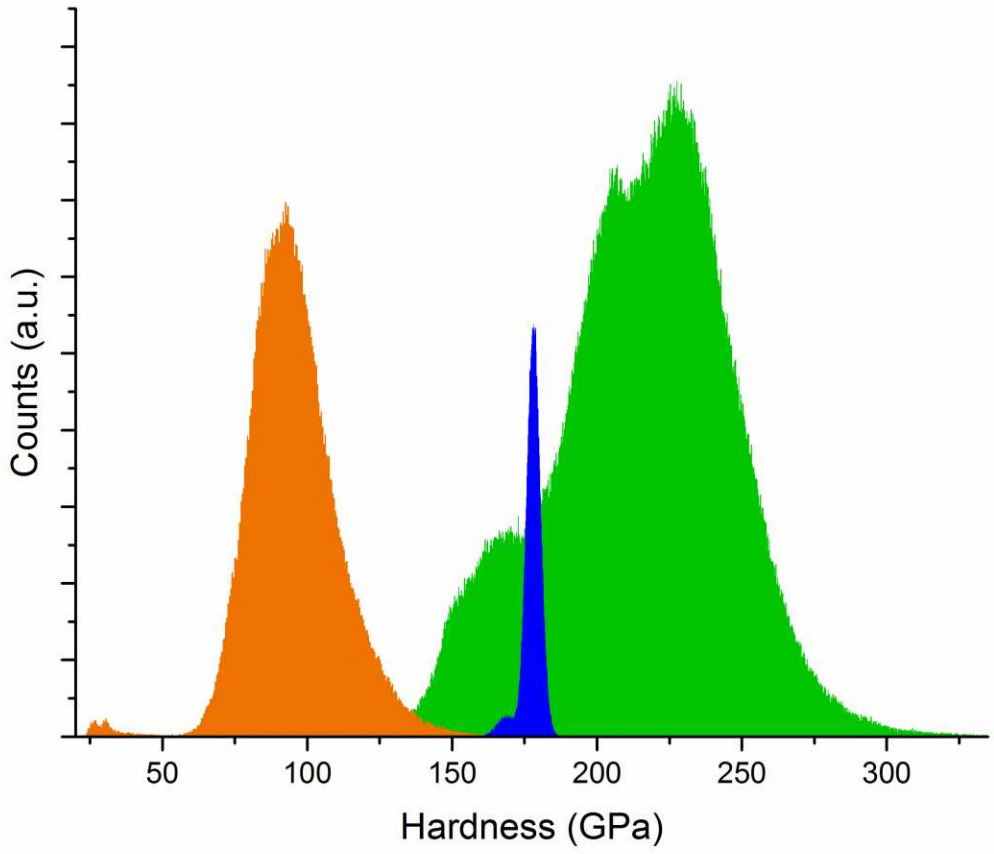

Supplementary Figure 7. Elastic moduli measured via AFM. The orange data are the results from β-coronene, the green from γ-coronene and the blue from a mica control sample. Coronene single crystals were measured on the $\bar{1}0\underline{11}$ and $10\underline{\bar{1}\bar{1}}$ crystal faces.

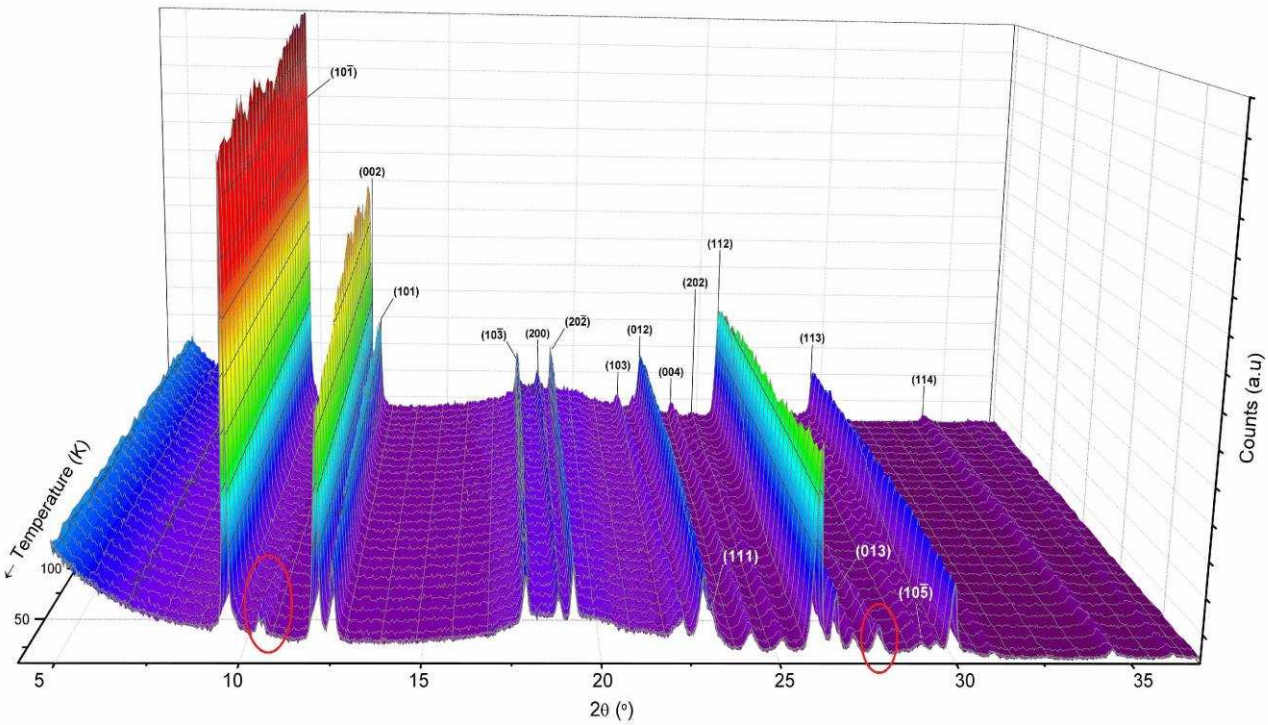

Supplementary Figure 8. 3D surface plot of powder XRD as a function of temperature for γ-coronene while cooling from 300 K to 12 K, without background correction. Arrow indicates forward direction of temperature. Color gradient is arbitrary used only for assisting with visualizing intensities. Red ovals identify emergent peaks due to the formation of β-coronene (viz. Fig. 5). The red oval near 10° 2θ encompasses two emergent peaks.

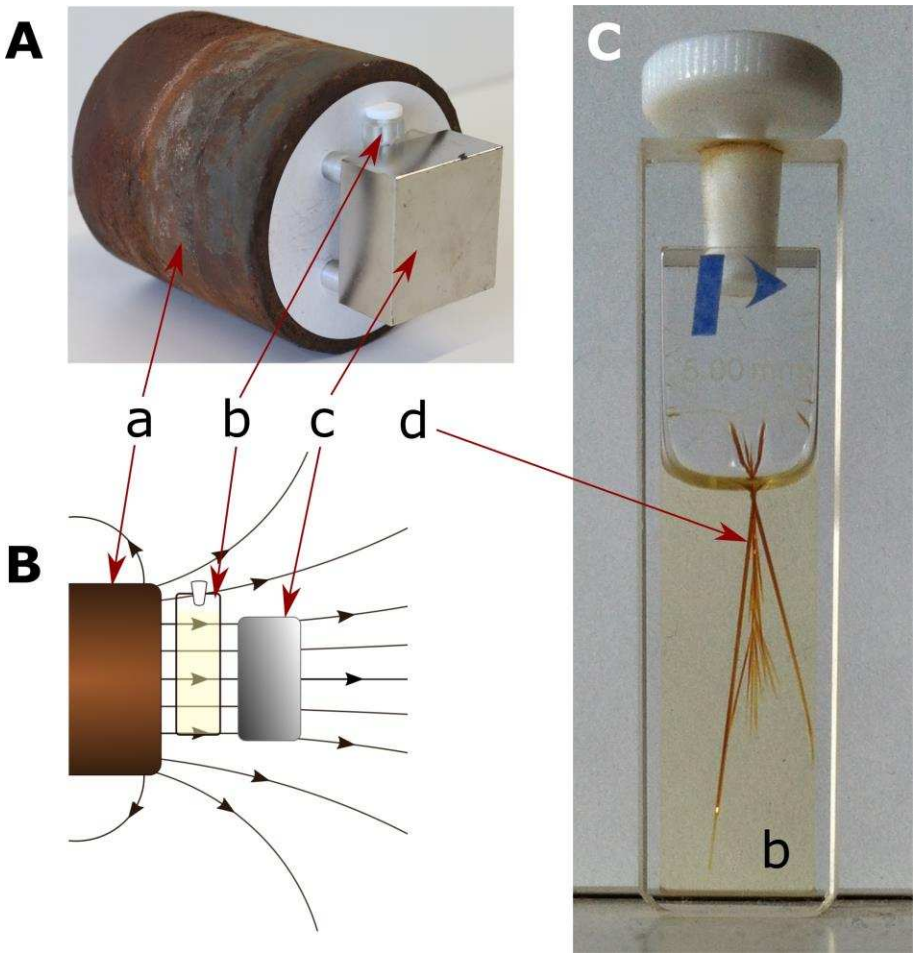

Supplementary Figure 9. Experimental configuration for the growth of β-coronene. (A) Optical image of the experiment, (B) schematic and (C) reaction vial with crystals of β-coronene *in-situ*. (a) is the 1 T magnet; (b) the sample vial; (c) the magnetic holding plate and (d) crystals of β-coronene. Field lines from the 1 T magnet through the experiment are indicated. Field strength was controlled by the application of paper shims (200 μm thickness) between the magnet and the sample vial. The magnetic field was quantified using a Model 5170 gaussmeter from F. W. Bell.

Code	vd W	form	*a* [Å]	*b* [Å]	*c* [Å]	*β* [°]	*d* [Å]	∠ [°]	*V* [Å^3]	E_γ-E_β [kJ/mol]
CASTEP	G06[a]	γ	9.779	4.548	15.422	107.26	3.29	87.4	655	4.3
		β	10.254	3.672	16.851	95.76	3.35	48.5	631	
CASTEP	GF[b]	γ	9.924	4.665	15.915	105.53	3.52	82.1	710	3.8
		β	10.336	3.871	17.264	95.04	3.58	44.9	688	
VASP	TS[c]	γ	9.954	4.566	15.443	106.57	3.35	85.6	673	3.4
		β	10.319	3.714	17.253	95.86	3.39	48.1	658	

[a] Grimme (2006) – ref. (*35*).
[b] Grimme (2006) with experimental van der Waal radii as suggested by Fedorov *et al* (*36*).
[c] Tkatchenko-Scheffler – refs. (*38, 39*).

Supplementary Table 1. Calculated structural parameters for coronene in the two crystal forms γ and β. Constructed from DFT-D calculations using codes and dispersion corrections (vdW) as indicated. Lengths *a*, *b*, *c* are the lattice parameters and *β* the monoclinic angle; *d* is the interplanar distance between parallel coronene molecules. The columns labelled ∠ and V report the herringbone angle between adjacent coronene molecules and the unit cell volume, respectively. The final column reports the lattice energy difference between the two structures; positive indicates β is the more stable.

Form	Temp [K]	Space Group	***a* [Å]**	***b* [Å]**	***c* [Å]**	***β* [°]**	**d[Å]**	**∠ [°]**	**V [Å^3]**
γ	150	$P2_1/n$	10.02	4.67	15.06	106.7	3.43	-	699
γ	200	$P2_1/n$	10.040	4.681	15.6041(19)	106.32	3.43	85.76	703.77
γ	250	$P2_1/n$	10.072(3)	4.6907(12)	15.650(6)	106.18	3.44	85.59	710.1(4)
β	80	$P2_1/n$	10.386	3.821	17.211	96.24	3.47	49.7	679
β	150	$P2_1/n$	10:392	3.839	17.229	96.24	3.48	50.0	683

Supplementary Table 2. Experimental structural parameters for coronene in the two crystal forms γ and β. The parameters *a*, *b*, *c* are the three unit cell axis and *β* the monoclinic angle, d represents the interplanar distance between parallel coronene molecules. The columns labelled ∠ and V report the herringbone angle between adjacent coronene molecules and the unit cell volume, respectively.

Further theoretical insight on Coronene β and γ crystals physical properties

A number of theoretical issues are entangled in this study, which deals mainly with the theoretical comparison of physical properties of Coronene β and γ crystals. *In primis*, the detailed evaluation of how include dispersion energy corrections within DFT calculations. Here, a subject of primary importance, because DFT calculations are performed to carry out geometrical optimization and theoretical check of a new molecular crystal; where the crystal structure is determined by non-covalent intramolecular interactions. In principle all possible interactions are accounted for in the Density Functional exchange and correlation, E_{XC}, term (equation 32). In fact, the approximations adopted in the practical implementation of the Density Functional theory led to results clearly indicating the inability for a correct and efficient description of van der Waals attraction. A result evident, with different weights, for various plane wave basis sets developed in different codes [1]: for instance strong differences are found between CASTEP and VASP results, when full (ions' positions, lattice vectors, cell volume) unit cell geometry optimization is involved [31].

PBE DFT plane wave calculations (PAW potentials, 500 eV energy cutoff, 3×4×2 k-point sampling), **without** dispersion energy interaction correction, yield unit cell volumes of 674.17 Å^3 (γ) and 659.01 Å^3 (β), and the herringbone angle between adjacent coronene molecules resulted 84.8 (γ) 131.8° (β). The volume unit cell values are slightly larger, about 0.3 % for both γ and β polymorphs, compared to the results including vdW interactions (Tkatchenko-Scheffler models[105,106]), as reported in out paper [31] while the angle between adjacent coronene molecules is almost the same with or without vdW correction. On the whole, the unit cell volume reduction, larger attractive potential energy between atoms (vdW correction), with a negligible change in the angle between adjacent coronene molecular planes, seems a reasonable outcome.

Indeed the unit cell contains a rather large number of ions, thus the final result of the unit cell geometrical full optimization could depend on the sampling mesh in k-space. To this end[2], geometrical full optimization (i.e. relaxation of the ions positions, lattice cell vectors and unit cell volume) of the geometrical parameters is performed (PBE-D, Tkatchenko-Scheffler model as implemented in the VASP code [107], PAW potentials, 500 eV energy cutoff) with a reasonably accurate, less time consuming, 3×4×2 k-point sampling grid. Then, the results are crossed-checked with a rather fine 6×6×6 k-point sampling grid, the two procedures yield 658.95 and 657.78 Å^3 unit cell volumes, respectively. On the contrary, a rather large difference is found in the β and γ polymorph energy dif-

[1] CASTEP optimization without vdW corrections leads to a unit cell of infinite value, i.e. the optimization diverges from the crystal to a gas phase transition, while VASP converges maintaining a finite unit cell value.
[2] β crystal only, this because, being the new unforeseen polymorph, it was more accurately analysed in terms of geometrical unit cell parameters.

ference, $\Delta E_{\beta\to\gamma} = E_\gamma - E_\beta$. $\Delta E_{\beta\to\gamma}$ is 32.1 and 3.4[31] kJ/mol, without and with dispersion correction (the γ phase is found as the most stable). For the sake of comparison, the coronene β and γ polymorphs stability was probed also using localized orbitals calculations, without geometrical optimization using experimental X-ray crystal structures; $\Delta E_{\beta\to\gamma}$ = 1037.0 kJ/mol with application of Periodic Boundary Condition (PBC) HSEh1PBE functional[108] and cc-pVDZ basis set, $\Delta E_{\beta\to\gamma}$ = 878.3 kJ / mol obtained comparing β and γ dimers, B3LYP hybrid functional and TZV basis set.

Dielectric function calculations are carried out as a predictive tool to unravel possible differences useful to discriminate between the β and γ coronene crystals. Here, the idea is to exploit a direct connection between the dielectric function and reflection spectra recorded in the visible energy range [109,110]. Some differences are present in the imaginary component, both in intensity and as a function of the crystal orientation. Thus, angle resolved UV/Vis reflectance spectroscopy is expected to discriminate between these two polymorphs.

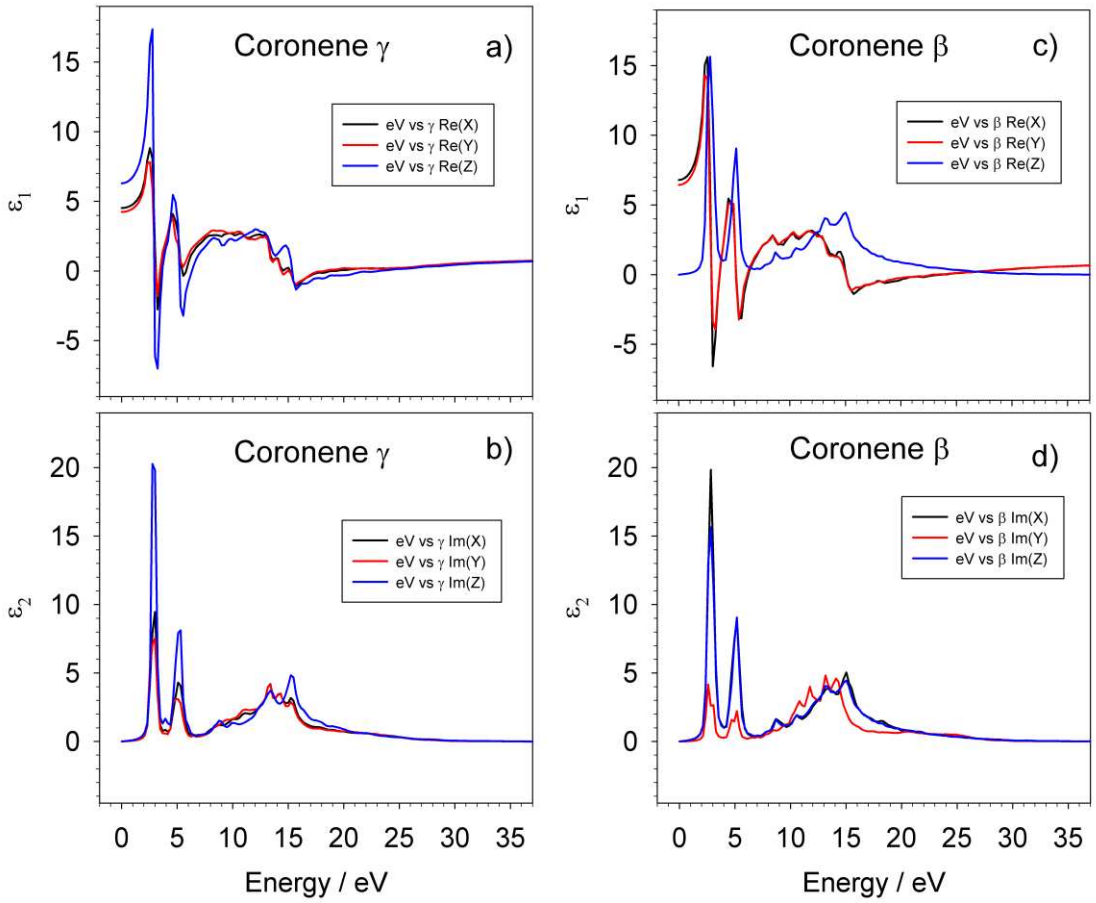

Figure 15. Coronene dielectric function, PBE plane wave calculation. Coronene γ phase a) real ε_1 b) imaginary ε_2. Coronene β phase c) real ε_1 d) imaginary ε_2. The components along the three lattice vectors are shown.

4.2.2 *Cryst. Growth & Des. 2016, 16, 3028-3036* [27]

Preamble

Charge Transfer (CT) molecular crystals constitute an intriguing class of organic based materials [111,112]. Within this field, the tetrathiafulvalene/tetracyanoquinodimethane (TTF–TCNQ), crystalline charge transfer salt, was the first compound recognized to show such a peculiar behaviour, evidenced by its metal-like conductivity [113]. The study of CT molecular crystals is important due to their possible applications ranging from organic solar cells [114], memory elements in computing machines [115], molecular magnets [116]. In particular, this study aims to rationalize the relationship between spatial arrangement in molecular polymorphs and the charge transfer process occurring in six different perylene/TCNQ-F_x (x = 0, 2, 4) co-crystals, where the donor (D) is perylene and the acceptor (A) are the TCNQ-F_x. Experimentally the six different co-crystals have been characterized by both by X-ray diffraction and vibrational spectroscopy measurements, in the 500 – 10000 cm^{-1} energy range. Moreover, vibrational spectra (IR and Raman) are exploited as tools to probe (indirectly) the amount of charge transfer. In particular, the comparison between pristine and co-crystal IR spectra, by looking at shift of selected charge sensitive modes (focusing on the $-(C=C)-$ stretching) allows for an estimate of the intermolecular, perylene/TCNQ-F_x, charge transfer (ρ). Here, the theoretical calculations dealt mainly with calculation of the HOMO/LUMO energy band gap, calculated via both localized atomic orbital and plane waves methods (using both the Gaussian and VASP codes, respectively), vide-infra "*Addendum: on the electronic/optical band gap in Perylene/TCNQ-Fx cocrystals*" section. On the whole, we observed a hierarchical ordering in the electronegativity of the acceptor and degree of charge transfer, modulated by the crystal structure (where trimeric DAD assemblies result in a higher ionicity). The candidate contribution concerned the theoretical part; in particular the calculation and comparison of results obtained by using plane waves *vs* localized orbitals (applying periodic boundary conditions). Intermolecular interaction energies, band gap (HOMO-LUMO energy difference as well), also optical band gap were calculated and critically compared.

Statement of Authorship

<table>
<tr><td colspan="5">This declaration concerns the article entitled:

Structure, Stoichiometry, and Charge Transfer in Cocrystals of Perylene with TCNQ-Fx</td></tr>
<tr><td colspan="5">Publication status (tick one)</td></tr>
<tr><td>draft manuscript</td><td>Submitted</td><td>In review</td><td>Accepted</td><td>Published X</td></tr>
<tr><td colspan="5">Publication details (reference): Cryst. Growth & Des. 2016, 16, 3028-3036</td></tr>
<tr><td colspan="2">Candidate’s contribution to the paper (detailed, and also given as a percentage).</td><td colspan="3">The candidate contributed to the theoretical interpretation and actual calculations (vide supra).

Formulation of ideas: 35 %

Design of methodology: 50 %

Experimental work: 0 %

Presentation of data in journal format: 20 %</td></tr>
<tr><td colspan="2">Statement from Candidate</td><td colspan="3">This paper reports on original research I conducted during the period of my Higher Degree by Research candidature.</td></tr>
<tr><td colspan="2">Signed  </td><td colspan="3">Date 15 May 2017</td></tr>
</table>

Title: Structure, Stoichiometry, and Charge Transfer in Cocrystals of Perylene with TCNQ-Fx

Author: Tommaso Salzillo, Matteo Masino, Gabriele Kociok-Köhn, et al

Publication: Crystal Growth and Design

Publisher: American Chemical Society

Date: May 1, 2016

PERMISSION/LICENSE IS GRANTED FOR YOUR ORDER AT NO CHARGE

This type of permission/license, instead of the standard Terms & Conditions, is sent to you because no fee is being charged for your order. Please note the following:

- Permission is granted for your request in both print and electronic formats, and translations.
- If figures and/or tables were requested, they may be adapted or used in part.
- Please print this page for your records and send a copy of it to your publisher/graduate school.
- Appropriate credit for the requested material should be given as follows: "Reprinted (adapted) with permission from (COMPLETE REFERENCE CITATION). Copyright (YEAR) American Chemical Society." Insert appropriate information in place of the capitalized words.
- One-time permission is granted only for the use specified in your request. No additional uses are granted (such as derivative works or other editions). For any other uses, please submit a new request.

Publication title:
Structure, Stoichiometry, and Charge Transfer in Cocrystals of Perylene with TCNQ-Fx

the thesis page numbers that it spans:
113 to 130

CRYSTAL GROWTH & DESIGN

Article

pubs.acs.org/crystal

Structure, Stoichiometry, and Charge Transfer in Cocrystals of Perylene with TCNQ-F_x

Tommaso Salzillo,[†,#] Matteo Masino,[‡] Gabriele Kociok-Köhn,[§] Daniele Di Nuzzo,[†,▽] Elisabetta Venuti,[#] Raffaele Guido Della Valle,[#] Davide Vanossi,[⊥] Claudio Fontanesi,[∥] Alberto Girlando,[‡] Aldo Brillante,[#] and Enrico Da Como*[,†]

[†]Department of Physics and [§]Chemical Characterisation and Analysis Facility (CCAF), University of Bath, Claverton Down, BA2 7AY Bath, United Kingdom

[‡]Dipartimento di Chimica, Parma University/INSTM-UdR Parma, 43124 Parma, Italy

[⊥]Dipartimento di Scienze Chimiche e Geologiche, Università di Modena e Reggio Emilia, Via Campi 103, 41125 Modena, Italy

[∥]Dipartimento di Ingegneria Enzo Ferrari, Università di Modena e Reggio Emilia, Via P. Vivarelli, 10, 41125 Modena, Italy

[#]Dipartimento di Chimica Industriale Toso Montanari, Università di Bologna/INSTM-UdR Bologna, Viale Risorgimento 4, 40136 Bologna, Italy

Supporting Information

ABSTRACT: Semiconductor charge transfer (CT) cocrystals are an emerging class of molecular materials which combines the characteristics of the constituent molecules in order to tune physical properties. Cocrystals can exhibit polymorphism, but different stoichiometries of the donor−acceptor (DA) pair can also give different structures. In addition, the structures of the donor and acceptor as pristine compounds can influence the resulting cocrystal forms. We report a structural study on several CT cocrystals obtained by combining the polyaromatic hydrocarbon perylene with 7,7,8,8-tetracyanoquinodimethane (TCNQ) and its fluorinated derivatives having increasing electronegativity. This is achieved by varying the amount of fluorine substitution on the aromatic ring, with TCNQ-F_2 and TCNQ-F_4. We find structures with different stoichiometries. Namely, the system perylene:TCNQ-F_0 is found with ratios 1:1 and 3:1, while the systems perylene:TCNQ-F_x (x = 2, 4) are found with ratios 1:1 and 3:2. We discuss the structures on the basis of the polymorphism of perylene as pure compound, and show that by a judicious choice of growth temperature the crystal structure can be in principle designed a priori. We also analyze the structural motifs taking into account the degree of charge transfer between the perylene donor and the TCNQ-F_x acceptors and the optical gap determined from infrared (IR) spectroscopy. This family of materials exhibits tunable optical gaps in the near-IR (NIR), promising applications in organic optoelectronics.

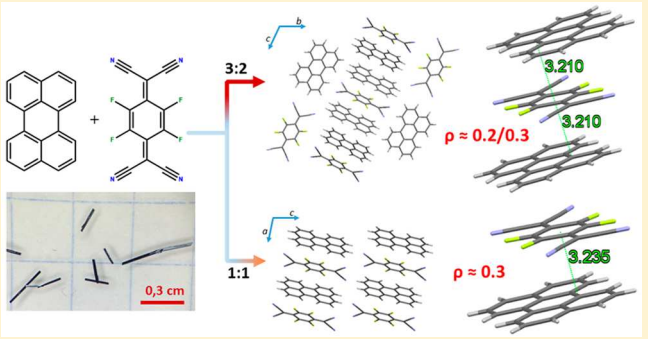

INTRODUCTION

Organic molecular materials for electronic applications are typically based on pi-conjugated systems. The extension of the pi-conjugation and the presence of heteroatoms determines the electronic structure and many of the resulting properties, although the molecular packing in the solid state plays a crucial role when transport of excitons or charges are of interest.[1,2] A more drastic approach in changing the properties of what are known as organic semiconductors is to combine materials in blends or cocrystals.[3] Recently, donor−acceptor (DA) CT crystals attracted substantial attention as candidates for ambipolar charge carrier mobility organic semiconductor materials.[4] This prediction, however, heavily relies on their crystal structure, because the supramolecular arrangement determines the bandwidth of the valence and conduction bands involved in the charge carrier transfer. Ideally, the bandgap, the bandwidth, and as a consequence the carrier transport characteristics could be tuned by performing small modifications to the donor or acceptor molecules in order to change their electronegativity. The issues in pursuing such an approach are intrinsically related to the crystal structure, since small variations in the chemical structure could promote novel unforeseen crystalline arrangements and polymorphs. In addition, if the DA pair of choice exhibits already polymorphism as pure compounds, i.e., exhibits different crystal structures, it is not immediately clear if polymorphism will be also encountered in the mixed crystal. In recent years the combination of aromatic hydrocarbons and halogenated

Received: November 23, 2015
Revised: April 8, 2016
Published: April 14, 2016

DOI: 10.1021/acs.cgd.5b01663
Cryst. Growth Des. 2016, 16, 3028−3036

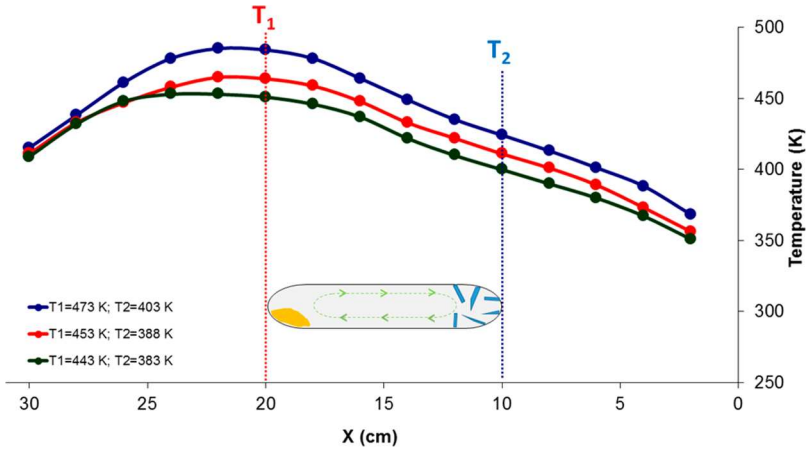

Figure 1. Scheme of the PVT crystal growth technique. The position of the quartz ampule with respect to the two heating zones of the furnace is shown together with some of the temperature profiles used for the crystal growth reported in this work.

acceptors attracted considerable attention for functional materials in electronics and photonics.[4−7] It is also well-known that some aromatic hydrocarbons exhibit polymorphism[8,9] and that the structure of halogenated compounds shows remarkable structural changes when more halogen atoms are inserted in the acceptor chemical skeleton. This is also one of the important aspects within the research focus of halogen bonding.[10]

Polymorphism developed as a massive research field, due to the opportunities that it offers for crystal engineering,[11] but also the challenges for structural purity in organic electronics applications.[12−14] The study of polymorphs, which was initially concentrated on pharmaceuticals, dyes, and pigments, has nowadays expanded toward other types of molecular materials such as semiconductors,[15] superconductors,[16] and conjugated polymers.[17,18] The nature of polymorphism is intrinsically linked to the intermolecular interactions which hold together the molecules in the solid and their directionality.[19] Polymorphism becomes more complex when the molecules constituting the crystal have different chemical identities, and, together with the dispersive intermolecular interactions, other forces are at play. Two interesting examples are CT or mixed-valence crystals and solvates,[20] where orbital hybridization may occur.

Strictly speaking, the term polymorphism is historically linked to different crystalline structures of the same single component material. However, polymorphism in cocrystals exists and has been found in several CT crystals.[3,21,22] When studying cocrystals, different structures may arise just as a consequence of different stoichiometry of the two compounds; therefore, we name the phenomenon of different structures from different stoichiometry, *stoichiomorphism*. This name is also used in the science studying networks for a different purpose, which is network mapping.[23]

In this paper we have chosen to work with DA couples based on perylene and TCNQ-F_x, where x = 0 (TCNQ), 2, 4. We performed single crystal growth from solution and by physical vapor transport (PVT). The mixed crystals obtained combining perylene and TCNQ have already demonstrated promising semiconductor characteristics in single crystal field effect transistors (FET), and their ambipolar behavior opens interesting possibilities for optoelectronic devices.[24,25] Besides reviewing the crystal structures of perylene:TCNQ, we also present three new crystals forms obtained by combining perylene with TCNQ-F_2 and TCNQ-F_4. These three crystal structures are classified by stoichiometry exhibiting a 1:1 or 3:2 perylene:TCNQ-F_x ratio. Interestingly, while the 1:1 structures exhibit a typical alternating DA stack, the 3:1 and 3:2 stoichiomorphs are different and exhibit a common structural motif, i.e., two perylene molecules in a sandwich configuration with the TCNQ based acceptor in between. This quasi-1D trimeric arrangements are also accompanied by orthogonally oriented molecular units. In 3:1 perylene:TCNQ these orthogonal units are just perylene molecules, whereas in the 3:2 structures of perylene:TCNQ-F_2 and:TCNQ-F_4 the units are alternating DA stacks. By performing a series of optical spectroscopy experiments in the middle IR and NIR we determine: (i) the degree of ionicity, ρ, between donor and acceptor analyzing the charge sensitive vibrations of TCNQ-F_x and (ii) the optical bandgap from the onset of CT exciton absorption band. The room temperature degree of charge transfer varies from a minimum of almost 0 for perylene:TCNQ (1:1) to a maximum of ∼0.3 for perylene:TCNQ-F_4 cocrystals. For the same compounds the optical gap, from the absorption onset, varies from ∼1.06 to 0.68 eV, respectively. We discuss the structures of cocrystals on the basis of ρ and the polymorphism in pure perylene. The possibility that the polymorphism of perylene could influence cocrystal structures is suggested by the different growth temperatures of the stoichiomorphs above and below the phase transition temperature of perylene phases.

EXPERIMENTAL SECTION

Perylene (purity 99%) and TCNQ (98%) were purchased from Aldrich, whereas TCNQ-F_2 (98%) and TCNQ-F_4 were obtained from TCI (98%). The materials were used as received. Solvents of spectroscopic grade were purchased from Aldrich. For PVT growth, the materials were mixed in a glass ampule which was sealed after three cycles of vacuum and nitrogen purging, with the last step of vacuum pumping overnight. The ampule was then placed horizontally in a two zone furnace with some of the typical temperature profiles used for growth illustrated in Figure 1. Single cocrystals of perylene with TCNQ-F2 and with TCNQ-F4 were also obtained from solution growth. Equimolar solutions of perylene and TCNQ-F2 or -F4 were dissolved in a solvent mixture of toluene/acetonitrile (5/1) heated at 324 K. The solutions were left to cool at room temperature in sealed bottles in the laboratory environment. The single crystals were gathered from the solutions.

Single crystal diffraction intensity data for all structures were collected at 150 K on an Agilent SuperNova-E Dual diffractometer

DOI: 10.1021/acs.cgd.5b01663
Cryst. Growth Des. 2016, 16, 3028−3036

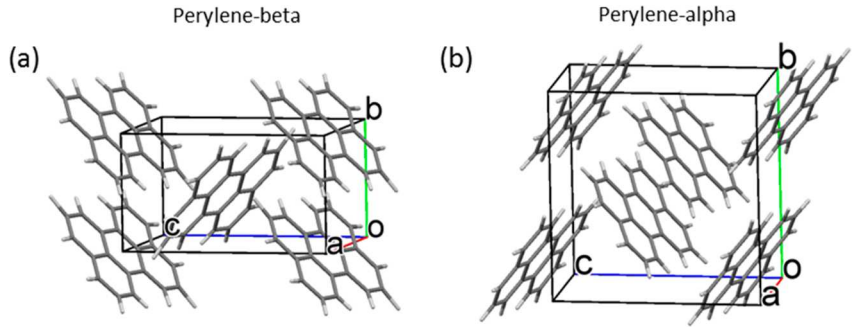

Figure 2. Two known polymorphs of perylene. (a) β Perylene unit cell with two inequivalent molecules per cell. (b) α Perylene with four molecules per unit cell.

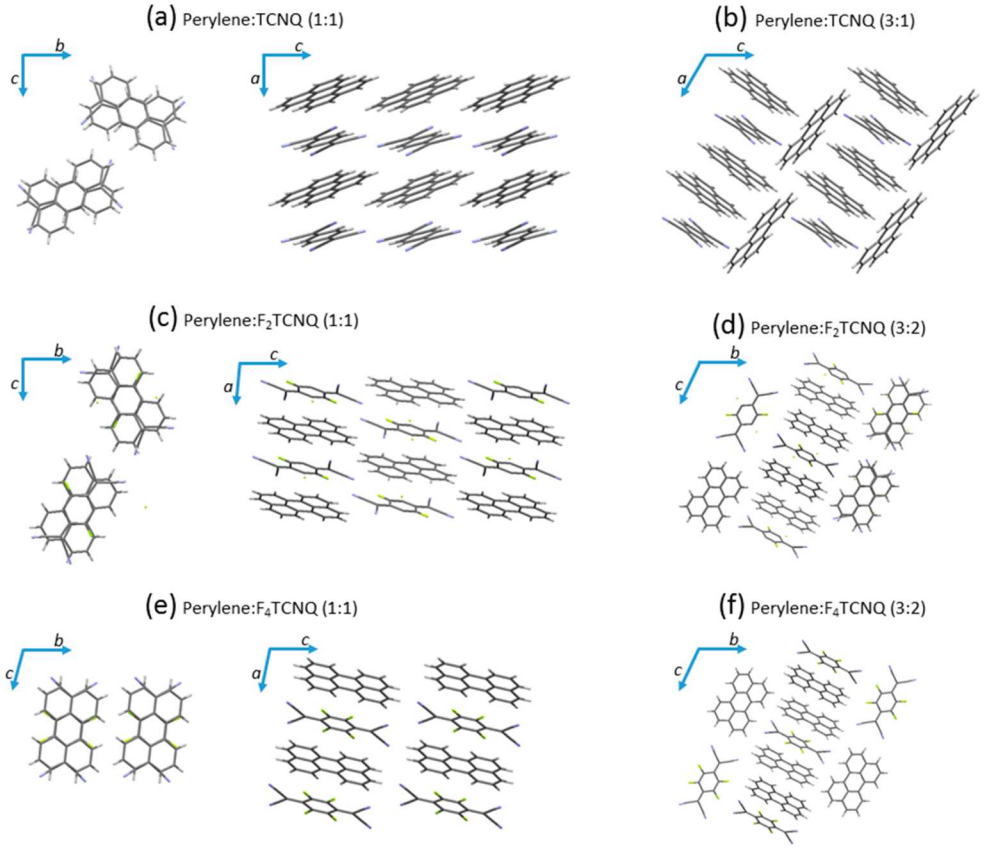

Figure 3. Crystal structures of (a) perylene:TCNQ 1:1, (b) perylene:TCNQ 3:1, (c) perylene:TCNQ-F_2 1:1, (d) perylene:TCNQ-F_2 3:2, (e) perylene:TCNQ-F_4 1:1, and (f) perylene:TCNQ-F_4 3:2.

equipped with an Oxford Cryosystem, using CuKα radiation (λ = 1.5418 Å). Data were processed using the CrysAlisPro software (CrysAlisPro, Agilent Technologies, Version 1.171.37.35, release 13-08-2014 CrysAlis171.NET). For all structures a symmetry-related (multiscan) absorption correction was applied. Crystal parameters are provided in Table S1. Structure solution, followed by full-matrix least-squares refinement, was performed using the WINGX-v2014.1 suite of programs throughout.[26]

Infrared spectra of the CT crystals were recorded with a Bruker ifs66 Fourier transform IR (FT-IR) spectrometer coupled to an IR microscope Hyperion 1000. The spectrometer is equipped with a liquid nitrogen cooled mercury cadmium telluride (MCT) detector. The instrument setup allows for reflection and transmission measurements with polarized light. The parameter ρ was obtained from the shift of charge sensitive modes of TCNQ-F_x specified below and by benchmarking with respect to the neutral acceptor and fully ionized salts of TCNQ-F_x with potassium.[27] We have preferred to use this method in contrast to TCNQ-F_x bond lengths from X-ray measurements, since the vibrational frequencies will provide the ionicity of the cocrystals at room temperature and thus are more relevant for optoelectronic device applications.

RESULTS

We start the presentation of our results by reviewing the crystal structure of the pure compounds perylene and TCNQ-F_x. This will help in discussing the stoichiomorphism in the mixed cocrystals.

Perylene. The donor, perylene, shows enantiotropic polymorphism, i.e., the Gibbs free energy of the two polymorphs, α and β, plotted as a function of temperature shows a crossing point before the respective melting points have been reached.[28] This is an important aspect, since above a certain temperature, 420 K for perylene, only the α phase is stable. Figure 2a,b shows the molecular packing of the two

DOI: 10.1021/acs.cgd.5b01663
Cryst. Growth Des. 2016, 16, 3028−3036

known polymorphs of perylene. The β polymorph in Figure 2a exhibits a herringbone arrangement, also known as the γ structure according to the classification of polyaromatic hydrocarbons (PAH) by Desiraju and Gavezzotti,[29] while the α is a sandwich herringbone. This different packing most remarkably results in a different number of molecules per unit cell, Z, which is 2 and 4 for β and α, respectively. The symmetry space group and crystal system are instead the same, $P2_1/c$ and monoclinic. The polymorph α can be obtained through a phase transition by heating the β phase above 420 K,[9] but can also be prepared as pure phase by different methods and is stable at room temperature.[30,31] The α polymorph melts at about 551 K. From a molecular point of view in the α-phase perylene molecules are not exactly planar, and an angle of 1.6° can be measured between planes identified by the two condensed biphenyls. In α the intermolecular interactions are due to $\pi-\pi$ dimer interactions in the sandwich, which accounts for 21% of the total contribution, and the other main contribution is from molecules constituting a nonparallel dimer within the same sandwich herringbone plane.[32]

TCNQ-F$_x$. Acceptors based on TCNQ are well-known in the literature and as pure materials form different crystalline structures depending on the number of fluorine atoms substituting the hydrogens on the aromatic core. To the best of our knowledge, we could not find any report of polymorphism for these compounds.[33] We have redetermined the crystalline structures of TCNQ and TCNQ-F$_4$ and examined them all; the one of TCNQ is shown in Figure S1a. It has a monoclinic crystal packing with space group $C2/c$ and four molecules in the unit cell and confirms the structure by Long et al.[34] and Krupskaya et al.,[35] CCDC: TCYQME and TCYQME03, respectively. The molecules are arranged in herringbone fashion, and it is possible to identify four different π-stacking directions. Figure S1b shows the crystal structure of TCNQ-F$_2$, characterized by two molecules per unit cell (BERZON02).[35] The space group is $C2/m$ and the unit cell is monoclinic. TCNQ-F$_4$ has four molecules in an orthorhombic unit cell with space group $Pcab$, and its structure is reported in Figure S1c and confirms the structures obtained by Emge et al.[36] (BAKPAE) and Krupskaya et al.[35] (BAKPAE01).

Perylene:TCNQ Cocrystals. The structures of the two stoichiomorphs of perylene:TCNQ are reported in Figure 3a,b. These are two of the three structures reported thus far, since Kloc and co-workers recently reported a 2:1 stoichiomorph, that we could not observe in our growth experiments.[25] In the 1:1 stoichiomorph, the unit cell is monoclinic with space group $P2_1/c$ and two inequivalent molecular pairs per cell as already presented in previous investigations (CCDC: PERCTQ).[37] The molecules are arranged in two alternating stacks with a tilt angle between the long axis of perylene molecules belonging to different stacks; see projection on the bc plane in side figure. There is also a tilt angle of 21.19° between the planes of perylenes from different stacks. Interestingly, the molecular planes of perylene and TCNQ in both the DA stacks are not parallel, but exhibit an inclination angle of 4.34°. This aspect, together with a DA distance of 3.3 Å (plane to centroid), has important implications for charge transfer and likely also transport. The inclinations in these stacking planes could be linked the structure of pure TCNQ, where the inclination of planes passing through the inequivalent TCNQ molecules is 47.23° and the C_2 molecular symmetry axes are not aligned, cf. Figure S1a.

Largely different is the arrangement of perylene in the 3:1 stoichiomorph first reported by Hanson (CCDC: TCQPER)[38] and then by Truong et al.[39] Here, each perylene molecule in the stack with TCNQ is paired with a second perylene, and further there are perylene molecules with their planes parallel to the a axis, thus not directly involved in CT with TCNQ.[40] The unit cell structure is triclinic with $P\bar{1}$ symmetry, with one *molecular trimer* per cell and the TCNQ molecule on the inversion center in accordance to previous reports. It is important to underline here the similarity in the arrangement of the perylene molecules in the 3:1 complex with respect to the polymorph α of pure perylene (Figure 2b). In comparing the two figures it appears as if TCNQ molecules are inserting in between the perylene dimers in the sandwich structure. The molecular planes of perylene and TCNQ are not parallel in the DAD stack, but form an angle of 2.99°. Therefore, it is not possible to quote a distance between the molecular planes, but we have calculated the distance between the perylene plane and the centroid on TCNQ, which is 3.249 Å. Further, perylene molecules in the DAD stack are not exactly planar with an angle of 0.86° between the biphenyls, in contrast to the perylenes parallel to the a axis, which are fully planar. An important aspect that will be further discussed below concerns the *growth temperatures* for the two polymorphs. In order to effectively guide the stoichiomorphic product, the 1:1 structure was obtained only by setting the high temperature side of the two zone furnace at 413 K while the cold at 373 K, thus both below the transition temperature for the pristine perylene phases of 420 K. For the 3:1 stoichiomorph the settings were instead 443 and 383 K, respectively.

In terms of optical gap and charge transfer, the 1:1 cocrystal is already rather well characterized. In early optical reflectance studies, the CT transition has been located around 10 800 cm^{-1} (1.34 eV) and 12 000 cm^{-1} (1.5 eV), with an onset at 8500 cm^{-1} (~1.05 eV) refs 41 and 42. From the frequency and the oscillator strength of this transition, Ida et al.[41] estimated the degree of charge transfer (or ionicity) ρ to be around 0.1, and the hopping integral, t_{DA}, about 0.25 eV. Recent estimates of ρ by Raman spectra and the X-ray bond length of TCNQ give ρ = 0.01 and t_{DA} = 0.375 eV by DFT calculations.[25] It has been known for a long time that Raman frequencies do not provide a reliable estimate of the ionicity in mixed stack CT crystals due to perturbing effect of electron-molecular vibration coupling.[43] Therefore, in our work we are using IR spectra, by looking at selected charge sensitive modes. The IR spectra of perylene:TCNQ 1:1 in Figure 4a are shown together with those of pristine perylene and TCNQ. In Figure S2 we also compare the IR spectra of TCNQ and of the ionic compound K:TCNQ, the latter representative of $(TCNQ^{\bullet})^-$ molecular vibrations. From this last comparison we identify the unique asymmetric C═C stretching at 1543 cm^{-1}, which shifts to 1509 cm^{-1} in charged $(TCNQ^{\bullet})^-$, as giving a reliable estimate of ρ. We have opted for this genuine reporter of ρ, in contrast to the quite often used frequencies of CN stretching modes above 2200 cm^{-1} which are subjected to extrinsic effects such as the crystal environment.[44] As shown in Figure 4a, for both light polarizations, parallel to the a axis (red curve) and parallel to b (blue curve) the C═C stretching coincides with the same mode measured in pristine TCNQ. The spectra of the 1:1 cocrystal is indeed the superposition of the spectra of neutral perylene and TCNQ, and we conclude that in this complex $0 \leq \rho < 0.1$. The agreement with the Raman estimations in ref 25 is not surprising in this case, as the perturbing effect of the

DOI: 10.1021/acs.cgd.5b01663
Cryst. Growth Des. 2016, 16, 3028−3036

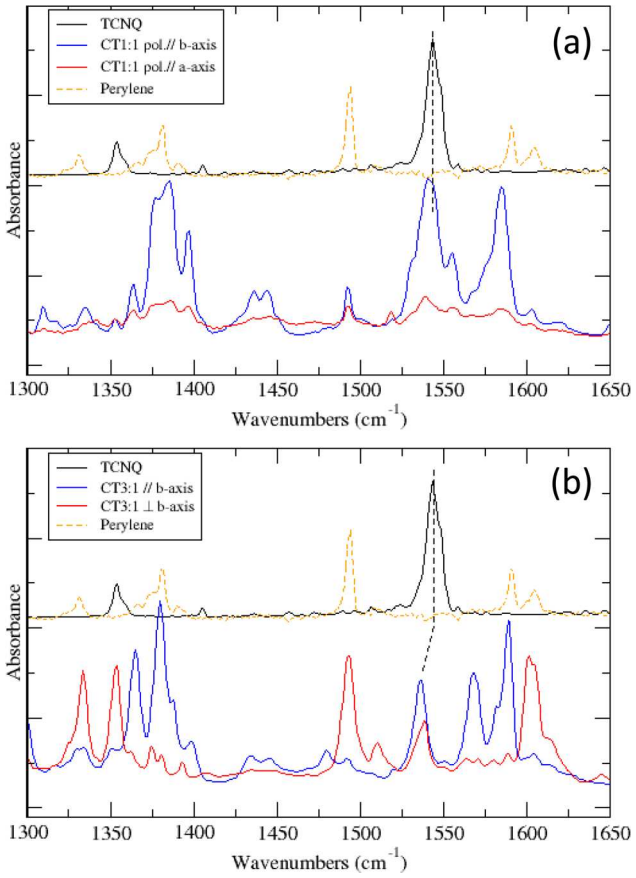

Figure 4. (a) Vibrational spectra of TCNQ (black solid line) and perylene (orange dashed line). The vibration at 1543 cm^{-1} for the neutral molecule is shifted to 1509 cm^{-1} when it is negatively charged in K:TCNQ (Figure S2). Perylene:TCNQ (1:1) for polarizations parallel to the *b* axis (blue) and parallel to the *a* axis (red). (b) Vibrational spectra of perylene:TCNQ 3:1 for polarizations parallel (blue) and perpendicular (red) to the *b* axis.

electron-molecular vibration becomes evident at intermediate ionicities.[43]

The optical reflectivity spectra of the 3:1 cocrystal from the literature shows a band at 10 500 cm^{-1} (1.3 eV) with onset at 9000 cm^{-1} (1.12 eV), ascribed to a charge transfer exciton, with a shoulder at 12 000 cm^{-1} (1.5 eV), whose origin is not clear.[40] Figure 4b shows the IR spectrum of the 3:1 cocrystal recorded with light impinging perpendicular to the *ab* crystal plane and polarized parallel and perpendicular to the *b* axis. For such polarizations the TCNQ antisymmetric C=C stretching has components in both polarizations. The charge sensitive mode is at 1535 cm^{-1}, yielding a value of ρ of about 0.2. With the help of earlier calculations[45] of the frequency of the CT transition as a function of the above estimate of ρ and the transition energy of the CT transition[40] yield an estimate of t_{DA} = 0.4 eV. This value can be compared with the above-reported estimate t_{DA} = 0.2 eV for the 1:1 cocrystal,[41] obtained from an analogous combination of experiment and calculations. We conclude that the mixing between D and A states is indeed larger in the DAD trimer of the 3:1 cocrystal than in the regular stack of the 1:1 cocrystal, as it can be expected from the shorter D−A distances by 0.051 Å.

Perylene:TCNQ-F_2 Cocrystals. We report two new structures from perylene combined with TCNQ-F_2, whose unit cells are shown in Figure 3c,d. The structure of the 1:1 cocrystal exhibits two alternating stacks along the *a* axis. The unit cell is monoclinic with symmetry $P2_1/n$ and two inequivalent pairs of molecules. In comparing this 1:1 structure with the one formed by perylene and TCNQ (Figure 3a), it can be noticed that the stacks with TCNQ-F_2 are slipped one respect to the other by one molecular unit. In addition, the relative orientation of the perylene in the two stacks is different from the one observed for perylene:TCNQ shown above. This can be clearly noticed in the two projections on the side of Figure 3a,c. The stack is regular (molecules on inversion centers), with 3.28 Å distance between D and A. The F atoms are disordered as a result of the rotational disorder, and the average occupation of the position pairs (2,5) and (3,6) is 70:30. The molecular planes of perylene and TCNQ-F_2 form an angle of 2.37° in both stacks. The perylene molecule is planar.

Figure 3d shows the structure of the 3:2 stoichiomorph which is isostructural to the one of perylene:TCNQ-F_4 presented below. The crystal structure is triclinic, with $P\bar{1}$ symmetry and two pairs of inequivalent molecules in the unit cell. The structure is characterized by DAD trimers arranged in a quasi-one-dimensional stack parallel to the *c* axis. There are two types of trimers characterized by different inclination angles between perylenes and TCNQ-F_2 of 1.75° and 1.89°. In addition, the two types of trimers are tilted by about 48°, a value measured for the planes passing through the TCNQ-F_2 of the two trimers. This latter inclination angle is reminiscent of the herringbone angle between sandwiches in α perylene. A slightly dimerized perylene-TCNQ-F_2 stack (distance between D and A is d = 3.28(1) Å) is found along the *a* axis, approximately perpendicular to the trimers' layer. In this dimerized DA stack the molecules are almost parallel with an angle of 0.52°. There are two equivalent DA stacks in the unit cell, slipped with respect to the other. This slipping is reminiscent of the 1:1 stoichiomorph from the same DA pair. In terms of intramolecular planarity the perylene molecules are planar in the DA stacks, while they exhibit an angle of ∼1.2° between the byphenyls in the DAD stacks. Like the 1:1 stoichiomorph, the 3:2 shows orientational disorder in the position of the fluorines. We notice that a good yield of the 1:1 structure was reached by performing the growth with the cold end of the ampule at 387 K, while for the 3:2 stoichiomorph the temperature was increased to 413 K.

In the 1:1 stoichiomorph we are able to observe the onset of the CT absorption band at 7000 cm^{-1} (0.88 eV) from IR spectroscopy (Figure S3a). Although we are not able to measure the frequency of the peak, it is clear that the CT frequency is well below the CT excitons of both perylene:TCNQ cocrystals presented above. The polarized IR spectra of the *ab* plane are compared in Figure 5a with those of neutral perylene and TCNQ-F_2. The IR spectra of TCNQ-F_2 and K:TCNQ-F_2 are reported in Figure S4, where we can identify three charge sensitive modes at 1575, 1550, and 1395 cm^{-1}, with ionization frequency shifts of 50, 63, and 44 cm^{-1}, respectively. The frequencies of these three bands in the 1:1 cocrystal yield an estimation of ρ of 0.13, 0.15, and 0.1, respectively. The two polarizations explored give very similar results and show mainly a difference in intensity correlated to the orientation of the TCNQ-F_2 molecules in the unit cell. On the basis of these results, we estimate that ρ is ∼0.14, considerably higher than in the 1:1 cocrystal of perylene:TCNQ.

DOI: 10.1021/acs.cgd.5b01663
Cryst. Growth Des. 2016, 16, 3028−3036

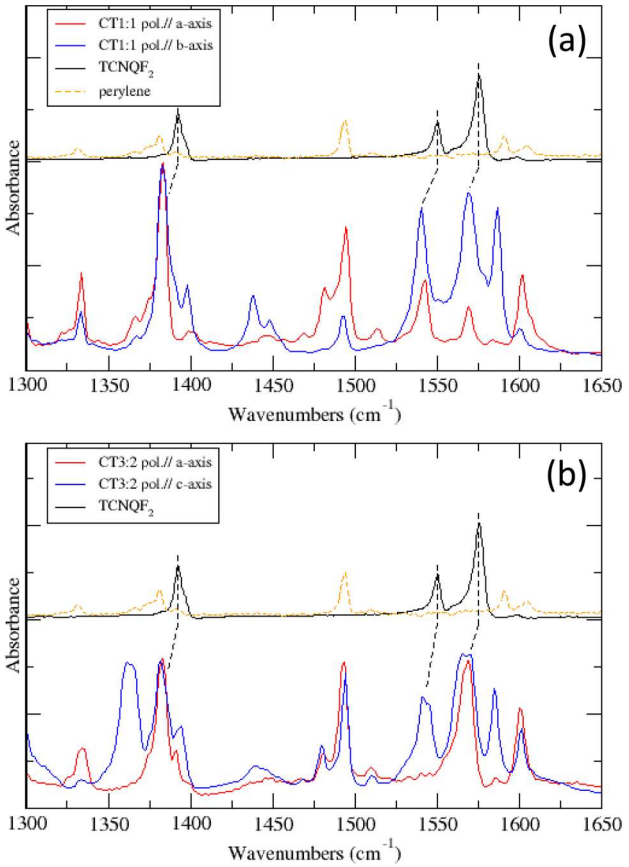

Figure 5. (a) Vibrational spectra of TCNQ-F_2 (black solid line) and perylene (orange dashed line) together with perylene:TCNQ-F_2 1:1 for polarizations parallel to the *a* axis (red) and parallel to the *b* axis (blue). The spectrum of K:TCNQ-F_2 is reported in Figure S4. (b) Vibrational spectra for perylene:TCNQ-F_2 3:2 for polarizations parallel to the *a* axis (red) and to the *c* axis (blue).

For the 3:2 cocrystal, similar to the 1:1, the onset of CT transition is about 7000 cm^{-1} (Figure S3b), but, at variance with the 1:1, does not show a detectable dichroism in our measurements, which are performed with light polarized along the *a* or *c* axis. From the structural data of Figure 3d, we associate the band polarized along *a* to the CT exciton along the DA stack, and the band polarized along *c* to a CT exciton in the DAD trimer. In order to estimate the degree of charge transfer, we have focused on the same spectral region as for the 1:1 cocrystal. However, the more complex structure of the unit cell requires a more detailed spectral analysis. Figure 5b compares the polarized IR spectra of the *ac* plane with the spectra of neutral TCNQ-F_2, evidencing the frequency shifts of the three charge sensitive bands. The vibrational bands at 1541 and 1383 cm^{-1} are sensitive to polarization, while the band at 1570 cm^{-1} exhibits weak dichroism. A more detailed analysis of the 1570 cm^{-1} band and comparison with the Raman spectra (Figure S5) reveals the presence of a vibronic band[46] superimposed to the charge sensitive mode in the spectrum polarized along the *c* axis. We note also that the bands at 1570 and 1541 cm^{-1} have a doublet structure. While it is difficult to interpret this last observation without calculations of vibrational modes, we suggest that this is due to a slightly different ionicity of TCNQ-F_2 in the DA stack and in the DAD trimer. The spectral shifts of these modes result in an estimated ionicity, dependent on which peak of the doublet is considered, ranging from 0.10 to 0.22. However, on the basis of the data collected so far it is not possible to clearly distinguish between the ionicity of TCNQ-F_2 in the DAD trimers from the one in DA stacks.

Perylene:TCNQ-F_4 Cocrystals. Figure 3e,f shows the two stoichiomorphs that we have obtained. While the 1:1 stoichiomorph shown here is not reported thus far, the 3:2 structure in Figure 3f confirms the structural data by Tsutsumi and co-workers (CCDC: NUSZUY).[47] The 1:1 structure was obtained only from solution growth and is characterized by a row of molecules with DA stacking. Initially we characterized a 1:1:1 solvated structure where the third component was a toluene molecule from the solvent, as reported in Figure S6 and Table S1. Note that the toluene molecule in the unit cell shows orientational disorder. A full desolvation of this system could be obtained after a few days in the atmosphere, resulting in the structure shown in Figure 3e. Several attempts to grow the perylene:TCNQ-F_4 by vapor transport did not produce crystals large enough for a detailed crystallographic analysis. In fact, the growth by vapor transport with the cold end of the ampule held at 403 K leads to the formation of the 3:2 stoichiomorph or very small crystals with undetermined structure.

The 1:1 perylene:TCNQ-F_4 crystal has a triclinic unit cell with $P\bar{1}$ symmetry and one pair of molecules per unit cell. The DA regular stack is along the *a* axis with the perylene and TCNQ-F_4 molecular planes tilted by 1.68°. The perylene molecule is planar and the DA distance between the perylene molecular plane and the TCNQ-F_4 centroid is one of the shortest among all compounds, 3.235 Å.

The 3:2 stoichiomorph is shown in Figure 3f and exhibits a structure similar to the one reported in Figure 3d for the 3:2 cocrystal with TCNQ-F_2, as the two crystals are isostructural. The unit cell is triclinic with space group $P\bar{1}$ and two pairs of inequivalent molecules. A detailed analysis of the inclination between the perylene and TCNQ-F_4 molecular planes reveals that in the two DAD trimer stacks there are angles of 2.17° and 1.95°, respectively. In the perpendicularly oriented DA stacks the molecular planes are instead parallel. The distances between perylene and TCNQ-F_4 are 3.269 and 3.210 Å in the two DAD trimers, respectively, and 3.284 Å in the DA stack. The perylene in the DA stack is not planar with an angle of 0.72° between the biphenyls.

The lowest electronic transition in the 1:1 structure has an onset at 5700 cm^{-1} (0.71 eV), which is mainly polarized parallel to the crystal growth direction, likely the *a* axis of the unit cell (Figure S7a). This is the lowest optical gap among the materials presented in this study and corresponds to an onset for light absorption of wavelength close to 1.82 μm. In Figure 6 (top) we report the vibrational spectra for polarizations parallel to the *a* (red curve) and *b* (blue curve) axes. Those are compared with the spectrum of neutral perylene and TCNQ-F_4. The spectra of neutral and fully ionized TCNQ-F_4 reported in Figure S8 have been extensively described in the literature, and we focus here on the charge sensitive modes at 1396, 1550, and 1599 cm^{-1} (ref 27). In the cocrystal the mode at 1599 cm^{-1} shifts down to 1581 cm^{-1} showing a weak dependence on polarization, which is mainly due to the orientation of its transition dipole moment, not perfectly aligned with the *a* crystallographic axis (Figure 3e). The ionicity ρ from the three modes is 0.30, 0.25, and 0.32, respectively, suggesting a substantial transfer of charge from the perylene to TCNQ-F_4.

In the 3:2 stoichiomorph the optical absorption from charge transfer excitons shows an onset at 5500 cm^{-1} (0.68 eV) when

DOI: 10.1021/acs.cgd.5b01663
Cryst. Growth Des. 2016, 16, 3028−3036

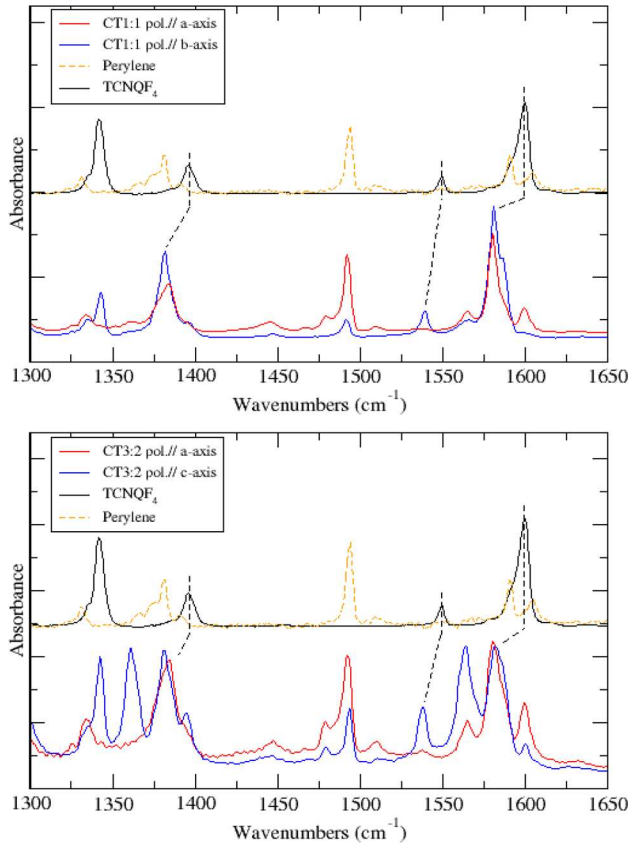

Figure 6. (Top) Vibrational spectra of TCNQ-F_4 (black solid line) and perylene (orange dashed line) together with perylene:TCNQ-F_4 1:1 for polarizations parallel to the *a* axis (red) and parallel to the *b* axis (blue). (Bottom) Vibrational spectra of perylene:TCNQ-F_4 3:2 for polarizations parallel to the *a* axis (red) and to the *c* axis (blue).

the light is polarized along the main direction of crystal growth. This onset is shifted to 6200 cm^{-1} (0.77 eV) when the light polarization is turned by 90° (Figure S7b). From these observations, we can extrapolate that the long axis of the crystal corresponds to the *a* axis of the unit cell, where the coupling with the transition dipole moment of CT excitons in the DA stack is optimal. When the light polarization is rotated we are instead probing in a direction almost parallel to the crystallographyc axis *c*, and therefore this band is associated with the CT excitons within the trimer. This assignment allows us to clearly distinguish the degree of charge transfer from the dichroism of the charge sensitive vibrations of TCNQ-F_4. Figure 6 (bottom) shows the spectra for the two polarizations in the range 1300−1650 cm^{-1}. The investigated modes are the same as for the 1:1 cocrystal, and small shifts can be noticed for the two polarizations, with the exception of the 1580 cm^{-1} band, in which the polarization parallel to *a* results in a weak intensity signal at the noise level. From the peaks and their polarizations, values of ρ of 0.29, 0.22, and 0.28 are found in the DA stack, whereas the values in the DAD trimers are 0.30 and 0.28. These are on average larger when compared to the interval of ρ (0.1−0.22) estimated for the isostructural stoichiomorph perylene:TCNQ-F_2. Considering that the structural differences between these 3:2 stoichiomorphs are minimal, the larger ρ and low optical bandgap for the TCNQ-F_4 based cocrystals arise from the larger electronegativity of this acceptor molecule.[48]

DISCUSSION

There is a similarity between the polymorphs of perylene and the stoichiomorphs that we have observed combining perylene with TCNQ-F_x in cocrystals. The sandwich structural motif of α perylene seems to be maintained with the insertion of a TCNQ acceptor in between the perylenes in all the stoichiomorphs with imbalanced ratios, i.e., 3:1 and 3:2. These structures are all characterized by perylene molecules deviating from perfect planarity, in a way similar to α perylene. In addition, both 3:2 structures have trimers with a herringbone arrangement. These structural similarities, together with the evidence that 3:1 and 3:2 stoichiomorphs are observed predominantly when the temperatures in the furnace are set above the phase transition temperature of β to α perylene (~420 K), indicate that the polymorphism of perylene could guide the stoichiomorphism in cocrystals. This rationale is also supported by the observation that 1:1 stoichiomorphs can be obtained only by setting below 420 K the low temperature part of the ampule, where nucleation and growth occur, or by growing the crystals from solution at room temperature (perylene:TCNQ-F_4). However, the recent preparation of DA stoichiomorphs from other compounds, coronene:TCNQ,[49] where pure coronene is not known to have room temperature stable polymorphs, indicates that stoichiomorphism in cocrystals can be encountered independently of the D aromatic hydrocarbon structures. Therefore, this guiding effect cannot be generalized and a more in depth analysis of the intermolecular interactions is required to understand the structural motifs guiding cocrystal formation. In the 1:1 stoichiomorphs there seems to be a more pronounced role of TCNQ-F_x in driving the details of the molecular arrangement in the cocrystals. For example, the increasing fluorine substitution leads to slipped stacks in perylene:TCNQ-F_2 and perylene:TCNQ-F_4. These slipped stacks are also encountered when looking along the *a* axis of the dimerized DA rows in the two almost identical 3:2 stoichiomorphs.

In general, the ionicity ρ reported in Table 1 for all compounds shows an increasing trend with the electro-

Table 1. Degree of CT ρ and Peak/Onset of CT Exciton Absorption in Perylene:TCNQ-Fx Cocrystals

compound	ρ	ω_{CT}(eV)
perylene:TCNQ (1:1)	~0.0	1.34[a] onset 1.05 eV[a]
perylene:TCNQ-F_2 (1:1)	0.13	onset 0.88
perylene:TCNQ-F_4 (1:1)	0.29	1 eV[b] onset 0.71
perylene:TCNQ (3:1)	0.20	1.3[c] onset 1.12 eV[c]
perylene:TCNQ-F_2 (3:2)	0.13/0.15	onset 0.88
perylene:TCNQ-F_4 (3:2)	0.26 (dimer) 0.29 (trimer)	onset 0.68

[a]From ref 40. [b]From ref 50. [c]From ref 40.

negativity of TCNQ-F_x in 1:1 cocrystals, but not a monotonic trend in the other stoichiomorphs, and it is strongly correlated with the structure of the cocrystals. A common aspect that we want to discuss here is how the ionicity changes from the DAD trimers to the DA dimer structures. We observe that, when considering the same starting perylene:TCNQ-Fx couple, trimers, i.e., DAD, exhibit larger values of ρ in all the cocrystals. This could have a simple explanation connected to the availability of nearest neighbor perylene donors in the structure.

DOI: 10.1021/acs.cgd.5b01663
Cryst. Growth Des. 2016, 16, 3028−3036

In other words, in a simple picture a TCNQ-F_x molecule in a dimer stack has only one perylene molecule with which can undergo a charge transfer interaction, whereas in a trimer more perylene donors can transfer charge density.

We now shortly comment on the perspective of charge transport and optoelectronic applications for the cocrystals reported here. Transport and optoelectronic properties of perylene-TCNQ 1:1 and 3:1 have been already characterized,[24,25] whereas the generation of photocarrier has been investigated in perylene:TCNQ-F_4 3:2.[47] The transport properties along the mixed stack chain are connected to the superexchange or effective integral t^{eff} (t_{DAD} for holes and t_{ADA} for electrons), which in 1:1 perylene:TCNQ has been calculated in the range 50−70 meV for both holes and electrons.[24,25] In perturbation theory the superexchange integral is connected to the direct CT integral t_{DA} and to Δ, the gap energy between DA and D^+A^- states in a DA pair:[4]

$$t^{eff} = \frac{t_{DA}^2}{\Delta}$$

For perylene-TCNQ 1:1 $t_{DA} \approx 0.3$ eV (see above), and from the optical gap we estimate $\Delta \approx 1$ eV, so that the above equation gives $t^{eff} \approx 90$ meV, against the calculated 50−70 meV. We can then use perturbation theory to predict that the 1:1 cocrystal of perylene:TCNQ-F_2 should have a greater t^{eff}, since preliminary calculations show that t_{DA} is more or less the same, whereas Δ is certainly lower than the perylene:TCNQ homologue. According to the experiments by Tsutsumi et al.,[47] the TCNQ-F_2 should exhibit good photocarrier generation and transport. We finally remark that for the three 1:1 cocrystals of perylene with TCNQ-F_x the optical gap, i.e., the energy of the CT transition, follows the well know linear relationship with ΔE_{REDOX}, i.e., the difference between the oxidation potential of D and the reduction potential of A.[50] Indeed, the reduction potential of TCNQ-F_2 (0.41 V vs SCE) is about halfway between that of TCNQ (0.22 V) and TCNQ-F_4 (0.60 V),[51] as does the optical gap (Table 1).

The 1:1 cocrystal with TCNQ-F_4 is the closest to the neutral-ionic transition boundary, like for the CT cocrystal tetrathiafulvalene-chloranil, and indeed it exhibits the neutral-ionic transition under pressure.[50] This characteristic may lead to interesting ferroelectric and ferromagnetic phenomena. Since crystals of this compound have been obtained from solution, it would be interesting to explore the possibility to finely control their yield by using different solvents as it was recently done for perylene:TCNQ.[52] The structure of 3:2 stoichiomorphs is particularly interesting, since they could show anisotropic exciton and charge carrier transport in two orthogonal directions. In addition, we note that very similar CT cocrystals are known to have a large third order optical nonlinearity and could be exploited in photonic applications for frequency conversion or light modulation.[53] Future work will focus on the nature of CT excitons and charge carrier photogeneration phenomena as well as nonlinear optical processes by time-resolved spectroscopy in the NIR.[54]

CONCLUSION

We have reported the growth and design of some novel crystal structures based on perylene and TCNQ-F_x DA compounds. Interestingly, we have found that the cocrystals differ in stoichiometry and crystal structure, giving rise to the phenomenon of stoichiomorphism, can be guided by choosing growth temperatures above and below the phase transition temperature between perylene polymorphs. We notice a correlation between electronegativity and degree of charge transfer in the DA couples, but also an important role of structure in which trimeric assemblies result in a higher ionicity of the TCNQ-F_x molecules. The 3:2 stoichiomorphs of perylene with TCNQ-F_2 and TCNQ-F_4 exhibit optical gaps in the NIR part of the spectrum and a structure that is ideal for transport of charge and excitations in two perpendicular directions. This unique features promise a great potential for applications in organic optoelectronics. The results are also of importance for understanding CT interfaces between laminated pairs of single crystals.[55−57]

ASSOCIATED CONTENT

Supporting Information

The Supporting Information is available free of charge on the ACS Publications website at DOI: 10.1021/acs.cgd.5b01663.

Infrared spectra of TCNQ, K:TCNQ, TCNQ-F_2, K:TCNQ-F_2, TCNQ-F_4, K:TCNQ-F_4. NIR spectra of all cocrystals and table with structural parameters (PDF)

Accession Codes

CCDC 1439123−1439130 and 1472427 contain the supplementary crystallographic data for this paper. These data can be obtained free of charge via www.ccdc.cam.ac.uk/data_request/cif, or by emailing data_request@ccdc.cam.ac.uk, or by contacting The Cambridge Crystallographic Data Centre, 12, Union Road, Cambridge CB2 1EZ, UK; fax: +44 1223 336033.

AUTHOR INFORMATION

Corresponding Author

*E-mail: edc25@bath.ac.uk.

Present Address

[∇]Cavendish Laboratory, University of Cambridge, JJ Thomson Avenue, CB3 0HE Cambridge, United Kingdom

Notes

The authors declare no competing financial interest.

ACKNOWLEDGMENTS

The work in Bath has been supported by the GW4 grant "Biomimetic Assemblies of Complex Functional Materials in Hierarchical Structures" and by the Royal Society with a Wolfson Laboratory Refurbishment grant. T.S. is grateful to Progetto Marco Polo for an exchange visiting program to University of Bath. Work in Parma and Bologna has been supported by the Italian Ministry of University and Research (M.I.U.R.) under the Project PRIN-2010ERFKXL.

REFERENCES

(1) Podzorov, V. *MRS Bull.* **2013**, *38*, 15.
(2) Schweicher, G.; Olivier, Y.; Lemaur, V.; Geerts, Y. H. *Isr. J. Chem.* **2014**, *54*, 595.
(3) Goetz, K. P.; Vermeulen, D.; Payne, M. E.; Kloc, C.; McNeil, L. E.; Jurchescu, O. D. *J. Mater. Chem. C* **2014**, *2*, 3065.
(4) Zhu, L. Y.; Yi, Y. P.; Li, Y.; Kim, E. G.; Coropceanu, V.; Bredas, J. L. *J. Am. Chem. Soc.* **2012**, *134*, 2340.
(5) Goetz, K. P.; Fonari, A.; Vermeulen, D.; Hu, P.; Jiang, H.; Diemer, P. J.; Ward, J. W.; Payne, M. E.; Day, C. S.; Kloc, C.; Coropceanu, V.; McNeil, L. E.; Jurchescu, O. D. *Nat. Commun.* **2014**, *5*, 5642.
(6) Park, S. K.; Varghese, S.; Kim, J. H.; Yoon, S. J.; Kwon, O. K.; An, B. K.; Gierschner, J.; Park, S. Y. *J. Am. Chem. Soc.* **2013**, *135*, 4757.

DOI: 10.1021/acs.cgd.5b01663
Cryst. Growth Des. 2016, 16, 3028−3036

(7) Sikdar, N.; Jayaramulu, K.; Kiran, V.; Rao, K. V.; Sampath, S.; George, S. J.; Maji, T. K. *Chem. - Eur. J.* **2015**, *21*, 11701.
(8) Hiszpanski, A. M.; Baur, R. M.; Kim, B.; Tremblay, N. J.; Nuckolls, C.; Woll, A. R.; Loo, Y. L. *J. Am. Chem. Soc.* **2014**, *136*, 15749.
(9) Botoshansky, M.; Herbstein, R. H.; Kapon, M. *Helv. Chim. Acta* **2003**, *86*, 1113.
(10) Metrangolo, P.; Neukirch, H.; Pilati, T.; Resnati, G. *Acc. Chem. Res.* **2005**, *38*, 386.
(11) Tiekink, E. R. T. *Chem. Commun.* **2014**, *50*, 11079.
(12) Brillante, A.; Bilotti, I.; Della Valle, R. G.; Venuti, E.; Girlando, A. *CrystEngComm* **2008**, *10*, 937.
(13) Mas-Torrent, M.; Rovira, C. *Chem. Rev.* **2011**, *111*, 4833.
(14) Ando, M.; Kehoe, T. B.; Yoneya, M.; Ishii, H.; Kawasaki, M.; Duffy, C. M.; Minakata, T.; Phillips, R. T.; Sirringhaus, H. *Adv. Mater.* **2015**, *27*, 122.
(15) Giri, G.; Verploegen, E.; Mannsfeld, S. C. B.; Atahan-Evrenk, S.; Kim, D. H.; Lee, S. Y.; Becerril, H. A.; Aspuru-Guzik, A.; Toney, M. F.; Bao, Z. A. *Nature* **2011**, *480*, 504.
(16) Ganin, A. Y.; Takabayashi, Y.; Jeglic, P.; Arcon, D.; Potocnik, A.; Baker, P. J.; Ohishi, Y.; McDonald, M. T.; Tzirakis, M. D.; McLennan, A.; Darling, G. R.; Takata, M.; Rosseinsky, M. J.; Prassides, K. *Nature* **2010**, *466*, 221.
(17) Grell, M.; Bradley, D. D. C.; Ungar, G.; Hill, J.; Whitehead, K. S. *Macromolecules* **1999**, *32*, 5810.
(18) Da Como, E.; Scheler, E.; Strohriegl, P.; Lupton, J. M.; Feldmann, J. *Appl. Phys. A: Mater. Sci. Process.* **2009**, *95*, 61.
(19) Desiraju, G. R. *Crystal Engineering: The Design of Organic Solids*; Elsevier: Amsterdam, 1989.
(20) Stahly, G. P. *Cryst. Growth Des.* **2007**, *7*, 1007.
(21) Stezowski, J. J.; Stigler, R. D.; Karl, N. *J. Chem. Phys.* **1986**, *84*, 5162.
(22) Bechgaard, K.; Kistenmacher, T. J.; Bloch, A. N.; Cowan, D. O. *Acta Crystallogr., Sect. B: Struct. Crystallogr. Cryst. Chem.* **1977**, *33*, 417.
(23) Cardelli, L. *BMC Syst. Biol.* **2014**, *8*, 18.
(24) Zhu, W. G.; Yi, Y. P.; Zhen, Y. G.; Hu, W. P. *Small* **2015**, *11*, 2150.
(25) Vermeulen, D.; Zhu, L. Y.; Goetz, K. P.; Hu, P.; Jiang, H.; Day, C. S.; Jurchescu, O. D.; Coropceanu, V.; Kloc, C.; McNeil, L. E. *J. Phys. Chem. C* **2014**, *118*, 24688.
(26) Farrugia, L. J. *J. Appl. Crystallogr.* **2012**, *45*, 849.
(27) Meneghetti, M.; Pecile, C. *J. Chem. Phys.* **1986**, *84*, 4149.
(28) Burger, A.; Ramberger, R. *Microchim. Acta* **1979**, *72*, 273.
(29) Desiraju, G. R.; Gavezzotti, A. *Acta Crystallogr., Sect. B: Struct. Sci.* **1989**, *45*, 473.
(30) Urbelis, J. H.; Swift, J. A. *Cryst. Growth Des.* **2014**, *14*, 5244.
(31) Pick, A.; Klues, M.; Rinn, A.; Harms, K.; Chatterjee, S.; Witte, G. *Cryst. Growth Des.* **2015**, *15*, 5495.
(32) Hammond, R. B.; Roberts, K. J.; Smith, E. D. L.; Docherty, R. *J. Phys. Chem. B* **1999**, *103*, 7762.
(33) Herbstein, F. H.; Kapon, M. *Crystallogr. Rev.* **2008**, *14*, 3.
(34) Long, R. E.; Sparks, R. A.; Trueblood, K. N. *Acta Crystallogr.* **1965**, *18*, 932.
(35) Krupskaya, Y.; Gibertini, M.; Marzari, N.; Morpurgo, A. F. *Adv. Mater.* **2015**, *27*, 2453.
(36) Emge, T. J.; Maxfield, M.; Cowan, D. O.; Kistenmacher, T. J. *Mol. Cryst. Liq. Cryst.* **1981**, *65*, 161.
(37) Tickle, I. J.; Prout, C. K. *J. Chem. Soc., Perkin Trans. 2* **1973**, 720.
(38) Hanson, A. *Acta Crystallogr., Sect. B: Struct. Crystallogr. Cryst. Chem.* **1978**, *34*, 2339.
(39) Truong, K. D.; Bandrauk, A. D. *Chem. Phys. Lett.* **1976**, *44*, 232.
(40) Ishii, K.; Yakushi, K.; Kuroda, H.; Inokuchi, H. *Bull. Chem. Soc. Jpn.* **1984**, *57*, 3043.
(41) Ida, T.; Yakushi, K.; Kuroda, H. *J. Chem. Phys.* **1989**, *91*, 3450.
(42) Bandrauk, A. D.; Truong, K. D.; Carlone, C. *Can. J. Chem.* **1982**, *60*, 588.
(43) Girlando, A.; Bozio, R.; Pecile, C.; Torrance, J. B. *Phys. Rev. B: Condens. Matter Mater. Phys.* **1982**, *26*, 2306.
(44) Bozio, R.; Zanon, I.; Girlando, A.; Pecile, C. *J. Chem. Soc., Faraday Trans. 2* **1978**, *74*, 235.
(45) Painelli, A.; Girlando, A. *J. Chem. Phys.* **1987**, *87*, 1705.
(46) Painelli, A.; Girlando, A. *J. Chem. Phys.* **1986**, *84*, 5655.
(47) Tsutsumi, J.; Matsui, H.; Yamada, T.; Kumai, R.; Hasegawa, T. *J. Phys. Chem. C* **2012**, *116*, 23957.
(48) Kanai, K.; Akaike, K.; Koyasu, K.; Sakai, K.; Nishi, T.; Kamizuru, Y.; Nishi, T.; Ouchi, Y.; Seki, K. *Appl. Phys. A: Mater. Sci. Process.* **2009**, *95*, 309.
(49) Yoshida, Y.; Shimizu, Y.; Yajima, T.; Maruta, G.; Takeda, S.; Nakano, Y.; Hiramatsu, T.; Kageyama, H.; Yamochi, H.; Saito, G. *Chem. - Eur. J.* **2013**, *19*, 12313.
(50) Torrance, J. B.; Vazquez, J. E.; Mayerle, J. J.; Lee, V. Y. *Phys. Rev. Lett.* **1981**, *46*, 253.
(51) Saito, G.; Sasaki, H.; Aoki, T.; Yoshida, Y.; Otsuka, A.; Yamochi, H.; Drozdova, O. O.; Yakushi, K.; Kitagawa, H.; Mitani, T. *J. Mater. Chem.* **2002**, *12*, 1640.
(52) Hu, P.; Ma, L.; Tan, K. J.; Jiang, H.; Wei, F.; Yu, C.; Goetz, K. P.; Jurchescu, O. D.; McNeil, L. E.; Gurzadyan, G. G.; Kloc, C. *Cryst. Growth Des.* **2014**, *14*, 6376.
(53) Gotoh, T.; Kondoh, T.; Egawa, K.; Kubodera, K. *J. Opt. Soc. Am. B* **1989**, *6*, 703.
(54) Fischbach, S.; Gorbach, A. V.; Di Nuzzo, D.; Da Como, E. *Appl. Phys. Lett.* **2015**, *107*, 021103.
(55) Krupskaya, Y.; Lezama, I. G.; Morpurgo, A. F. *Adv. Funct. Mater.* **2016**, *26*, 2334.
(56) Alves, H.; Molinari, A. S.; Xie, H. X.; Morpurgo, A. F. *Nat. Mater.* **2008**, *7*, 574.
(57) Mathis, T.; Mattenberger, K.; Moll, P.; Batlogg, B. *Appl. Phys. Lett.* **2012**, *101*, 023302.

DOI: 10.1021/acs.cgd.5b01663
Cryst. Growth Des. 2016, 16, 3028−3036

Supporting information for the paper:

Guiding Structure in Cocrystals of Perylene with TCNQFx by Stoichiometry and Polymorphism

Tommaso Salzillo[±,§], Matteo Masino[¶], Gabriele Kociok-Köhn[⌉], Daniele Di Nuzzo[±], Elisabetta Venuti[§], Raffaele Guido Della Valle[§], Davide Vanossi[♦], Claudio Fontanesi[♣], Alberto Girlando[¶], Aldo Brillante[§], Enrico Da Como[±]*

[±] Department of Physics, University of Bath, Claverton Down, BA2 7AY Bath, United Kingdom

[¶] Dipartimento di Chimica, Parma University/INSTM-UdR Parma, 43124 Parma, Italy

[⌉] Chemical Characterisation and Analysis Facility (CCAF), University of Bath, Claverton Down, Bath, BA2 7AY, United Kingdom

[♦] Dipartimento di Scienze Chimiche e Geologiche, Universita' di Modena e Reggio Emilia, Via Campi 103, 41125 Modena, Italy

[♣] Dipartimento di Ingegneria Enzo Ferrari, Universita' di Modena e Reggio Emilia, Via P. Vivarelli, 10, 41125 Modena, Italy

[§] Dipartimento di Chimica Industriale Toso Montanari, Universita' di Bologna, Via Risorgimento 4, 40136 Bologna, Italy

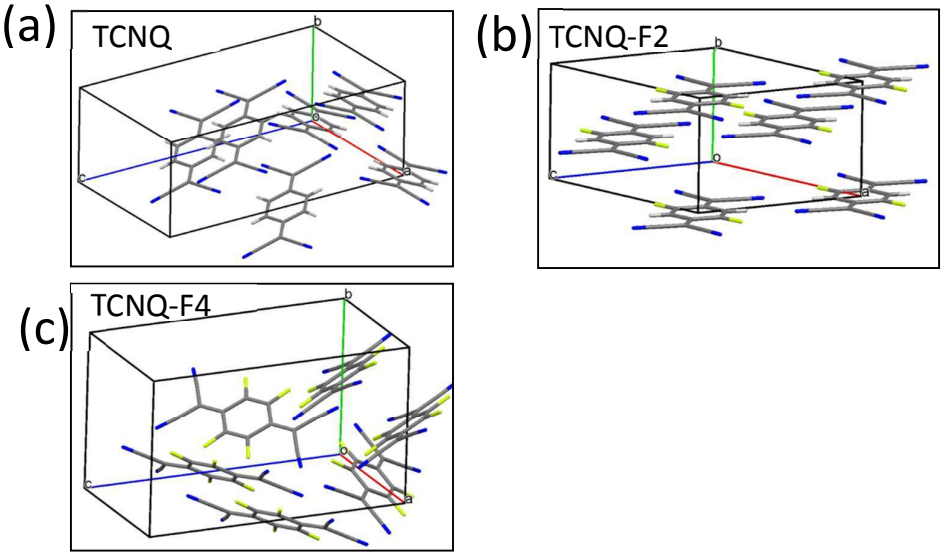

Figure S1. Crystal structures of (a) TCNQ, (b) TCNQ-F2 (from CCDC BERZON02), and (c) TCNQ-F4.

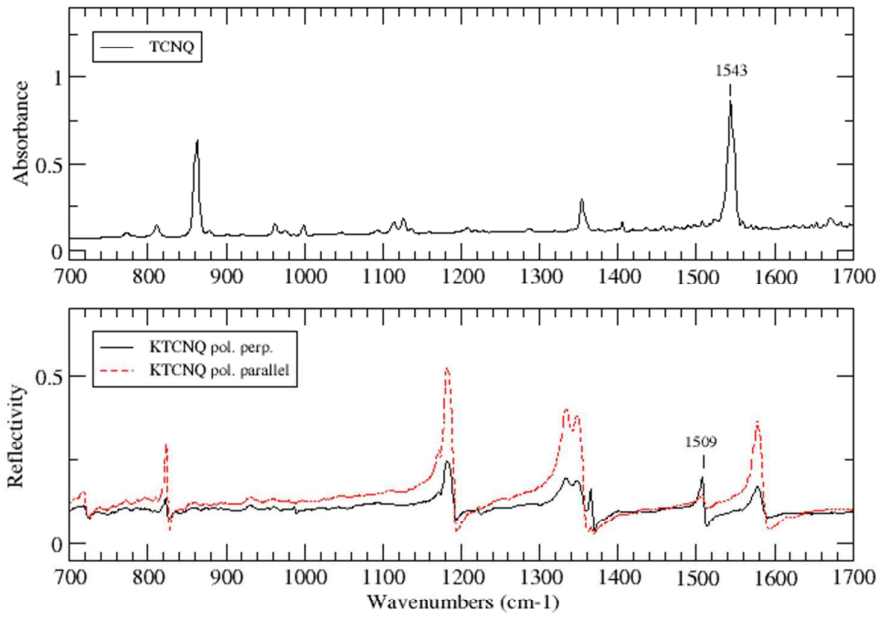

Figure S2. Upper panel: IR absorption spectrum of TCNQ. Lower panel: IR reflectivity spectra of K:TCNQ single crystal. Red dashed line corresponds to light polarized parallel to the TCNQ stacks, while black line refers to the perpendicular direction.

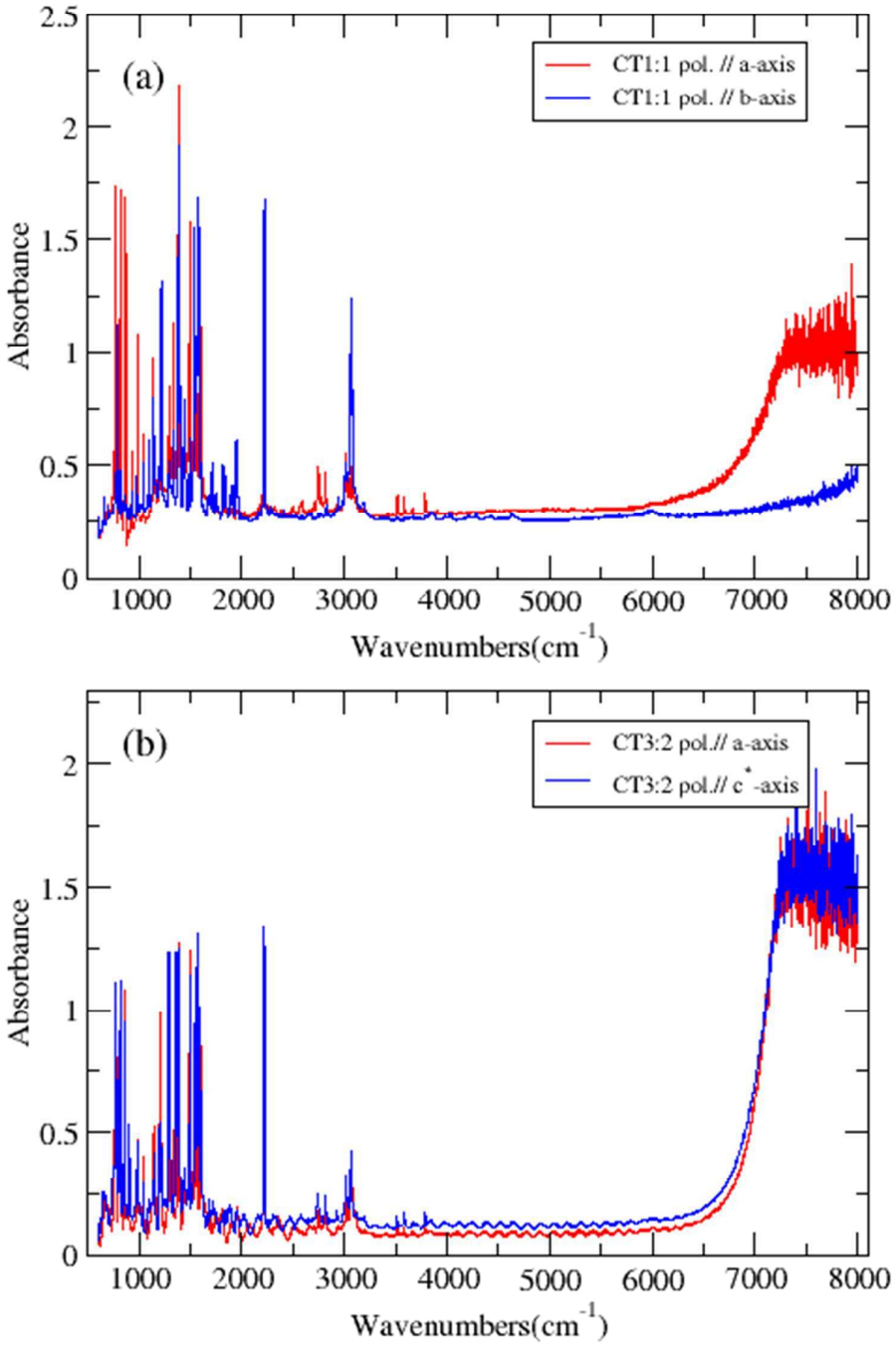

Figure S3. Extended polarized IR spectra (a) perylene:TCNQ-F_2 1:1 and (b) perylene:TCNQ-F_2 3:2.

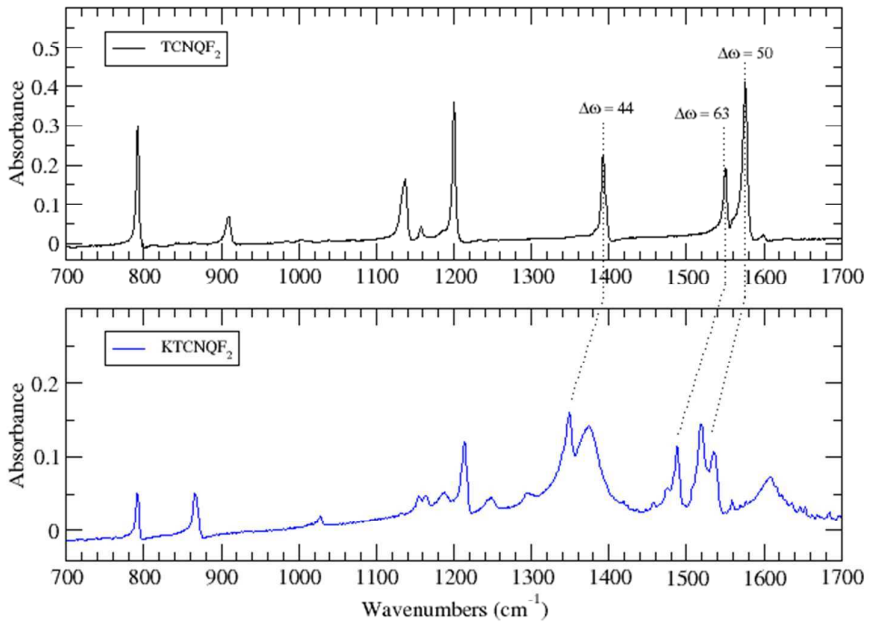

Figure S4. IR absortption spectra of TCNQ-F_2 (upper panel) and K:TCNQ-F_2 (lower panel).

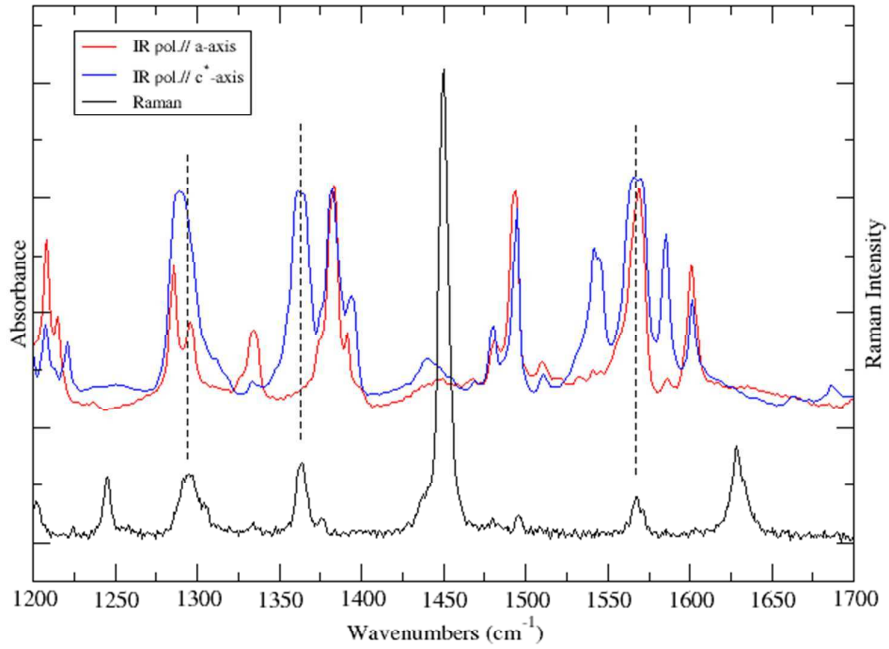

Figure S5. IR and Raman spectra of perylene:TCNQ-F_2 3:2. The vibronic features which are present in both IR and Raman spectra are indicated with dashed vertical lines.

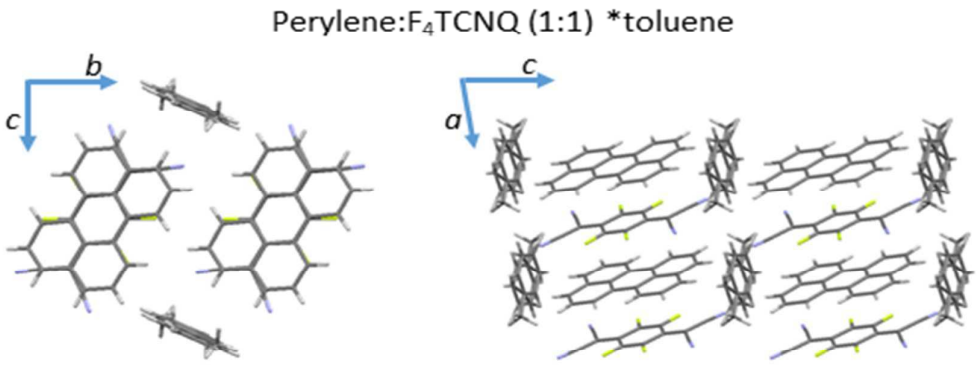

Figure S6. Crystal structure of perylene:TCNQ-F_4:Toluene 1:1:1. Projections on the *bc* and *ac* planes.

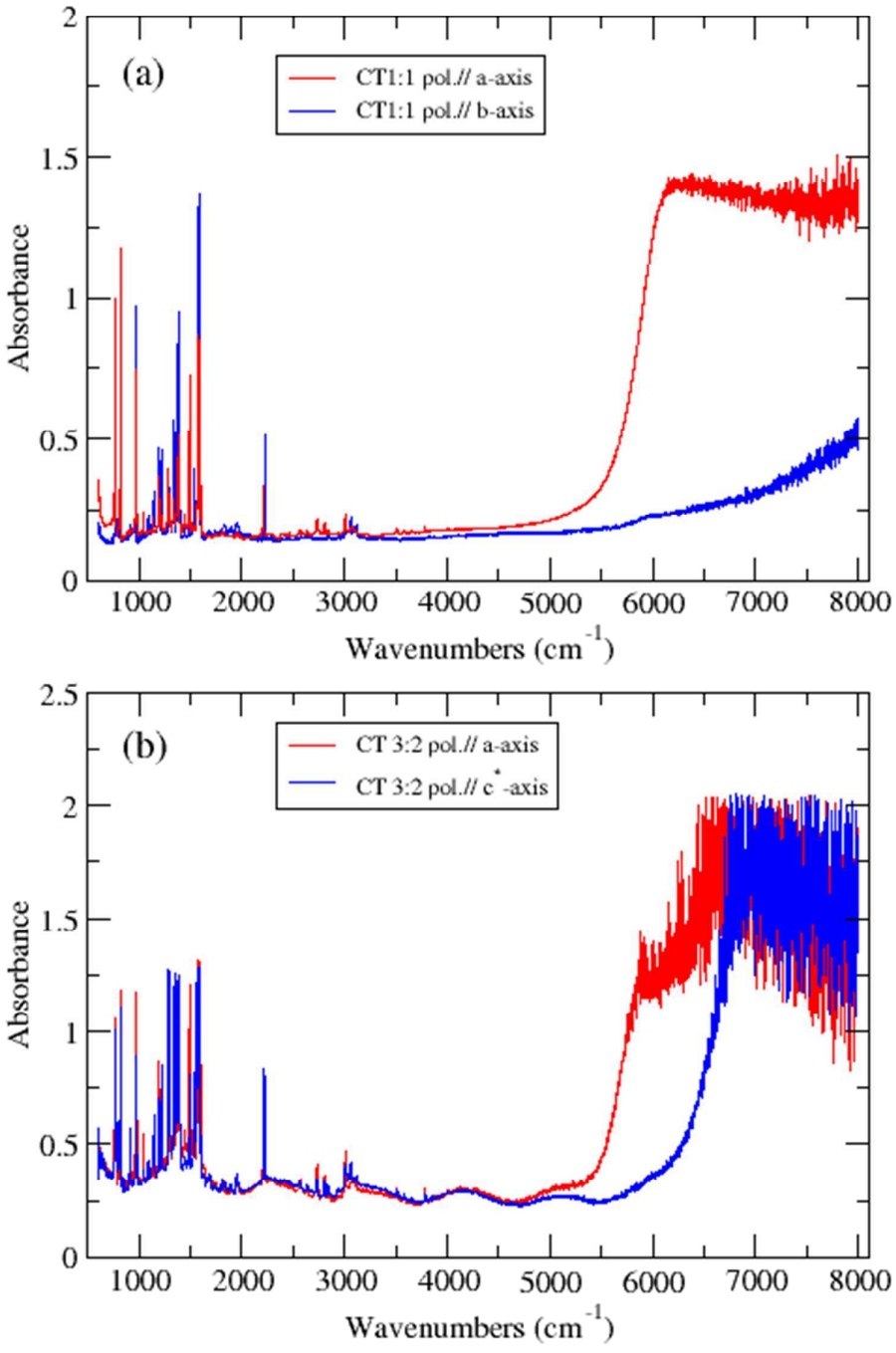

Figure S7. Extended polarized IR spectra (a) perylene:TCNQ-F4 1:1 and (b) perylene:TCNQ-F4 3:2 (b). The onset of the CT exciton bands is clearly observable in both systems.

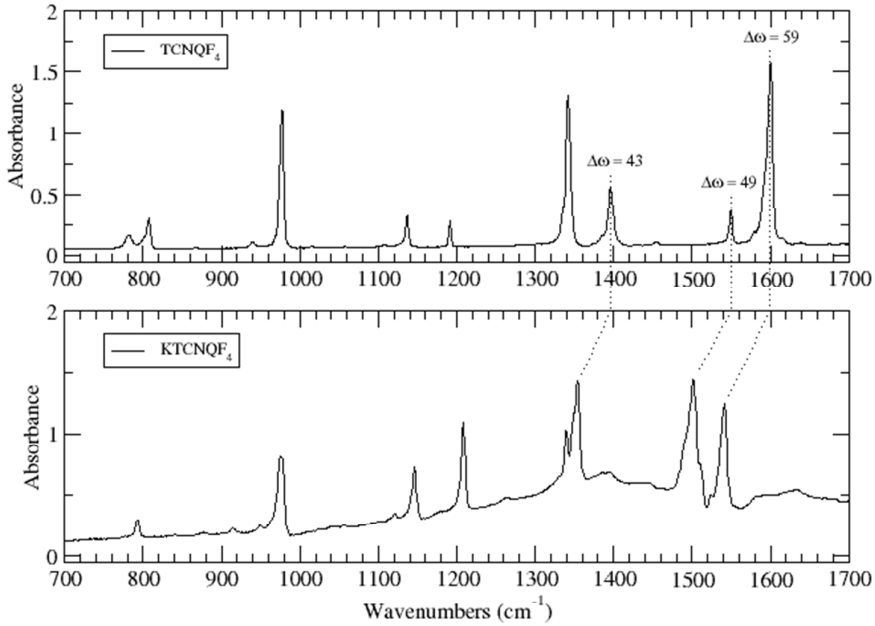

Figure S8. IR absortption spectra of TCNQ-F_4 (upper panel) and KTCNQ-F_4 (lower panel).

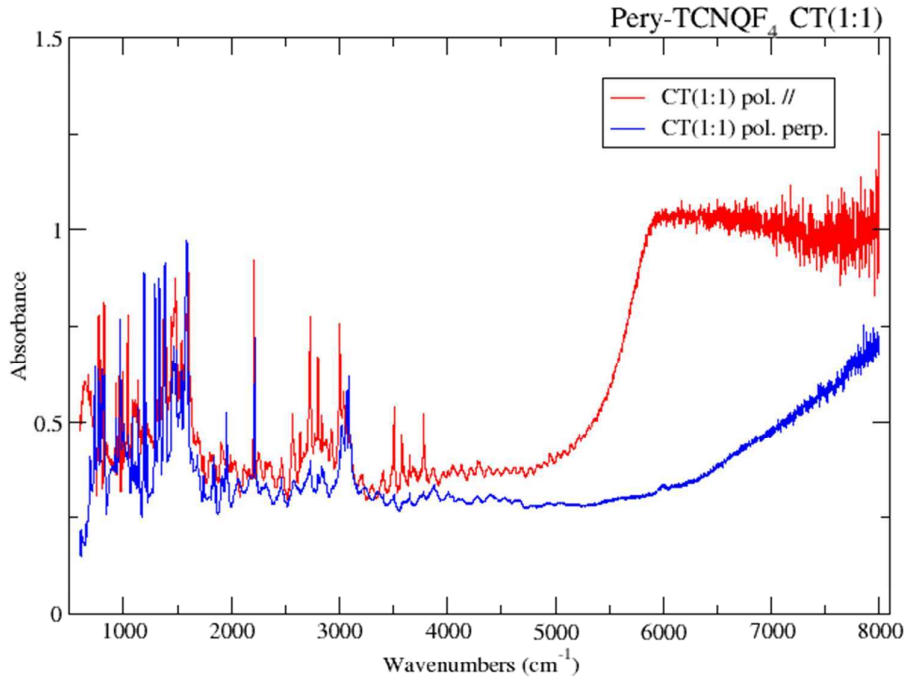

Figure S9. Extended polarized IR spectra of the solvated crystal perylene:TCNQ-F4:Toluene 1:1

Compound	Stoichiometry	Z	Space Group	*a* [Å]	*b* [Å]	*c* [Å]	α [°]	β [°]	γ [°]	Cell volume [Å^3]
Perylene: TCNQ	1:1	2	$P2_1/c$	7.2013 (5)	10.8390 (8)	14.4747 (11)	90	90.324 (4)	90	1129.8
	3:1	1	$P\bar{1}$	10.3446 (2)	10.8429 (3)	12.5107 (3)	112.4861 (13)	114.2810 (14)	91.3733 (13)	1154.2
Perylene: TCNQ-F_2	1:1	2	$P2_1/n$	7.0207 (3)	8.3738 (3)	19.2045 (6)	90	96.261 (3)	90	1122.3
	3:2	2	*P-1*	7.2307 (1)	19.1407 (3)	22.2723 (5)	112.2834 (8)	90.1900 (8)	93.7559 (12)	2844.85
Perylene: TCNQ-F_4	1:1:(1) (Toluene)	1	*P-1*	7.0293 (4)	8.4804 (8)	11.8703 (12)	89.557 (8)	81.968 (7)	86.069 (6)	699.013
	1:1	1	*P-1*	7.0298 (5)	7.2997 (4)	11.2870 (9)	104.116 (6)	101.913 (7)	90.449 (5)	548.576
	3:2	2	*P-1*	7.2066 (2)	19.0974 (6)	22.4050 (7)	111.8014 (14)	90.0472 (17)	94.1283 (17)	2854.3

Table S1. Structural parameters for all the investigated mixed compounds.

Compound	Space Group	*Z*	*a* [Å]	*b* [Å]	*c* [Å]	α [°]	β [°]	γ [°]	Cell volume [Å^3]
TCNQ	C2/c	4	8.8746(4)	6.9335(3)	16.4071(6)	90	98.315(4)	90	998.95
TCNQ-F$_4$	Pcab	4	8.0828(2)	9.2231(2)	14.5974(4)	90	90	90	1088.21

Table S2. Structural parameters for the pure TCNQ and TCNQ-F$_4$.

Addendum: on the electronic/optical band gap in Perylene/TCNQ-Fx cocrystals

This section deals with the calculation of intermolecular/intramolecular energy variations (accounting for geometrical differences between vacuum and condensed phases), also including dispersion interactions. This aiming to assess experimental data that can be obtained by elaborating both UV visible spectra (allowing to estimate the optical band gap) and Ultraviolet Photoelectron Spectroscopy (UPS) for the HOMO and Inverse Emission Electron Spectroscopy (IEES) for the LUMO. Knowledge of the HOMO and LUMO energies allows for the calculation of the electronic band gap. Indeed, experimentally estimated values of the optical bandgap, corresponding to the absorption onset and peak by charge transfer excitons, are reported in ref [[27]]. Theoretical calculations, both using localized orbital and de-localized planed wave basis sets (Gaussian 09 and VASP codes respectively), were exploited aiming to estimate the electronic, and optical, band gap. In this case experimental geometries were used, extracting the relevant dimers, and trimers, geometry parameters from the X-ray structures and used a localized orbitals code to calculate the HOMO-LUMO energy difference, net localized charges on the perylene and TCNQ-F_x molecules. TDDFT calculations, only in two selected cases, were used to evaluate the optical band gap. In addition, because our materials are single crystals, we have also used plane wave codes (PBE pure functional as well as B3LYP hybrid functional), VASP (Vienna Ab-initio code), to calculate the band structure and electron band gap. All the calculated results presented in this section are obtained, essentially, within the DFT framework. Moreover, we have included corrections for the van der Waals interactions, based on the Grimme model [104] as implemented in both the Gaussian and VASP codes. As reported in the table 1, see below, the calculated electronic band gap depends strongly on the level of the theory, in general showing a rather poor agreement with the experimental evidence. Eventually, also GW (time-ordered Green's function, within the Hedin's [117] dynamically screened interaction W) calculations were attempted, but definitively the computational run-time is well far beyond our present (and maybe also future) capabilities.

Table 1. Charge Transfer, ρ, and onset of CT exciton absorption in perylene/TCNQ-Fx cocrystals.

	Experimental[27]		**mPW2PLYPD/6-31G(d,f)⊥**			**Band Gap ‖**	
Compound	**ρ**	**ω_{CT}**	**Charge on FnTCNQ Mulliken**	**Interaction Energy (kcal/mol)**	**HOMO LUMO Energy gap**	**432 PBE**	**432 B3LYP**
		eV	**e**	**kcal/mol**	**eV**	**eV**	**eV**
perylene-TCNQ (1:1)	~ 0.0	1.34	-0.13207	-13.3374	3.0738	0.6412	1.3858
perylene-TCNQ-F_2 (1:1)	0.13	onset 0.88	-0.15293	-24.1980	2.9198	0.5662	1.24
perylene-TCNQ-F_4 (1:1)	0.26	onset 0.68	-0.22293	-28.5928	2.8213	0.5615	1.1812
perylene-TCNQ (3:1)	0.20	1.24	-0.15296	-22.5425	3.1146	0.6672	1.4143
perylene-TCNQ-F_2 (3:2)	0.13/0.15	onset 0.88					
perylene-TCNQ-F_4 (3:2)	0.26 (dimer) 0.29 (trimer)	onset 0.68	-0.2097	-17.7076	2.9089	0.3701	#
Perylene DIMER 05 α			NO CT	-6.9245	4.9797		
Perylene06 β - DIMER-T			NO CT	-4.8267	4.7285		
Perylene06 β - DIMER-Staggered			NO CT	-4.2862	4.9144		
Coronene DIMER Trotter			NO CT	-7.9662	5.746		

⊥ spin unrestricted, localize orbitals calculation, performed with Gaussian 09 [87]. The

mPW2PLYPD level of the theory (which includes dispersion energy correction by Grimme [104]) was selected as recently found to perform in a comparable way to CCSD (Coupled Cluster Single- Double substitutions) in small, non-covalently bound, molecular clusters [118].

‖ plane wave calculation, Projector augmented-wave PBE, 432 Monkhorst-Pack reciprocal space sampling, 400 eV energy cutoff. Calculations performed by using the VASP code [107,119]

calculation killed after six weeks running time

TD-DFT spin unrestricted, mPW2PLYPD/6-31G** level of the theory Gaussian 09 [87] calculations (only results for two sample systems are obtained due to very long computational run-time) yielded an optical band gap of 0.3593, 0.5309 eV for perylene-TCNQ (1:1) and the perylene-TCNQ-F_4 (3:2) trimer systems, respectively. The result for the perylene-TCNQ-F_4 (3:2) trimer compares reasonably with the experimental, 0.68 eV, value. The outcome for the perylene-TCNQ (1:1) cocrystal is definitively far from the experimental, 1.34 eV, value. Again, the theoretical calculation of the optical band gap, even exploiting localized basis sets, is an issue yet to be solved.

4.3 Hybrid Interface

4.3.1 Ferrocene Molecular Architectures Grafted on Si(111): a theoretical calculation of the standard oxidation potentials and electron transfer rate constant.

Preamble

In this work it is theoretically studied the charge transfer process active at a hybrid, donor/acceptor (D/A), interface: Si(111)–molecular spacer–Ferrocene, where the Ferrocene group is adsorbed on the Si(111) via a covalent bond. In this peculiar case the choice of the theoretical tools is not straightforward: both plane-waves and localized orbitals methods were considered, as well as the application of periodic boundary conditions (the system is thought to show translational symmetry in two dimensions). The main objective is the calculation of the charge transfer rate constant (K_{ET}), between the Silicon and the Ferrocene moieties by using the Marcus theory. The localized orbital approach was selected, using the "embedded cluster model" (that is, a "supermolecule" assumed to catch the essential properties of the infinite condensed system) to simulate such a system, which is actually infinite in the two dimensional domain. Two different spacers are considered: represented by a short, –O–CH_2–, and a long –$(CH_2)_{10}$–COO–CH_2– alkyl chains. Of course the use of the localized orbitals approach has advantages and disadvantages. Here, in particular, the main advantage is the possibility to "force" the electron distribution (quantitatively expressed by the Mulliken net charges) to simulate the not-ionized (D/A) and charge separated (D^+/A^-) states (such a results can be obtained following two different strategies i) suitable selection of the initial molecular orbitals guess and virtual MOs energy shifting, to avoid MOs swapping during the SCF iterations ii) the use of the Constrained DFT (CDFT), which allows to calculate the energy of a system with a "constrained", desired/arbitrary, net charge on an atom or group of atoms. The results (the K_{ET} values) are discussed as a function of the "length" of the two selected molecular spacers and discussed on the basis of experimental data available in the literature. While the theoretical values of K_{ET} reasonably agrees with experimental results, the value obtained for the longer molecular spacer (which features eleven –CH_2– alkyl carbons) yields a too low charge transfer rate constant. In particular, in the case of the long spacer, a dramatic experimental difference is found between the covalent or physically adsorbed Ferrocene systems, a situation which seems not correctly foreseen by the charge transfer rate constant calculated following Marcus theory.

The candidate contribution concerned the design of the research, the design and realization of the theoretical calculations (exploiting the Constrained DFT approach), and critical assembly of the global outcome leading to the final manuscript.

Statement of Authorship

<table>
<tr><td colspan="5">This declaration concerns the article entitled:

Ferrocene Molecular Architectures Grafted on Si(111): a theoretical calculation of the standard oxidation potentials and electron transfer rate constant.</td></tr>
<tr><td colspan="5">Publication status (tick one)</td></tr>
<tr><td>draft manuscript</td><td>Submitted X</td><td>In review</td><td>Accepted</td><td>Published</td></tr>
<tr><td colspan="5">Publication details (reference): submitted</td></tr>
<tr><td colspan="2">Candidate’s contribution to the paper (detailed, and also given as a percentage).</td><td colspan="3">The candidate contributed to the design of the research, theoretical interpretation and actual calculations (vide supra).

Formulation of ideas: 90 %

Design of methodology: 90 %

Experimental work: 50 %

Presentation of data in journal format: 70 %</td></tr>
<tr><td colspan="2">Statement from Candidate</td><td colspan="3">This paper reports on original research I conducted during the period of my Higher Degree by Research candidature.</td></tr>
<tr><td colspan="2">Signed  </td><td colspan="3">Date 15 May 2017</td></tr>
</table>

Publication title:
Ferrocene Molecular Architectures Grafted on Si(111): a theoretical calculation of the standard oxidation potentials and electron transfer rate constant.

the thesis page numbers that it spans:
137 to 148

Ferrocene Molecular Architectures Grafted on Si(111): a theoretical calculation of the standard oxidation potentials and electron transfer rate constant.

Claudio Fontanesi [a,d*], Massimo Innocenti[b], Davide Vanossi[c], Enrico Da Como[d*]

[a]DIEF, Univ. of Modena and Reggio Emilia, via Vivarelli 10, 41125 Modena, Italy.

[b]Dept. of Chemistry, Univ. of Firenze, via della Lastruccia 3, 50019 Sesto Fiorentino, FI, Italy.

[c]DSCG, Univ. of Modena and Reggio Emilia, via Campi 183, 41125 Modena, Italy.

[d]Dept. of Physics, Univ. Of Bath, Claverton Down, Bath BA2 7AY, United Kingdom

Abstract

The standard oxidation potential and the charge transfer rate constants of two silicon-based hybrid interfaces, Si(111)/organic–spacer/Ferrocene, are theoretically calculated and assessed. The two organic moieties –O–CH_2– and –$(CH_2)_{10}$–COO–CH_2– are selected as opposite *short* and *long* spacers, respectively. Standard potentials, calculated at the PBE0/6-31G* level of theory, indicate that the relevant electrochemical behaviour can be studied within normally accessible experimental conditions. Also the electron transfer (ET) rate constants, k_{ET}, are calculated and assessed within the "Marcus theory" framework (k_{ET} values are obtained making use of the Constrained Density Functional Theory (CDFT) formalism).

* author to whom correspondence should be addressed

1. Introduction

Beyond any possible doubt Silicon is a base material of uttermost importance for both applicative purposes and fundamental studies as well. [1] Indeed, in recent years we have seen a growing interest in hybrid silicon based molecular electronics (i.e. silicon based hybrid interfaces), driven by the possible applications in technological fields like biosensors, photovoltaic cells, and optoelectronic devices. [2,3] Different methodologies exist for the creation of hybrid silicon-based interfaces, relying on the covalent grafting of organic molecules, and these are generally based on ultra-high vacuum (UHV) depositions [4–6], wet chemistry exploiting UV curing [7,8], electrochemical based methodologies. [9,10] Among the possible species, grafting of redox-active molecules on the surface of silicon is of particular interest due to the excellent model system that these architectures provide for the study of electron transfer (ET) at interfaces, this allows for a tight comparison to the ample number of papers dealing with ferrocene-derivatives self-assembled monolayers adsorbed on gold [11]. Within this picture, the ferrocene/silicon interface is an intriguing system representative of the more than classical Donor-Spacer-Acceptor molecular system, due to ferrocene's peculiar electrochemical properties: low oxidation potential, almost ideal ET reversibility, fast ET rate and only two stable redox states. [12] Because of this, chemiadsorbed ferrocene moieties on silicon surfaces could be exploited in technical organic electronics applications, for instance as a memory element, where the ferrocene redox centre is used as the charge storage component and considering the molecule oxidation state (in the neutral or oxidized form) as the two states of a bit. [13] This kind of supramolecular architectures were experimentally characterized in a very wide manner as far the ET process is concerned [14–20], while from a theoretical point of view the fundamental knowledge of the ET dynamics, at an hybrid interface, is a subject yet open to discussion. [21,22] Within this picture, we study two different ferrocene molecular architectures onto a Si(111) surface, modelled as grafted via a covalent bond. The two systems here studied are characterized by the different length of the alkyl-chain (spacer) linking the ferrocene moiety to the surface: 1) methanol-ferrocene directly grafted on the surface (i.e. –O–CH_2– *short* spacer) 2) ferrocene grafted through a 1-iodoundecanoic acid (UA) monolayer (i.e. –$(CH_2)_{10}$–COO–CH_2– *long* spacer). The ET process is considered to occur from the ferrocene-donor (D) to the silicon-acceptor (A), following the ubiquitous two-diabatic-states reaction mechanism ($\boldsymbol{D\text{–}A \longrightarrow D^{+}\text{–}A^{-}}$) as shown in Scheme I [21,23]:

Scheme I

$$\boldsymbol{Si_M^{+}\text{–}Me-FC \longrightarrow Si_M\text{–}Me-FC^{+}}$$

$$\boldsymbol{Si_M^{+}\text{–}UA\text{–}FC \longrightarrow Si_M\text{–}UA\text{–}FC^{+}}$$

where: *Me* and *UA* represent the –O–CH_2– and –$(CH_2)_{10}$–COO–CH_2– spacers, respectively; Si_M is representative of the silicon electrode surface. Note that, the two hybrid interfaces devised in this paper are supposed to be of easy-common-lab practice synthesis: $\boldsymbol{Si_M–Me-FC}$ can be prepared by heating the Si(111) hydrogen terminated surface just in direct contact with methanol ferrocene, while $\boldsymbol{Si_M–UA–FC}$ can be obtained following a two-step procedure i) electrochemical grafting of 11-Bromoundecanoic acid ii) condensation reaction of the methanol ferrocene (all of these compounds are commercially available), experimental synthesis and electrochemical characterization are underway in our lab [24–27]. From the theoretical point of view, our main goal is the application, of the Marcus theory for the calculation of the ET rate constant [28,29] coupled with "Constrained Density Functional Theory (CDFT)" calculations, a theoretical tools allowing to evaluate and compare quantitatively energies of systems featuring a discrete net charge localization on suitably selected moieties [30,31]. Theoretical results are then discussed in the view of the experimental evidence present in the literature [9,7,17,32–37]. It is worthwhile to stress that the theoretical calculation of ET rate constants is none of a common business in the literature [38,39]. Moreover, some recent papers [21,22] point out that the Marcus model, which describes the ET dynamics in the incoherent limit [40], is not effective for a correct prediction of the ET rate constant.

2 Computational Details

DFT calculations were performed by using the NWChem [41] and Firefly (Firefly QC package [42], the latter is based on the GAMESS (US) [43] source code) programs. The interfaces here studied are modelled as a silicon cluster of ten Si atoms connected to the ferrocene group by Me (i.e. –O–CH_2– moiety) and UA (i.e, –$(CH_2)_{10}$–COO–CH_2– moiety) molecular spacers, compare Figure 1 (the valence of the silicon atoms not bound to the redox moiety is saturated with the suitable number of hydrogens). In the following the $Si_{10}H_{15}$ moiety will be indicated as Si_M. Screening full optimization geometry calculations were performed at the B3LYP/3-21G and PBE0/3-21G level of the theory, final geometries are obtained at the PBE0/6-31G* level of the theory. Geometries optimized in the gas phase were used to perform solvation energy calculation of the various species involved in the determination of the redox potential, following the modellistic approach proposed by Cramer and Truhlar [44–46]. The solute-solvent interaction was taken into account using the Barone and Cossi's polarizable conductor model (CPCM) [47]. Ionization potentials and solvation energies, needed to reckon the oxidation standard potentials, Cramer and Truhlar [44–46], are obtained at the PBE0/6-31G* level of the theory, which can be considered a reliable level of the theory in the calculation of standard potentials, on the basis of previous works. [25,44,45,48,49] Note that, PBE0/6-31G* level calculations proved to produce results

comparable, semi-quantitatively, to MP4/6-31G* data, when dealing with the redox reactivity of Fe acetylacetonate complex [50]. The overall computational procedure was finalized in obtaining not only the data needed for the computation of the standard potentials, but also the parameters that are necessary to calculate the physical quantities entering the Marcus equation [28,29] for the ET rate constant: k_{ET}, compare equation 2. To this end, the Constrained Density Functional Theory (CDFT) paradigm, developed by Van Voorhis as implemented in the NWChem suite of program [30,31,41], was used.

Figure 1

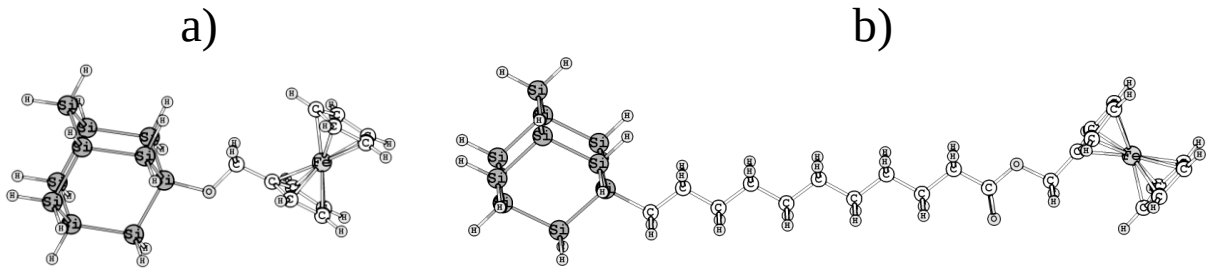

Figure 1. Molecular architectures grafted on the Si(111) slab: a) $Si_{10}H_{15}$–O–CH_2–FC cluster, in the text addressed as Si_M–Me–FC b) $Si_{10}H_{15}$–$(CH_2)_{10}$–COO–CH_2–FC cluster, in the text addressed as Si_M–*UA*–*FC*.

3 **Results and Discussion**

3.1 Standard oxidation potential calculation

The redox processes underlying the electrochemical behaviour of the chemi-adsorbed ferrocene is considered as a reversible single-step single-electron oxidation process, as it is shown in Scheme II, where: IP is the ionization potential and E^0_{OX} is the standard oxidation potential.

Scheme II

Si_M–$MeFC \rightleftharpoons Si_M$–$MeFC^+ + e^-$	⇔	IP (Si_M–$MeFC$)	⇔	E^0_{OX} (Si_M–$MeFC$)
Si_M–*UA*–*FC* $\rightleftharpoons Si_M$–*UA*–$FC^+ + e^-$	⇔	IP (Si_M–*UA*–*FC*)	⇔	E^0_{OX} (Si_M–*UA*–*FC*)

The calculation of the oxidation standard potential absolute value is carried on by using the Nernst equation, $\Delta G° = -nFE°$. Then, the standard reduction potential of the redox couple in solution is calculated as the sum of the individual contributions as sketched in Scheme II, which allows for the calculation of the standard potential for the redox process [44], in this case

$$H^+_{(aq)} + \mathbf{FC}_{(solv)} \leftrightharpoons 1/2\ H_{2(aq)} + \mathbf{FC}^+_{(solv)} \qquad \text{Eq. 1}$$

Where FC and FC^+ stand for both grafted and bulk ferrocene.

Scheme III

Thermodynamic cycle for the calculation of the redox potential.				
	$\mathbf{FC}_{(g)}$	$\rightarrow$ $\Delta G^0(I)$	$\mathbf{FC}^+_{(g)} + e^-$	
$\Delta G^0(II)_{(solv)}$	$\downarrow$		$\downarrow$	$\Delta G^0(III)_{(solv)}$
	$\mathbf{FC}_{(solv)}$	$\rightarrow$ $\Delta G^0(IV)$	$\mathbf{FC}^+_{(solv)} + e^-$	
	$H^+_{(aq)} + e^-$	$\rightarrow$ $\Delta G^0(H)$	$1/2\ H_{2(aq)}$	
$\Delta G^0(H)$ = 4.44 eV, see: Trasatti, S. Pure Appl.Chem.1986, 58, 955				

The standard Gibbs energy variation of the whole redox process, equation 1, is determined as the sum of the two contributions due to the **FC**/**FC**$^+$ couple and hydrogen reduction half-reactions; thus, $\Delta G°_{ox}$(**FC**/**FC**$^+$ vs NHE) = $\Delta G°$(IV) + $\Delta G°$(H). In Scheme III, the step IV is the half-reaction Gibbs energy variation of the oxidation process: $\Delta G°(IV) = \Delta G°(I) + \Delta G^0(III)_{(solv)} - \Delta G^0(II)_{(solv)}$. In detail: $\Delta G°(I) = IP + \Delta G°_{evr,gas}$. IP is the ionization potential and the $\Delta G°_{evr,gas}$ term reflects the difference in thermal contributions to the Gibbs energy of the redox system due to changes in the electronic, vibrational, and rotational partition functions, upon the oxidation process (where reference is made to the $\mathbf{FC}_{(g)} \rightarrow \mathbf{FC}^+_{(g)} + e^-$ reaction). In the present work the contribution of the $\Delta G°_{evr,gas}$ has been neglected because its value is often found negligible, despite the time and resource costs needed for its calculation; a course of procedure already adopted and justified in the literature [25,44,45,48,49,51]. $\Delta G^0(II)_{(solv)}$ and $\Delta G^0(III)_{(solv)}$ are the solvation Gibbs energies of the reduced and oxidized species respectively, the two lateral branches of Scheme III. Note that, the solvation terms in Scheme III actually refer to a bulk solvation process, in the present case the situation is somehow different in that the redox couple is adsorbed on the electrode surface. We calculated the solvation energy of the clusters as they are shown in Figure 1, i.e. the whole cluster is considered solvated. The solvation energy contribution of the silicon cluster[1] is assumed both negligible in absolute value and almost constant (thus, cancelling out in the calculation of the whole variation of the solvation energy contribution, when the difference between the solvation energies of the reduced and oxide species, $\Delta G°_s$(III) - $\Delta G°_s$(II), is reckoned). Gas phase optimized geometries were used for all the calculations, following the approach proposed by Cramer and Truhlar [44–46]. Table I sets out the actual data needed for the calculation of the theoretical standard potential values: E° values of 0.609 and 0.627 V vs SCE are obtained for the Si_M–$MeFC$ and Si_M–UA–FC species,

[1] The part which is not in contact with the solution, i.e. the hydrogens bound to the silicon atoms.

respectively. In the case of bulk ferrocene, considered as a relevant benchmark in this context, following our approach, we obtain E^0 = 0.528 V vs SCE oxidation potential, which has to be compared with the experimental value 0.551 V vs SCE [52]. The good agreement[2] between experimental and theoretical data (usually larger errors are found [25,44,48,49]) indicates that the selected level of the theory and modelistic representation of this hybrid interface is able to i) "describe" reliably the electronic characteristics of the species involved in the charge transfer process ii) the molecular clusters (Figure 1), simulating the Si(111)/organic–spacer/Fc interface, are able to account for the essential physical features of the electronic properties of the experimental system.

Table I. PBE0/6-31G* theoretical values used to calculate the standard potential

	Energy Ox species	$\Delta G^0(III)_{(solv)}$		Energy Red species	$\Delta G^0(II)_{(solv)}$	
	a.u.	kcal mol^{-1}		a.u.	kcal mol^{-1}	
		Total	Elec. [a]		Total	Elec. [a]
$Si_M–UA–FC$	–5172.168587	–5.78	–47.14	–5172.41199	35.55	–5.81
$Si_M–Me–FC$	–4666.305597	–5.65	–42.34	–4666.544377	33.21	–3.48
FC	–1649.745848	–40.38	–44.53	–1649.986325	1.43	–2.66

[a] Electrostatic contribution

3.2 Dynamics

To assess on a quantitative basis the kinetics of the ET process, k_{ET} (Table I) values are calculated using the Marcus theory framework [21,23,41]:

$$k_{ET} = \frac{2\pi}{\hbar} V_{RP}^2 \frac{1}{\sqrt{4\pi\lambda k_B T}} exp\left(-\frac{\Delta E_f^{act}}{k_B T}\right) \qquad \text{Eq. 2}$$

where k_{ET} is ET rate constant. The theoretical calculation of k_{ET} (at T = 298 K) requires knowledge of the values of the reorganization energy (λ) the activation energy (ΔE_f^{act}) and the electronic coupling constant, V_{RP}, often addressed as the "matrix element or direct transfer integral" [56]. λ is

[2] We selected a 4.44 V value for the absolute hydrogen electrode potential following Trasatti [53], which is different from the 4.42 V estimation by Tissandier. [54] See also a quite interesting and thoroughly discussion on this subject published by Tripkovic and Rossmeisl. [55] Eventually note that also the experimental values are affected by a ±5 mV error in accuracy, in the best case scenario. All in all, to pursue a difference much less than 70 mV, between experimental and theoretical potential values, is not physically sensible.

usually factorized in the two inner (λ_i) and outer (λ_o) reorganization energies terms, with $\lambda = \lambda_i + \lambda_o$ and, for an electrode reaction [23]:

$$\lambda_o = \frac{e^2}{4\pi\varepsilon_0}\left(\frac{1}{a_0} - \frac{1}{R}\right)\left(\frac{1}{\varepsilon_{op}} - \frac{1}{\varepsilon_s}\right) \quad \text{Eq. 3}$$

where λ_o is computed by assuming that the solvent is a dielectric continuum, a_0 is the reactant radius (a sphere is assumed) and R is taken as twice the distance of the centre of the molecule from the electrode surface (page 121, chapter 3.6.1). [23] ε_{op} and ε_s are the solvent optical and static dielectric constants, respectively (in the case of acetonitrile: ε_{op}=1.8066 and ε_s=37.5). [57] Moreover:

$$\Delta E_f^{act} = \frac{\lambda}{4}\left(1 + \frac{\Delta E_{react}}{\lambda}\right)^2 \quad \text{Eq. 4}$$

where: ΔE_{react} is the difference in energy between the reagents and the products, i.e. the thermodynamic "driving force". The Constrained Density Functional Theory (CDFT) formalism, Q. Wu and T. Van Voorhis, [30,31] is exploited to build the initial and final model-diabatic states. For the *initial state* a single positive net charge is constrained on the $Si_{10}H_{15}$ moiety (Si_M^{+1}–FC), for in the *final state*: a single positive net charge is constrained on the iron atom of the ferrocene moiety (Si_M–Fe^{+1}). In the following the notation $E(a|b)$ is used to indicate the energy of state a calculated at the equilibrium geometry of state b, where a and b states may or may not be the same. In any case, equilibrium structures of both the initial and final states mentioned above were obtained with two CDFT geometry optimizations. Then, for any fixed nuclear structure, CDFT provides a direct way to calculate energies of both states [31]. The driving force (ΔE_{react}) and inner-sphere reorganization energy (λ_i) are calculated using the CDFT paradigm accordingly to the following relations:

$$\Delta E_{react} = E(Si_M - Fe^+|Si_M - Fe^+) - E(Si_M^+ - Fe|Si_M^+ - Fe) \quad \text{Eq. 5}$$

$$\lambda_i = E(Si_M - Fe^+|Si_M^+ - Fe) - E(Si_M^+ - Fe|Si_M^+ - Fe) \quad \text{Eq. 6}$$

where: Fe^+ indicates a +1 net charge localized on the iron, Si_M^+ indicates a +1 net charge localized on the $Si_{10}H_{15}$ moiety.

Figure 2.

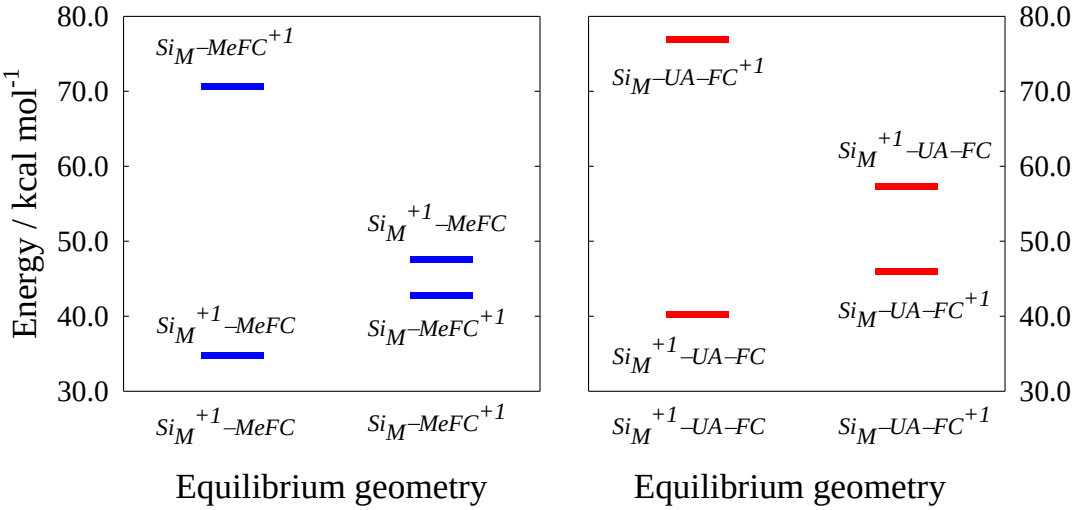

Figure 2. CDFT energies as a function of the initial and final equilibrium geometries: **left**) *Si_M–MeFC* **right**) *Si_M–UA–FC*. Energies are scaled with respect to the relevant neutral closed shell species. See the text for details.

Probably, one of the most crucial task, in order to reproduce rather balanced k_{ET} value by means of equation 2, is the evaluation of the electron transfer matrix element, V_{RP}. In the present work V_{RP} has been calculated, at the HF level, exploiting the Corresponding Orbital Transformation Method, (proposed by Farazdel [56]) as it is implemented in NWChem [41]. Figure 3 shows the relevant MOs involved in the calculation, the results are summarized in Table II. Then, the ET rate constant k_{ET} is calculated by using relationship (1) [21,23]. At the 6-31G* level of theory $k_{ET} = 77.8\ s^{-1}$ and $k_{ET} = 1.3 \times 10^{-9}\ s^{-1}$, for the *$Si_M$–MeFC* and *$Si_M$–UA–FC* species respectively, compare Table II for the values used in the calculations.

Table II. Theoretical values used in the calculation of k_{ET}, equation (2).

	λ_i [a)]	λ_o [b)]	ΔE_{react} [a)]	V_{RP}
	$kcal\ mol^{-1}$			eV
Si_M–MeFC	28.9	22.0	7.93	0.019
Si_M–UA–FC	30.9	40.1	5.71	10^{-6}

[a)] calculated at the PBE0/6-31G* CDFT level of the theory

[b)] calculated using equation (3)

Comparison with the experimental results of similar molecular architectures shows an encouraging agreement concerning the *Si_M–MeFC* system (experimentally k_{ET} values are found in the 4 to 160 s^{-1} range [32–34,37]). On the contrary, for the *Si_M–UA–FC* system extremely large differences are found (experimentally k_{ET} values are found in the 30 to 50 s^{-1} range [35,36]), suggesting that

some physics underlying the ET process is missing in the Marcus model; indeed the experimental result indicates a much more fast charge transfer process, then expected on the basis of the application of the Marcus theory. The latter result is in line with other findings recently reported in the literature, where unexpectedly high currents are found for systems featuring ET processes occurring on long distances, in the case of molecular spacers not "suitable" (single bond – not conjugated – carbon based chains) for charge conduction, like DNA/PNA systems [21,13,58–60].

Figure 3

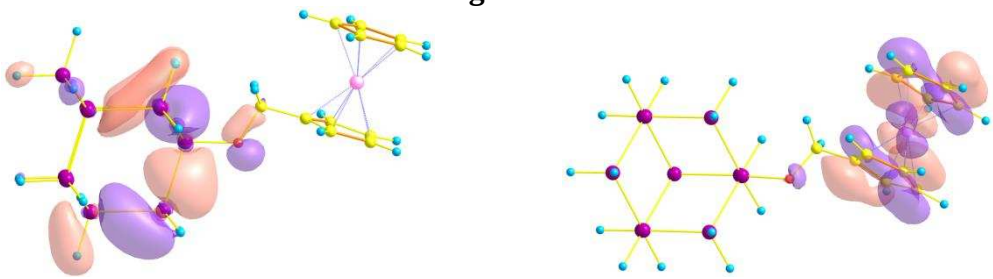

Figure 3. Sketches of the MOs involved in the V_{RP} calculation for the Si_M–*MeFC* species. Shown only for Si_M–*MeFC*. **Left**: Si_M^{+1}–*FC* species. **Right**: Si_M–FC^{+1} species.

4. Conclusions

a) The electron transfer behaviour of complex molecular architectures chemisorbed on Si(111) surfaces is theoretically assessed, where a redox probe (ferrocene) is covalently bound to the silicon surface through molecular spacers of different chain length. Remarkably and unexpectedly, charge transport through the saturated alkyl bond, *please note* just when the ferrocene is bonded via a covalent bond to the electrode, is effective enough to yield the appearance of well-defined current peaks in the experimental CVs Nishino [62], and the surprising results obtained also in the case of the ferrocene moiety grafted via polypeptide (single covalent bonds) molecular spacers. [63,64] This at variance of the case when the iron redox couple is not covalently bound to the SAM (i.e. the iron redox couple is in the bulk solution), then negligible current peaks in the CV are found. [24,65] The striking result is that the connection of the iron redox couple via a single (N.B: not conjugated) covalent bond acts as an on/off switch on the ET process.

b) To the best of our knowledge, this is one of the few works in the literature where theoretical k_{ET} values are quantitatively calculated. An encouraging semi-quantitative agreement between the experimental and theoretical values is found for the "short spacer" Si_M–*MeFC* system. While in the case of the Si_M–*UA*–*FC* system, much larger, than theoretically expected, experimental k_{ET} value are reported in previous works. A result in line with findings recently discussed in the literature, where high current values are found (i.e. CVs featuring evident redox current peaks)

even dealing with long saturated alkyl-carbon chains, where a non-conducting behaviour is expected. [21,22,13,58,64] Compare in particular the results discussed in A. Nitzan, *Chemical dynamics in condensed phases relaxation, transfer and reactions in condensed molecular systems*: page 600 Figure 16.9 or Launay and Verdaguer, *Electrons in Molecules* page 264 [66]

References

[1] H. S. Nalwa, in *Silicon-Based Mater. Devices* (Academic Press, Burlington, 2001).
[2] F. Shimura, *Semiconductor Silicon Crystal Technology* (Academic Press, 1989).
[3] G. Korotcenkov, *Porous Silicon From Formation to Application: Formation and Properties, Volume One*, CRC press (2015).
[4] G. P. Lopinski, T. M. Fortier, D. J. Moffatt, and R. A. Wolkow, J. Vac. Sci. Technol. A **16**, 1037 (1998).
[5] R. J. Hamers, J. S. Hovis, S. Lee, H. Liu, and J. Shan, J. Phys. Chem. B **101**, 1489 (1997).
[6] G. P. Lopinski, D. J. Moffatt, D. D. M. Wayner, and R. A. Wolkow, Nature **392**, 909 (1998).
[7] J. M. Buriak, Chem. Rev. **102**, 1271 (2002).
[8] S. Ciampi, J. B. Harper, and J. J. Gooding, Chem. Soc. Rev. **39**, 2158 (2010).
[9] P. Allongue, C. H. de Villeneuve, J. Pinson, F. Ozanam, J. N. Chazalviel, and X. Wallart, Electrochimica Acta **43**, 2791 (1998).
[10] P. Hartig, J. Rappich, and T. Dittrich, Appl. Phys. Lett. **80**, 67 (2002).
[11] H. O. Finklea, in *Encycl. Anal. Chem.* (John Wiley & Sons, Ltd, 2006).
[12] N. G. Tsierkezos, J. Solut. Chem. **36**, 289 (2007).
[13] J. D. Slinker, N. B. Muren, S. E. Renfrew, and J. K. Barton, Nat. Chem. **3**, 230 (2011).
[14] C. E. D. Chidsey, C. R. Bertozzi, T. M. Putvinski, and A. M. Mujsce, J. Am. Chem. Soc. **112**, 4301 (1990).
[15] J. M. Buriak, Chem. Rev. **102**, 1271 (2002).
[16] D. D. M. Wayner and R. A. Wolkow, J. Chem. Soc. Perkin Trans. 2 **0**, 23 (2002).
[17] K. M. Roth, A. A. Yasseri, Z. Liu, R. B. Dabke, V. Malinovskii, K.-H. Schweikart, L. Yu, H. Tiznado, F. Zaera, J. S. Lindsey, W. G. Kuhr, and D. F. Bocian, J. Am. Chem. Soc. **125**, 505 (2003).
[18] B. Fabre and F. Hauquier, J. Phys. Chem. B **110**, 6848 (2006).
[19] F. Hauquier, J. Ghilane, B. Fabre, and P. Hapiot, J. Am. Chem. Soc. **130**, 2748 (2008).
[20] A. Calborean, L. Buimaga-Iarinca, and F. Graur, Phys. Scr. **90**, 055803 (2015).
[21] A. Nitzan, *Chemical Dynamics in Condensed Phases Relaxation, Transfer and Reactions in Condensed Molecular Systems* (Oxford University Press, Oxford; New York, 2006).
[22] A. Paul, R. M. Watson, E. Wierzbinski, K. L. Davis, A. Sha, C. Achim, and D. H. Waldeck, J. Phys. Chem. B **114**, 14140 (2010).
[23] A. J. Bard and L. R. Faulkner, *Wiley: Electrochemical Methods: Fundamentals and Applications, 2nd Edition* (Wiley, New York, 2001).
[24] C. Fontanesi, F. Tassinari, F. Parenti, H. Cohen, P. C. Mondal, V. Kiran, A. Giglia, L. Pasquali, and R. Naaman, Langmuir (2015).
[25] D. Vanossi, R. Benassi, F. Parenti, F. Tassinari, R. Giovanardi, N. Florini, V. De Renzi, G. Arnaud, and C. Fontanesi, Electrochimica Acta (2012).
[26] F. Tassinari, D. Vanossi, A. Mucci, F. Parenti, and C. Fontanesi, J. Electroanal. Chem. (2013).
[27] C. Fontanesi, C. A. Bortolotti, D. Vanossi, and M. Marcaccio, J. Phys. Chem. A **115**, 11715 (2011).
[28] R. A. Marcus and H. Sumi, J. Electroanal. Chem. Interfacial Electrochem. **204**, 59 (1986).
[29] R. A. Marcus, Rev. Mod. Phys. **65**, 599 (1993).
[30] Q. Wu and T. Van Voorhis, Phys. Rev. A **72**, 024502 (2005).

[31] Q. Wu and T. Van Voorhis, J. Phys. Chem. A **110**, 9212 (2006).
[32] E. A. Dalchiele, A. Aurora, G. Bernardini, F. Cattaruzza, A. Flamini, P. Pallavicini, R. Zanoni, and F. Decker, J. Electroanal. Chem. **579**, 133 (2005).
[33] F. Decker, F. Cattaruzza, C. Coluzza, A. Flamini, A. G. Marrani, R. Zanoni, and E. A. Dalchiele, J. Phys. Chem. B **110**, 7374 (2006).
[34] M. Lu, T. He, and J. M. Tour, Chem. Mater. **20**, 7352 (2008).
[35] A. G. Marrani, E. A. Dalchiele, R. Zanoni, F. Decker, F. Cattaruzza, D. Bonifazi, and M. Prato, Electrochimica Acta **53**, 3903 (2008).
[36] D. Zigah, C. Herrier, L. Scheres, M. Giesbers, B. Fabre, P. Hapiot, and H. Zuilhof, Angew. Chem. Int. Ed. **49**, 3157 (2010).
[37] G. Riveros, G. González, and B. Chornik, J. Braz. Chem. Soc. **21**, 25 (2010).
[38] I. Kondov, M. Cizek, C. Benesch, H. Wang, and M. Thoss, J. Phys. Chem. C **111**, 11970 (2007).
[39] J. Li, I. Kondov, H. Wang, and M. Thoss, J. Phys. Chem. C **114**, 18481 (2010).
[40] V. May and O. Kuhn, *Wiley: Charge and Energy Transfer Dynamics in Molecular Systems, 3rd, Revised and Enlarged Edition - Volkhard May, Oliver Kuhn* (n.d.).
[41] M. Valiev, E. J. Bylaska, N. Govind, K. Kowalski, T. P. Straatsma, H. J. J. Van Dam, D. Wang, J. Nieplocha, E. Apra, T. L. Windus, and W. A. de Jong, Comput. Phys. Commun. **181**, 1477 (2010).
[42] A. Granovsky A., *Firefly Version 8.0.0, Http://Classic.chem.msu.su/Gran/Firefly/Index.html* (2016).
[43] M. W. Schmidt, K. K. Baldridge, J. A. Boatz, S. T. Elbert, M. S. Gordon, J. H. Jensen, S. Koseki, N. Matsunaga, K. A. Nguyen, S. Su, T. L. Windus, M. Dupuis, and J. A. Montgomery, J. Comput. Chem. **14**, 1347 (1993).
[44] P. Winget, E. J. Weber, C. J. Cramer, and D. G. Truhlar, Phys. Chem. Chem. Phys. **2**, 1231 (2000).
[45] P. Winget, C. J. Cramer, and D. G. Truhlar, Theor. Chem. Acc. **112**, (2004).
[46] C. J. Cramer, *Essentials of Computational Chemistry: Theories and Models* (John Wiley & Sons, 2005).
[47] V. Barone and M. Cossi, J. Phys. Chem. A **102**, 1995 (1998).
[48] C. Bruno, R. Benassi, A. Passalacqua, F. Paolucci, C. Fontanesi, M. Marcaccio, E. A. Jackson, and L. T. Scott, J. Phys. Chem. B **113**, 1954 (2009).
[49] C. Bruno, F. Paolucci, M. Marcaccio, R. Benassi, C. Fontanesi, A. Mucci, F. Parenti, L. Preti, L. Schenetti, and D. Vanossi, J. Phys. Chem. B **114**, 8585 (2010).
[50] L. Cigarini, D. Vanossi, F. Bondioli, and C. Fontanesi, Phys Chem Chem Phys **17**, 20522 (2015).
[51] D. Vanossi, L. Pigani, R. Seeber, P. Ferrarini, P. Baraldi, and C. Fontanesi, J. Electroanal. Chem. (2013).
[52] I. Noviandri, K. N. Brown, D. S. Fleming, P. T. Gulyas, P. A. Lay, A. F. Masters, and L. Phillips, J. Phys. Chem. B **103**, 6713 (1999).
[53] S. Trasatti, Electrochimica Acta **35**, 269 (1990).
[54] M. D. Tissandier, K. A. Cowen, W. Y. Feng, E. Gundlach, M. H. Cohen, A. D. Earhart, J. V. Coe, and T. R. Tuttle, J. Phys. Chem. A **102**, 7787 (1998).
[55] V. Tripkovic, M. E. Björketun, E. Skúlason, and J. Rossmeisl, Phys. Rev. B **84**, 115452 (2011).
[56] A. Farazdel, M. Dupuis, E. Clementi, and A. Aviram, J. Am. Chem. Soc. **112**, 4206 (1990).
[57] S.-H. Ma, X.-D. Zhang, H. Xu, L.-L. Shen, X.-K. Zhang, and Q.-Y. Zhang, J. Photochem. Photobiol. Chem. **139**, 97 (2001).
[58] D. Mishra, T. Z. Markus, R. Naaman, M. Kettner, B. Gohler, H. Zacharias, N. Friedman, M. Sheves, and C. Fontanesi, Proc. Natl. Acad. Sci. **110**, 14872 (2013).

[59] M. Kettner, B. Göhler, H. Zacharias, D. Mishra, V. Kiran, R. Naaman, C. Fontanesi, D. H. Waldeck, S. Sęk, J. Pawłowski, and J. Juhaniewicz, J. Phys. Chem. C (2014).
[60] F. Li, V. M. Basile, and M. J. Rose, Langmuir **31**, 7712 (2015).
[61] V. Jouikov and J. Simonet, Langmuir **28**, 931 (2012).
[62] P. T. Bui and T. Nishino, Phys. Chem. Chem. Phys. **16**, 5490 (2014).
[63] S. Sek, B. Palys, and R. Bilewicz, J. Phys. Chem. B **106**, 5907 (2002).
[64] S. Sek, K. Swiatek, and A. Misicka, J. Phys. Chem. B **109**, 23121 (2005).
[65] C. Fontanesi, G. Camurri, and F. Tassinari, J. Appl. Electrochem. **43**, 101 (2012).
[66] J.-P. Launay and M. Verdaguer, *Electrons in Molecules: From Basic Principles to Molecular Electronics* (Oxford University Press, Oxford, New York, 2013).

5) Conclusions and Perspectives

Conclusions

A) The following fundamental aspects of "theoretical physics" have been considered: ***i)*** polaron quasi-particle spectroscopic signature in doped polythiophenes, with focus on the relevant IR signature [43]. A detailed systematic study clarified the interplay between geometrical/structural issues (number of repeating units in the oligomers and extension of π conjugation, the latter in relation to disorder, i.e. conformational degrees of freedom) underlying the observation of the IR polaron signature. This well beyond the simple notion of "size" of the oligomer (compare ref [26,31] and the Chapter 4.1.1 *Electronic/structural interplay detailed study of the polaron "Giant IR signature"* section). What is more, a clear hierarchy ladder is established in relation to the level of the theory needed to correctly calculate the appearance of the "Giant IR polaron signature". It must be remembered that here the main problem is the calculation of the vibrational mode **intensitiy** (CPHF/CPKS approximation, Appendix 2). Within this field of research calculations have been performed using the HF and DFT methods, as well as using hybrid B3LYP and long range corrected CAMB3LYP functional. Definitively, in the case of system featuring an "important" degree of "charge localization/separation" both pure HF and DFT methods yield wrong, even qualitatively, results. Eventually, the long range corrected (accounting for long range coulomb interactions) CAMB3LYP functional yielded the most satisfactory picture compared with the experimental evidence. This both in the case of calculations dealing with an overall neutral system, F4TCNQ/PCTDT-BT and F4TCNQ/PCPDT (CT system studied within the embedded-cluster approach paradigm) [31], and also in the case of radical cation open shell positively charged oligomers. Notably only well coded functionals have been used, no fine tuning has been attempted. This because the number and variety of functional already implemented in QM based codes is extremely large. ii) critical assessment of the comparison between experimental and theoretical results concerning the calculation of the optical and electronic band gap (HOMO/LUMO gap in localized molecular architectures), with particular reference to CT crystal systems and hybrid interfaces. also on the basis of the so-called embedded-cluster approach ref [27,32] and Ferrocene chemiadsorbed on Silicon iii) characterization of electronic properties in molecular crystals, with particular reference to optical and electronic band gap. Results are critically discussed in the view of results obtained by means of the embedded-cluster approach and PBC (Periodic Boundary Conditions). Here also results obtained using localized orbitals and plane wave calculations were compared, compare Chapter 4.2.

B) Technicalities: i) a number of case studies was analyzed using a systematic approach, where theoretical results obtained both within the embedded-cluster model (localized orbital basis sets), as well as performing plane wave based calculations with application of periodic boundary conditions (PBC) are compared with the experimental evidence. Together with the critical evaluation of the inclusion of vdW energy correction, in particular concerning solid state crystal geometry optimization: compare chapter 4.2 results and discussion. ii) from this work it emerges in a rather neat way that CAMB3LYP functional should be used when dealing with the calculation of electronic related properties of CT systems, or molecular architectures featuring localized-charged states (ions, open/shell systems, and even CT co-crystals with a small amount of charge transfer). This in relation of some of the well-known challenges related to further development in DFT based methods, especially in the case where electron localization or charge transfer systems are considered (definitively PBE or SVWN pure DFT functionals are doomed to yield inaccurate results in the molecular systems considered in this thesis).

Perspectives

Some of the peculiar aspects related to the relationship between electronic structure and conducting properties (as probed by the comparison between theoretical results and spectroscopic evidence (vibrational and electronic spectroscopy) have been addressed in the present study. Some aspects seem worth of a further development.

Experimental

Simultaneous measurement of conductivity (by using Impedance spectroscopy) as a function of doping, the doping will be controlled electrochemically (oxidation/reduction regime): the polymer will be drop-casted on three conductive electrodes within an electrochemical cell, where the central electrode (working electrode of the electrochemical system) will control the amount doping (exploiting the control of the potential with respect to a reference electrode), then the impedance will be measured maintaining the potential (doped state of the polymer) constant.

Theoretical

The development of a different theory able to relate vibrational (giant IR) and electronic (polaron signature in the NIR range) excitations. These are clearly entangled (experimental evidence), but

the vibronic analysis pursued on the present models failed to unravel the underlying physics. The latter subject is the subject of further studies, yet concerning the polaron IR (vibrational) and UV/Vis (electronic) signature and mapping of the Giant-mode with respect to the vibrational modes of the neutral pristine species [98].

References

1 A. D. Becke, *Phys. Rev. A*, 1988, **38**, 3098–3100.

2 C. Lee, W. Yang and R. G. Parr, *Phys. Rev. B*, 1988, **37**, 785–789.

3 *Organic Electronics: Materials, Processing, Devices and Applications, Edited by Franky So*, CRC Press Taylor & Francis Group, 6000 Broken Sound Parkway NW, Boca Raton, FL, 2009.

4 *Organic Electronics, Volume Editors: Meller, G., Grasser, T.*, Springer, Heidelberg Dordrecht London New York, 2010.

5 *Organic Electronics: Emerging Concepts and Technologies, Fabio Cicoira and Clara Santato editors*, Wiley-VCH Verlag GmbH & Co. KGaA, Boschstr. 12, 69469 Weinheim, Germany, 2013.

6 G. Likhtenshtein, in *Solar Energy Conversion*, Wiley-VCH Verlag GmbH & Co. KGaA, 2012, pp. 1–44.

7 W. Bruttig and C. Adachi, *Wiley: Physics of Organic Semiconductors, 2nd, Completely New Revised Edition*, Wiley, New York, NY, 2012.

8 J. L. Bredas and S. Marder, *The WSPC Reference on Organic Electronics: Organic Semiconductors*, World Scientific Publication Co., Singapore, 2016, vol. 7.

9 C. Yang, Z. V. Vardeny, A. Köhler, M. Wohlgenannt, M. K. Al-Suti and M. S. Khan, *Phys. Rev. B*, 2004, **70**, 241202.

10 C. Fuchs, P.-A. Will, M. Wieczorek, M. C. Gather, S. Hofmann, S. Reineke, K. Leo and R. Scholz, *Phys. Rev. B*, 2015, **92**, 245306.

11 L. Kinner, S. Nau, K. Popovic, S. Sax, I. Burgués-Ceballos, F. Hermerschmidt, A. Lange, C. Boeffel, S. A. Choulis and E. J. W. List-Kratochvil, *Appl. Phys. Lett.*, 2017, **110**, 101107.

12 S.-J. Yoo, J.-H. Lee, J.-M. Kim and J.-J. Kim, *Appl. Phys. Lett.*, 2017, **110**, 053303.

13 F. Villafiorita-Monteleone, E. Kozma, M. Pasini, M. Paolino, A. Cappelli, G. Bongiovanni, A. Mura and C. Botta, *Appl. Phys. Lett.*, 2017, **110**, 183301.

14 E. Da Como, F. De Angelis, H. Snaith and A. Walker, *Unconventional Thin Film Photovoltaics*, The Royal Society of Chemistry, Cambridge, UK, 2016.

15 *Synthetic Metals - ScienceDirect.com*, 1979.

16 *Organic Electronics. A journal devoted to relevant Materials, Physics, Chemistry and Applications, Springer B. V.*, 2000.

17 C. K. Chiang, J. C. R. Fincher, Y. W. Park, A. J. Heeger, H. Shirakawa, E. J. Louis, S. C. Gau and A. G. MacDiarmid, *Phys. Rev. Lett.*, 1977, **39**, 1098.

18 K. G. Swapan and K. C. Pratim, *Concepts and Methods in Modern Theoretical Chemistry: Statistical Mechanics*, CRC Press, 2013.

19 J. L. Bredas and G. B. Street, *Acc. Chem. Res.*, 1985, **18**, 309–315.

20 E. A. Weiss, J. K. Kriebel, M.-A. Rampi and G. M. Whitesides, *Philos. Trans. R. Soc. Lond. Math. Phys. Eng. Sci.*, 2007, **365**, 1509–1537.

21 M. Hallermann, E. D. Como, J. Feldmann, M. Izquierdo, S. Filippone, N. Martín, S. Jüchter and E. von Hauff, *Appl. Phys. Lett.*, 2010, **97**, 023301.

22 C. Wiebeler, R. Tautz, J. Feldmann, E. von Hauff, E. Da Como and S. Schumacher, *J. Phys. Chem. B*, 2013, **117**, 4454–4460.

23 J. Yamamoto and Y. Furukawa, *J. Phys. Chem. B*, 2015, **119**, 4788–4794.

24 D. Emin, *Polarons*, Cambridge University Press, Cambridge, 2012.

25 D. Mühlbacher, H. Neugebauer, A. Cravino, N. S. Sariciftci, J. K. J. V. Duren, A. Dhanabalan, P. A. V. Hal, R. A. J. Janssen and J. C. Hummelen, *Mol. Cryst. Liq. Cryst.*, 2002, **385**, 85–92.

26 D. Vanossi, L. Cigarini, A. Giaccherini, E. da Como and C. Fontanesi, *Molecules*, 2016, **21**, 110.

27 T. Salzillo, M. Masino, G. Kociok-Köhn, D. Di Nuzzo, E. Venuti, R. G. Della Valle, D. Vanossi, C. Fontanesi, A. Girlando, A. Brillante and E. Da Como, *Cryst. Growth Des.*, 2016, **16**, 3028–3036.

28 G. Sini, J. S. Sears and J.-L. Brédas, *J. Chem. Theory Comput.*, 2011, **7**, 602–609.

29 A. J. Cohen, P. Mori-Sánchez and W. Yang, *Chem. Rev.*, 2012, **112**, 289–320.

30 A. Pribram-Jones, D. A. Gross and K. Burke, *Annu. Rev. Phys. Chem.*, 2015, **66**, 283–304.

31 D. Di Nuzzo, C. Fontanesi, R. Jones, S. Allard, I. Dumsch, U. Scherf, E. von Hauff, S. Schumacher and E. Da Como, *Nat. Commun.*, , DOI:10.1038/ncomms7460.

32 J. Potticary, L. R. Terry, C. Bell, A. N. Papanikolopoulos, P. C. M. Christianen, H. Engelkamp, A. M. Collins, C. Fontanesi, G. Kociok-Köhn, S. Crampin, E. Da Como and S. R. Hall, *Nat. Commun.*, 2016, **7**, 11555.

33 Z. G. Soos and D. J. Klein, in *Treatise on Solid State Chemistry*, ed. N. B. Hannay, Springer US, 1976, pp. 679–767.

34 O. Sato, *Nat. Chem.*, 2016, **8**, 644–656.

35 J.-L. Brédas, D. Beljonne, V. Coropceanu and J. Cornil, *Chem. Rev.*, 2004, **104**, 4971–5004.

36 N. Castagnetti, G. Kociok-Köhn, E. Da Como and A. Girlando, *Phys. Rev. B*, 2017, **95**, 024101.

37 E. von Hauff, E. Da Como and S. Ludwigs, in *Elementary Processes in Organic Photovoltaics | Karl Leo | Springer*, Springer, 2017, vol. 272.

38 B. Ulgut, J. E. Grose, Y. Kiya, D. C. Ralph and H. D. Abruña, *Appl. Surf. Sci.*, 2009, **256**, 1304–1308.

39 K. Lee, A. J. Heeger and Y. Cao, *Phys. Rev. B*, 1993, **48**, 14884–14891.

40 K. Lee, A. J. Heeger and Y. Cao, *Synth. Met.*, 1995, **69**, 261–262.

41 K. Lee, A. J. Heeger and Y. Cao, *Synth. Met.*, 1995, **72**, 25–34.

42 J. C. R. Fincher, M. Ozaki, A. J. Heeger and A. G. MacDiarmid, *Phys. Rev. B*, 1979, **19**, 4140.

43 E. Ehrenfreund, Z. Vardeny and O. Brafman, in *Methods of Laser Spectroscopy*, eds. Y. Prior, A. Ben-Reuven and M. Rosenbluh, Springer US, 1986, pp. 421–424.

44 Enrico Da Como, *Pers. Commun.*

45 R. Österbacka, X. M. Jiang, C. P. An, B. Horovitz and Z. V. Vardeny, *Phys. Rev. Lett.*, 2002, **88**, 226401.

46 G. Zerbi, *Appl. Spectrosc. Rev.*, 1969, **2**, 193–261.

47 V. Coropceanu, J. Cornil, D. A. da Silva Filho, Y. Olivier, R. Silbey and J.-L. Brédas, *Chem. Rev.*, 2007, **107**, 926–952.

48 M. Zamadar, S. Asaoka, D. C. Grills and J. R. Miller, *Nat. Commun.*, , DOI:10.1038/ncomms3818.

49 V. Podzorov, V. M. Pudalov and M. E. Gershenson, *Appl. Phys. Lett.*, 2003, **82**, 1739–1741.

50 D. Mihailovic, in *Polarons in Advanced Materials*, Springer, Dordrecht, 2007, pp. 547–567.

51 L. D. Landau and S. I. Pekar, *Ukr. J. Phys.*, 2008, **53**, 71–74.

52 W. P. Su and J. R. Schrieffer, *Proc. Natl. Acad. Sci.*, 1980, **77**, 5626–5629.

53 H. Fröhlich, *Phys. Rev.*, 1950, **79**, 845–856.

54 H. Fröhlich, *Proc. R. Soc. Lond. Math. Phys. Eng. Sci.*, 1952, **215**, 291–298.

55 G. D. Mahan, *Many-Particle Physics*, Springer US, Boston, MA, 2000.

56 F. Giustino, *Rev. Mod. Phys.*, 2017, **89**, 015003.

57 L. D. Landau and L. M. Lifshitz, *Quantum Mechanics - 3rd Edition*, Pergamon Press, New York, NY, 1977, vol. Volume 3.

58 N. Newbury, M. Newman, J. Ruhl, S. Staggs and S. Thorsett, *Princeton Problems in Physics with Solutions.*, Princeton University Press, 1991.

59 L. Mihály and M. Martin, *Solid State Physics, 2nd Edition*, Wiley-VCH Verlag GmbH, 2008.

60 T. Kato and T. Yamabe, *J. Phys. Chem. A*, 2005, **109**, 4804–4815.

61 T. Kato and T. Yamabe, *J. Phys. Chem. A*, 2006, **110**, 2785–2795.

62 Z. G. Zoos, A. Painelli, A. Girlando and A. Mukhopadhyay, in *Handbook of Coducting Polymers*, Marcel Dekker Inc., New York, Second Edition., 1998, pp. 165–196.

63 N. E. Gruhn, D. A. da Silva Filho, T. G. Bill, M. Malagoli, V. Coropceanu, A. Kahn and J.-L. Brédas, *J. Am. Chem. Soc.*, 2002, **124**, 7918–7919.

64 V. Coropceanu, M. Malagoli, D. A. da Silva Filho, N. E. Gruhn, T. G. Bill and J. L. Brédas, *Phys. Rev. Lett.*, 2002, **89**, 275503.

65 A. Troisi, in *Organic Electronics*, eds. T. Grasser and G. Meller, Springer Berlin Heidelberg, 2009, pp. 259–300.

66 A. Troisi, *Chem. Soc. Rev.*, 2011, **40**, 2347–2358.

67 E. Kaxiras, *Atomic and Electronic Structure of Solids - Cambridge University Press*, Cambridge University Press, 2003.

68 C. J. Cramer, *Essentials of Computational Chemistry: Theories and Models*, John Wiley & Sons, 2005.

69 M. L. Cohen and S. G. Louie, *Fundamentals of Condensed Matter Physics*, Cambridge University Press, Cambridge, 2016.

70 H. B. Schlegel and M. J. Frisch, in *Theoretical and Computational Models for Organic Chemistry*, eds. S. J. Formosinho, I. G. Csizmadia and L. G. Arnaut, Springer Netherlands, 1991, pp. 5–33.

71 F. Jensen, *Introduction to Computational Chemistry, 2nd Edition*, John Wiley & Sons, Ltd, Chichester, 2006.

72 O. Madelung, *Introduction to Solid-State Theory*, Springer, Heidelberg Dordrecht London New York, 1978.

73 P. W. Atkins, *Molecular Quantum Mechanics*, Oxford University Press, Oxford; New York, 1982.

74 N. H. March, W. H. Young and S. Sampanthar, *The Many-Body Problem in Quantum Mechanics*, Cambridge University Press, Cambridge, UK, 1967.

75 I. Shavitt and R. Bartlett, *Many-Body Methods in Chemistry and Physics. MBPT and Coupled-Cluster Theory*, Cambridge University Press, 2009.

76 P. Hohenberg and W. Kohn, *Phys. Rev.*, 1964, **136**, B864.

77 W. Kohn and L. J. Sham, *Phys. Rev.*, 1965, **140**, A1133–A1138.

78 A. J. Heeger, *Rev. Mod. Phys.*, 2001, **73**, 681–700.

79 A. G. MacDiarmid, *Rev. Mod. Phys.*, 2001, **73**, 701–712.

80 H. Shirakawa, *Rev. Mod. Phys.*, 2001, **73**, 713–718.

81 M. Pope and C. E. Swenberg, *Electronic Processes in Organic Crystals and Polymers*, Oxford University Press 1982, Oxford, 1982.

82 J. Rawson, P. J. Angiolillo and M. J. Therien, *Proc. Natl. Acad. Sci.*, 2015, **112**, 13779–13783.

83 S. Baniya, S. R. Vardeny, E. Lafalce, N. Peygambarian and Z. V. Vardeny, *Phys. Rev. Appl.*, 2017, **7**, 064031.

84 U. N. V. Huynh, T. P. Basel, E. Ehrenfreund, G. Li, Y. Yang, S. Mazumdar and Z. V. Vardeny, *Phys. Rev. Lett.*, 2017, **119**, 017401.

85 T. A. Skotheim, *Handbook of Conducting Polymers, Second Edition*, 1997.

86 T. P. Farrell and R. B. Kaner, in *Encyclopedia of Polymeric Nanomaterials*, eds. S. Kobayashi and K. Müllen, Springer Berlin Heidelberg, 2013, pp. 1–8.

87 J. A. Pople, *Gaussian suite of programs*, Wallingford, Connecticut, 2017.

88 M. W. Schmidt, K. K. Baldridge, J. A. Boatz, S. T. Elbert, M. S. Gordon, J. H. Jensen, S. Koseki, N. Matsunaga, K. A. Nguyen, S. Su, T. L. Windus, M. Dupuis and J. A. Montgomery, *J. Comput. Chem.*, 1993, **14**, 1347–1363.

89 A. Granovsky A., *Firefly version 8.0.0, http://classic.chem.msu.su/gran/firefly/index.html*, 2016.

90 W. A. Goddard, *Phys. Rev.*, 1967, **157**, 81–93.

91 K. I. Ramachandran, G. Deepa and K. Namboori, *Computational Chemistry and Molecular Modeling - Principles and Applications*, Springer, 2008.

92 S. H. Vosko, L. Wilk and M. Nusair, *Can. J. Phys.*, 1980, **58**, 1200–1211.

93 A. Troisi and A. Shaw, *J. Phys. Chem. Lett.*, 2016, **7**, 4689–4694.

94 N. Vukmirović and L.-W. Wang, *J. Phys. Chem. B*, 2009, **113**, 409–415.

95 R. Noriega, J. Rivnay, K. Vandewal, F. P. V. Koch, N. Stingelin, P. Smith, M. F. Toney and A. Salleo, *Nat. Mater.*, 2013, **12**, 1038–1044.

96 P. Kordt, O. Stenzel, B. Baumeier, V. Schmidt and D. Andrienko, *J. Chem. Theory Comput.*, 2014, **10**, 2508–2513.

97 D. Tahk, H. H. Lee and D.-Y. Khang, *Macromolecules*, 2009, **42**, 7079–7083.

98 E. Da Como, G. D'Avino and C. Fontanesi, paper in preparation, 2017.

99 S. Aitipamula, R. Banerjee, A. K. Bansal, K. Biradha, M. L. Cheney, A. R. Choudhury, G. R. Desiraju, A. G. Dikundwar, R. Dubey, N. Duggirala, P. P. Ghogale, S. Ghosh, P. K. Goswami, N. R. Goud, R. R. K. R. Jetti, P. Karpinski, P. Kaushik, D. Kumar, V. Kumar, B. Moulton, A. Mukherjee, G. Mukherjee, A. S. Myerson, V. Puri, A. Ramanan, T. Rajamannar, C. M. Reddy, N. Rodriguez-Hornedo, R. D. Rogers, T. N. G. Row, P. Sanphui, N. Shan, G. Shete, A. Singh, C. C. Sun, J. A. Swift, R. Thaimattam, T. S. Thakur, R. Kumar Thaper, S. P. Thomas, S. Tothadi, V. R. Vangala, N. Variankaval, P. Vishweshwar, D. R. Weyna and M. J. Zaworotko, *Cryst. Growth Des.*, 2012, **12**, 2147–2152.

100 Y. Kubozono, H. Mitamura, X. Lee, X. He, Y. Yamanari, Y. Takahashi, Y. Suzuki, Y. Kaji, R. Eguchi, K. Akaike, T. Kambe, H. Okamoto, A. Fujiwara, T. Kato, T. Kosugi and H. Aoki, *Phys. Chem. Chem. Phys.*, 2011, **13**, 16476–16493.

101 J. P. Perdew and Y. Wang, *Phys. Rev. B*, 1992, **45**, 13244–13249.

102 J. P. Perdew, K. Burke and M. Ernzerhof, *Phys. Rev. Lett.*, 1996, **77**, 3865–3868.

103 S. J. Clark, M. D. Segall, C. J. Pickard, P. J. Hasnip, M. I. J. Probert, K. Refson and M. C. Payne, *Z. Für Krist. - Cryst. Mater.*, 2009, **220**, 567–570.

104 S. Grimme, *J. Comput. Chem.*, 2006, **27**, 1787–1799.

105 A. Tkatchenko and M. Scheffler, *Phys. Rev. Lett.*, 2009, **102**, 073005.

106 T. Bučko, S. Lebègue, J. Hafner and J. G. Ángyán, *Phys. Rev. B*, 2013, **87**, 064110.

107 G. Kresse and J. Furthmüller, *Phys. Rev. B*, 1996, **54**, 11169–11186.

108 A. F. Izmaylov, G. E. Scuseria and M. J. Frisch, *J. Chem. Phys.*, 2006, **125**, 104103.

109 F. Wooten, *Optical Properties of Solids - 1st Edition*, Academic Press, New York and London, 1972.

110 M. Fox, *Optical Properties of Solids*, Oxford University Press, Oxford, New York, Second Edition., 2010.

111 F. Wudl, G. M. Smith and E. J. Hufnagel, *J. Chem. Soc. Chem. Commun.*, 1970, **0**, 1453–1454.

112 J. Ferraris, D. O. Cowan, V. Walatka and J. H. Perlstein, *J. Am. Chem. Soc.*, 1973, **95**, 948–949.

113 L. Ouahab, J. Padiou, D. Grandjean, C. Garrigou–Lagrange, P. Delhaes and M. Bencharif, *J. Chem. Soc. Chem. Commun.*, 1989, **0**, 1038–1041.

114 B. P. Rand and H. Richter, *Organic Solar Cells: Fundamentals, Devices, and Upscaling*, CRC Press, 2014.

115 R. T. Weitz, A. Walter, R. Engl, R. Sezi and C. Dehm, *Nano Lett.*, 2006, **6**, 2810–2813.

116 F. Di Maiolo, C. Sissa and A. Painelli, *Sci. Rep.*, , DOI:10.1038/srep19682.

117 L. Hedin, *Phys. Rev.*, 1965, **139**, A796–A823.

118 K. Remya and C. H. Suresh, *J. Comput. Chem.*, 2013, **34**, 1341–1353.

119 G. Kresse and J. Hafner, *Phys. Rev. B*, 1993, **47**, 558–561.

120 M. Valiev, E. J. Bylaska, N. Govind, K. Kowalski, T. P. Straatsma, H. J. J. Van Dam, D. Wang, J. Nieplocha, E. Apra, T. L. Windus and W. A. de Jong, *Comput. Phys. Commun.*, 2010, **181**, 1477–1489.

121 E. Runge and E. K. U. Gross, *Phys. Rev. Lett.*, 1984, **52**, 997.

122 C. A. Ullrich, *Time-Dependent Density-Functional Theory: Concepts and Applications*, Oxford University Press, 2011.

123 C. A. Ullrich and Z. Yang, *Braz. J. Phys.*, 2014, **44**, 154–188.

124 A. Dreuw and M. Head-Gordon, *Chem. Rev.*, 2005, **105**, 4009–4037.

Appendix 1

HF fundamental operators

Hamiltonian, Coulomb and Exchange operators within the HF equations ansatz: $\boldsymbol{h}_i$ accounts for the motion of electron i in the field of the fix nuclei (positive ions), $\boldsymbol{J}_i$ and $\boldsymbol{K}_i$ are the Coulomb and Exchange operators, respectively [71,73]:

$$\boldsymbol{h}_i = -\frac{1}{2m}\nabla_i^2 - \sum_a^{nuclei} \frac{Z_a}{|\boldsymbol{R_a} - \boldsymbol{r_i}|} \tag{33}$$

$$\boldsymbol{g}_{ij} = \frac{1}{|\boldsymbol{r_i} - \boldsymbol{r_j}|} \tag{34}$$

$$\boldsymbol{J}_i|\phi_j(2)\rangle = \langle\phi_i(1)|\boldsymbol{g}_{12}|\phi_i(1)\rangle|\phi_j(2)\rangle \tag{35}$$

$$\boldsymbol{K}_i|\phi_j(2)\rangle = \langle\phi_i(1)|\boldsymbol{g}_{12}|\phi_j(1)\rangle|\phi_i(2)\rangle \tag{36}$$

Appendix 2

On the Coupled Perturbed HF (CPHF) response calculation.

CPHF response theory is exploited when system/molecular properties can be studied as the variation (response) of a system (whose physical behaviour is represented by a wave function) to an external perturbation, where the perturbation may be, in principle, represented by any kind of operator not accounted for in the Hamiltonian operator used to solve the Schrödinger equation. Having the HF/KS equation written as [71,70]:

$$\boldsymbol{F}^{(\boldsymbol{0})}\boldsymbol{C}^{(\boldsymbol{0})} = \boldsymbol{S}^{(\boldsymbol{0})}\boldsymbol{C}^{(\boldsymbol{0})}\boldsymbol{\varepsilon}^{(\boldsymbol{0})} \tag{37}$$

where the $\boldsymbol{F}^{(\boldsymbol{0})}$, $\boldsymbol{C}^{(\boldsymbol{0})}$, $\boldsymbol{S}^{(\boldsymbol{0})}$ and $\boldsymbol{\varepsilon}^{(\boldsymbol{0})}$ are the suitable Fock, coefficient, overlap and orbital energy (Lagrange multiplyer) matrices. Of each of the $\boldsymbol{F}, \boldsymbol{C}, \boldsymbol{S}$ and $\boldsymbol{\varepsilon}$ matrices is taken the first-order expansion term, as a function of a generic perturbation parameter λ, eventually yielding:

$$\left(\boldsymbol{F}^{(\boldsymbol{0})} - \boldsymbol{S}^{(\boldsymbol{0})}\boldsymbol{\varepsilon}^{(\boldsymbol{0})}\right)\boldsymbol{C}^{(\boldsymbol{1})} = \left(-\boldsymbol{F}^{(\boldsymbol{1})} + \boldsymbol{S}^{(\boldsymbol{1})}\boldsymbol{\varepsilon}^{(\boldsymbol{0})} + \boldsymbol{S}^{(\boldsymbol{0})}\boldsymbol{\varepsilon}^{(\boldsymbol{1})}\right)\boldsymbol{C}^{(\boldsymbol{0})} \tag{38}$$

Eq. 38 is the first-order Coupled Perturbed Hartree–Fock (CPHF) equation, where perturbed molecular orbitals coefficients can be reckoned *i)* as a function of unperturbed (0-th order) quantities *ii)* as a function of first-order matrices: Fock ($\boldsymbol{F}^{(\boldsymbol{1})}$), Lagrange ($\boldsymbol{\varepsilon}^{(\boldsymbol{1})}$) and overlap ($\boldsymbol{S}^{(\boldsymbol{1})}$). Essential to the

calculation of the perturbed coefficient matrix, ($\boldsymbol{C^{(1)}}$), is the calculation of the $\boldsymbol{S^{(1)}}$, $\boldsymbol{h^{(1)}}$ and $\boldsymbol{g^{(1)}}$ terms, they are the result of the first derivative of the basis functions, with respect to the perturbation λ, of one- and two-electrons integrals:

$$S_{\alpha\beta}^{(1)} = \langle \chi_\alpha | \chi_\beta \rangle^{(1)} = \frac{\partial}{\partial \lambda} \langle \chi_\alpha | \chi_\beta \rangle \tag{39}$$

$$h_{\alpha\beta}^{(1)} = \langle \chi_\alpha | \boldsymbol{h} | \chi_\beta \rangle^{(1)} = \frac{\partial}{\partial \lambda} \langle \chi_\alpha | \boldsymbol{h} | \chi_\beta \rangle \tag{40}$$

$$g_{\alpha\beta\gamma\delta}^{(1)} = \langle \chi_\alpha \chi_\beta | \boldsymbol{g} | \chi_\gamma \chi_\delta \rangle^{(1)} = \frac{\partial}{\partial \lambda} \langle \chi_\alpha \chi_\beta | \boldsymbol{g} | \chi_\gamma \chi_\delta \rangle \tag{41}$$

Application of the variational theorem, as in the case of the HF equations solution, grants the solution of the set of equations relevant to the $\boldsymbol{F}$ operator (indeed $\boldsymbol{F^{(1)}}$, because the solution for $\boldsymbol{F^{(0)}}$, is the, known, ground state). The solution of the CPHF equations goes through the determination of a matrix, $\boldsymbol{U}$, which accounts for the MOs change (the coefficients matrix) upon application of a perturbation ($\phi_i{}' = \sum_j^{Mbasis} u_{i,j}\phi_j$, with no perturbation $\boldsymbol{U}$ corresponds to the identity matrix). The size of $\boldsymbol{U}$ are determined as the number of occupied MOs multiplied the number of virtual MOs; as a result $\boldsymbol{U}$ makes a combination of occupied with virtual MOs, because *i)* the energy of the system is independent by a unitary transformation of the occupied and virtual MOs *i)* occupied-occupied and virtual-virtual MOs mixing can be fixed by the ortho-normality condition. CPHF equation can be solved for any specific perturbation (in general associated with three different components), in the present study its application is due to the fact that infrared spectra intensities are calculated as the result of the application of an electric field perturbation (i.e. the calculation of the dipole second derivative: once with respect to the electric field and once with respect to nuclear coordinates) determine the infra-red intensities [71,70]. This method is implemented for the calculation of IR intensities in the Gaussian, GAMESS, NWChem and Firefly suite of programs [88,120,89,87].

Appendix 3

On the TDDFT response calculation.

Hohenberg-Kohn-Sham set of equations, underlying the DFT method, are rigorously valid only for a system ground state. The subsequent development of the so-called Time Dependent DFT (TDDFT) paradigm allowed for the calculation of electronic excited-state properties. The crucial move is due to Runge and Gross who, in a fashion similar to the Hohenberg-Kohn, showed that a one-to-one relationship holds between the electron density and the potential energy of a system, but including also the time dependence [121–123]:

$$\rho(\boldsymbol{r},t) \leftrightarrow V(\boldsymbol{r},t) \tag{42}$$

Invocation of the variational principle allows to write the Kohn Sham equations featuring an explicit time depend dependence (TD-KS) [124]:

$$i\frac{\partial}{\partial t}\varphi_i(\boldsymbol{r},t) = \left(-\frac{1}{2}\nabla_i^2 + \mathrm{V}(\boldsymbol{r},t) + \int \frac{\rho(\boldsymbol{r}',t)}{|\boldsymbol{r}-\boldsymbol{r}'|}d\boldsymbol{r} + \frac{\partial E_{XC}[\rho]}{\partial\rho(\boldsymbol{r},t)}\right)\varphi_i(\boldsymbol{r},t) \tag{43}$$

Thus allowing for the calculation of the electron density including the time dependence:

$$\rho(\boldsymbol{r},t) = \sum_i |\varphi_i(\boldsymbol{r},t)|^2 \tag{44}$$

Again the $E_{XC}[\rho]$ term is not exactly known, in a totally parallel way with the time-independent DFT. Solution, to the fundamental problem of the TD-KS equation, goes through the application of linear response TDDFT, where the perturbation is considered to be represented by the relation:

$$V_{perturbation} = V_0(\boldsymbol{r})e^{i\omega t} \tag{45}$$

where V_0 is the perturbing field amplitude, ω the pulsation. In the case of a weak perturbation, then

the relevant induced change in the electron density can be calculated within application of first-order perturbation theory (i.e. assuming a linear response of the system to the external perturbation).

After Fourier transform from the time to energy domain, the so-called Casida equation is obtained, in the form of a non-hermitian eigenvalue equation:

$$\begin{bmatrix} A & K \\ K & A \end{bmatrix}\begin{bmatrix} X \\ Y \end{bmatrix} = \Omega\begin{bmatrix} -1 & 0 \\ 0 & 1 \end{bmatrix}\begin{bmatrix} X \\ Y \end{bmatrix} \tag{46}$$

where:

$$A_{ia\sigma,i'a'\sigma'}(\omega) = \delta_{ii'}\delta_{aa'}\delta_{\sigma\sigma'}\omega_{ai\sigma} + K_{ia\sigma,i'a'\sigma'}(\omega) \tag{47}$$

$$K_{ia\sigma,i\prime a\prime\sigma\prime}(\omega) = \int d^3r \int d^3r\,' \varphi^*_{i\sigma}(\boldsymbol{r})\varphi_{a\sigma}(\boldsymbol{r}) \times f_{Hxc\sigma\sigma\prime}(\boldsymbol{r},\boldsymbol{r}',\omega)\varphi_{i\prime\sigma\prime}(\boldsymbol{r}')\varphi^*_{a\prime\sigma\prime}(\boldsymbol{r}') \quad (48)$$

$$f_{Hxc}(\boldsymbol{r},\boldsymbol{r}',\omega) = |\boldsymbol{r}-\boldsymbol{r}'|^{-1} + f_{xc}(\boldsymbol{r},\boldsymbol{r}',\omega) \quad (49)$$

the $f_{xc}(\boldsymbol{r},\boldsymbol{r}',\omega)$ term is the derivative (resulting in a functional) of the time-dependent exchange potential energy, again the $E_{XC}[\rho]$ term, with respect to the time-dependent density. The derivative is reckoned at the ground-state density [122,123]. The iterative solution of the Casida equation provides the excitation (and de-excitation) energies, the eigenvalues of the matrix Ω. X and Y are the relevant excitations and de-excitations eigenvectors, respectively. Notably, the $E_{XC}[\rho]$ term depends, in principle, on ω thus making the Casida equation non-linear. To a first approximation, the dependence on ω is neglected: adiabatic approximation (making the Casida equations linear). Then the $E_{XC}[\rho]$ ground-state functional is used in the calculations [123], this implies that multiple excitations are neglected. Notably, the neglect of correlation effects in the TDDFT exchange-correlation potential makes TDDFT calculations to be equivalent to TDHF calculations, then disregarding de-excitation processes (i.e. pose $K = 0$ in the Casida equation, Tamm–Dancoff approximation) makes TDFTF equivalent to CIS calculations. The TDDFT method for the calculation of electronic spectra, and relevant optical band gap, is used in the theoretical characterization of the series of ploythiophenes studied in ref [26] and perylene/TCNQ-Fx cocrystals case study, 4.2.2 section of this thesis [27].

Appendix 4

Acronyms

B3LYP	Becke 3-Parameter (Exchange), Lee, Yang and Parr functional
CAM	Coulomb Attenuating Method, long range corrected functional
CDFT	Constrained Density Functional
CI	Configuration Interaction
DFT	Density Functional Theory
HF	Hartree Fock
HOMO	Highest Occupied Molecular Orbital
IR	Infra red
LUMO	Lowest Unoccupied Molecular Orbital
MCSCF	MultiConfiguration Self Consistent Field
Method-D	Calculation *Method* including (-D) dispersion force (Van der Waals) correction
MO	Molecular Orbital
MPn	Moller-Plesset (*n*-th order) perturbation method
PAH	Polycyclic Aromatic Hydrocarbon
PAW	projector augmented wave
PBC	Periodic Boundary Conditions
PBE	Perdew, Burke, and Ernzerhof exchange-correlation functional
PCPDT-BT	Poly[2,6-(4,4-bis-(2-ethylhexyl)-4H-cyclopenta [2,1-b;3,4-b′]dithiophene)-alt-4,7(2,1,3-benzothiadiazole)]
PES	Potential Energy Surface
QM	Quantum mechanics
RHF	Restricted HF
ROHF	Restricted Open-Shell HF
SCF	Self Consistent Field
SOMO	Singly Occupied Molecular Orbital
SVWN	Slater exchange Vosko, Wilk and Nusair functional
TCNQ	tetracyanoquinodimethane
TDDFT	Time Dependent DFT
TTF	tetrathiafulvalene
UHF	Unrestricted HF